Ion-specific and pore-size effects on electrochemical performance of graphene-based electrodes and machine learning-assisted device-level design

A thesis submitted in total fulfillment for the
degree of Doctor of Philosophy

Longbing Qu

ORCID: 0000-0001-9725-2738

Supervisors: A/Prof. Zhe Liu[1], Prof. Dan Li[2]

1. Department of Mechanical Engineering
2. Department of Chemical Engineering

The University of Melbourne

February 2020

Abstract

Electrochemical energy storage devices (EESDs), such as supercapacitors and batteries, are important players in the energy field with the ability to store energy resources and supply continuous electrical energy. A key challenge of EESDs lies in the trade-off between energy density and power delivery. The performance of the EESDs mainly depends on the electrolytes and nanopore size of the electrodes. However, due to the highly complex interplay of the electrolytes (such as ions type, ion concentration, etc.) and electrodes (such as pore size, surface charge property, and electrode thickness, etc.), the designing of EESDs with high energy density and fast power delivery is a very challenging task.

This thesis aims to address some of the challenging issues in this field. Taking advantage of the nanoporous graphene-based electrodes with relatively simple and tunable structures, the research reported therein is devoted to studying the types of ion and slit-pore size effects on the electrochemical performance and the development of a new method for the efficient design of energy storage devices. Generally, this thesis presents three research works for energy storage. The first work is to identify the ion-specific effects on electrical double layer (EDL) capacitance, especially the co-ion effects on the EDL performance. Through a comprehensive study of monovalent ions, such as H^+, Li^+, Na^+, K^+, Cs^+, $BMIM^+$, and Cl^-, in 10 nm, 1 nm, and 0.7 nm slit-pores, our research results indicate the intrinsic ion surface adsorption effect plays an important role in determining the EDL capacitance. Secondly, this thesis investigates the interface redox-reaction under nanoconfinement, in which the electrochemical reaction rates of nanoconfined I^- and Zn^{2+} ions were systematically investigated. The results show the ions in a slit-pore of 1nm exhibit a higher electrochemical reaction rate than in a slit-pore of 10nm, which could provide valuable clues for establishing new electrochemical theories related to nanoconfinement. Lastly, the machine learning method is used to establish a comprehensive quantitative relationship between capacitance and structure of supercapacitors, helping to accelerate the optimal design of graphene-based EESDs on an integrated system device level for practical applications.

In summary, the comprehensive discussion of the ion type effects under different nanoconfinement levels on EDL capacitance and slit-pore size effects on charge transfer across the interface in graphene-based electrodes could improve our understanding of the charge storage mechanism of nanoporous electrodes for the energy storage community. In addition, the successful demonstration of the machine learning method for the efficient design of supercapacitor on device-level could stimulate similar device-level design ideas in other research fields related to electrocatalysis, capacitive deionization, and nanofluidic devices.

Declaration of Authorship

I, Longbing Qu, declare that this thesis titled, 'Ion-specific and pore-size effects on electrochemical performance of graphene-based electrodes and machine learning-assisted device-level design' and the work presented in it are my own. I confirm that:

1. This thesis comprises only my original work towards the PhD.
2. Due acknowledgment has been made in the text to all other materials used.
3. This thesis is less than 100,000 words in length, exclusive of tables, figures, maps, bibliography and appendices as approved by the Research Higher Degrees Committee.

Longbing Qu

February 2020

Preface

i. **Chapter 3** is “Ion-specific effect on the EDL capacitance of nanoporous graphene-based electrodes”

- All the results in this chapter are my work.

ii. **Chapter 4** is “Nanoconfinement effects on the electrochemical performance of the redox-active electrolytes”

- All the results in this chapter are my work.

iii. **Chapter 5** is “Machine learning-assisted device-level design of graphene-based supercapacitors”

- All the results in this chapter are my work.
- Random forest regressor is developed under the guidance of Dr. Benyamin Motevalli from CSIRO, Australia.

Acknowledgment

The past four years of PhD study journey in Melbourne have been an important part of my life. Taking this opportunity, I would like to express my sincere thanks to many people who have helped me during these years.

First, I would like to express my gratitude to my supervisors Associate Professor Zhe Liu and Professor Dan Li, for their guidance, patience, support, and in-depth discussions with me about my PhD research. Their knowledge, personality, passion, and views on science have made my PhD experience rewarding.

Next, I would like to thank Advisory Committee Members for their time and precious suggestions to me about my PhD research. I would like to thank Melbourne School of Engineering for the scholarship support for my PhD study. I would like to thank ARC for the funding support of this PhD research.

Also, I would like to thank Ben for the guidance and discussion of the machine learning project. I also would like to thank Gregory Hill for his help in doing some grammar editing of my thesis.

I am grateful to all the group members from Zhe and Dan’s group. It has been an enjoyable experience working with them. I would like to give special thanks to Peiyao Wang for her accompanying and support during the whole PhD study. Many thanks to Pei Yu, Lianhai Zu, and Yang Cao for their kindness help on SEM characterization.

Last but not least, I would like to thank the selfless support from my parents, my old sister, my brother-in-law, and all my friends.

Contents

Abstract ii

Preface v

Acknowledgment vi

Contents vii

List of Figures x

List of Tables xx

Abbreviations xxi

Symbols xxii

Chapter 1 Introduction 1

Chapter 2 Literature Review 7

2.1 Basic knowledge of EDLCs and electrochemical redox-type energy storage devices 7
2.2 Research progress on electrochemical double-layer electrodes 10
  2.2.1 Capacitance of nanoporous electrodes under nanoconfinement 10
  2.2.2 Charging storage mechanism of nanoporous electrodes under nanoconfinement 13
2.3 Research progress on pseudocapacitive electrodes 23
2.4 Research progress on the supercapacitor devices (EDLCs) design 26
2.5 Research aims 29

Chapter 3 Ion-specific effect on the EDL capacitance of nanoporous graphene-based electrodes 30

3.1 Introduction 30
3.2 Materials and methods 32
  3.2.1 Synthesis and characterization of nanoporous graphene-based materials 32
  3.2.2 Electrochemical characterization of multilayered graphene-based materials 34
3.3 Results and discussion 35
  3.3.1 Nanoconfined counter-ion effects on the EDL capacitance of nanoporous electrodes under negative polarization 35
  3.3.2 Nanoconfined co-ion effects on the EDL capacitance of nanoporous electrodes 40
  3.3.3 Proton effect on the EDL capacitance of nanoporous graphene-based electrodes 43
3.4 Discussions of proton effects on EDL capacitance from electrochemical characterization 47
3.5 Discussions of proton effects on EDL capacitance from simulations 53

3.5.1 Classic Poisson-Nernst-Plank (PNP) model with one stern layer....................................... 54
3.5.2 Classic PNP model accounting for the stern layer thickness of cations and anions. 57
3.5.3 Poisson-Boltzmann (PB) theory accounting for the ion volume-exclusion effect.............. 58
3.6 Conclusion... 59

Chapter 4 Nanoconfinement effects on the electrochemical performance of the redox-active electrolytes 62

4.1 Introduction 62
4.2 Materials and Methods 64
4.2.1 Synthesis of nanoporous graphene-based electrodes. 64
4.2.2 Electrochemical characterization of nanoporous graphene-based electrodes. 65
4.2.3 The simulation model for EDL structure of nanoporous graphene-based electrodes 65
4.3 Experimental Results and Discussion 66
4.3.1 Nanoconfined iodide ions on the charge storage performance of nanoporous graphene-based electrodes. 66
4.3.2 Nanoconfined zinc ions on the charge storage performance of nanoporous graphene-based electrodes. 87
4.3.3 Nanoconfinement effects on the charge storage performance of nanoporous graphene-based devices 90
4.4 Conclusion.. 92

Chapter 5 Machine learning-assisted device-level design of graphene-based supercapacitors 95

5.1 Introduction 95
5.2 Overall picture of this project.. 97
5.3 Methodology 97
5.3.1 Synthesis and characterization of NPGEs. 97
5.3.2 Electrochemical characterization of NPGEs... 98
5.3.3 Artificial neural network model.. 99
5.4 Results.. 100
5.4.1 Experimental results 100
5.4.2 Results of the ANN model.. 103
5.4.3 Electrode performance prediction of positive and negative electrodes using developed ANN models. 107
5.4.4 On-demand optimizing design of supercapacitors on device-level 109
5.5 Discussion 112
5.5.1 Experiment confirmation based on the predictive matching parameters........................... 112
5.5.2 Other design parameters and design results.. 113
5.5.3 Important Design Parameters.. 117

5.6 Conclusions 119
Chapter 6 Conclusions and Perspective 120
6.1 Conclusions 120
6.2 Perspective 121
References 123

List of Figures

Figure 1.1. (a) A conceptual presentation of electrical energy storage devices.[9] **(b)** Ragone plot for various electrical energy storage devices.[17] 1

Figure 1.2. A tale of two plots. Ragone plots of different scale electrical energy storage devices.[29] 2

Figure 2.1. (a) Stern model of the electrical double-layer formed at a positively charged electrode in an aqueous electrolyte; **(b)** An electrical double-layer capacitor using porous electrodes.[94] 8

Figure 2.2. The features of EDL and redox-type energy storage devices. **(a)** cyclic voltammetry, galvanostatic profile, storage mechanism, and intrinsic kinetics of EDLCs; **(b)** and **(c)** cyclic voltammetry, galvanostatic profile, storage mechanism, and intrinsic kinetics of pseudocapacitors. (examples: hydrated RuO_2 birnessite MnO_2). **(d)** cyclic voltammetry, galvanostatic profile, storage mechanism, and intrinsic kinetics of batteries.[9] 9

Figure 2.3. Relationship between specific capacitance and average pore size of nanoporous electrode in1.5 M NEt4BF4/CAN.[119] 10

Figure 2.4. (a) Volumetric capacitances with varied charging/discharging current densities for different channel size graphene membranes in 1.0 M H_2SO_4 electrolyte; **(b)** Volumetric capacitances with varied charging/discharging current densities for different channel size graphene membranes in the $EMIMBF_4$/AN electrolyte; **(c)**The relation between the volumetric capacitance and the mass loading (thickness).[47] 11

Figure 2.5. The capacitance of pillared graphene materials with the pore size of 0.78 nm, 0.80 nm, and 0.86 nm and reduced graphene materials in different 1 M BF4 based ionic liquid/ACN electrolytes with a scan rate of 20 mV/s in the potential ranges of **(a)** −1.0 to 0.1 V *vs.* Ag and **(b)** 0.1 to 1.0 V *vs.* Ag.[129] 13

Figure 2.6. In-pore ion populations for supercapacitor electrodes at different states of charge in the range −1.5 V to +1.5 V. a–c, In-pore ion populations for electrolyte concentrations of 1.5M **(a)**, 0.75M **(b)** and 0.5M **(c)**.[135] 14

Figure 2.7. in situ measurement of ion diffusion and population inside the nanopore. **(a)** and **(b)** are the cations and anions diffusion in YP50F- PEt_4BF_4/CAN with different working voltages; **(c)** total in-pore ion populations at different cell voltages; **(d)** schematic figures of

charge storage mechanisms; **(e)** relationship between total in-pore population and in-pore cations diffusion coefficient.[139] 16

Figure 2.8. Effect of confinement on the efficiency of charge storage for applied potentials of 0V **(a)** and 1V **(b)** in the case of the ACN-based electrolyte.[48] 17

Figure 2.9. Specific capacitance of nanoporous electrodes tested in 1 and 0.05 M aqueous working electrolytes with the scan rate of 0.5 mV/s; **(b)** Charge transfer ration of different alkaline cations on nano-slit porous graphene and graphene basal plane surface; **(c)** Binding energies and intercalation barrier of various alkaline cations on nano-slit porous graphene and basal plane graphene surface; **(d)** Calculating Binding energy of the various alkaline cations on nanoporous graphene with different pore diameters from density functional theory.[54] 19

Figure 2.10. The relative number density of different electrolyte ions as a function of distance from the graphene cathode surface with a charge of 0, –0.015, and –0.041 e/C-atom, respectively. The shaded regions represent the IHL and OHL.[70] 20

Figure 2.11. Cyclic voltammetry curves of the YP-50F electrode in four different SiO_2-grafted ILs with the same concentration of 0.25M in propylene carbonate (PC) at the different working potential range for 5 mV/s. **(a)** SiO_2-IL-$BMIM^+$; **(b)** SiO_2-IL-$NTf2^-$; **(c)** SiO_2-IL-$NBu4^+$, and d SiO_2-IL-$PF6^-$.[128] 21

Figure 2.12. **(a)** CV curves of the $Ti_3C_2T_x$-based supercapacitor electrodes in NaOH, KOH, and LiOH electrolytes at the scan rate of 20 mV/s; **(b)** CV curves of the $Ti_3C_2T_x$-based supercapacitor electrodes in K_2SO_4, $Al_2(SO_4)_3$, and $Al(NO_3)_3$ electrolytes at 20 mV/s; **(c)** Rate performances of the $Ti_3C_2T_x$-based supercapacitor electrodes in different aqueous working electrolytes.[155] 24

Figure 2.13. **(a)** XRD spectra of the achieved 1T phase MoS_2 nanosheets (i) and cycled MoS_2 film (ii–vi) in different aqueous sulfate-based electrolytes: Li_2SO_4 (ii), Na_2SO_4 (iii), K_2SO_4 (iv), H_2SO_4 (v), and in TEA BF4/MeCN organic electrolyte (vi). **(b)** Schematics of restacked non-intercalated and intercalated 1T MoS_2 nanosheets.[156] 25

Figure 2.14. **(a)** Molecule structure of BMImTFSI IL and the bi-redox IL; **(b)** Self-discharge current for the devices based on PICA with BMImTFSI (blue line) or 0.5Mbiredox IL in BMImTFSI (red line) at room temperature; **(c)** Cyclic voltammetry at 5mV/s with 0.5M bi-redox IL in BMIm TFSI (solid line) and pure BMIm TFSI (dashed line), respectively; **(d)** CVs at 5mV/s of the PICA cell with 0.5M bi-redox IL in BMImTFSI (solid line), pure BMImTFSI (dashed line), and pure bi-redox IL (green line).[157] 26

Figure 2.15. (a) Relation among cell voltage retention, mass ratio and specific energy retention at the middle (circle) and one-third points (triangular) cases.[159] **(b)** Cyclic voltammograms for cells assembled with EMI-TFSI electrolyte showing the response of the whole cell (black line) as well as the individual electrodes at different operating voltage.[91] 28

Figure 3.1. Illustration of synthesizing of graphene-based electrodes with tunable nanopore size. 33

Figure 3.2. Illustration of the electrochemical test setup. 34

Figure 3.3. (a), (b), (c) and **(d)** show the CV curves of NPGE-10nm in 1 M LiCl, 1 M NaCl, 1 M KCl, 1 M CsCl, 1 M BmimCl and 1 M HCl electrolytes under the scan rates of 2 mV/s, 20 mV/s, and 200 mV/s and 1,000 mV/s, respectively...37

Figure 3.4. (a), (b), (c) and **(d)** show the CV curves of NPGE-1nm in 1 M LiCl, 1 M KCl, 1 M BmimCl and 1 M HCl electrolytes under the scan rates of 2 mV/s, 20 mV/s, and 200 mV/s and 1,000 mV/s, respectively...38

Figure 3.5. (a), (b), (c) and **(d)** show the CV curves of NPGE-0.7nm in 1 M LiCl, 1 M KCl, 1 M BmimCl and 1 M HCl electrolytes under the scan rates of 2 mV/s, 20 mV/s, and 200 mV/s and 1,000 mV/s, respectively...40

Figure 3.6. (a), (b), (c) and **(d)** show the CV curves of NPGE-10nm in 1 M LiCl, 1 M KCl, 1 M BmimCl and 1 M HCl electrolytes for positive charge under the scan rates of 2 mV/s, 20 mV/s, and 200 mV/s and 1,000 mV/s, respectively...42

Figure 3.7. (a), (b), (c) and **(d)** show the CV curves of NPGE-1nm in 1 M LiCl, 1 M KCl, 1 M BmimCl and 1 M HCl electrolytes for positive charge under the scan rates of 2 mV/s, 20 mV/s, and 200 mV/s and 1,000 mV/s, respectively...42

Figure 3.8. (a), (b), (c) and **(d)** show the CV curves of NPGE-0.7nm in 1 M LiCl, 1 M KCl, 1 M BmimCl and 1 M HCl electrolytes for positive charge under the scan rates of 2 mV/s, 20 mV/s, and 200 mV/s and 1,000 mV/s, respectively...43

Figure 3.9. (a) and **(b)** show the CV curves of NPGE-10nm in 1 M KCl, 1 M HCl and mixture electrolytes for positive charge under the scan rates of 2 mV/s and 1,000 mV/s, respectively; **(c)** and **(d)** show the capacitance and normalized capacitance of the NPGE-10nm in 1 M KCl, 1 M HCl, and mixture electrolytes for the positive charge under different charge rates.........45

Figure 3.10. (a) and **(b)** show the CV curves of NPGE-1nm in 1 M KCl, 1 M HCl, and mixture electrolytes for the positive charge under the scan rates of 2 mV/s and 1000 mV/s, respectively;

(c) and **(d)** show the capacitance and normalized capacitance of the NPGE-1nm in 1 M KCl, 1 M HCl, and mixture electrolytes for the positive charge under different charge rates...........46

Figure 3.11. **(a)** and **(b)** show the CV curves of NPGE-0.7nm in 1 M KCl, 1 M HCl, and mixture electrolytes for the positive charge under the scan rates of 2 mV/s and 1000 mV/s, respectively; **(c)** and **(d)** show the capacitance and normalized capacitance of the NPGE-0.7nm in 1 M KCl, 1 M HCl, and mixture electrolytes for the positive charge under different charge rates. 47

Figure 3.12. **(a)** and **(b)** show OCP and PZC results of the NPGE-10nm in 1 M KCl, 1 M HCl, and mixture electrolytes. 48

Figure 3.13. **(a)** Nyquist plots of NPGE-10nm in 1 M KCl, 1 M HCl, and mixture electrolytes at the frequency of 1000 kHz to 10 mHz at the potential of PZC; **(b)** A zoom at high frequencies; **(c)** Nyquist plots of NPGE-10nm in 1 M KCl, 1 M HCl, and mixture electrolytes at the frequency of 1000 kHz to 10 mHz at the 0.1 V vs. PZC; **(d)** A zoom at high frequencies. 49

Figure 3.14. **(a)** Potential changes (‘self-discharge profile’) of the NPGE-10nm under open-circuit conditions (after galvanostatic charging at 0.2 A/g for 60s); **(b)** Galvanostatic discharge curves of the NPGE-10nm after self-discharge for 30 mins in 1 M HCl and KCl electrolytes. 50

Figure 3.15. **(a)** and **(b)** show OCP and PZC results of the NPGE-0.7nm in 1 M KCl, 1 M HCl, and mixture electrolytes. 51

Figure 3.16. **(a)** Nyquist plots of NPGE-0.7nm in 1 M KCl, 1 M HCl, and mixture electrolytes at the frequency of 1000 kHz to 10 mHz at the potential of PZC; **(b)** A zoom at high frequencies; **(c)** Nyquist plots of NPGE-0.7nm in 1 M KCl, 1 M HCl, and mixture electrolytes at the frequency of 1000 kHz to 10 mHz at the 0.1 V *vs.* PZC. (d) A zoom at high frequencies. 52

Figure 3.17. **(a)** Potential changes (‘self-discharge profile’) of the NPGE-0.7nm porous electrode under open-circuit conditions (after galvanostatic charging at 0.2 A/g for 60s); **(b)** galvanostatic discharge curves of the NPGE-0.7nm after self-discharge for 30 mins in 1 M HCl and KCl electrolytes. 53

Figure 3.18. 2D continuum modeling system with 6 layers of graphene sheets with L = 55 nm, h = 10 nm, and d = 2 nm. 55

Figure 3.19. (a), (b) and **(c)** show the simulated CV curves of 10 nm pore size graphene layers in 1 M KCl and 1 M HCl electrolytes under the scan rates of 5 V/s, 500,000 V/s, and 5,000,000 V/s, respectively 56

Figure 3.20. (a), (b) and **(c)** show the ion distribution curves of 10 nm pore size graphene layers in 1 M KCl, and 1 M HCl electrolytes charged to 0.35V with the scan rates of 5 V/s (10th cycle charge), 5,000,000 V/s (10th cycle charge), and 5,000,000 V/s (first cycle charge), respectively 57

Figure 3.21. (a) shows the ion distribution curves of 10 nm pore size graphene layers in 1 M KCl and 1 M HCl electrolytes charged to 0.35V with thermodynamic charging condition; **(b)** The stored surface charge density of the electrode in 1 M KCl and 1 M HCl electrolytes. 58

Figure 3.22. (a) shows the ion distribution curves of 10 nm pore size graphene layers in 1 M KCl and 1 M HCl electrolytes charged to 0.35V with thermodynamic charging condition; **(b)** Potential profiles of the EDL inside the slit channel; **(c)** The stored surface charge density of the electrode in 1 M KCl and 1 M HCl electrolytes. 59

Figure 4.1. Reduction potential and demonstrated volumetric capacity for various aqueous redox couples.[116] 65

Figure 4.2. CV curves of NPGE-10nm and NPGE-1nm in 0.1 M ZnI_2 aqueous electrolyte under the scan rates of 0.5 mV/s **(a)**, 2 mV/s **(b)**, and 5 mV/s **(c)** and 20 mV/s **(d)**, respectively. 68

Figure 4.3. Nyquist plots of NPGE-10nm and NPGE-1nm in 0.1 M ZnI_2 electrolytes at the frequency of 1,000 kHz to 100 mHz at the working potential of 1.3 V vs. Zn/Zn^{2+} **(a)**, 1.4 V vs. Zn/Zn^{2+} **(b)**, 1.5 V vs. Zn/Zn^{2+} **(c)** and 1.6 V vs. Zn/Zn^{2+} **(d)**. Ref: Zn/Zn^{2+}. 69

Figure 4.4. CV curves of NPGE-10nm and NPGE-1nm in 0.1 M ZnI_2 electrolytes at the scan rate of 0.5 mV/s **(a)**, 2 mV/s **(b)**, and 20 mV/s **(c)** with the capacitive working potential range. 70

Figure 4.5. Fitting line of the CV curves of NPGE-10nm **(a)** and NPGE-1nm **(b)** at the scan rates of 0.5 mV/s with low overpotential range; **(c)** The onset potential of the I^-/I^{3-} redox-reaction inside NPGE-10nm and NPGE-1nm. **(d)** The slope of the fitting line at the overpotential range of [0, 0.01V]. 72

Figure 4.6. (a) ln (i)-potential curves of electrodes with 10 nm pore size and the corresponding linear fitting line at the potential range of [1.225V, 1.35 V]; **(b)** ln (i)-potential curves of the

electrodes with 1.0 nm pore size and the corresponding linear fitting line at the potential range of [1.225V, 1.46 V]; **(c)** current-potential curves of the electrodes with 10 nm and 1nm pore sizes. Electrolyte: 0.1 M ZnI_2. 74

Figure 4.7. 2D continuum modeling system with 6 layers of graphene sheets with L=55 nm, h = 10 nm, and d = 2 nm. 75

Figure 4.8. (a) shows the surface charge density of the GSE-10 nm and GSE-1nm at the scan rate of 5 V/s; **(b)** and **(c)** show the ion distribution curves of the GSE-10nm and GSE-1nm at the scan rate of 5 V/s; **(d)** shows the average surface concentration of I^- on the GSE-10nm and GSE-1nm at the scan rate of 5 V/s. Electrolyte: 0.1 M ZnI_2, working voltage: 0-0.5 V. 76

Figure 4.9. (a) shows the surface charge density of the GSE-10 nm and GSE-1nm with cycling charge/discharge at the scan rate of 5,000,000 V/s; **(b)** and **(c)** show the ion distribution curves of the GSE-10 nm and GSE-1nm after initial charging at the scan rate of 5,000,000 V/s; **(d)** and **(e)** present the average surface concentration of I^- during the cycling dynamic charging process on the GSE-10 nm and GSE-1nm at the scan rate of 5,000,000 V/s; **(f)** shows the average surface concentration of I^- on the GSE-10 nm and GSE-1nm for the initial charging process at the scan rate of 5,000,000 V/s. Electrolyte: 0.1 M ZnI_2, working voltage: 0-0.5 V. one cycle: 200 ns. 78

Figure 4.10. CV curves of NPGE-10nm and NPGE-1nm in 1.0 M ZnI_2 aqueous electrolyte under the scan rates of 0.5 mV/s **(a)**, 2 mV/s **(b)**, and 5 mV/s **(c)** and 20 mV/s **(d)**, respectively. 80

Figure 4.11. Nyquist plots of NPGE-10nm and NPGE-1nm in 1.0 M ZnI_2 electrolyte at the frequency of 1000 kHz to 100 mHz at the working potential of 1.2 V vs. Zn/Zn^{2+} **(a)**, 1.3 V vs. Zn/Zn^{2+} **(b)**, 1.4 V vs. Zn/Zn^{2+} **(c)** and 1.5 V vs. Zn/Zn^{2+} **(d)**. Ref: Zn/Zn^{2+}. 81

Figure 4.12. CV curves of NPGE-10nm and NPGE-1nm in 1.0 M ZnI_2 electrolyte with the scan rate of 0.5 mV/s **(a)**, 2 mV/s **(b)**, and 20 mV/s **(c)** at the capacitive working potential range. 82

Figure 4.13. Fitting line of the CV curves of NPGE-10nm **(a)** and NPGE-1nm **(b)** with the scan rates of 0.5 mV/s at low overpotential range; **(c)** The onset potential of the I^-/I^{3-} redox-reaction inside the NPGE-10nm and NPGE-1nm; **(d)** The slope of the fitting line at the overpotential range of [0, 0.01V]. 83

Figure 4.14. (a) ln (i)-potential curves of NPGE-10nm and the corresponding linear fitting line at the potential range of [1.25V, 1.38 V]; **(b)** ln (i)-potential curves of NPGE-1nm and the

corresponding linear fitting line at the potential range of [1.25V, 1.38 V]; **(c)** Current-potential curves of NPGE-10nm and the corresponding linear fitting line at the potential range of [1.25V, 1.38 V]; **(d)** Current-potential curves of NPGE-1nm and the corresponding linear fitting line at the potential range of [1.25V, 1.38 V]. 84

Figure 4.15. **(a)** shows the surface charge density of the GSE-10 nm and GSE-1nm at the scan rate of 5 V/s; **(b)** and **(c)** show the ion distribution curves of the GSE-10nm and GSE-1nm at the scan rate of 5 V/s; **(d)** shows the average surface concentration of I^- on the GSE-10nm and GSE-1nm at the scan rate of 5 V/s. Electrolyte: 1.0 M ZnI_2, working voltage: 0-0.5 V. 85

Figure 4.16. **(a)** shows the surface charge density of the GSE-10 nm and GSE-1nm with cycling charge/discharge at the scan rate of 5,000,000 V/s; **(b)** and **(c)** show the ion distribution curves of the GSE-10 nm and GSE-1nm after initial charging at the scan rate of 5,000,000 V/s; **(d)** and **(e)** present the average surface concentration of I^- during the cycling dynamic charging process on the GSE-10 nm and GSE-1nm at the scan rate of 5,000,000 V/s. Electrolyte: 1.0 M ZnI_2, working voltage: 0-0.5 V. one cycle: 200 ns. 86

Figure 4.17. CV curves of NPGE-10nm and NPGE-0.7nm at the scan rate of 0.5 mV/s **(a)**, 20 mV/s **(b)**, at the capacitive working potential range. CV curves of NPGE-10nm and NPGE-0.7nm with the electrochemical working potential at the scan rate of 0.5 mV/s **(c)**, 20 mV/s **(d)**. Fitting line of the CV curves of NPGE-10nm **(e)** and NPGE-0.7nm **(f)** with the scan rates of 0.5 mV/s at low overpotential range (5 mV); **(g)** The onset potential of the Zn^{2+}/Zn on the NPGE-10nm and NPGE-0.7nm; **(h)** The slope of the fitting line at the overpotential range of [0, 0.005V]. 88

Figure 4.18. Initial charge curves of NPGE-10nm and NPGE-0.7nm at the charge rate of 0.5 mA/cm^2 **(a)**, 25 mA/cm^2 **(b)**; CE performance of NPGE-10nm and NPGE-0.7nm at different charge rates **(c)**; **(d)**. cycling performance of NPGE-10nm and NPGE-0.7nm at the charge rate of 25 mA/cm^2. 90

Figure 4.19. CV curves of NPG-10nm and NPG-1nm devices under the scan rates of 0.5 mV/s **(a)**, 2 mV/s **(b)**, and 5 mV/s **(c)** and 20 mV/s **(d)**, respectively. 91

Figure 4.20. **(a)** Charge/discharge curves of NPGD-10nm and NPGD-1nm at the charge rate of 1 mA/cm^2; **(b)** Cycling performance of NPGD-10nm and NPGD-1nm at the charge rate of 10 mA/cm^2. The capacity retention of NPGD-10nm and NPGD-1nm after resting at OCV for 2 hours **(c)** and 6 hours **(d)**. 92

Figure 5.1. Flow chart of this project. 97

Figure 5.2. (a) and **(b)** are the SEM images of our synthesized freezing dry and H_2SO_4 mediated NPGEs respectively....................98

Figure 5.3. Three-electrode configuration setup, where the reference electrode is a saturated calomel electrode (SCE), the counter electrode is the hydrogel graphene membranes, which the mass is two times that of working electrodes. 99

Additionally, according to the previous research and published papers, pore size, electrode thickness, charging rate, working voltage, and electrolytes play a significant role in determining the capacitance of electrodes. Therefore, to obtain the insightful quantitative relationship of these parameters and electrode performance, we firstly applied nanoporous graphene-based membranes with different pore size and thickness as the materials platform in 1 M KCl electrolyte. Then we studied the positive and negative charging/discharging under a dynamic process using the three-electrode configuration. Some preliminary experimental results and data were collected....................100

Figure 5.4. (a), **(b)**, and **(c)** show the capacitance of NPGEs with various pore size and thickness under the scan rates of 2 mV/s, 10 mV/s, and 50 mV/s for the positive electrodes; **(d)**, **(e)**, and **(f)** show the capacitance of graphene membrane electrodes with various pore size and thickness under the scan rates of 2 mV/s, 10 mV/s, and 50 mV/s for the negative electrodes, respectively. 101

Figure 5.5. (a) (b) and **(c)** show the differential charging capacitance of graphene membrane positive (0.25-0.8 V) and negative (0.25- (-0.8) V) electrodes with 0.8 nm, 1.0 nm, and 1.7 nm pore size at the mass loading of 12 mg/cm2 under various scan rates in 1 M KCl; **(a1) (b1)** and **(c1)** show the differential charging capacitance of graphene membrane positive (0.25-0.8 V) and negative (0.25-(-0.8) V) electrodes with 0.8 nm, 1.0 nm, and 1.7 nm pore size with different mass loading or thickness at the scan rate of 50 mV/s in 1 M KCl. *vs.* Saturated Calomel Electrode (SCE). 102

Figure 5.6. ANN model simplification based on experiment results and domain knowledge. 103

Figure 5.7. Distribution of specific volumetric capacitance for **(a)** positive and **(b)** negative electrode. Using stratification to split the experimental dataset: **(c)** positive and **(d)** negative. 104

Figure 5.8. (a) and **(b)** are the loss function value of positive and negative models with 56 different learning rates, respectively.....................105

Figure 5.9. (a), **(b)** and **(c)** are the model training results *vs.* experimental data, model validation results *vs.* experimental data and model test results *vs.* experimental data for positive electrode ANN model when the learning rate is 0.62; **(d)**, **(e)** and **(f)** are the model training results *vs.* experimental data, model validation results *vs.* experimental data and model test results *vs.* experimental data for negative electrode ANN model when the learning rate is 0.2. 106

Figure 5.10. (a) and **(b)** are the cross-validation learning curves of the built positive and negative ANN models 107

Figure 5.11. (a), **(b)**, and **(c)** are the 3D surface figures (specific volumetric capacitance *vs.* pore size and thickness) based on the designed ANN model under the scan rates of 2 mV/s, 10 mV/s, and 50 mV/s for the positive electrodes, respectively; **(d)**, **(e)** and **(f)** are the 3D surface figures (specific volumetric capacitance *vs.* pore size and thickness) based on the designed ANN model under the scan rates of 2 mV/s, 10 mV/s, and 50 mV/s for the negative electrodes, respectively. The Triangle with black color located at the surface of 3D figures are the corresponding experimental data. 108

Figure 5.12. (a), **(b)**, and **(c)** are the 3D surface figures (specific volumetric capacitance *vs.* pore size and thickness) based on the designed ANN model under the scan rates of 2 mV/s, 10 mV/s, and 50 mV/s for the positive electrodes with the consideration of separator and current collectors, respectively. (d), (e) and (f) are the 3D surface figures (specific volumetric capacitance *vs.* pore size and thickness) based on the designed ANN model under the scan rates of 2 mV/s, 10 mV/s, and 50 mV/s for the negative electrodes with the consideration of separator and current collectors. The total thickness of separator and current collectors are 65 um. ... 109

Figure 5.13. (a), **(d)** and **(g)** are the top 100 specific volumetric capacitances of supercapacitor and the corresponding specific volumetric capacitances of positive and negative electrodes at the scan rate of 6 mV/s, 30 mV/s and 75 mV/s, respectively. **(b)**, **(e)** and **(h)** are the corresponding pore size of positive and negative electrodes for the top 100 matching combinations. **(c)**, **(f)** and **(i)** are the corresponding thickness of positive and negative electrodes for the top 100 matching combinations. 111

Figure 5.14. (a), **(d)** and **(g)** are the experiment CV curves of graphene-based supercapacitor devices based on predictive matching parameters at the scan rates of 6, 30 and 75 mV/s respectively; **(b)**, **(e)** and **(h)** are the experiment potential-time curves of the positive electrodes based on predictive matching parameters at the scan rates of 6, 30, and 75 mV/s respectively;

(c), **(f)** and **(i)** are the experiment and prediction capacitances based on predictive matching parameters at the scan rates of 6, 30, and 75 mV/s respectively. 113

Figure 5.15. Capacitance results comparison for the 6 mV/s design study 114

Figure 5.16. **(a)** and **(b)** are the experiment potential-time curve of the positive electrode and experiment CV curve of graphene-based supercapacitor device for the symmetric design with pore size of 0.8 nm, thickness of 22 um for both positive and negative electrodes at the scan rate of 30 mV/s; **(c)** the experiment capacitances based on predictive optimal and 75 mV/s optimal design parameters for the 30 mV/s design study; **(d)** and **(e)** are the experiment potential-time curves of the positive electrodes and experiment CV curves of graphene-based supercapacitor devices for the symmetric design with pore size of 1.25 nm, thickness of 100 um for both positive and negative electrodes at the scan rate of 30 mV/s; **(f)** the experiment capacitances based on predictive optimal and symmetric optimal design parameters for the 30 mV/s design study. 115

Figure 5.17. **(a)** and **(b)** are the experiment potential-time curve of the positive electrode and experiment CV curve of graphene-based supercapacitor device for the symmetric design with pore size of 0.8 nm, thickness of 15 um for both positive and negative electrodes at the scan rate of 75 mV/s; **(c)** the experiment capacitances based on predictive optimal and 6 and 30 mV/s optimal design parameters for the 75 mV/s design study; **(d)** and **(e)** are the experiment potential-time curves of the positive electrodes and experiment CV curves of graphene-based supercapacitor devices for the symmetric design with pore size of 1.35 nm, thickness of 73 um for both positive and negative electrodes at the scan rate of 75 mV/s; **(f)** the experiment capacitances based on predictive optimal and symmetric optimal design parameters for the 75 mV/s design study. 116

Figure 5.18. Correlation matrix for **(a)** positive and **(c)** negative electrodes; Feature importance for **(b)** positive and **(d)** negative electrodes. 118

Figure 5.19. **(a)** and **(d)** are the distribution of specific volumetric capacitance of supercapacitor at 6 and 75 mV/s; **(b)** and **(e)** are the correlation matrix among specific volumetric capacitance of supercapacitor and various design parameters at 6 and 75 mV/s; **(c)** and **(f)** are the important level of different design parameters for the final supercapacitor capacitance at the scan rate of 6 and 75 mV/s. 119

List of Tables

Table 3.1 Ion hydrated and dehydrated radius and ionic diffusion coefficients and hydration enthalpies.[167-170] 36

Table 5.1 Pore size and thickness of NPGEs 98

Abbreviations

ANN	Artificial Neural Network
CCG	Chemically Converted Graphene
CV	Cyclic Voltammetry
EDL	Electric Double Layer
EDLCs	Electrochemical Double-Layer Capacitors
EESDs	Electrochemical Energy Storage Devices
EIS	Electrochemical Impedance Spectroscopy
EQCM	Electrochemical Quartz Crystal Microbalance
MGM	Multilayered Graphene Membranes
MD	Molecule Dynamics
ML	Machine Learning
NMR	Nuclear Magnetic Resonance
OCP	Open Circuit Potential
PB	Poisson-Boltzmann
PNP	Poisson-Nernst-Plank
PSD	Pore Size Distributions
PZC	Potential of Zero Charges
SCE	Saturated Calomel Electrode
SDC	Self-DisCharge

Symbols

p	Pore size
v	Charging potential window
$\emptyset$	Electric potential
C	Capacitance of supercapacitor
c_-	Capacitance of negative electrode
c_+	Capacitance of positive electrode
C_s	Specific capacitance of the supercapacitor devices
d	Effective thickness of the electrical double layer
D_i	Diffusivity for species *i*
E	Specific energy density
N_A	Avogadro constant
n_i	Concentration for species *i*
S	Surface area of electrode
S_{trc}	The steric functional
t	Discharge time
V	Voltage
z_i	Valence number for species *i*
ε_0	Vacuum dielectric constant
ε_r	Relative dielectric constant
μ_i	Electro-mobility for species *i*
ρ	Net charge density
Q	Stored charge
d	Average interlayer spacing
f	Charge rate
j	Gravimetric current density
s	Scan rate
t	Thickness of electrodes

Chapter 1 Introduction

Due to the fast depletion of fossil fuels and environmental problems, clean energy presents much higher advantages and exhibits a very promising prospect in the future energy filed.[1-8] At the forefront of clean energy, electrochemical energy storage devices (EESDs) as the green and renewable energy storage devices are suitable and promising for supplying the power and energy for next-generation vehicles and for storing extra energy generated from the solar cell and other clean energy generating systems (**Fig. 1.1a**).[9-16] Based on the charge storage mechanism, there are two types of rechargeable EESDs (**Fig. 1.1b**).[17,18] One is electrochemical double-layer capacitors (EDLCs), which store and delivers energy through ion adsorption/desorption at the interface of electrolyte/electrode.[19-24] The other one is electrochemical redox-active energy storage devices (including pseudocapacitors and batteries), which is based on the reversible faradic redox-reaction to store and deliver electricity.[25-28] Nowadays, nanoporous electrodes with two-dimensional (2D) structure and high specific surface area are widely studied and used to enhance the charge storage capacity in the EES field.[10,13,14]

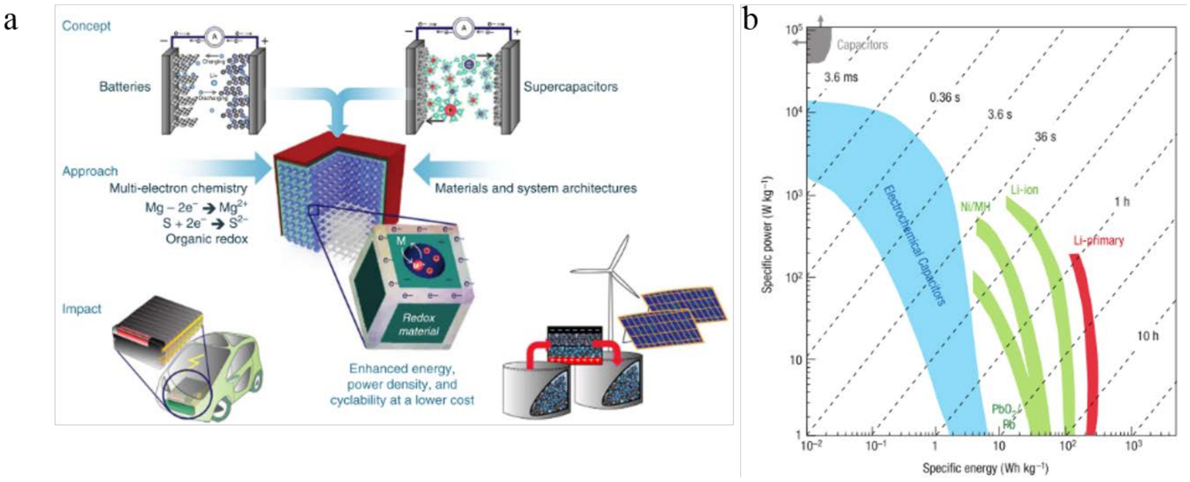

Figure 1.1. (a) A conceptual presentation of electrical energy storage devices.[9] **(b)** Ragone plot for various electrical energy storage devices.[17]

Normally, one individual EESD module is composed of electrodes (positive and negative electrodes), electrolyte, separator, and current collectors (**Fig. 1.2**).[12,29] Currently, most of the published research work for the EESDs is focusing on the discovery of new active materials with high electrochemical activity and design of electrode nanostructures with fast electrode/ion transport properties, aiming for achieving the optimal active materials or morphologies which could exhibit better electrochemical performance, such as high capacity at suitable voltage, fast charge ability, and stable cyclability.[15,30-37] The fundamental understanding focusing on the ion storage and redox electron transfer at the electrode-electrolyte interface for energy storage under different nanoconfinement level is much less.[38-41] The research on the rational and quantitative design of the EESD on device level is rare. A better fundamental understanding of the ion storage and redox electron transfer at the electrolyte-electrode interface is the basis for advancing the design of energy storage devices.[22,42-54] A quantitative and ration design methodology for enhanced performance on the supercapacitor device-level instead of the performance of the individual electrode is vital for practical applications of the developed energy storage systems.[29,55] However, most of the previous works on supercapacitor device design apply the trial and error strategy in experiments, which is neither efficient nor cost-effective.[56-60] Using the trial and error strategy also misses the opportunity to gain an in-depth understanding of rational energy storage device designs.

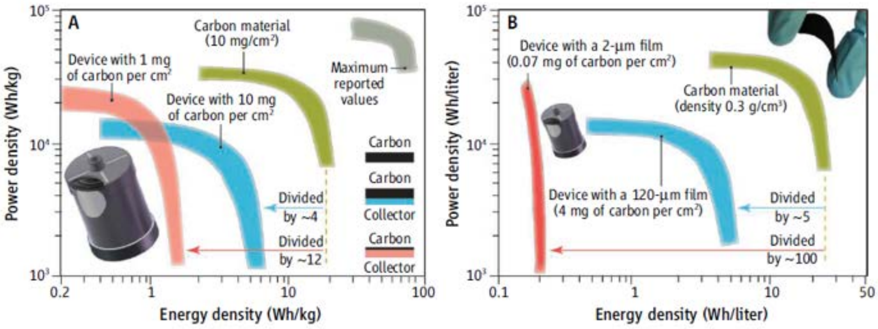

Figure 1.2. A tale of two plots. Ragone plots of different scale electrical energy storage devices.[29]

It is now well recognized that electrodes and electrolytes are two heart components for an EESD module.[29] Therefore, to optimally design the electrochemical performance of EESDs at the integrated device level for practical application, the first key challenge is to systematically study the electrode-electrolyte interactions and interface properties to gain an in-depth understanding of charge storage mechanisms.[43] This is necessary to efficiently engineer the electrode-electrolyte interface and electrical double layer (EDL) structure for increasing the electrochemical performance of electrodes. The second challenge to achieve the optimal design of EESDs at an integrated level is to establish a reliable, comprehensive quantitative relationship between electrode parameters and electrochemical performance to efficiently guide and accelerate the energy storage device design for practical applications within this community.

Importantly, the dominating feature of the electrode-electrolyte system is the transport, distribution, and concentration of electrons and ions at or near the interface.[46,61] As the graphene-based 2D electrodes have good electrical conductivity, the dynamic charge storage behaviours of graphene-based 2D electrodes are primarily controlled and determined by the ion properties.[13,62] The behaviour of ions inside active materials is the key fundamental issue for improving the capacity and fast charge ability of the EESDs.

Recent research works also show that ion properties at the nanoscale pore (channel) exhibit drastic differences from that of bulk counterparts.[46,63-69] The features of electrolyte ions and the surface properties of the nanochannels in porous electrodes play a decisive role in the ion transport/distribution properties.[46,70-76] There have been recent studies of the relationship between pore size and ion size for EDLCs.[77-80] The distribution of the ions inside the EDL structure also significantly impact on the EDL capacitance as well as the interfacial electrochemical reaction rate, due to the nature of intrinsic charge storage.[81-88] Considering the decisive role of the nanopore structure of the electrodes in improving the energy storage performance for both electrodes and devices,[10,13] it is highly desirable to systematically study the electrode/electrolyte charging storage performance under nanoconfinement under dynamic charging conditions. Due to the limitation of the electrodes which exhibit disorder and complex porous structure and untenable pore size,[89,90] the fundamental research issues regarding how the ion transport and distribution under nanoconfinement affects the electrode-electrolyte interactions and electrochemical reaction have not been well studied and addressed. This is particularly so in regard to the effects of ion transport and distribution properties in the nanochannels on the electrode-electrolyte interface redox reaction. A suitable material model system is helpful for fundamental quantitative studies.

At the device design level, taking supercapacitors as an example, the positive and negative electrodes are porous materials that are used to accommodate electrolyte anions and cations.[23] Due to the different properties of cations and anions,[91-94] the positive and negative electrodes should be appropriately designed and matched to achieve superior performance for practical applications. However, the optimal design of supercapacitors at the device-level is still a tremendous challenge because of the high dimensional design space consisting of the electrode structure (pore size and thickness) of both electrodes, the working voltage, and the operation charging rate. Recently machine learning techniques have been extensively demonstrated as a very effective approach to address this high-dimension sophisticated parameter space for engineering applications.[95-101] It is a good option to use machine learning to help us address the complex design task of supercapacitors.

In this thesis, we will try to address some questions in the two challenging directions of EESD research, i.e., fundamental study of ion storage and electron transfer process at electrode/electrolyte interface, as well as the rational and quantitative design of EESD devices. We will take advantage of our chemically converted graphene membranes (CCGMs) with tunable pore size in the sub-10 nm range.[102] The CCGM has relatively simple but tunable structures, which is a good model system for both experiments and theoretical simulations. It will allow us to carry out a quantitative study of the ion type and slit-pore size effects on the electrochemical energy storage performance. CCGMs also provide two key structure advantages on device-level design. First, CCGM electrode structure is clearly defined. It is a membrane enclosing uniformly distributed slit-pores. Other widely used material systems, such as amorphous carbon, have complex nanoporous structures that are difficult to quantify. In addition, the amorphous carbon electrodes have binders and complex cavities between carbon particles, which are also very difficult to quantify. Second, the structures of CCGM can be precisely tuned. Its slit-pore size can be continuously tuned in the sub-10nm range (details in methodology). Its thickness can be easily changed by increase graphene mass loading or stacking multiple membranes on top of each other. There are no binders in the electrodes.[103]

Following this chapter, Chapter 2 provides a brief introduction to energy storage electrodes and devices, as well as the current research progress on confined ion effects on energy storage. According to previous research about the nanoconfinement effects on energy storage, it is proposed that comprehensive experiments to measure the electrochemical performance for a range of fine-tuning nano-sized electrodes and electrolytes is necessary to fully capture the confined ion effect on performance, which will enable further evaluation of the ion properties under confined charge space. Additionally, the electrochemical confinement study could also identify possible new charge storage mechanisms for the nanoporous electrodes to effectively design the next-generation high-performance electrode-electrolyte energy storage systems.

Chapter 3 studies the confined ion effects on the EDL capacitance of graphene-based membrane electrodes. This chapter details a systematic electrochemical study of graphene membrane electrodes in various aqueous electrolytes and demonstrates the confined ion effects for the EDL capacitance of graphene-based electrodes, especially the different test results in 1.0 M KCl and 1.0 M HCl. In this research, attention is given to the fact that all these electrolytes have the same anion (Cl^-) with the same concentration. Based on previous understanding, the identical tested graphene-based electrodes should perform close capacitance in these aqueous electrolytes under positive polarization with a very low charging rate. Therefore, a series of electrochemical characterizations in the mixed KCl/HCl electrolytes with the various ratio of KCl/HCl were carried out. The open-circuit potential and potential of zero charges of graphene electrodes in these electrolytes demonstrate that the effect could come from the specific adsorption of the proton. The continuum simulation further analyses the ion distribution and density near the graphene-based electrode surface in 1.0 M HCl and 1.0 M KCl. The results of this research could provide guidelines for choosing electrolytes suitable for enabling the electrodes to have high capacitance, applying for both positive and negative components for the supercapacitor devices. Moreover, the enhanced understanding of proton EDL structure achieved in this chapter could also lead to further discoveries within the hydrogen evolution reaction and metallic corrosion community.

Chapter 4 studies the nanoconfined redox-active ions in regard to the charge storage performance of graphene-based nanoporous electrodes. Electrochemical studies of iodine and zinc-based redox-active ions inside the nanoporous graphene-based electrodes are detailed. The findings indicate that the nanoconfinement has a significant effect on the solid/liquid interface charge transfer when charging the graphene-based electrodes with different pore sizes in the identical electrolyte. The cyclic voltammetry and electrochemical impedance spectroscopy results demonstrate that the graphene-based electrode with a small pore size (1 nm) shows a higher charge transfer reaction rate than that of large pore size (10 nm) graphene-based electrodes. The study of this systematical research could help to stimulate the development of new electrochemical theories and new strategies for the design of the next-generation high-performance electrode-electrolyte system.

Chapter 5 studies the design of supercapacitors on the device level by applying a machine learning method to assist and accelerate the optimization design of graphene-based supercapacitors. Here, we produce a comprehensive dataset consisting of 100 capacitances of electrodes with various thickness and pore size under dynamic operating conditions for positive and negative electrodes. Using the achieved dataset, we apply an artificial neural network method to the performance prediction of positive and negative electrodes and use random forest regressors to extract the important design parameters for electrodes and supercapacitor devices. The numerical method is applied to search the optimal design parameters of the devices based on the predicted dataset using domain knowledge, and experiments further confirm the predictive optimal design parameters. This work strongly indicates that the combination of a suitable materials platform, a deliberated experiment database, and data-drive models result in the ability to predict the performance and obtain the optimal design of complicated dynamic systems.

Chapter 6 summarizes the major findings and contributions of this PhD research. Some future work based on the research results presented in this thesis is proposed.

In summary, this PhD study will help us gain some in-depth understanding of the nanoconfinement effects on the electrochemical performance of ion adsorption as well as redox reaction, especially in relation to the interface charge transfer properties under nanoconfinement. Fundamentally, the presented comprehensive ions and confinement studies could further increase the understanding of nanoconfinement effects on the charge storage mechanism, also provide new insightful charge storage mechanism at the nanoconfined interface. Concerning performance, such quantitative experimental studies of ions inside nanopore could help to provide a novel concept for guiding the design of the next-generation high-performance electrode-electrolyte system. Additionally, through the introduction of the machine learning method into the energy storage devices design, we will have the chance to quickly design various energy storage devices at the integrated system level based on demand, which is a breakthrough for the energy storage field. The outcome of this PhD research also could provide some new ideas in other related research fields, such as catalysis, capacitive deionization, and nanofluidics.

Chapter 2 Literature Review

It has been well established that the ions inside nanopores or nanochannels appear to have special physical or chemical properties compared with that of the bulk solution.[46,63,69] Currently, nanoporous materials with continuing pores in the nanoscale, are widely utilized for energy storage owing to their favorable nano-ionic properties as well as their enhanced active sites for electro-absorption of ions and charge storage.[9,19,22,24] Additionally, some preliminary results on electrochemical redox-active materials also demonstrate that metal oxide nanoparticles inside the nanoconfinement environment often lead to the different electrochemical activity of the active materials compare to that of the same metal oxides deposited on the exterior surface.[104-107] This review introduces the concept and properties of energy storage devices as well as the recent research progress for energy storage, especially the nanoconfinement study for ion adsorption on EDL capacitance and interface charge transfer on pseudocapacitors. Lastly, this chapter details the current design concepts for supercapacitors.

2.1 Basic knowledge of EDLCs and electrochemical redox-type energy storage devices

Charge storage in EDLCs is characterized by the physical electrostatic attraction that lies between the electrolyte counter-ions and the electrode surface charges. The Helmholtz-stern model (**Fig.2.1a**) describes the electrode/electrolyte interface charge separation when an electrode of active surface area S (m^2) is polarized.[19,94] This double layer is regarded as EDL, and the capacitance can be approximated by the following equation[94]:

$$c = \frac{\varepsilon_r \, \varepsilon_0 \, S}{d} \tag{2-1}$$

where ε_r is the electrolyte's relative dielectric constant, ε_0 is the vacuum dielectric constant, d is the effective thickness of the electrical double layer, and S is the surface area of the electrode.[94]

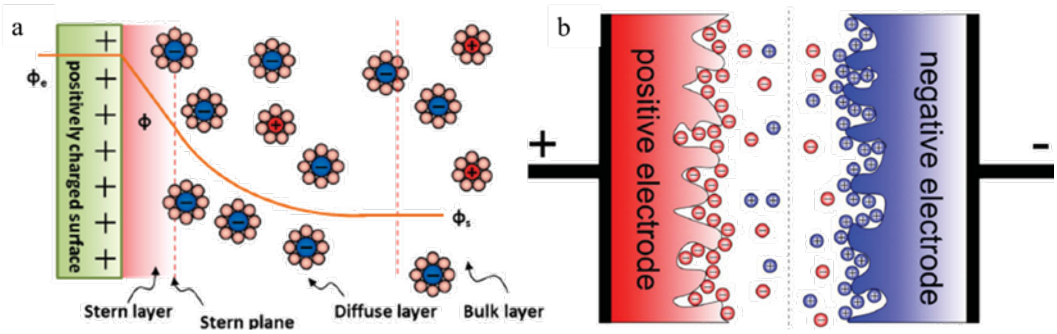

Figure 2.1. (a) Stern model of the electrical double-layer formed at a positively charged electrode in an aqueous electrolyte; **(b)** An electrical double-layer capacitor using porous electrodes.[94]

Currently, the materials used for the EDLCs are mainly porous nanoporous carbon-based materials, such as activated carbon, amorphous carbon, carbide-derived carbon, carbon nanotube, graphene, and chemically converted graphene (CCG).[47,79,108-114] During the charge and discharge for the EDLCs at constant current, there is an accumulation of positive and negative charges in positive and negative electrodes (**Fig.2.1b**).[94] The total storage charge of positive and negative electrodes should always be the same to balance charge distribution in the whole device. The overall capacitance of the supercapacitor device is equivalent to two capacitors in series. The capacitance is calculated with the following equation[23]:

$$\frac{1}{c} = \frac{1}{c_+} + \frac{1}{c_-} \qquad (2\text{-}2)$$

where c, c_+, and c_- are the capacitance of the supercapacitor device, the positive electrode, and the negative electrode, respectively. Thus, the match of positive and negative electrodes using given electrolytes is important for the final performance of the supercapacitors.[23,24]

The energy and power density of the supercapacitor can be calculated using the following equations.[23]

$$E = \frac{1}{2} C_s V^2 \qquad (2\text{-}3)$$

$$P = \frac{E}{t} \qquad (2\text{-}4)$$

where E is the specific energy density, C_s is the specific capacitance of the supercapacitor devices that depends on the capacitance of positive and negative electrodes as well as the electrolyte properties, V is the voltage that depends on the electrolyte properties as well as the configuration of the supercapacitor, and t is the discharge time.[23] Considering the physical electro-adsorption charge storage mechanism of EDLCs, the EDLCs have a lower energy density but with a higher power density compared with that of the electrochemical redox-type energy storage devices.

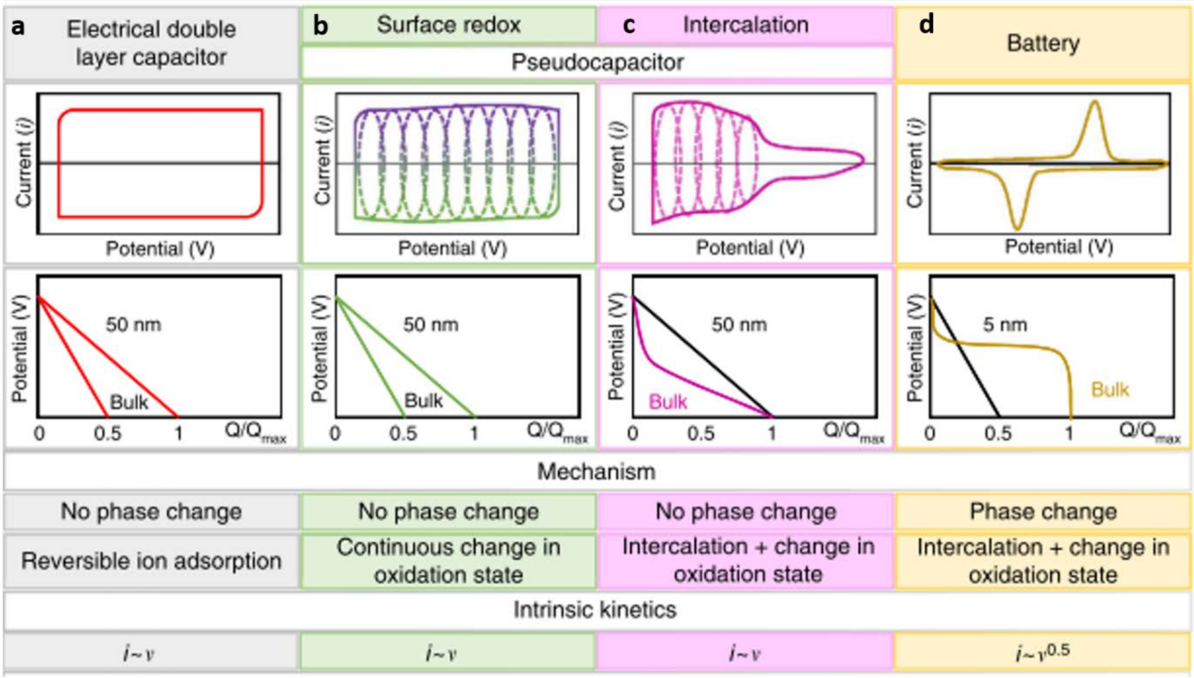

Figure 2.2. The features of EDL and redox-type energy storage devices. **(a)** cyclic voltammetry, galvanostatic profile, storage mechanism, and intrinsic kinetics of EDLCs; **(b)** and **(c)** cyclic voltammetry, galvanostatic profile, storage mechanism, and intrinsic kinetics of pseudocapacitors. (examples: hydrated RuO_2 birnessite MnO_2). **(d)** cyclic voltammetry, galvanostatic profile, storage mechanism, and intrinsic kinetics of batteries.[9]

Charge storage in electrochemical redox-type materials is characterized by an electrochemical reversible redox reaction, which is faradaic charge-transfer, converting the electrical energy to the chemical energy.[9] Based on the different faradic redox reactions, there are mainly two types of redox reactions. One is the reaction that occurs at the solid buck active material, where the reactions are always limited by the solid-state ion diffusion.[12] The other one is the reaction that occurred at or near the surface of active materials.[115,116] In this latter reaction, the solid-state ion diffusion does not limit the reactions, and the reaction rate is mainly controlled by the diffusion of the liquid ions (reactant) to the solid surface as well as the surface charge transfer (**Fig. 2.2**).[9,20] In the project of the redox-type energy storage study, I will mainly study the surface-redox reactions due to the hope of achieving both high power and energy densities for next-generation energy storage devices.

2.2 Research progress on electrochemical double-layer electrodes

2.2.1 Capacitance of nanoporous electrodes under nanoconfinement

According to equations (2) and (3), C_s and V are the two key parameters for energy density. Most previous research works focus on increasing the C_s or expanding the working voltage of supercapacitor devices through using the organic or ionic liquid electrolyte.[47,50,117,118] As the C_s depends on the specific surface area of the nanoporous electrodes, before 2000, many scientists in the EDLC field believed that maximizing the specific surface area of the conductive active materials could be the best strategy for increasing the capacitance, thus leading to the storage of more charge on the specific mass or volume. Therefore, the research direction and emphasis on EDLCs during that time was to develop advanced nanoporous high-conductive active materials with the highest specific surface area.[19]

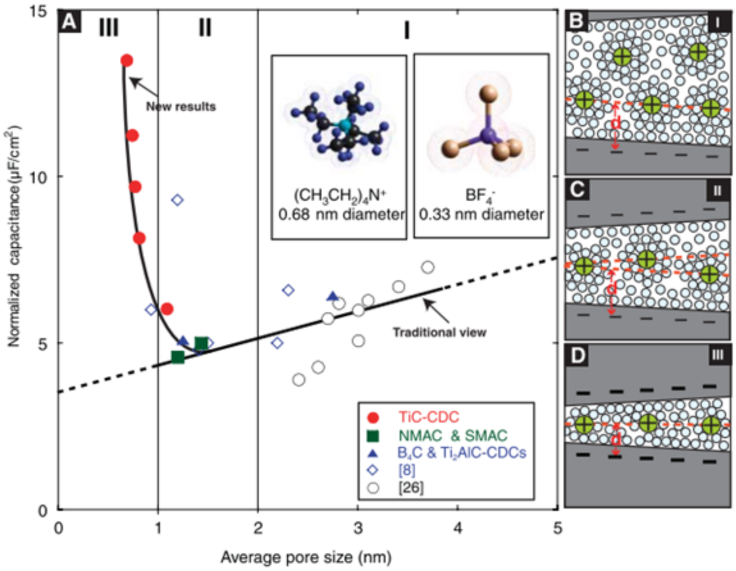

Figure 2.3. Relationship between specific capacitance and average pore size of nanoporous electrode in1.5 M NEt4BF4/CAN.[119]

Over time, researchers realized that at the nanoscale level, especially for microporous materials, the pore and ion properties also have a large effect on the capacitance of electrodes. As a result of this, some research was carried out on the relationship between confined nanopore and ion properties on the capacitance of electrodes.[78,79,86,111,112,120-125] One significant study by Gogotsi and co-workers reported an anomalous increase in carbon capacitance at the pore size of less than 1 nanometre in 1.5M NEt_4BF_4/ACN electrolyte (**Fig. 2.3**).[119] This finding strongly challenges the long-held opinion that pores smaller than the size of ion-solvent do not have the contribution to the surface charge storage. It also indicates the significance of pore size distribution on the electrode capacitance. Even though this result is a breakthrough in the EDLC field, in such sub-nanometre pore size, the increase of capacitance sacrifices fast charge ability, especially in comparison to the mesoporous carbon.

Later, due to the encouraging capacitive features of graphene, our group also did some research on capacitance and nanopore electrodes using the electrolyte mediated-graphene gel membrane in H_2SO_4 and $EMIMBF_4$/AN electrolytes (**Fig. 2.4**).[47] Our results show that high volumetric capacitance can be achieved in the channel size of 0.67 nm for the thin electrode based on the two-electrode test system, (255.5 F cm^{-3} at 0.1 A g^{-1}, 130 F cm^{-3} at 100 A g^{-1} in 1.0 M H_2SO_4 electrolyte; 261.3 F cm^{-3} at 0.1 A g^{-1}, 80 F cm^{-3} at 100 A g^{-1} in $EMIMBF_4$/AN electrolyte). But in such sub-nanometre channels, the high volumetric capacitance could not be maintained in a fast-charging condition. Nota that, a fast-charging rate ability is a key character for supercapacitors. From the results (**Fig 2.4c**), we can observe that with the increase of mass loading (thickness), there is a decrease of specific capacitance, especially for the more compact electrodes.[47] Additionally, the two-electrode configuration characterizes the electrochemical performance of the supercapacitor device instead of the individual electrode. Therefore, considering the charge storage information loss in the two-electrode test configuration, and the important role of pore size on the EDL capacitance of positive and negative electrodes, more well-designed research work is still needed to better understand the relationship between the nanoporous structure and the electrode capacitance of the graphene-based electrodes. This is necessary to guide the predictive design of electrode with fast charge ability under a large and thick electrode compact level.

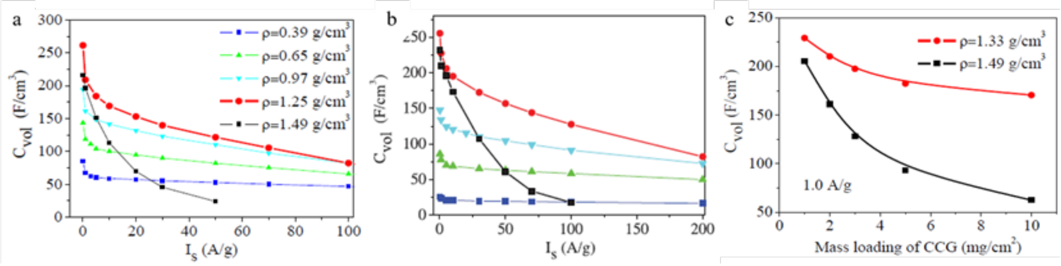

Figure 2.4. (a) Volumetric capacitances with varied charging/discharging current densities for different channel size graphene membranes in 1.0 M H_2SO_4 electrolyte; **(b)** Volumetric capacitances with varied charging/discharging current densities for different channel size graphene membranes in the $EMIMBF_4$/AN electrolyte; **(c)**The relation between the volumetric capacitance and the mass loading (thickness).[47]

Complementing the important research of electrode-nanostructure on capacitance, other research results on the ion effects on the capacitance of nanoporous electrodes were also reported.[81,93,126-130] Aurbach and co-workers systematically studied the ion sieving effects in the electrical double layer of porous carbon electrodes to estimate the effect of ion size on the EDL capacitance. In their research work, the microporous carbons have the pore size of 3.62, 4.21, 5.1, and 5.8 Å, the electrolyte ions used in the study are Cs^+, K^+, Na+, Li^+, Ba^{2+}, Ca^{2+}, Mg^{2+}, NO_3^-, Cl^-, F^-, Br^- and ClO_4^-. With the polarization of the high electronic conductivity of the achieved microporous carbon in these different electrolytes, Aurbach et al. studied the electro-adsorption and electro-desorption of the ions in achieving the electrochemical signature. The findings of this research were that all the cations were electro-adsorbed in the electrode pores with hydrated states, while monovalent anions adsorbed inside the nanopores with a non-hydrated state. Accompanying these findings, they also found that the doubly charged sulfate anion adsorbed onto the surface with the hydrated state. Finally, they found that being a multiatom planar anion, the nitrate had a smaller effective dimension than the monoatomic halogen anions.[80] This pioneering work highlights the fact that the charge storage of the EDL electrode largely depends on ion properties, such as ion size, ion valance, and especially the significant role of ions under nanoconfined pore for the EDL performance.

Following this, research by Patrice Simon and co-workers studied the electro-sorption of ions in chemically tuned pillared graphene materials for electrochemical capacitors in various 1 M ionic liquid/ACN (acetonitrile) electrolytes (**Fig 2.5**).[129] In their work, the pillared graphene electrodes had pore sizes of 7.8, 8.0, and 8.0 Å. The electrolytes used in the study were $TEABF_4$/ACN, $TPABF_4$/ACN, $TBABF_4$/ACN, and $THABF_4$/CAN. The size of the ions, BF_4^-, TAA^+, TEA^+, TPA^+, TBA^+, and THA^+ were 0.48 nm, 0.68 nm, 0.76 nm, 0.82 nm, and 0.95 nm. The results of this research were that based on size steric effect, the well-controlled interlayer space could sieve electrolyte ions. In detail, ions with bared sizes, which are smaller than the interlayer space, could access into the interlayer. In contrast, the larger ions were not able to penetrate inside the small interlayer space, leading to much lower EDL capacitance. Particularly, their results revealed that when the naked ion size for cations and anions are both smaller than the interlayer space, there is no specific difference between cations and anions adsorption. This is the case even when they have a different ion size. There is still the negligible ion size effect on the EDL capacitance for the large pore size electrodes. When the cation size was larger than that of the interlayer space, a clear difference could be seen between the electro-sorption of cations and anions.[129] In summary, the research by Simon et al. on ion sieving in pillared graphene-based materials for positive and negative electrodes further demonstrated the importance of ion size effect on the EDL capacitance, as well as the difference between the electro-adsorption of cations and anions on the identical nanoporous electrodes.

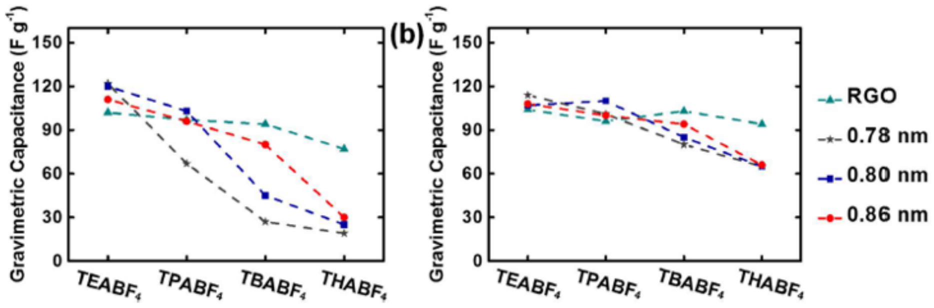

Figure 2.5. The capacitance of pillared graphene materials with the pore size of 0.78 nm, 0.80 nm, and 0.86 nm and reduced graphene materials in different 1 M BF4 based ionic liquid/ACN electrolytes with a scan rate of 20 mV/s in the potential ranges of **(a)** −1.0 to 0.1 V *vs.* Ag and **(b)** 0.1 to 1.0 V *vs.* Ag.[129]

2.2.2 Charging storage mechanism of nanoporous electrodes under nanoconfinement

2.2.2.1 Charging storage mechanism study mainly based on advanced technique characterization

The charging mechanism of supercapacitor strongly depends on the polarization of the electrode, and the choice of the electrolyte and electrode materials.[83] The charging mechanism determines the capacitance of the supercapacitor.[19] Therefore, from the aspect of the charging mechanism, the suitable matching of electrolyte and electrode is crucial for the capacitance increase. Based on these, many advanced techniques have been applied to interpret the charging mechanism of EDLCs.[131-140] Particularly, Deschamps and co-workers explore the electrolyte organization in supercapacitor electrodes with solid-state NMR for investigating the behaviour of the ion under the dynamic charging process. The electrolyte used for this study is 1 M tetraethylammonium tetrafluoroborate in acetonitrile (TEABF$_4$ in ACN), the applied two carbon materials have the specific surface area of 1071 and 1191 m^2/g with the pore size range from 1.2 nm to 50 nm. Their research results show that when charging the nanoporous activated carbons, the ion exchange is the predominant charge storage mechanism for both positive and negative polarization processes. Additionally, acetonitrile molecules are expelled from the adsorption sites when charging the nanoporous electrodes with a negative charge. The more disordered carbon shows a better capacitance and stability at high working voltages.[88]

After that, Grey and co-workers also did some fundamental research for the purpose of gaining insight into the dynamic charge mechanism of EDLCs using in situ nuclear magnetic resonance (NMR) and electrochemical quartz crystal microbalance (EQCM) techniques. The studied electrode was commercial YP-50F activated carbon with an average pore size of 0.9 nm, and 90% of its pore size distribution was lower than that of 2 nm. Their results show that the charge storage mechanism is very different for the positive and negative electrodes in PEt_4BF_4/ACN electrolyte. For the positive polarization charging process, the charging mechanism is the exchange of cations for anions, while for the negative polarization electrode, cations adsorption is the dominant charging mechanism (**Fig. 2.6**).[135] Additionally, the in situ EQCM measurement results indicated that the electro-adsorption of ions is only partially solvated.[135] These results advance our understanding of the charge storage of anions and cations for positive and negative electrodes. They also indicate a need for further deep exploration of the charging mechanism of positive and negative electrodes with confined nanostructure in a wide range of electrolytes.

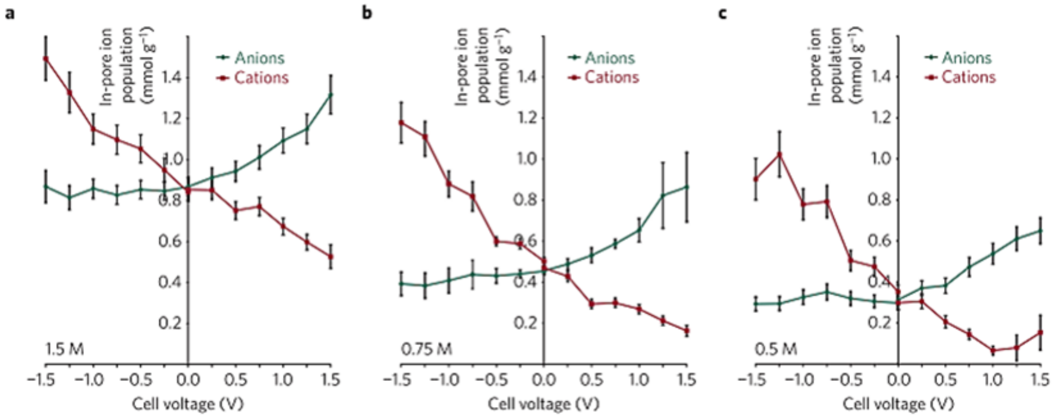

Figure 2.6. In-pore ion populations for supercapacitor electrodes at different states of charge in the range −1.5 V to +1.5 V. a–c, In-pore ion populations for electrolyte concentrations of 1.5M **(a)**, 0.75M **(b)** and 0.5M **(c)**.[135]

Later, Grey and co-workers further studied the ion dynamics inside the EDL electrodes using in situ diffusion NMR spectroscopy for controlling the charging storage mechanism and tuning the energy and power densities of the EDLCs (**Fig. 2.7**).[139] The tested electrodes used for this research are two different commercial activated carbons, which are YP-50F and YP-80F with different porosities, and the electrolyte is PEt_4BF_4/ACN electrolyte with two different concentration (1.5 M and 0.75 M). Their in-situ pulsed field gradient NMR measurement results show that the ion diffusion coefficient inside the confined nanopore is around two orders of magnitude lower compared with that of the bulk electrolyte ions, and the in-pore ion diffusion coefficient was determined by the pore size, electrolyte concentration, and working potential. In detail, for the negative polarization, increasing the polarized potential, there is a linear decrease in the diffusion coefficient of both cations and anions, and the decreasing level of anions is larger than that of cations (**Fig 2.7a and b**).[139] While for the positive polarization, increasing the positive potential, only a minor diffusion coefficient variation of cations and anions was observed. The observed diffusion coefficient variation perhaps comes from an in-pore ionic concentration with different charging potentials (**Fig. 2.7c**).[139] For example, charging the electrode with negative potential, the main ion charging mechanism is the adsorption of counter ions, which induced an increase of the overall in-pore ionic concentration (**Fig. 2.7d**).[139] The enhanced ion-ion interaction, leading to a decrease of the ion diffusion coefficient inside the nanopore (**Fig. 2.7e**).[139] On the other hand, charging the electrode with positive surface charge, the primary charging storage mechanism is ion swapping/exchanging with minor ion population change inside the nanopore, leading to the negligible effect on the ion-ion interaction inside the confined nanopore. This research demonstrates the important interplay between charging mechanisms and dynamics and provides a wealth of information for increasing the understanding of ions' dynamic features under confined nanoporous electrodes. Importantly, these significant results indicate that controlling the charging storage mechanisms purely with the co-ion desorption instead of counter-ion adsorption could be an effective strategy to achieve the fastest charging ability at the high working voltage for thick electrodes.

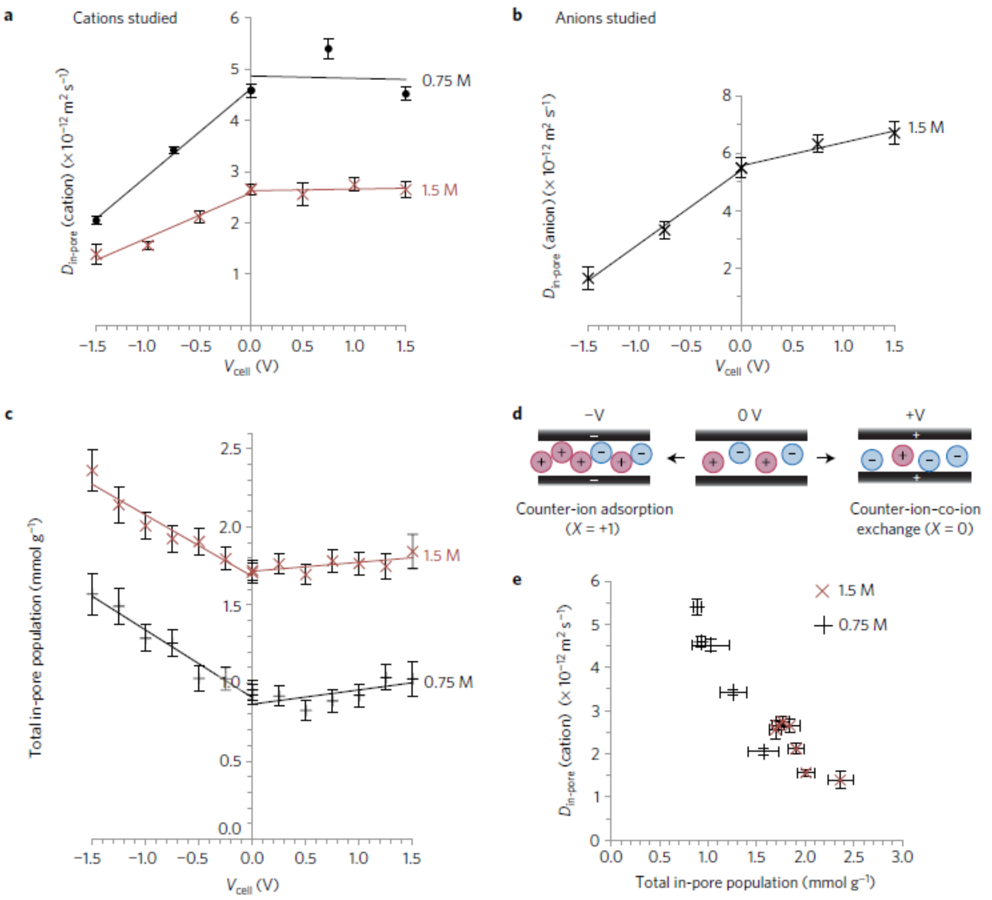

Figure 2.7. in situ measurement of ion diffusion and population inside the nanopore. **(a)** and **(b)** are the cations and anions diffusion in YP50F- PEt_4BF_4/CAN with different working voltages; **(c)** total in-pore ion populations at different cell voltages; **(d)** schematic figures of charge storage mechanisms; **(e)** relationship between total in-pore population and in-pore cations diffusion coefficient.[139]

At about the same time, O. Paris and co-workers studied the quantification of ion confinement and de-solvation in nanoporous carbon supercapacitors with in-situ X-ray scattering.[140] The electrodes used for this research were those of commercial activated carbon (YP-80F), activated carbon, and carbide-derived carbon with an average pore size of 1.3 nm, 0.9 nm, and 0.65 nm, respectively. The measured scattering data indicated that Cs^+ and Cl^- ions present a partial de-hydration in the mixed micro-mesoporous carbons with a mean pore size above 1 nm. Additionally, the high interaction force between ions and inner solvated molecules could effectively prevent the complete de-solvation of ions penetrated into the nanoporous carbons even when the pore size is less than 1 nm. Moreover, their results show that there is a correlation between the degree of confinement and the degree of de-solvation.[140] This infers that the performance of nanoporous electrodes not only depends on the nanoporous structure but also on the degree of de-solvation. Therefore, if we could successfully control the confinement degree and solvation-number of ions, the performance prediction of nanopore carbon-based materials for EDLCs could be possible.

2.2.2.2 Charging storage mechanism study based on simulation.

Compare to advanced techniques with a high cost and complex for the study of the EDL charging mechanism, the simulation method with low cost and high efficiency could provide a molecule level observation and understanding of ion distribution and density profiles inside the nanoporous electrodes under both equilibrium and dynamic charging condition for the EDLCs.[70,84,125,141-146] For instance, M. Salanne and co-workers studied the charge storage mechanism under a high nanoconfinement space using molecular dynamics simulations at the microscopic scale.[48] In detail, they studied four different adsorption structures, which are edge, planar, hollow, and pocket sites, respectively. Their work demonstrated the important role of the local structure and the coordination and solvation for the charge storage of EDLCs. Additionally, the simulation results reveal that the distribution of the absorbed ions is quite different in these four types of charged sites, and the ion distribution and density for the nanoporous electrodes also largely depend on the applied potential (**Fig. 2.8**).[48] Lastly, the results indicate that with the increasing degree of nanoconfinement, the de-solvation, and the stored local charge on the electrode increases.

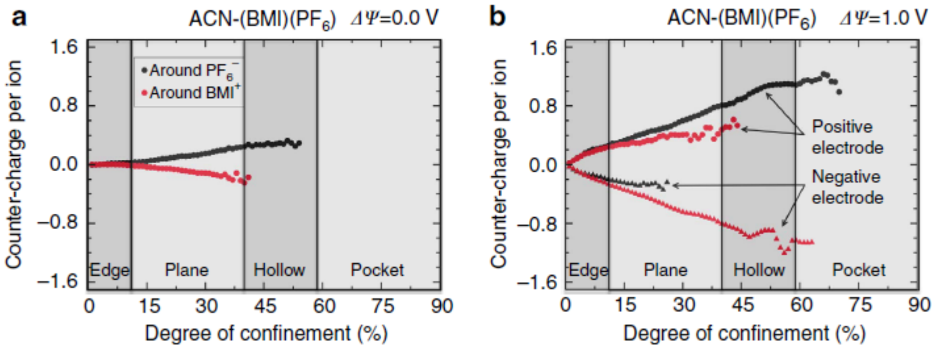

Figure 2.8. Effect of confinement on the efficiency of charge storage for applied potentials of 0V **(a)** and 1V **(b)** in the case of the ACN-based electrolyte.[48]

Later, a theoretical and simulation study indicated that charging dynamics in sub-nanometre pores can be very different from than in the bulk electrolyte, which could accelerate up to 30 times when the pore and the ion properties are well matched.[51] Charging of the initially filled pores can lead to an overfilling of the porosity. This corresponds to a temporary state where there is a higher density of ions than that of the charging end-stage.[51] This finding indicates that there is a difference between static and dynamic charging of supercapacitors. It further indicates that the suitable matching of the nanoporous electrode-electrolyte system has the potential to achieve the EDLCs with both high energy and power density for the compact nanoporous electrodes with fast charging rates.

Afterward, Patrice Simon and co-workers also studied the distribution of the ionic liquid inside the confined carbon nanopores to reveal a new charge storage mechanism for designing better materials for electrochemical applications.[53] Their results show that the Coulombic ordering reduces in responses to the pores accommodate only a single layer of ions. In detail, EMI-TFSI and EMI-BF_4 ionic liquid electrolytes can adopt a single layer or bilayer ions arrangement, which depends on the average pore size of the applied nanoporous electrodes. The Bilayer ions distribution does not break the coulombic ordering because of the ordered layers formed on each carbon wall. Single-layer inside ions, on the contrary, could break Coulombic ordering. This would lead to the formation of co-ion pairs. This non-Coulombic phenomenon could due to the repulsive electrostatic interactions between co-ions, which are being offset by the image charges induced in the carbon walls.[53] This compensation effect could provide the potential to induces a highly dense ionic structure of counter-ions, which provides a reasonable explanation for the capacitance increase when the ion sizes and the average pore size of the electrodes are well matched. Furthermore, this significant research work indicates that the suitable ions-pore matching could be able to create a new charge storage mechanism for building the EDLC with both high energy and fast charge ability under sub-nanometer porous.

Recently, Campbell and co-workers investigated the adsorption of several alkali-metal cations within graphene slit-pores with 0.6 nm pore size through the combination of hybrid first-principle and continuum simulations.[54] Their results show that lithium ions presented the capacitance of 75 F/g and 83 F/g, which is much lower than that of Cs^+ ions (**Fig. 2.9a**).[54] Importantly, inside the nanoporous electrode with 0.6 nm pore size, the ionic charge of cations is smaller than that of the bulk values, which is mainly due to the charge transfer inside the nanoporous (**Fig. 2.9b**).[54] From **Fig. 2.9c**, we can see that with the increase of the ion size, there is higher accessibility of the ion into the graphene slit pores. In this case, the binding energy of the cations with graphene slit pores also shows a decrease with the slit pore size between 0.6 nm to 1.5 nm (**Fig. 2.9d**).[54] Their interesting results indicate the suitable choice of working electrolytes with highly polarizable ions could have the advantage of increasing the overall capacitance of the EDLCs.

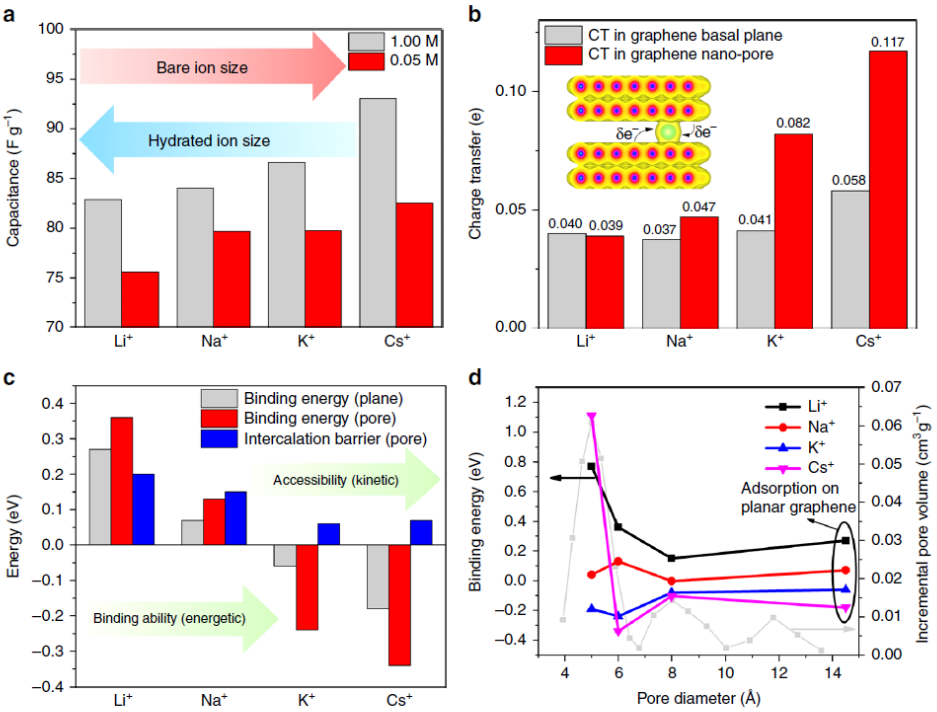

Figure 2.9. Specific capacitance of nanoporous electrodes tested in 1 and 0.05 M aqueous working electrolytes with the scan rate of 0.5 mV/s; **(b)** Charge transfer ration of different alkaline cations on nano-slit porous graphene and graphene basal plane surface; **(c)** Binding energies and intercalation barrier of various alkaline cations on nano-slit porous graphene and basal plane graphene surface; **(d)** Calculating Binding energy of the various alkaline cations on nanoporous graphene with different pore diameters from density functional theory.[54]

In our previous research, we carried out molecular dynamics simulations to gain a comprehensive understanding of how ions size, solvent properties, and charging potential affect the EDL structures.[70] This was in reference to 5 nm graphene membrane electrode surface for different symmetrical monovalent aqueous electrolytes and thereby their contribution to the capacitance. The simulation results show that different electrolytes indeed have distinctive EDL structures (**Fig. 2.10**).[70] Some larger ions (such as Rb^+, Cs^+, Cl^-, and I^-) exhibit partial dehydration, and in the process of this, they penetrate through the first water layer, which is next to the charged graphene surfaces. Additionally, the electrical potential distribution of the EDL and dielectric constant of water depend on the ion type and charging process. These findings confirm that the electrolyte properties and charging process (positive and negative) affect the capacitance of identical nanoporous electrode, and demonstrate the necessity of investigating the performance of positive and negative electrodes separately under the dynamic charging/discharging process.

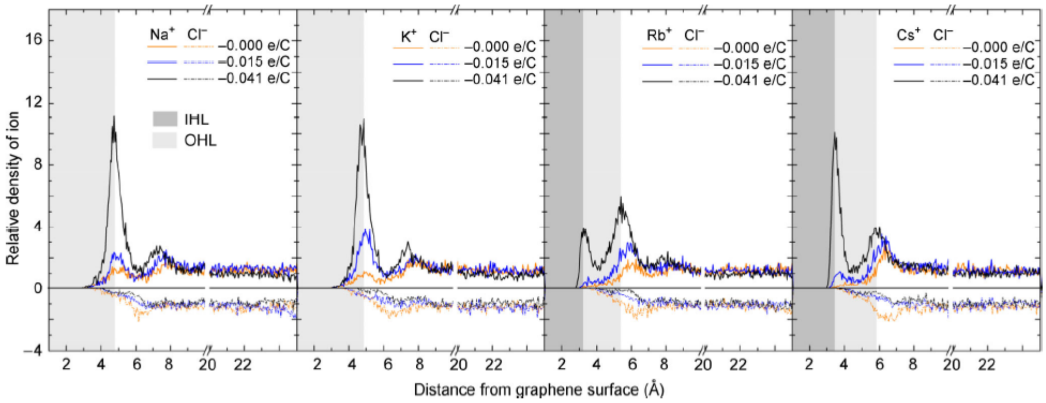

Figure 2.10. The relative number density of different electrolyte ions as a function of distance from the graphene cathode surface with a charge of 0, –0.015, and –0.041 e/C-atom, respectively. The shaded regions represent the IHL and OHL.[70]

2.2.2.3 Charging storage mechanism study mainly based on electrochemical characterization

The combination of various electrochemical methods also could provide valuable information about ion effects of confined nanoporous electrodes with positive and negative surface charge densities on the charge storage mechanism of EDLCs.[93,128] A. Striolo and co-workers studied the electrochemical performance of graphitic carbon electrodes with a pore-size range between 0.65 nm to 1.6 nm in various aqueous electrolytes using electrochemical impedance spectroscopy (EIS) and cyclic voltammetry (CV) methods.[93] They observed that when increasing the polarization potential of the sub-nanometre pore electrodes, there is a large increase in the capacitance. On the other hand, the capacitance of graphite carbon with larger pores (above 1 nm) does not significantly correlate with the applied working potential window. The reason for this is that the electro-adsorption of the ions inside the sub-nanometre pore is quite difficult to compare to the adsorption into the large pore.[93] Therefore, if there is a need for the ions to penetrate into the sub-nanometre pore, the high energy needs to be provided to overcome the penetration energy barrier. Their experimental results indicate that there will be a pore and ion size-dependent charging storage mechanism of the active materials when the pore size of the electrode is comparable to the size of the hydrated ions.

Later, Yan and co-workers studied the charging behaviours of cations and anions in supercapacitors based on their developed silica nanoparticle-grafted ionic liquids.[128] Generally, they developed a method that has the ability to separately detect cations ($BMIM^+$, NBu_4^+) and anions (NTf_2^-, PF_6^-) in the nanoporous of activated carbon electrodes through utilizing their developed SiO_2-grafted ILs. They applied a conventional CV characterization method to study the charging storage behaviours of $BMIM^+$, NBu_4^+, NTf_2^-, and PF_6^- ions at different polarization states with a scan rate of 5 mV/s (**Fig. 2.11**).[128] Their CV test of the effects of cations and anions on the capacitance demonstrates that the capacitance charge storage mechanism mainly comes from the counter-ion adsorption or counter-ions and co-ions exchange. Particularly, the adsorption of counter-ions is the predominate charging storage mechanism when the working potential is below -0.1 V/ref and above 0.9 V/ref. However, in the low polarized working potential range, the dominated charging storage mechanisms are counter-ion adsorption and ion swapping because of the competition between cations and anions. Finally, their results show that traditional electrochemical characterizations do allow the direct measurement of the ion effect information on the charge storage mechanism of nano-porous electrodes through the suitable choice of electrolytes and electrodes. Their work is of great significance for the engineering of electrolytes involved in the efficient design of high-performance EDLCs.

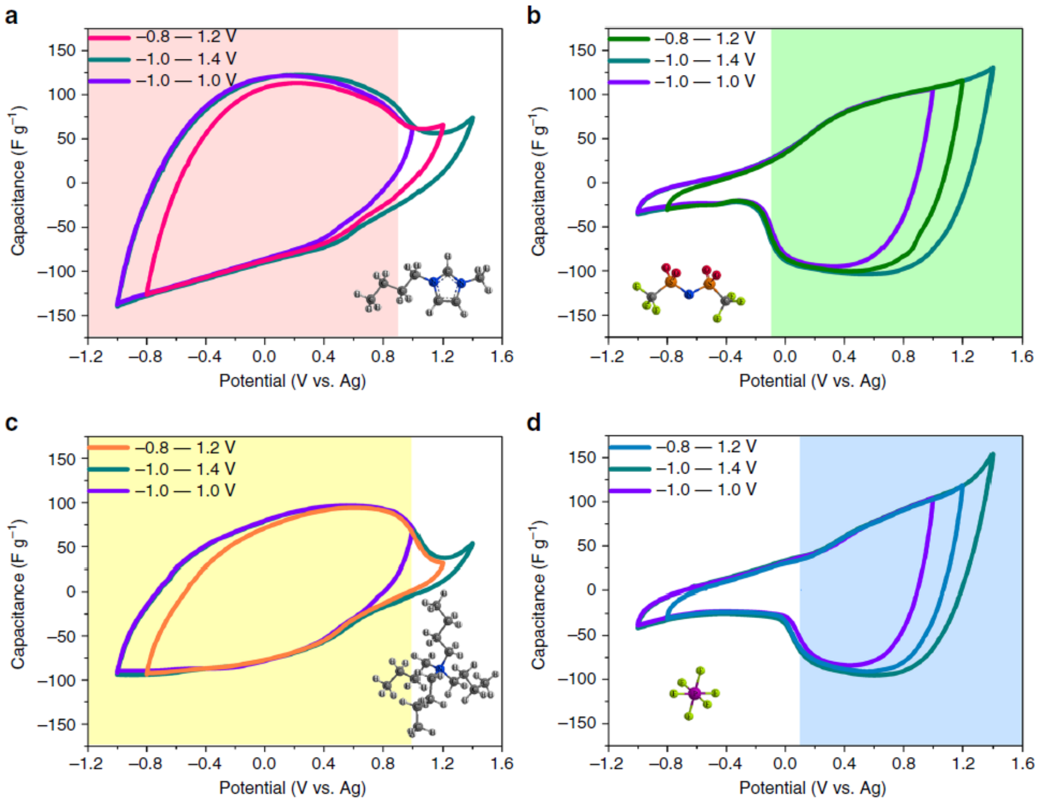

Figure 2.11. Cyclic voltammetry curves of the YP-50F electrode in four different SiO_2-grafted ILs with the same concentration of 0.25M in propylene carbonate (PC) at the different working potential range for 5 mV/s. **(a)** SiO_2-IL-BMIM$^+$; **(b)** SiO_2-IL-NTf2$^-$; **(c)** SiO_2-IL-NBu4$^+$, and d SiO_2-IL-PF6$^-$.[128]

In conclusion, the matching of pore size structure and electrolyte ions under nanoconfinement could significantly affect the electrode performance of EDLCs under dynamic conditions. Currently, the published research work demonstrates the effects of ion de-solvation, ion size, ion valance, ion diffusion coefficients, ion adsorption, cations, and anions on the EDL capacitance for the nanoporous electrodes. Nevertheless, the importance of each ion effect on the EDL capacitance is not well studied and compared, a deep understanding of these confined ion effects on the EDL are still not fully established. Therefore, a comprehensive and well designable electrochemical characterization of confined ion effects on EDL/EDL capacitance is desirable to overcome these research gaps and contribute to the knowledge of charge storage mechanism, for accelerating the optimal design of next-generation EDL materials with both high capacitance and rate performance in large electrode thickness.

2.3 Research progress on pseudocapacitive electrodes

When introducing a reversible redox reactant to the supercapacitor system, the whole supercapacitor system will possess charge-transfer features, which could increase the energy density of the energy storage devices. Based on the different faradic redox reactions, the redox-reaction features can also be distinguished. One of these is the surface charge transfer controlled redox reaction, where the faradic reaction occurs at the solid/electrolyte interface.[9,19] The other one is the bulk redox-reaction, where the redox reaction leads to the valence state change of the solid component and controlled by the solid-ion diffusion.[3,147] In regard to this second type, examples include several widely studied rechargeable batteries, such as lead-acid batteries, alkaline batteries, lithium-ion batteries, lithium-sulfur batteries, lithium-oxygen batteries as well as another alkali (Na^+. K^+) and multivalence ions batteries (Mg^{2+}, Ca^{2+}, Zn^{2+}, and Al^{3+}).[12,148,149] With the ion transport advantage at the solid-liquid interface compared to that of the solid bulk phase,[9,19] the energy storage devices with the surface redox reaction (called pseudocapacitors) present a high potential to achieve high energy density and fast power delivery.

Currently, except for the new materials exploring and research in the electrochemical energy storage field, most research on pseudocapacitors is focusing on engineering electrode materials with new nanostructures (or nano-morphologies) to improve the dynamic capacity and cycling lifetime.[4,150-154] The fundamental understanding focusing on ion storage and redox electron transfer at the electrode-electrolyte interface under different nanoconfinement level is much less. A better fundamental understanding of the ion storage and redox electron transfer at the electrolyte-electrode interface is the basis for advancing the design of energy storage devices. Based on the currently published research papers, some important and significant research work on the pseudocapacitors under nanoconfined space for energy storage is reviewed.

Maria R. Lukatskaya and co-workers studied the intercalation of Li^+, Na^+, Mg^{2+}, K^+, NH_4^+, and Al^{3+} ions between the 2D $Ti_3C_2T_x$ layers for exploring the cation effects on the interaction charge storage of MXenes (**Fig. 2.12**).[155] Their electrochemical results show that the ion interaction could happen in all these applied aqueous electrolytes for both multilayers exfoliated $Ti_3C_2T_x$ and MXene paper electrodes made of several layers of $Ti_3C_2T_x$. The results also indicate that the achieved intercalation capacitances are also comparable to the activated carbon electrodes for supercapacitors. Specifically, the interaction performance largely depends on the pH and the natural properties of the cations. The best performance of the nanoconfined MXene electrodes was observed in basic solutions, such as KOH and NaOH, which could reach to 350 F/cm^3.[155]

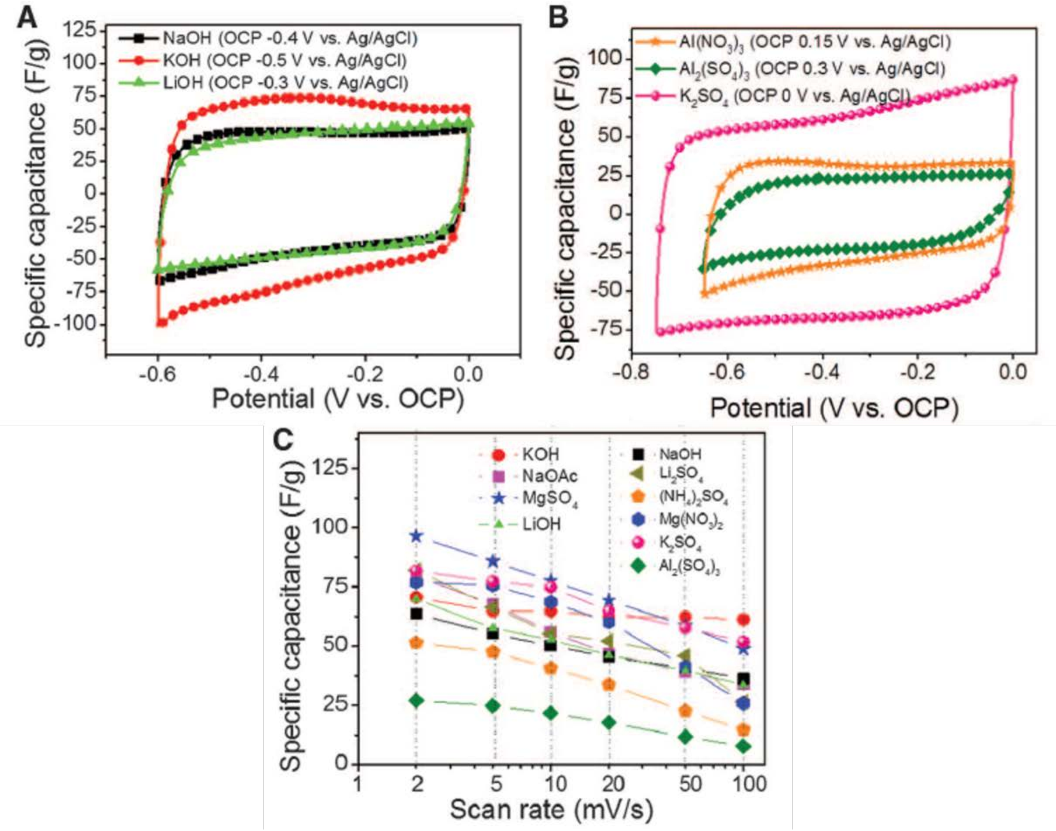

Figure 2.12. (a) CV curves of the $Ti_3C_2T_x$-based supercapacitor electrodes in NaOH, KOH, and LiOH electrolytes at the scan rate of 20 mV/s; **(b)** CV curves of the $Ti_3C_2T_x$-based supercapacitor electrodes in K_2SO_4, $Al_2(SO_4)_3$, and $Al(NO_3)_3$ electrolytes at 20 mV/s; **(c)** Rate performances of the $Ti_3C_2T_x$-based supercapacitor electrodes in different aqueous working electrolytes.[155]

Later, Manish Chhowalla and co-workers studied the ions intercalation on metallic 1T phase MoS_2 nanosheets in various aqueous electrolytes intending to design the electrodes with high intercalation capacitance. Their research results show that the interlayer space expansion during the charging/discharging process largely depends on ion-types (**Fig. 2.13**).[156] For example, the spacing expansions between the nanosheets of MoS_2 because of the intercalation are 6.63, 6.09, 3.7 and 4.83 Å for Li_2SO_4, Na_2SO_4, K_2SO_4, and $TEABF_4$, respectively. Furthermore, these level interlayer spacing increases are higher than that of the corresponding bare ions, indicating the co-intercalation of solvated molecules in this nanoconfined MoS_2 electrode instead of the bare ion intercalation for the normal battery cathode materials.

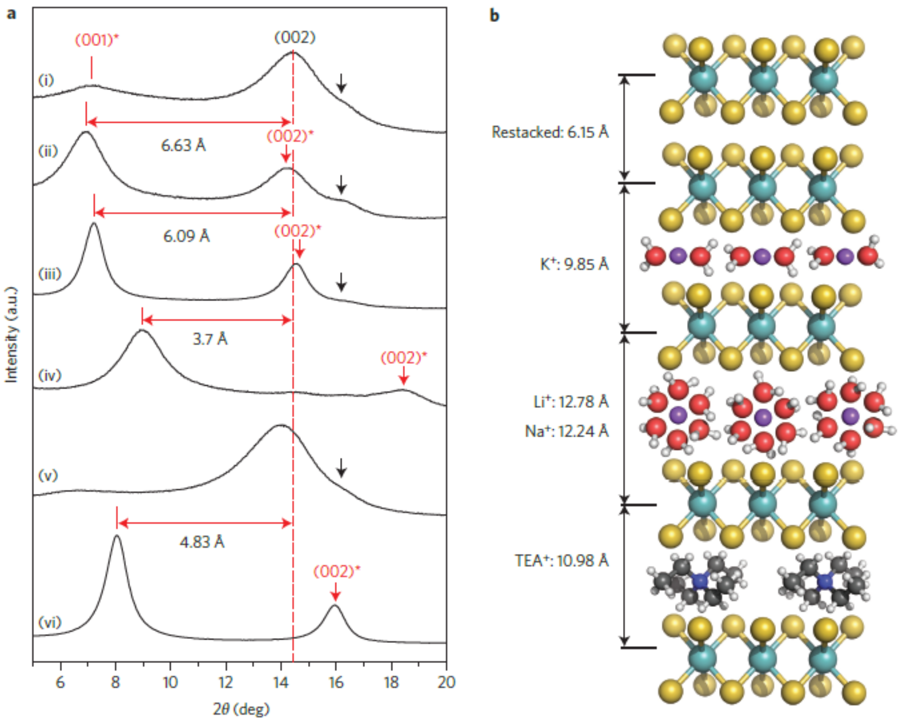

Figure 2.13. (a) XRD spectra of the achieved 1T phase MoS_2 nanosheets (i) and cycled MoS_2 film (ii–vi) in different aqueous sulfate-based electrolytes: Li_2SO_4 (ii), Na_2SO_4 (iii), K_2SO_4 (iv), H_2SO_4 (v), and in TEA BF4/MeCN organic electrolyte (vi). **(b)** Schematics of restacked non-intercalated and intercalated 1T MoS_2 nanosheets.[156]

Recently, Olivier Fontaine and co-workers studied the bi-redox ionic liquid electrolyte charge storage inside nanoporous electrodes (**Fig. 2.14**).[157] The research results show that the specific energy of supercapacitors based on nanoporous activated carbon and graphene oxide electrodes is doubled with the bi-redox ionic liquid electrolyte when compared to the same cell without redox-active electrolyte. Additionally, as the redox ions are confined inside the nanoporous structure of the electrodes, the self-discharge and leakage current is largely suppressed due to the confinement effect. Generally, this significant research demonstrates the necessity of studying interface redox electrolyte-based charge storage to further enhance the energy and power density of energy storage devices.

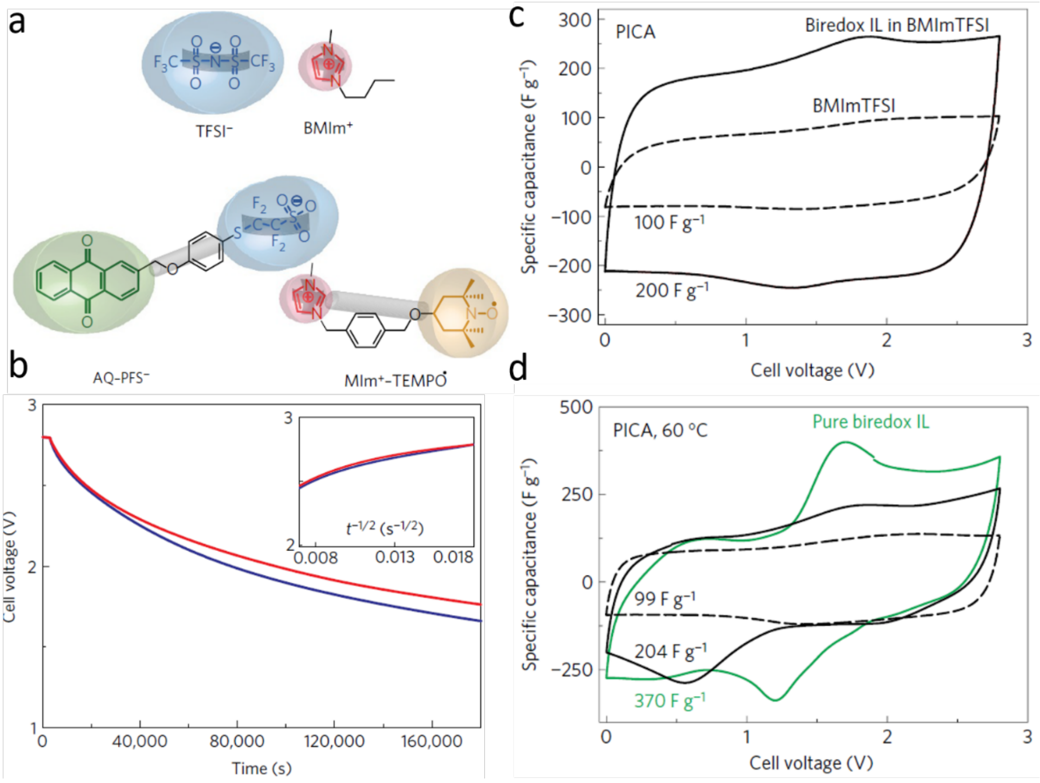

Figure 2.14. (a) Molecule structure of BMImTFSI IL and the bi-redox IL; **(b)** Self-discharge current for the devices based on PICA with BMImTFSI (blue line) or 0.5Mbiredox IL in BMImTFSI (red line) at room temperature; **(c)** Cyclic voltammetry at 5mV/s with 0.5M bi-redox IL in BMIm TFSI (solid line) and pure BMIm TFSI (dashed line), respectively; **(d)** CVs at 5mV/s of the PICA cell with 0.5M bi-redox IL in BMImTFSI (solid line), pure BMImTFSI (dashed line), and pure bi-redox IL (green line).[157]

In summary, the above-reviewed research work significantly demonstrates the importance of redox-reactions under nanoconfinement for the observation of new charge storage behaviour as well as the enhanced electrochemical performance for the engineered redox-type charge storage electrodes. Currently, research work about redox-reaction at interfaces under different nanoconfined space levels is still in its infancy stage. The further deep understanding and the discovery of new charge storage features on the electrode-electrolyte interface charge transfer under nanoconfinement could contribute to building new charge storage theory for the redox-type energy storage devices.

2.4 Research progress on the supercapacitor devices (EDLCs) design

Equation (2-2) indicates that the capacitance of the supercapacitor is determined by the capacitance of both negative and positive electrodes. Due to the different intrinsic properties of cations and anions, identical electrodes can show different capacitance responses under negative and positive polarization in dynamic charging conditions. The stable operating potential window of negative and positive electrodes for the identical active materials can be very different due to the existence of the lowest unoccupied and highest occupied molecular orbitals (LUMO and HOMO) of the electrolytes. Therefore, it is important to investigate the capacitance/capacity of positive and negative electrodes separately by using the three-electrode test system instead of the two-electrode system. A better understanding of positive and negative dynamic charging/discharging processes provides chances for an optimal matching of positive and negative electrodes, which lays the foundation for the better design of supercapacitors at the integrated system level.

Some preliminary research works have been done to address the matching strategy for positive and negative electrodes.[55-58,60,91,158,159] In 2007, Wang and co-workers reported a supercapacitor composed of carbon electrodes with different pore size distributions (PSD) for the study of the fundamental relationship between the PSD of positive and negative electrodes and the performance of the EDLCs.[56] These results showed that the asymmetric configuration (positive and negative electrodes are different) for the EDLCs exhibited better performance compared to the symmetric one (positive and negative electrodes are the same) because of the big size difference between cations and anions. Later in 2008, they reported the predominant contribution of the negative electrode for the EDLCs. The experiment result demonstrated that constructing asymmetric EDL electrodes could increase the overall performance of EDLCs because of the larger size of cations compared to the anions in 1.0 M TEMA BF_4/PC electrolyte.[160] Afterward, in 2013, Wu and co-workers investigated the important parameters affecting the cell voltage of aqueous EDLCs using several different configurations, demonstrating the importance of charge balance for the expanding of working voltage and the full utilization of active materials for the EDLC (**Fig 2.15a**).[159] In 2015, the Gogotsi group studied the effect of electrolyte on the capacitance of EDLCs. These results showed that identical electrodes provide different responses to the anion and cation of the electrolyte, and the working voltage could be expanded by introducing suitable electrolytes for the EDLCs (**Fig. 2.15b**).[91]

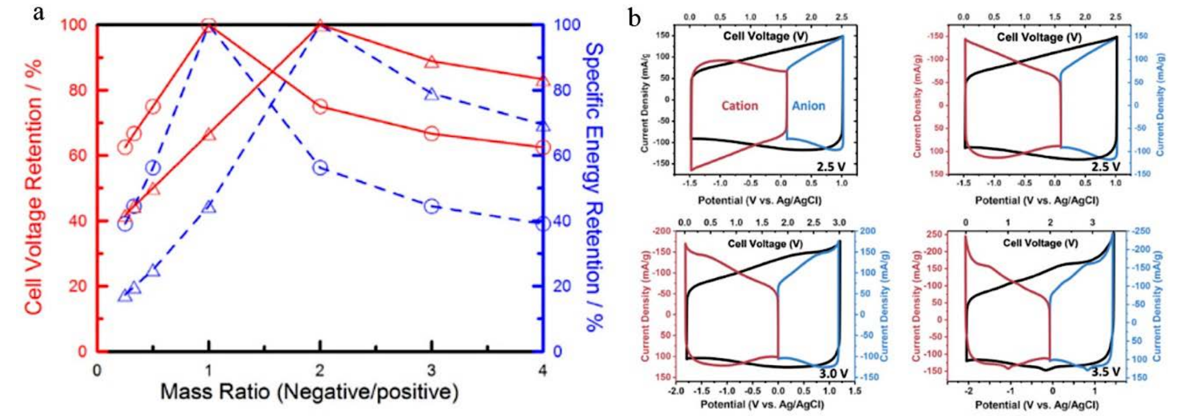

Figure 2.15. (a) Relation among cell voltage retention, mass ratio and specific energy retention at the middle (circle) and one-third points (triangular) cases.[159] **(b)** Cyclic voltammograms for cells assembled with EMI-TFSI electrolyte showing the response of the whole cell (black line) as well as the individual electrodes at different operating voltage.[91]

These works have demonstrated the importance of matching positive and negative electrodes for the EDLC device design. However, due to the limitation of electrode materials, and the use of the trial and error matching strategy on supercapacitors, the optimal matching design for positive and negative electrodes (pore size, thickness) under the dynamic charging process on device-level has not been achieved in supercapacitors. This severely restrains the development of high-performance supercapacitors on the integrated device level.

2.5 Research aims

Based on the literature review, this PhD project will investigate the nanoconfinement effects on the electrochemical performance of nanoporous multilayered graphene-based electrodes in various energy storage electrolytes (such as aqueous electrolytes with different ions, redox-reactive electrolytes with I^- and Zn^{2+}) under dynamic charging/discharging conditions. It will also explore the device-level design of energy storage devices.

First, I study the nanoconfinement effects on EDL capacitance of positive and negative electrodes in various chlorine ion-based aqueous electrolytes. I will conduct these by using experimental and simulation methods for guiding the next-generation high-performance electrolyte selection and increasing the charge storage behaviour understanding, for accelerating the design of a high-performance electrode-electrolyte system.

Second, I study the nanoconfinement effects on the redox-reactive electrolyte system, especially the nanoconfined ion effects on surface electrochemical reaction rates for the new charge storage phenomenon observation. This will lead to the building of new fundamental charge storage knowledge and new charge storage systems for the electrochemical community.

Finally, I apply the machine learning method to the performance prediction of positive and negative electrodes, with the combination of the numerical method and the domain knowledge, assisting the optimal design of energy storage devices on the integrated system level. As a result, the research methods, techniques, and results presented in this PhD thesis could advance the understanding of confined ion effects on the performance of energy storage electrodes and accelerate the next-generation high-performance energy storage device design.

Chapter 3 Ion-specific effect on the EDL capacitance of nanoporous graphene-based electrodes

3.1 Introduction

The electric double layer (EDL) is an interface structure that appears between an electrode and an electrolyte when a charged electrode is exposed to an electrolyte.[19] The electrolyte counter ions (counter-ions: having an opposite charge to that of the electrode surface charge) are closely attracted to the electrode surface via the electrostatic force to form an EDL structure to store charge.[24] Usually, the EDL is comprised of two layers; one is the stern layer, which electrically screens the surface charge via the adsorption of counterions. The second layer is loosely associated with the charged surface, which is called the diffusion layer. The ion information in these layers plays a priority role in the in-depth exploration of charge storage as well as the ions dynamic behavior under nanopores.[161] The EDL capacitance depends on the type of ions (also called ion-specific effect on EDL capacitance).[130] A better understanding of ion features inside the electric double layer (EDL) structure could, therefore, advance the engineering of the electrode/electrolyte interface to increase the charge storage ability of the supercapacitor electrodes, and thus efficiently increase the energy and power density of supercapacitor devices.

Currently, most research within the supercapacitor community is focused on developing new capacitive materials and electrode structures, high working voltage electrolytes, and asymmetric and hybrid supercapacitors devices for obtaining supercapacitor devices with high power and high energy density.[23,24] The exploration and profound fundamental studies of EDL for revealing the detailed charge storage mechanism and ions information of supercapacitors are wholly insufficient, especially from the combination of experiment and simulation aspects. Because of the high importance of nanoporous structure and ion distribution, comprehensive exploration studies and new fundamental understanding of various ions inside the nanoporous electrode are demanded, which could contribute to the predictive design of the next-generation electrode-electrolyte system with excellent electrochemical performance.

Notably, molecular dynamic (MD) simulation results have shown that under nanoconfinement space, the ions could present ion-specific effects, which come from the ion size, ion-specific adsorption, ion distribution, ion hydration energy and ion-ion correlation, etc.[83,86,162-164] These effects have an essential role in determining the resulted EDL structure, ion dynamic behaviour, and EDL capacitance.[83,161] However, due to the limitations of MD simulations (big gaps in time and length scale compared to the practical application), whether these observed confined ion effects on performance achieved from MD could directly transfer to the practical electrochemical electrodes is still questionable. Additionally, due to the limitation of the previously reported electrodes which exhibit disorder and complex porous structure and broad pore size distribution, the well designed electrochemical characterization experiments focusing on ion-specific effects on the EDL capacitance have not been fully achieved. The behind mechanism of ion-specific effects on the EDL capacitance is also not clear.

Electrolytes used for supercapacitors have a high concentration to ensure a high ionic conductivity, which decreases the internal resistance of the device. When the ion concentrations are high, the natural difference between ions cannot be ignored, especially in the EDL region, where the different ions can induce different EDL structures even with identical nanoporous electrodes.[54,70,165] It is well-known that the charge storage of the conductive pore-electrode is highly influenced by the EDL structure when polarizing the electrode, where the EDL structure profile is the position and intensity distribution of counter-ions and co-ions (co-ions: having charge with the same sign as electrode surface charge).[83] Therefore, we propose our research hypothesis that besides the counter-ion effects on the EDL capacitance, the co-ions also present the possible ability to induce a difference of EDL structure, thus leading to different charge storage capacitance and charge storage mechanisms for the supercapacitor electrodes.

Until now, the comprehensive electrochemical experiment of the co-ion effects on the EDL capacitance is not well studied and designed, and effective results are also not precise. Therefore, with the consideration of the complexity and importance of ion-specific effects on the electrode performance under nanoconfinement, comprehensive experiments to measure the electrochemical performance for a range of tunable nano-sized electrodes and electrolytes are necessary to reveal a better understanding of ion-specific effects on EDL capacitance, and identify or discovery a new charging storage mechanisms on EDL electrodes.

In this chapter, we systematically do the electrochemical characterization of various aqueous chloride ion-based electrolytes in nanoporous graphene-based electrodes. The experimental results help to identify the ion-specific effects on the electrode performance. Interestingly, the co-ion does indeed present an impact on the EDL capacitance (the capacitance in HCl is higher compared to KCl) when charging porous electrodes with a positive charge at a low charging rate. We also carried out a series of electrochemical characterization in the mixed KCl/HCl electrolytes with varying amounts of HCl. The open-circuit potential and potential of zero charges of graphene-based electrodes observed in these electrolytes indicated that there is the specific adsorption of the proton to the electrodes, indicating a possible new charging storage mechanism when polarizing the porous-electrodes with the positive charge. Furthermore, we also conducted comprehensive continuum simulation studies to discuss the possible charge storage mechanism for the enhanced capacitance based on modified Poisson-Nernst-Plank and Poisson-Boltzmann theory.

As a result, this research study could provide new insights into ion behaviour inside the EDL in various aqueous electrolytes and contribute an in-depth, comprehensive understanding of confined ion-specific effects on EDL capacitance for the supercapacitor community. Additionally, this fundamental research of EDL and electrolytes could reshape the guidelines for choosing suitable electrolytes for supercapacitor design, resulting in high EDL capacitance of electrodes used as both positive and negative components for the supercapacitor devices. Lastly, the substantial understanding of proton EDL structure achieved in this work could also stimulate the discovery of new knowledge and theory for hydrogen evolution reaction and metallic corrosion communities.

3.2 Materials and methods

3.2.1 Synthesis and characterization of nanoporous graphene-based materials

Chemically converted graphene (CCG) dispersion was synthesized by following the method described in Reference.[166] Briefly, graphene oxide colloid (0.5 mg/ml, 200 ml) made from the modified Hummers' method was mixed with 0.35 ml hydrazine (64wt% in water) and 0.8 ml ammonia (28wt% in water) solution in a glass vial. After being vigorously shaken for a few minutes, the flask was put in a water bath (~100 °C) for 3 hr.

The nanoporous graphene-based electrodes (NPGEs) were fabricated by following the method we previously reported.[47] Generally, taking 20 ml of the reduced CCG dispersion for the vacuum filtration until no CCG solution on the top of the membrane. After that, the achieved membranes were washed with distilled water several times to remove the extra hydrazine and ammonia. Then, the membranes were exchanged with the H_2SO_4 solution with different concentrations for two days, followed by a freezing dry process for two days. Afterword, the freezing dry membranes were washed with distilled water to remove the inside H_2SO_4. The filtration dry sample is achieved by overnight filtration (around 19 h filtration).

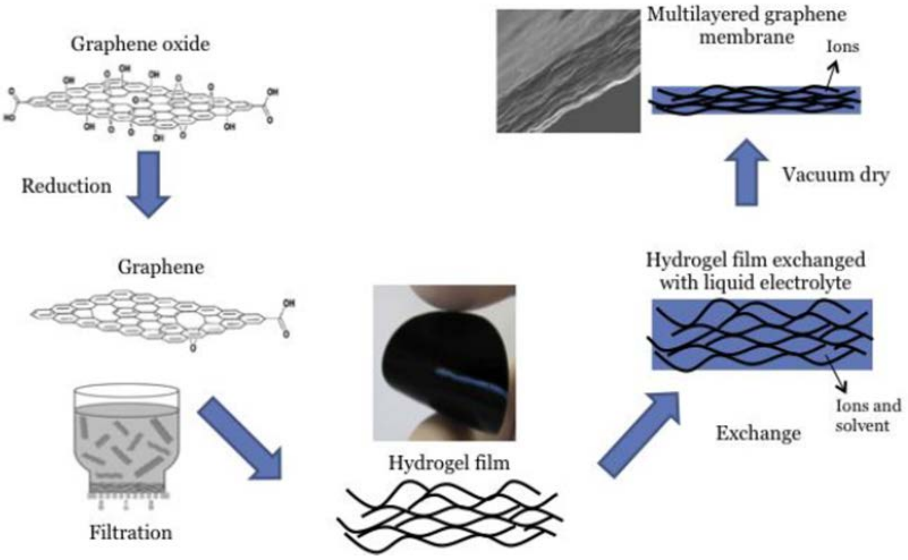

Figure 3.1. Illustration of synthesizing of graphene-based electrodes with tunable nanopore size.

The physical methods for characterizing the pore-size of nano-porous membrane electrodes mainly include Brunauer–Emmett–Teller (BET) gas adsorption method,[117] methylene blue adsorption method,[167] dynamic electrosorption analysis method,[168] and x-ray diffraction analysis method.[129] The comparisons and limitations of applying these methods to characterize the pore size of our synthesized graphene-based membranes have been discussed and reported by our group's previous publication.[47,102,168,169] Briefly, the BET gas adsorption method has the thermal annealing and vacuum cleaning procedures during the characterization. These procedures could change the pore size of our fabricated graphene-based membranes because of the removal of interlayered water molecules.[169] The methylene blue adsorption method is not suitable for characterizing the micropore.[47] The dynamic electrosorption analysis method has the limitation of quantifying the pore size.[168,169] The x-ray diffraction analysis method is difficult to determine the interlayer space of our graphene-based membranes due to the microscopically corrugated structure of the chemical converted graphene.[47,102] Our synthesized graphene-based membranes are formed by parallel chemical converted graphene sheets. There is a simple relationship between membrane thickness and the average interlayer distance (also called slit pore size). Following the method developed by our group,[46,102] I measured the thickness of the graphene-based membranes and then calculated the average interlayer distance (slit pore size) according to the following formula[102]:

$$d = \frac{Areal\ density\ of\ graphene\ \times Thickness\ of\ CCGM}{Areal\ mass\ loading\ of\ CCGM}$$

Where the areal mass density of graphene is reported to be 0.77 mg/m^2, the thickness of the NPGE was measured using a digital micrometer at 1 um resolution.[102]

3.2.2 Electrochemical characterization of multilayered graphene-based materials

The electrochemical characterizations include open-circuit potential (OCP), electrochemical impedance spectroscopy (EIS), cyclic voltammetry (CV) and galvanostatic charge-discharge (G-CD). They were performed using Bio-logic VSP-300. Three-electrode configuration setup is applied for the comprehensive electrochemical studies, where the reference electrode is saturated calomel electrode (SCE), the counter electrode is the hydrogel graphene membranes, and the mass loading is two times that of working electrodes to prevent the electrolyte decomposition on the counter electrode side.

The electrolytes used in this chapter are 1 M LiCl, 1 M NaCl, 1 M KCl, 1 M CsCl, 1 M BmimCl, 1 M HCl electrolyte. 0.01 M HCl+1 M KCl mixture electrolyte, 0.1 M HCl+0.9 M KCl mixture electrolyte.

The electrodes used for the research study are the synthesized hydrogel nanoporous graphene-based electrode with an average pore size of 10 nm (NPGE-10nm), 0.1 M H_2SO_4 solution mediated nanoporous graphene-based electrode with an average pore size of 1.0 nm (NPGE-1nm), filtration dry nanoporous graphene-based electrode with the average pore size of 0.7 nm (NPGE-0.7nm). The area density of the electrodes is around 0.6 mg/cm^2.

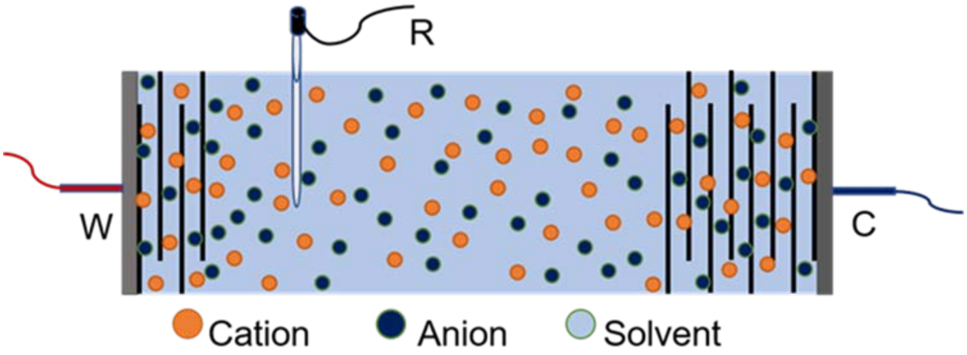

Figure 3.2. Illustration of the electrochemical test setup.

The equation used for calculating the capacitance of various NPGEs (different pore size and thickness at different scan rates) are based on CV results: $C=\int_0^{v/s} j dt/v$, where C is gravimetric capacitance (F/g), j is absolute gravimetric current density (A/g), s is the scan rate (V/s), and v

is the potential window (V).[4] To calculate the volumetric capacitances, the gravimetric capacitance was multiplied by the volumetric (g/cm^3) density of the electrodes.

3.3 Results and discussion

3.3.1 Nanoconfined counter-ion effects on the EDL capacitance of nanoporous electrodes under negative polarization

3.3.1.1 Nano-porous graphene-based electrode with an average pore size of 10 nm

To explore the ion-specific effect (ion type dependent) on the EDL capacitance of nanoporous electrodes, I first studied the electro-adsorption of various monovalent cations at different charge rates under negative polarization using a three-electrode configuration setup. **Fig. 3.3a** presents the curves of differential capacitance-negative polarization in various chloride ion-based monovalent ions aqueous electrolytes at the low scan rate (2 mV/s). All these curves show ideal EDLC features with a rectangular shape, and the differential capacitance is almost constant and independent of the applied voltage at this slow scan rate. In detail, the achieved differential capacitance for the identical NPGE-10nm in these alkaline electrolytes are quite similar, while the differential capacitance in 1 M HCl is much higher than that of other electrolytes, which possibly due to the extra specific ion adsorption sites for the proton adsorption due to the existence of oxygen functional groups of our synthesized graphene-based electrode.

Interestingly, the Bmim$^+$ ion with the largest ion size also exhibited higher capacitance compare to that of K$^+$ and Cs$^+$. This impressive result may be because BMIM$^+$ ions prefer to adsorb significantly on neutral and negatively charged electrodes, and with the increase of the surface charge, the BMIM$^+$ ions tend to be more close to the charged surface,[86] which could induce the higher capacitance of BMIM$^+$ ions in compared to that of the smaller K$^+$ and Cs$^+$ ions. When I further increased the charge rate to 20 mV/s, the differential capacitances in LiCl, NaCl, KCl, CsCl, and BmimCl electrolytes are almost the same, while the capacitance in 1 M HCl is much higher than that of the above electrolytes (**Fig. 3.3b**).

Comparing **Fig. 3.3 a** and **b**, we could see that the capacitance of prepared electrodes (NPGE-10nm) at 20 mV/s show a slightly higher capacitance than that of the capacitance at 2 mV/s. After a comprehensive literature searching, we did not find reasonable clues to understand this observed unusual result. In the following, we provide some discussions. First, the electrode has an average slit pore size of 10 nm and areal mass loading of 0.6 mg/cm^2. At such a large pore size and low areal mass loading, the ion diffusion resistance should be small. It is reasonable to expect that the electrodes could maintain the capacitance at a relatively high charging rate. In our experiments, the capacitance at 20 mV/s is close to the capacitance at 2 mV/s (**Fig. 3.9**). Second, based on the self-discharge results of these electrodes (**Fig. 3.14**), we could see that after resting the electrodes for 1,800 s, there is a decrease of the stored charge due to the self-discharge. There is a possibility that during charging, the electrodes simultaneously undergo self-discharge. The self-discharge at 2 mV/s is likely more significant than that at 20 mV/s, leading to the observed slightly lower capacitance.

Furthermore, when we increase the charge rate to 200 and 1,000 mV/s (**Fig 3.3c and d**), the results show that the differential capacitance is in the order of $C\_{}_{\mathrm{1M\ HCl}} > C\_{}_{\mathrm{1M\ KCl}} = C\_{}_{\mathrm{1M\ CsCl}} > C\_{}_{\mathrm{1M\ LiCl}} = C\_{}_{\mathrm{1M\ NaCl}} > C\_{}_{\mathrm{1M\ BmimCl}}$, which is quite different to the results observed at a slow charge rate. These results agree with the diffusion coefficient of these ions in the aqueous solution (**Tab. 3.1**). The electrochemical characterization results for ion confined in the 10 nm nanopore electrode suggest that the effect of the ions on EDL capacitance also largely depends on the charging rates and electrode surface properties (especially the oxygen functional groups).

Table 3.1 Ion hydrated and dehydrated radius and ionic diffusion coefficients and hydration enthalpies.[170-173]

Ion	Hydrated Radius[1] (Å)	Dehydrated Radius[1] (Å)	diffusion coefficients (10^{-6} cm^{2}s^{-1})	Hydration Enthalpies[4] (kJ mol^{-1})
K^{+}	3.31	1.49	1.96	-322
Li^{+}	3.82	0.94	1.0	-519
Na^{+}	3.58	1.17	1.3	-406
Cs^{+}	3.29	1.86	2.0	-264
Bmim^{+}	NA	2.9 in width	0.4-0.8	NA
H^{+}	2.8	NA	9.3	-1091
Cl^{-}	3.32	1.64	2.0	-381

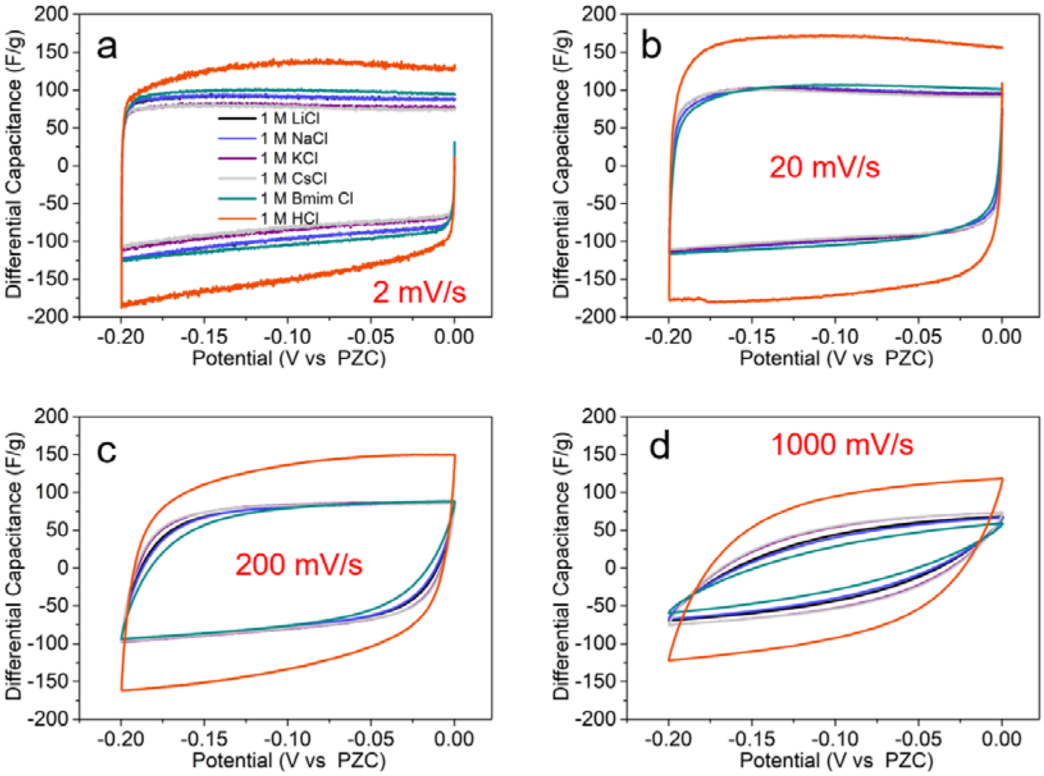

Figure 3.3. (a), (b), (c) and **(d)** show the CV curves of NPGE-10nm in 1 M LiCl, 1 M NaCl, 1 M KCl, 1 M CsCl, 1 M BmimCl and 1 M HCl electrolytes under the scan rates of 2 mV/s, 20 mV/s, and 200 mV/s and 1,000 mV/s, respectively.

3.3.1.2 Nano-porous graphene-based electrode with an average pore size of 1 nm

Next, I narrowed down the average pore size of our developed graphene-based membrane electrodes to 1.0 nm to further evaluate the ion type effect on the EDL capacitance response at such a nanoconfined interface. **Fig. 3.4a** presents the curves of differential capacitance-negative polarization in the chloride ion-based monovalent ion aqueous electrolytes at the low scan rate (2 mV/s). The shape of the curves are very similar to that of the 10 nm pore size electrodes, and the HCl electrolyte also has the best capacitance compared to other tested electrolytes. Notably, as the pore size narrows down to 1.0 nm, the EDL capacitance in 1 M LiCl and 1 M KCl is almost the same, which is different from the observed capacitance of NPGE-10nm. The decrease of EDL capacitance in LiCl electrolyte maybe comes from the larger hydration size of Li^+, demonstrating the nanoconfined effect about lithium ions on the EDL capacitance. To explore the confined ion effect under dynamic charging/discharging conditions, we further increase the scan rate to 200 and 1,000 mV/s (**Fig.3.4c and d**), the capacitance-potential curves quite agree with that achieved on NPGE-10nm, while notably, there is a larger capacitance decrease compared to that of NPGE-10nm, especially for the ions with large hydration sizes and low diffusion coefficients.

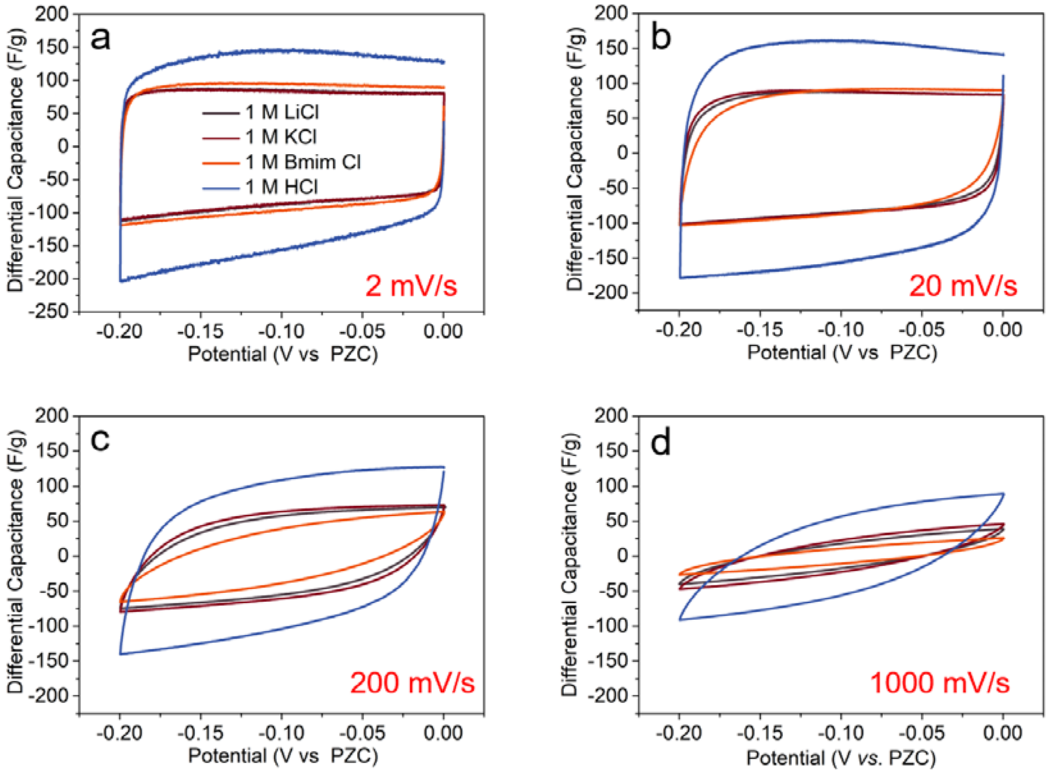

Figure 3.4. (a), (b), (c) and **(d)** show the CV curves of NPGE-1nm in 1 M LiCl, 1 M KCl, 1 M BmimCl and 1 M HCl electrolytes under the scan rates of 2 mV/s, 20 mV/s, and 200 mV/s and 1,000 mV/s, respectively.

3.3.1.3 Nano-porous graphene-based electrode with an average pore size of 0.7 nm

Later, I further engineered the average pore size of the graphene-based membrane electrodes down to 0.7 nm to characterize the electrochemical performance in the mentioned above electrolytes. Generally, comparing **Fig. 3.5a** and Fig 3.3a, the capacitance tested in these test electrolytes for the sub-nanometer electrode is smaller than that of the NPGE-10nm. This result is quite different from the previously reported results,[119] where the observation of capacitance increased in the sub-nanopore electrode due to partial dehydration. Based on recently published research, with the decrease of the nanopore size, there is a decrease in the dielectric constant of the water molecules.[70,174] Therefore, the capacitance decrease of the NPGE-0.7nm indicates that the dielectric constant possibly plays a decisive role in the EDL capacitance instead of ion (ion de-hydration) size effect.

Additionally, we also observed that the charging curve obtained in 1 M BmimCl electrolyte is quite different compared to other tested electrolytes, even at a very low scan rate, the differential capacitance achieved in BmimCl electrolyte is smaller than that of the other tested electrolytes. These results may be due to the much larger ion size of the $Bmim^+$ (with the length of 1.1 nm, a width of 0.58 nm),[173] which is not favorable to the penetration of $Bmim^+$ ions into these sub-nanometer pores, resulting in the decrease of the EDL capacitance. This result indicates the importance of pore size on the EDL capacitance, especially for the working electrolyte with large counter ions.

After further increasing the scan rate to 200 and 1,000 mV/s (**Fig.3.5 c** and **d**), we can see the EDL capacitance in the BmimCl electrolyte decrease almost down to 0. Even for protons with a high diffusion coefficient, with the increase of the charge rate, there is still a considerable decrease of the EDL capacitance (the integrated area of the discharge curve) of NPGE-0.7nm. In general, the electrochemical characterization results achieved here highly indicate the importance of each ion effects (such as ion steric, ion diffusion coefficient, ion dehydration, ion-specific adsorption) on the EDL capacitance depends on the charging rate, pore size and surface chemistry of electrodes. Mainly, due to the large capacitance difference between HCl and other studied electrolytes on all the three tested confined electrodes with the pore size of 10 nm, 1 nm and 0.7 nm under various dynamic charging rates, we propose the charge storage mechanism of the proton is quite different with other ions.

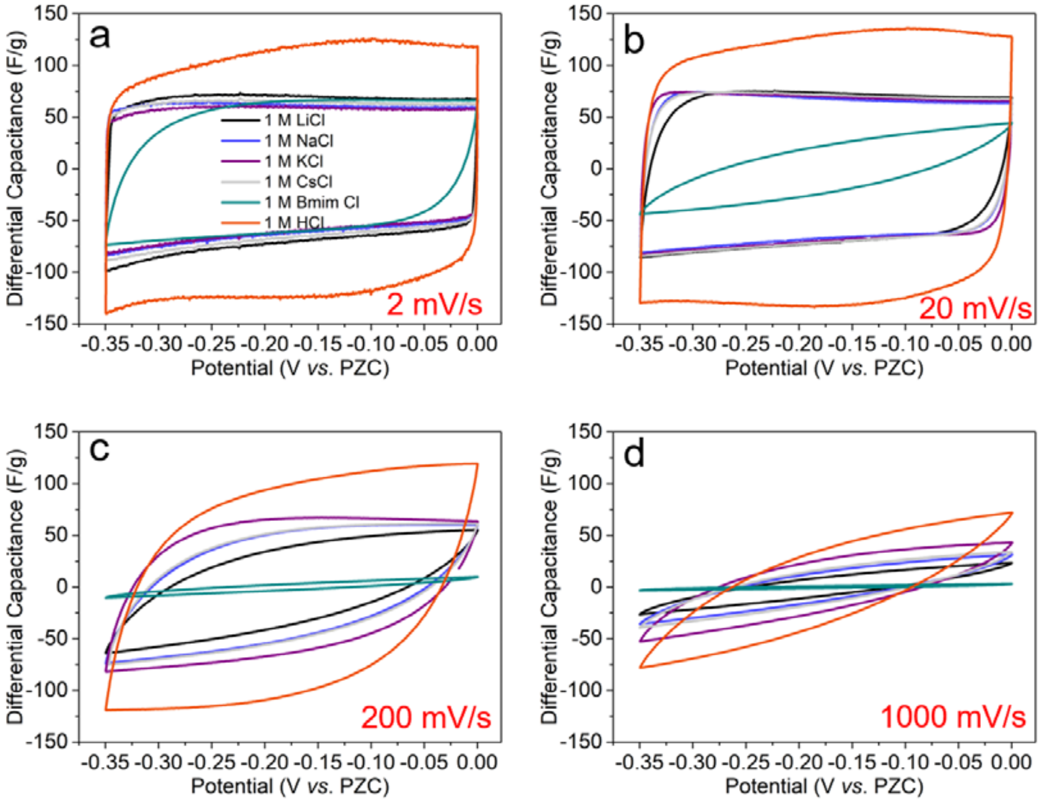

Figure 3.5. (a), (b), (c) and **(d)** show the CV curves of NPGE-0.7nm in 1 M LiCl, 1 M KCl, 1 M BmimCl and 1 M HCl electrolytes under the scan rates of 2 mV/s, 20 mV/s, and 200 mV/s and 1,000 mV/s, respectively.

3.3.2 Nanoconfined co-ion effects on the EDL capacitance of nanoporous electrodes

3.3.2.1 Nano-porous graphene-based electrode with an average pore size of 10 nm

According to the above-nanoconfined ion effect studies, we could conclude that with the change of the used electro-adsorption counter ions, there is the variation of the EDL capacitance. The ion effects on the EDL capacitance largely depend on the charging rates and pore sizes. Compare to the research study of counter-ion effects on the EDL capacitance. I am also interested in co-ion effects on the EDL capacitance because the device performance depends on both positive and negative electrodes. The understanding of co-ion effects on the EDL capacitance could provide valuable information on engineering an electrolyte for both positive and negative electrodes with high performance. Based on this research idea, and the importance of nanopore structure on performance, we continued to do the comprehensive cyclic voltammetry (CV) study of the NPGE-10nm, NPGE-1nm and NPGE-0.7nm in the above electrolytes (same counterion: Cl^-, different co-ion: Li^+, Na^+, K^+, Cs^+, $Bmim^+$, H^+) under positive polarization to evaluate the co-ion effects on EDL capacitance. To remove the negative charge effect on the EDL capacitance, the starting potential is the potential of zero charges (PZC), meaning the surface charge of the electrode is zero at this potential. The method of determining PZC has been widely reported.[175] **Fig. 3.6** presents the EDL capacitance of 10 nm pore size electrodes in these six electrolytes at different charge rates. Interestingly, considering the electro-adsorption of the same counter ions, the identical electrodes in these same counter-ion electrolytes show different EDL capacitance at a very slow charge rate (**Fig. 3.6a**), especially for the HCl electrolyte, and the capacitance order in these electrolytes are quite agreement with that presented for the negative charge process (counter-ion effect study).

Additionally, with the increase of scan rate, the capacitance ratio of the identical electrode charged in 1 M HCl and other electrolytes also increased. Especially, when the scan rate increase to 1,000 mV/s (**Fig. 3.6d**), the EDL capacitance in 1 M HCl electrolyte is around 2 times that in 1 M BmimCl, even for the same Cl^- adsorption for the EDL capacitance. These results indicate there may be a co-ion exchange charge storage mechanism for the positive polarization of the confined graphene-based electrodes under a fast charge rate condition. Importantly, the observed electrochemical results also demonstrate that there is a co-ion effect for the EDL capacitance, especially for the fast charge rate demand.

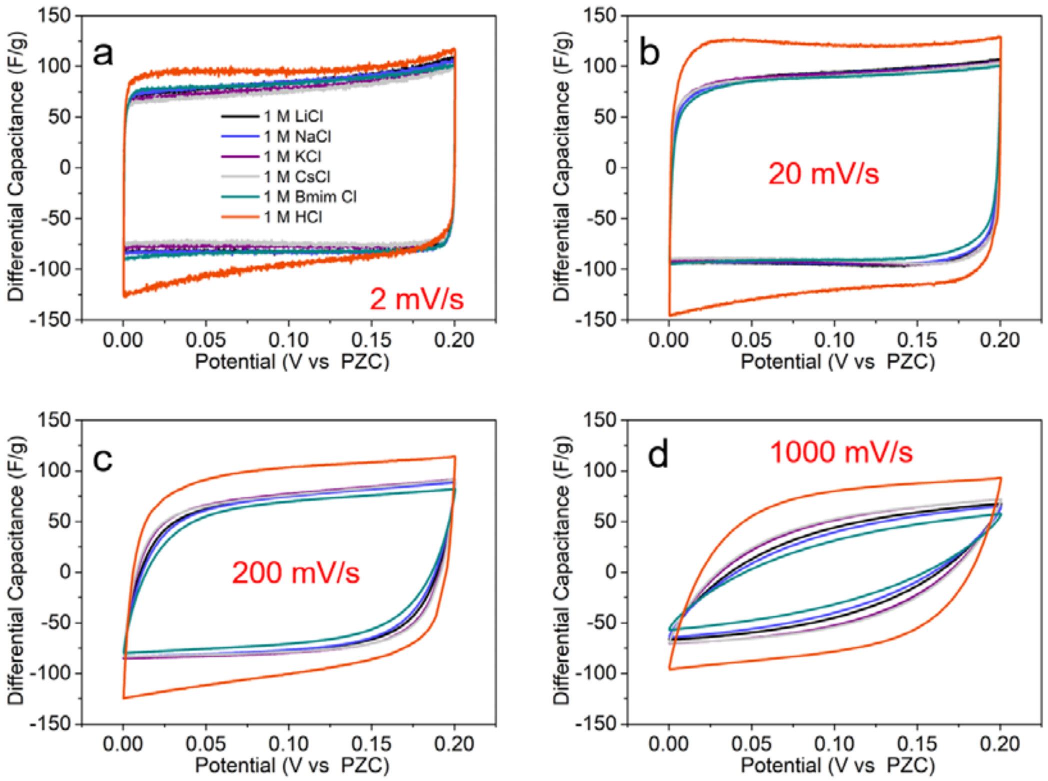

Figure 3.6. (a), (b), (c) and **(d)** show the CV curves of NPGE-10nm in 1 M LiCl, 1 M KCl, 1 M BmimCl and 1 M HCl electrolytes for positive charge under the scan rates of 2 mV/s, 20 mV/s, and 200 mV/s and 1,000 mV/s, respectively.

3.3.2.2 Nano-porous graphene-based electrode with an average pore size of 1 nm

Next, we decreased the pore size of graphene-based nanoporous electrodes to further study the nanoconfined co-ion effect on the EDL capacitance in the above electrolytes. The shape of the capacitance-potential curve of the NPGE-1nm is quite similar to that of the NPGE-10nm, with a slight difference at high charging rates (**Fig. 3.7**). At 1,000 mV/s, we can see the EDL capacitance in 1 M HCl electrolyte is much higher than that of 1 M BmimCl electrolyte (around three times for NPGE-1nm *vs*. two times for NPGE-10nm). Additionally, the EDL capacitance response in these electrolytes with the same counter ions (Cl^- as electro-absorption ion) is quite similar to the EDL capacitance with the different counter ion (Li^+, Na^+, K^+, Cs^+, $Bmim^+$, and H^+ as the electro-adsorption ions). These interesting results have not yet been well observed or reported.

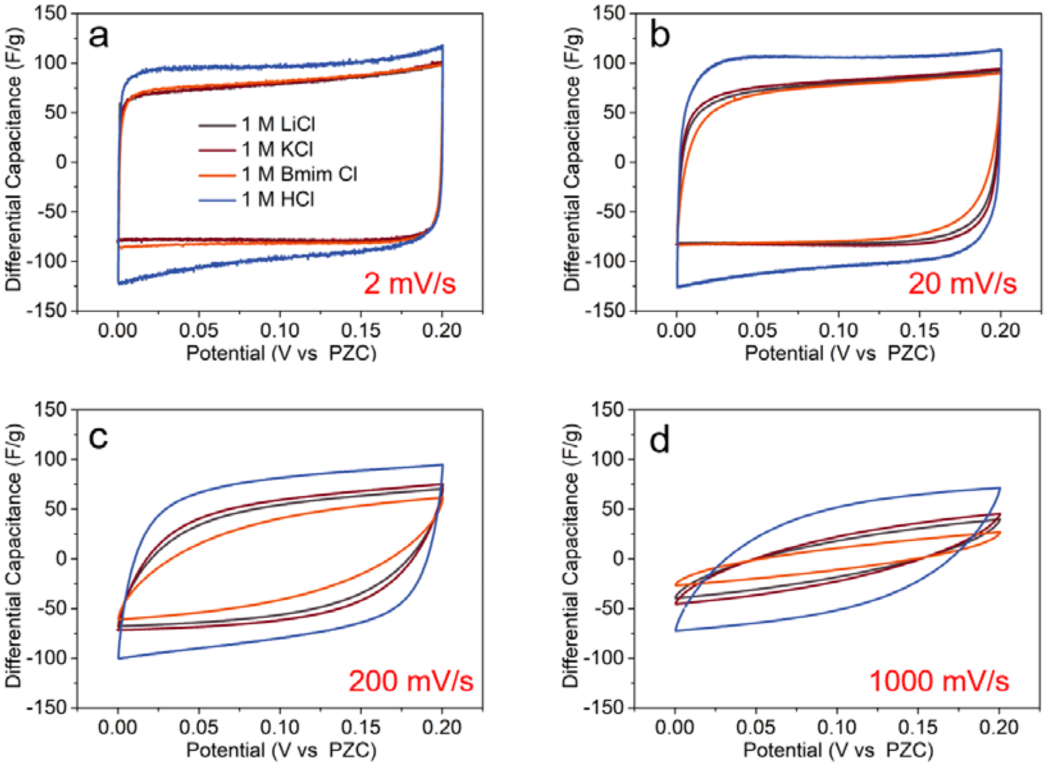

Figure 3.7. (a), (b), (c) and **(d)** show the CV curves of NPGE-1nm in 1 M LiCl, 1 M KCl, 1 M BmimCl and 1 M HCl electrolytes for positive charge under the scan rates of 2 mV/s, 20 mV/s, and 200 mV/s and 1,000 mV/s, respectively.

3.3.2.3 Nano-porous graphene-based electrode with an average pore size of 0.7 nm

Afterward, we further decreased the pore size of the graphene-based nanoporous electrodes to 0.7 nm, which is smaller than the hydrated ion size, to evaluate the co-ion effect on the EDL capacitance under such sub-nanometer confined nanopore. The curves of the capacitance-potential of the NPGE-0.7nm are quite similar to that of the NPGE-10nm and NPGE-1nm (**Fig. 3.8**). The difference mainly comes from the high charge rates. At 200 and 1,000 mV/s, we can see the EDL capacitance in 1 M BmimCl electrolyte is close to zero with the positive surface charge, and the EDL capacitance of the identical electrode in 1 M HCl and 1 M KCl electrolytes are more than fifty times and ten times than that in 1 M BmimCl electrolyte. These interesting results demonstrate that the possible predominant charge storage mechanism is co-ion repulsion and exchange instead of counter-ion adsorption at a fast charging rate.

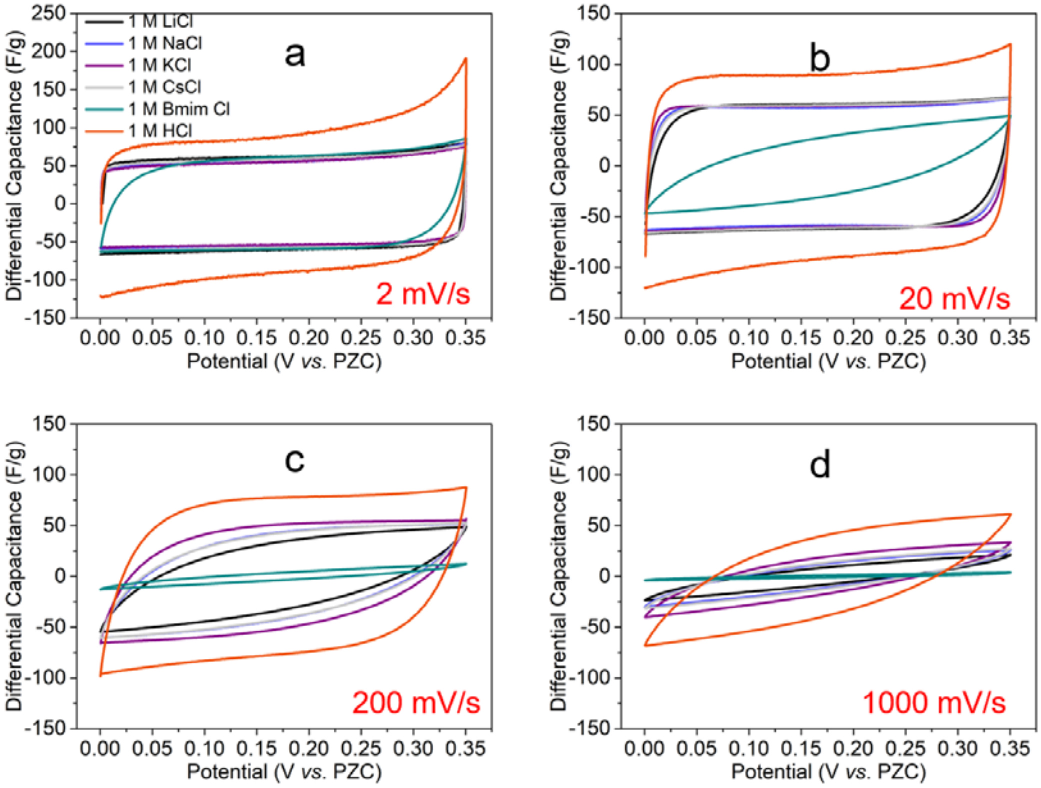

Figure 3.8. (a), (b), (c) and **(d)** show the CV curves of NPGE-0.7nm in 1 M LiCl, 1 M KCl, 1 M BmimCl and 1 M HCl electrolytes for positive charge under the scan rates of 2 mV/s, 20 mV/s, and 200 mV/s and 1,000 mV/s, respectively.

3.3.3 Proton effect on the EDL capacitance of nanoporous graphene-based electrodes

The above-observed results on co-ion effects on the EDL capacitance indicate that the different nanoconfined ion-ion combinations could lead to different EDL capacitance, especially for the proton. To further evaluate the role of proton in determining the EDL capacitance and charge storage mechanism under positive surface charge process, we also did a comprehensive electrochemical characterization of the developed graphene-based nanoporous electrodes in 1 M KCl, 1 M HCl, and mixture KCl/HCl electrolytes under positive polarization.

We conducted the comprehensive cyclic voltammetry (CV) studies of the NPGE-10nm, NPGE-1nm, and NPGE-0.7nm in KCl and mixed HCl/KCl electrolytes with different H^+ concentrations (same counterion: Cl^-, different co-ion: K^+, H^+) for the positive polarization. To eliminate the negative charge effect on the EDL capacitance, the starting potential is the potential of zero charge.

Fig. 3.9 presents the EDL capacitance of NPGE-10nm in these electrolytes at different charging rates. Interestingly, besides the similar results achieved in the previous positive polarization test (Fig. 3.6), the performance of the identical electrode weakly depended on the proton concentration at a very slow charge rate (**Fig. 3.9a**). With the addition of 0.01 M HCl to the 1 M KCl electrolyte, there is a significant increase of the capacitance during the positive surface charge. Considering there is no observation of peaks from these CV curves, and the working potential range also beyond the redox potential of protons and quinone-type groups, the indication is that the capacitance increase in HCl electrolytes with various concentrations is not primarily due to the faradic reaction between proton and surface oxygen functional groups.[176,177] With the increase of scan rates (increase to 1,000 mV/s), the capacitance achieved in KCl and mixture KCl/HCl electrolytes is close (**Fig. 3.9b and c**), indicating the importance of ion centration on the EDL capacitance at a fast charging rate. Especially, with the increase of the charging rate, there is an increase of the normalized capacitance (capacitance ratio of the identical electrode in HCl and KCl electrolytes). The above-observed results indicate that with the increase of the charging rate, there is an increase of the co-ion repulsion charge storage mechanism for the positive polarization of the confined graphene-based electrodes. Importantly, at a low charge rate, there is enough time and space for the electro-adsorption of Cl^- to screen the surface charge of the NPGE-10nm. Therefore, the capacitance difference at the slow charge rate for the NPGE-10nm in these electrolytes should not come from the counter ion adsorption mechanism.

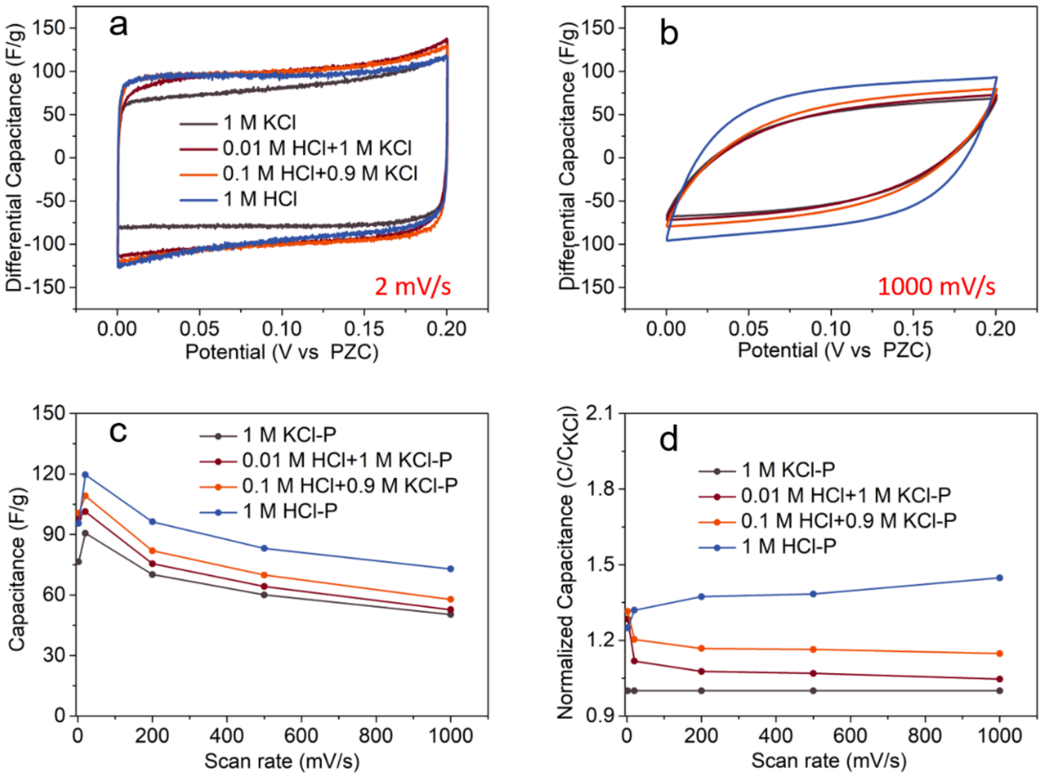

Figure 3.9. (a) and **(b)** show the CV curves of NPGE-10nm in 1 M KCl, 1 M HCl and mixture electrolytes for positive charge under the scan rates of 2 mV/s and 1,000 mV/s, respectively; **(c)** and **(d)** show the capacitance and normalized capacitance of the NPGE-10nm in 1 M KCl, 1 M HCl, and mixture electrolytes for the positive charge under different charge rates.

Furthermore, we decreased the pore size of the graphene-based nanoporous electrodes to further study the nanoconfined proton effect on the EDL capacitance in the above electrolytes (**Fig. 3.10**). The curves of the capacitance-potential of the NPGE-1nm are quite similar to that of the NPGE-10nm. The difference mainly comes from the high charge rates. With the increase of the proton concentration, there is an increase in the rate ability of the electrode, especially at 1,000 mV/s. We can see the EDL capacitance in the 1 M HCl electrolyte is much higher than that in 1 M KCl electrolyte (around 1.8 times of NPGE-1nm *vs*. 1.5 times of NPGE-10nm).

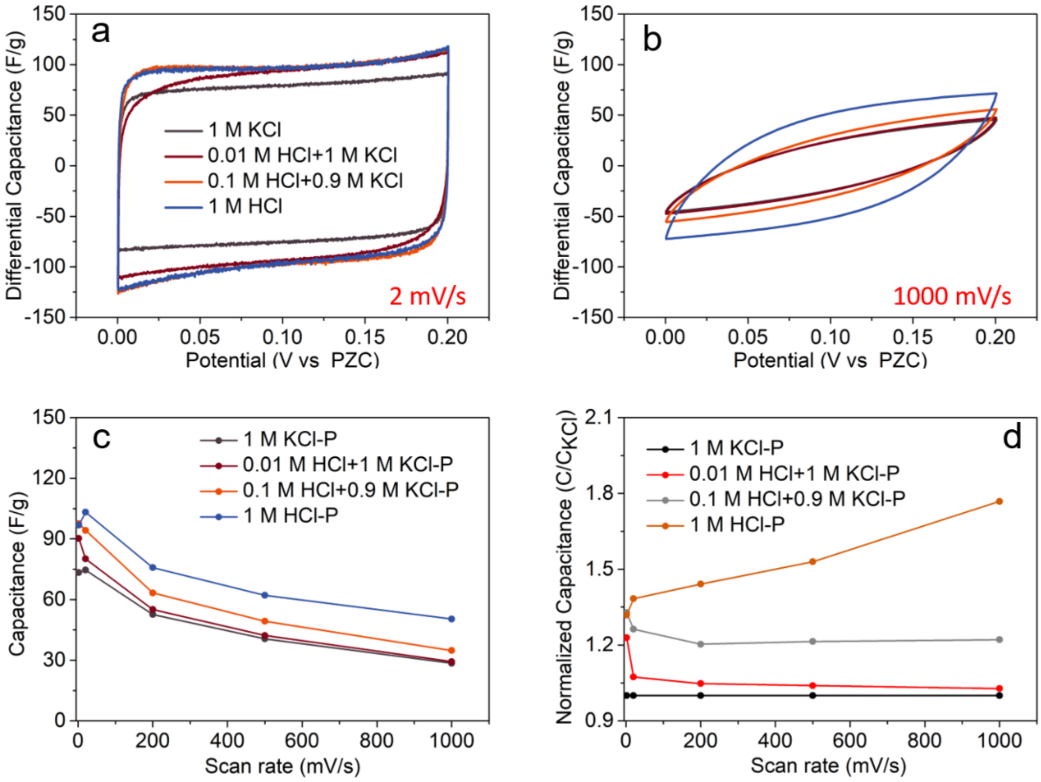

Figure 3.10. (a) and **(b)** show the CV curves of NPGE-1nm in 1 M KCl, 1 M HCl, and mixture electrolytes for the positive charge under the scan rates of 2 mV/s and 1000 mV/s, respectively; **(c)** and **(d)** show the capacitance and normalized capacitance of the NPGE-1nm in 1 M KCl, 1 M HCl, and mixture electrolytes for the positive charge under different charge rates.

Afterward, we further decreased the pore size of the graphene-based nanoporous electrodes to 0.7 nm, which is smaller than the hydrated ion size of K^+ and Cl^-, to evaluate the proton effect on the EDL capacitance under such sub-nanometer confined space. The curves of the capacitance-potential of the NPGE-0.7nm are quite similar to that of the NPGE-10nm and NPGE-1nm (**Fig. 3.11**). Notably, even with the slow charge rate, the normalized capacitance can still reach 1.5, which is higher than 1.2 (for NPGE-10nm) and 1.25 (for NPGE-1nm). At 1000 mV/s, we can see the EDL capacitance in 1 M KCl electrolyte is less than 15 F/g, the EDL capacitance in 1 M HCl electrolyte is higher than 45 F/g, more than three times of that in 1 M KCl electrolyte (around 1.8 times for NPGE-10nm and 1.5 times for NPGE-1nm), highly indicating the importance of confined ion effect and appearance of special ion effect under nanoconfined pore electrodes.

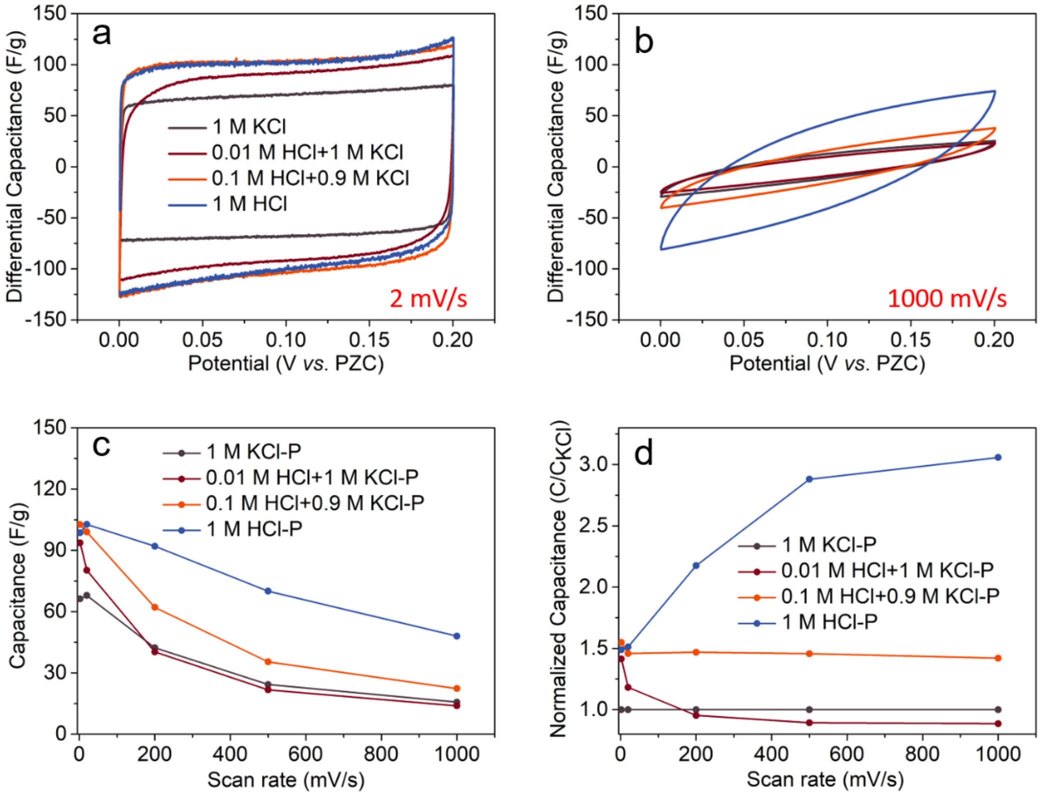

Figure 3.11. (a) and **(b)** show the CV curves of NPGE-0.7nm in 1 M KCl, 1 M HCl, and mixture electrolytes for the positive charge under the scan rates of 2 mV/s and 1000 mV/s, respectively; **(c)** and **(d)** show the capacitance and normalized capacitance of the NPGE-0.7nm in 1 M KCl, 1 M HCl, and mixture electrolytes for the positive charge under different charge rates.

3.4 Discussions of proton effects on EDL capacitance from electrochemical characterization

Although interesting and surprising results were observed for the co-ion effects, especially proton, on the EDL capacitance of different pore size electrodes. However, the behind charge storage mechanism has not been well understood in regard to its surprising capacitance increase in HCl electrolyte (compare to KCl electrolyte) during the positive surface charging process from the cyclic voltammetry characterization study. Therefore, we continued to apply other electrochemical characterizations to understand the possible un-explored mechanism for this interesting result.

Firstly, we did the open circuit potential (OCP) test of the NPGE-10nm in the above electrolytes (before the test, the electrode was immersed in the tested electrolyte and stirred continuously at a rate of 350 rpm for 24 hours). The results showed that with the increase of the HCl, there is an increase in the electrode OCP (**Fig. 3.12a**). Considering the identical physical and chemical properties of the electrodes, the increase of the OCP should come from the proton. The specific reason for this kind of potential increase in HCl electrolyte is the adsorption of the proton on the electrode surface, leading to an increase in the surface potential of the graphene-based electrodes. When we compared the electrochemical results of OCP and PZC (**Fig. 3.12b**), we could conclude that the proton adsorption is mainly physical adsorption instead of chemical adsorption, which means the interaction force between proton and pore surface is not very strong.

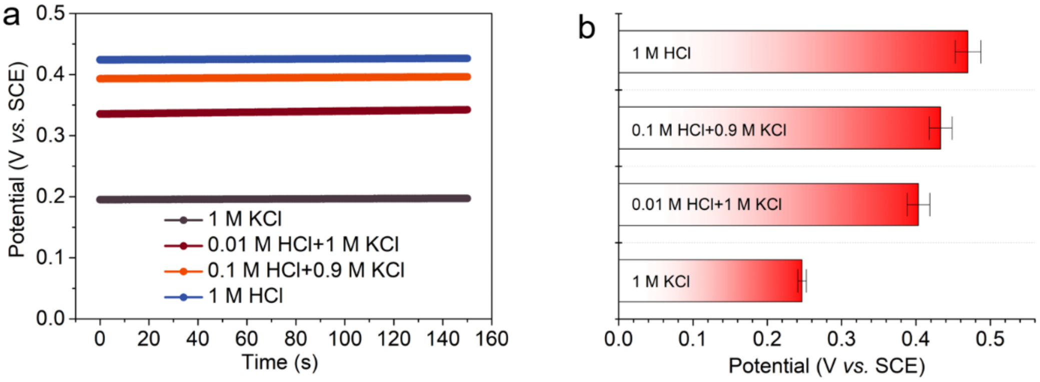

Figure 3.12. (a) and **(b)** show OCP and PZC results of the NPGE-10nm in 1 M KCl, 1 M HCl, and mixture electrolytes.

Fig. 3.13 shows the experimental Nyquist plots of the identical 10 nm nanoporous sample investigated above in different aqueous electrolytes. At 0 V and 0.1 V/PZC (**Fig. 3.13a and c**), when applying the amplitude voltage, the anions are adsorbed into the nanopores, and cations are repulsed from the pores. In the middle frequency range (**Fig. 3.13b and d**), quite different plot shapes are observed for the large pore size sample in these tested electrolytes. A higher value of the real impedance of the electrode in the 1 M KCl electrolyte is observed, revealing the higher polarization resistance of the identical electrode in 1 M KCl electrolyte. Indicating there is proton repulsion when charging the positive charge at a high frequency. In the low-frequency regime, the NPGE-10nm exhibited the vertical lines in the above electrolytes, which stands for ideal capacitive behaviour. It appears that the NPGE-10nm tested in 1 M KCl electrolyte has a higher imaginary resistance at the same low frequency (10 mHz), indicating the lower EDL capacitance for the KCl electrolyte. The observed EIS results are quite in agreement with the CV characterization results.

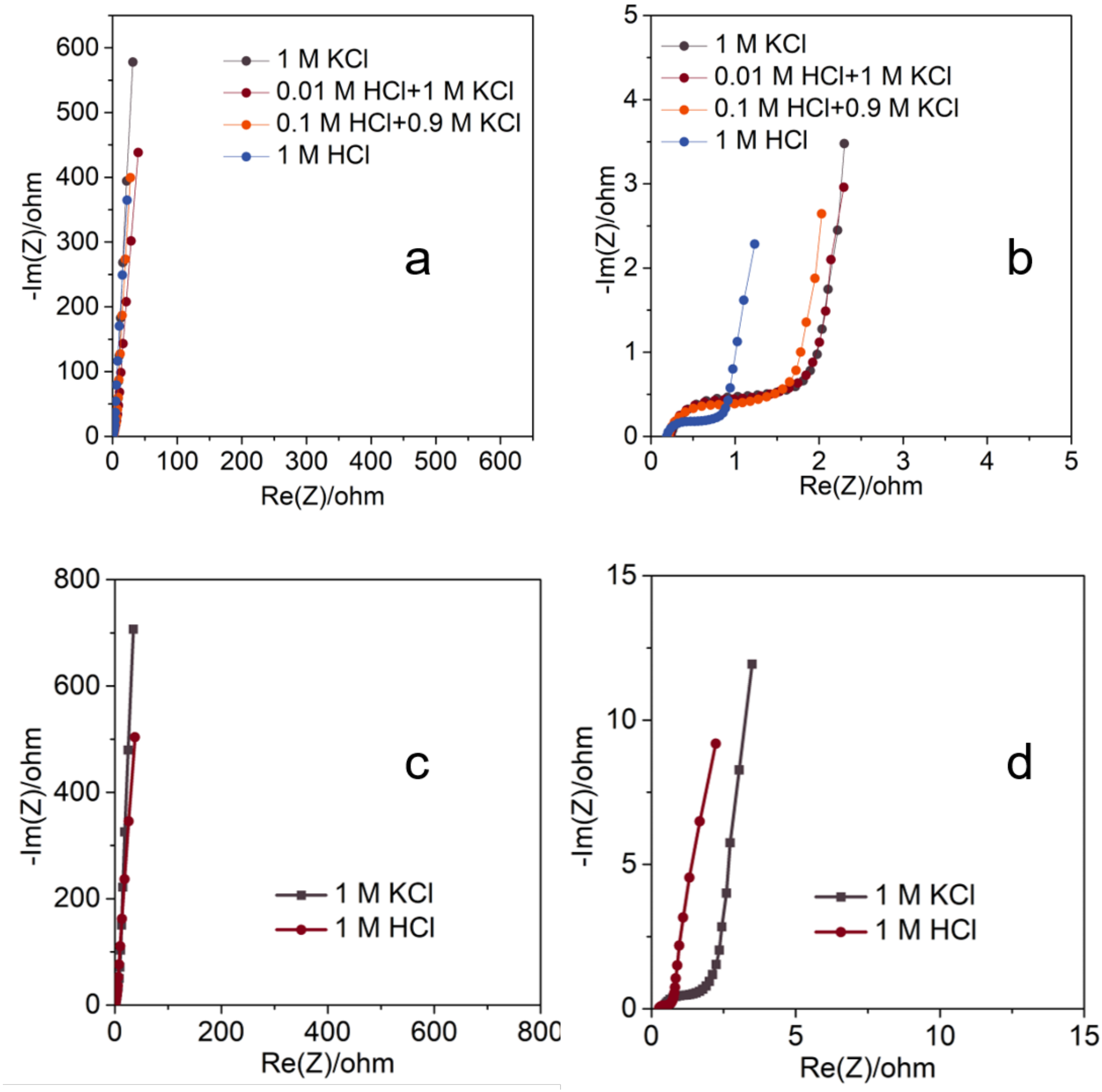

Figure 3.13. (a) Nyquist plots of NPGE-10nm in 1 M KCl, 1 M HCl, and mixture electrolytes at the frequency of 1000 kHz to 10 mHz at the potential of PZC; **(b)** A zoom at high frequencies; **(c)** Nyquist plots of NPGE-10nm in 1 M KCl, 1 M HCl, and mixture electrolytes at the frequency of 1000 kHz to 10 mHz at the 0.1 V vs. PZC; **(d)** A zoom at high frequencies.

To evaluate the EDL properties, we conducted the self-discharge (SDC) test of our porous electrode in 1 M HCl, 1 M KCl, and mixture electrolytes. The results show that the SDC process of the identical electrode (NPGE-10nm) in 1 M KCl is much faster than that in 1 M HCl and 0.1 M HCl/0.9 M KCl electrolytes (**Fig. 3.14 a** and **b**). We charged the identical electrodes with the same surface charge in these electrolytes and then rested the electrodes for 1,800 s. The measured electrode potential decrease in 1 M KCl, 0.01 M HCl/1 M KCl, 0.1 M HCl/0.9 M KCl, and 1 M HCl electrolytes are around 68 mV, 54 mV, 42 mV, and 37 mV, respectively (**Fig. 3.14a**). These results suggest that at the positively charged surface, proton might change the EDL structure (i.e., the distribution of cations and anions), which could enhance the capacitance and lower self-discharge.

With the same surface charge, the electric potential increase of the NPGE-10nm electrodes in 1 M KCl, 0.01 M HCl/1 M KCl, 0.1 M HCl/0.9 M KCl, and 1 M HCl electrolytes is about 0.27 V, 0.21 V, 0.2 V, and 0.17 V, respectively (**Fig. 3.14a**). We postulate that the positively charged surface could repel the absorbed protons away from the surface. The removal of protons at the electrode surface would lead to a reduced electrode potential (without charge, the higher surface potential in 1 M HCl comes from the proton adsorption), which is consistent to our OCP test results. If we would keep the electrode at the same electrical potential level, more positive charges should be injected to the electrode surface to balance the removed surface protons. Therefore, there is an increase of the stored charge for the porous electrode in 1 M HCl electrolyte.

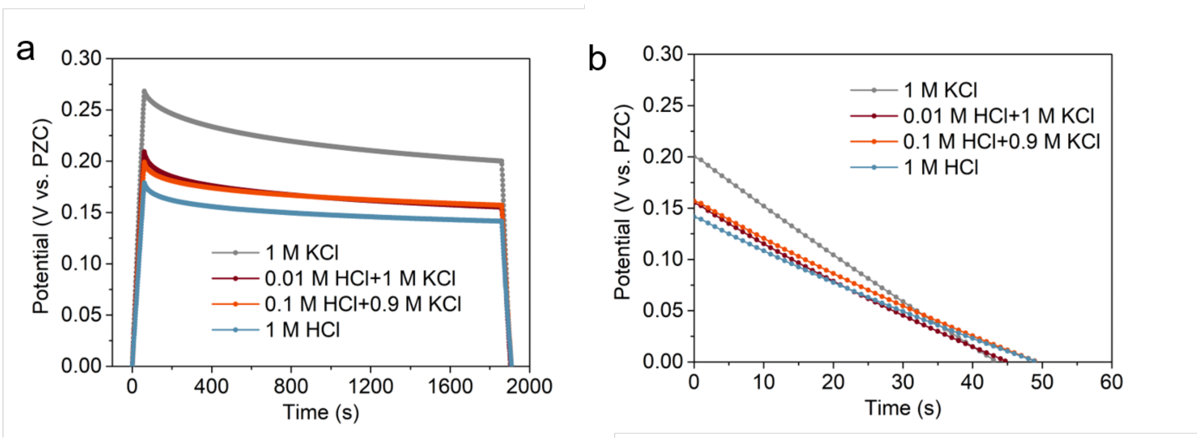

Figure 3.14. (a) Potential changes (‘self-discharge profile’) of the NPGE-10nm under open-circuit conditions (after galvanostatic charging at 0.3 A/g for 60s); **(b)** Galvanostatic discharge curves of the NPGE-10nm after self-discharge for 30 mins in 1 M HCl, 1 M KCl, and mixture electrolytes.

After this, we further conducted the open circuit potential (OCP) test of the sub-nanometer porous electrode in the above electrolytes. Before the test, the sub-nanometer porous electrode was immersed in the tested electrolyte and stirred continuously at a rate of 350 rpm for 24 hours. The results indicate that with the concentration increase of HCl, there is an increase of the OCP for the sub-nanometer electrode (**Fig. 3.15a**), indicating the penetration of protons into the sub-nanometer pore. Notably, with the decrease of the pore size of the electrode, there is the increase of the OCP in the tested electrolytes, especially in 1 M HCl electrolyte with around 30 mV potential increase for the sub-nanometer electrode compared to the large pore size electrode (the surface chemistry of the two electrodes is the same). This observation confirms the pore size effect on the ion adsorption. When we compare the PZC of NPGE-0.7nm and NPGE-10nm (**Fig. 3.15b**), we could see that the PZC for these two pore size electrodes is almost the same, which means the PZC of the electrode tends to be the intrinsic properties of the electrode-electrolyte system.

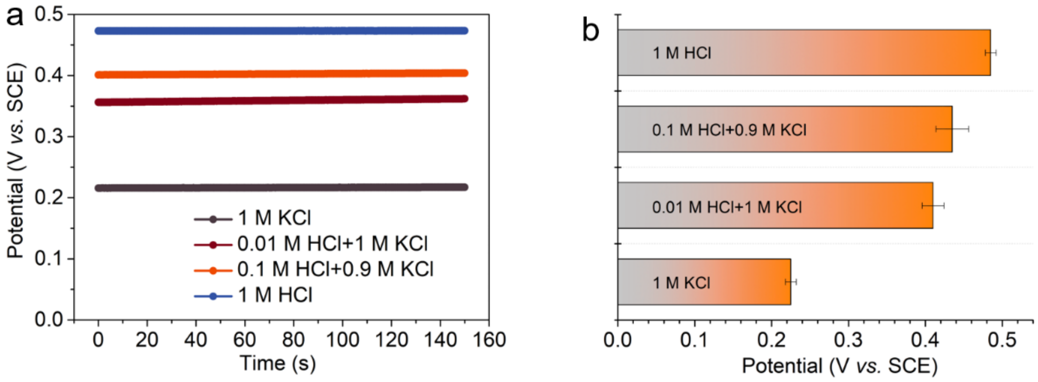

Figure 3.15. (a) and **(b)** show OCP and PZC results of the NPGE-0.7nm in 1 M KCl, 1 M HCl, and mixture electrolytes.

Fig. 3.16 shows the experimental Nyquist plots of the identical NPGE-0.7nm in different aqueous electrolytes at 0 V and 0.1 V/PZC (**Fig. 3-16a and c**). When applying the amplitude voltage, the anions are adsorbed into the nanopores, and cations are repulsed from the pores. In the middle frequency range (**Fig. 3-16b and d**), quite different plot shapes are also observed for the large pore size sample in these tested electrolytes. The higher value of the real impedance of the electrode in the 1 M KCl electrolyte was observed, revealing the higher polarization resistance of the identical electrode in 1 M KCl electrolyte. Additionally, compared to the low ion diffusion resistance (the projection length of the 45-degree line) of the NPGE-10nm, the NPGE-0.7nm has much higher ion diffusion resistance, around ten times that of the NPGE-10nm. In the low-frequency regime, the NPGE-0.7nm exhibits the lines with deviation from the theoretical vertical line, indicating a relatively poor capacitive behavior compared to the NPGE-10nm, demonstrating the confined size effect for the EDL capacitance. It appears that the identical sample tested in 1 M KCl electrolyte has a higher imaginary resistance at the same low frequency (10 mHz), indicating the lower EDL capacitance for the KCl electrolyte. The observed EIS results are quite in agreement with the CV characterization results.

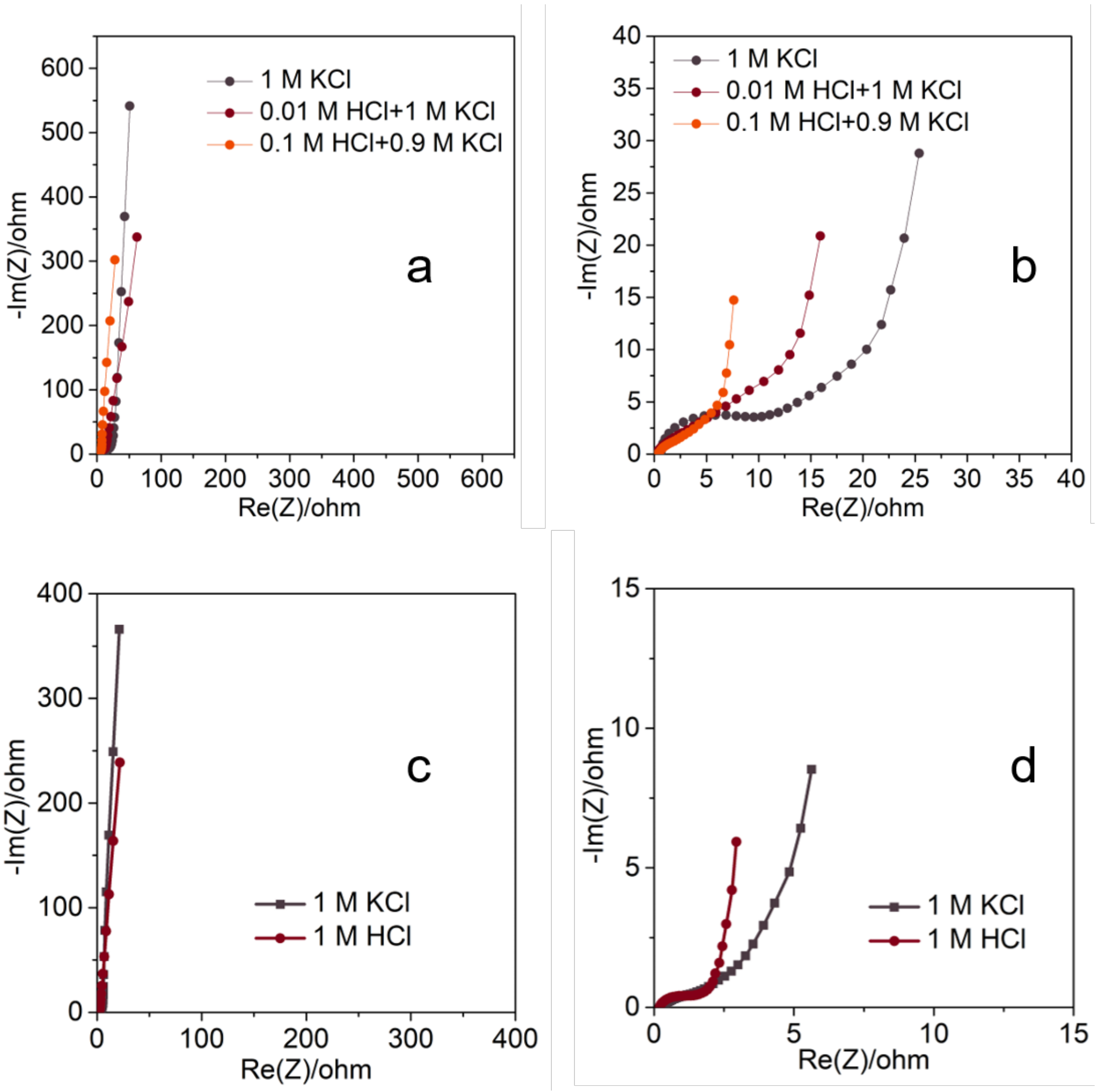

Figure 3.16. (a) Nyquist plots of NPGE-0.7nm in 1 M KCl, 1 M HCl, and mixture electrolytes at the frequency of 1000 kHz to 10 mHz at the potential of PZC; **(b)** A zoom at high frequencies; **(c)** Nyquist plots of NPGE-0.7nm in 1 M KCl, 1 M HCl, and mixture electrolytes at the frequency of 1000 kHz to 10 mHz at the 0.1 V *vs.* PZC. (d) A zoom at high frequencies.

Then, we did the SDC test of the NPGE-0.7nm electrode in 1 M HCl, 1 M KCl, and mixture electrolytes (**Fig. 3.17**). The results show that the SDC process of the identical electrode in 1 M KCl is also much faster than that in 1 M HCl and 0.1 M HCl/0.9 M KCl electrolytes for the sub-nanometer porous electrode. After charging the same surface charge of the identical electrode in these electrolytes and resting for 1,800 s, the electrode potential decrease in 1 M KCl, 0.01 M HCl/1 M KCl, 0.1 M HCl/0.9 M KCl, and 1 M HCl electrolytes are around 88 mV, 61 mV, 45 mV, and 41 mV (**Fig. 3.17a**). Moreover, when charging the electrodes with the same surface charge in these electrolytes for 60 s at the charge rate of 0.3 A/g, the potential increase for the 0.7 nm pore size electrode in 1 M KCl, 0.01 M HCl/1 M KCl, 0.1 M HCl/0.9 M KCl, and 1 M HCl electrolytes are around 0.31 V, 0.23 V, 0.22 V, and 0.18 V, respectively (**Fig. 3.17a**). The potential increase of the NPGE-0.7nm tested in these electrolytes is higher than that of the NPGE-10nm. When comparing the potential loss of the two electrodes with different pore sizes after the rest for 1,800 s, we observe that the potential decrease for NPGE-0.7nm is slightly more than that of the NPGE-10nm tested in these electrolytes. The discharge time for these two electrodes is the same in both KCl and HCl electrolytes (**Fig. 3.14b and 3.17b**). These observation results presented here indicate that decreasing the pore size of graphene-based electrodes has a negligible effect on suppressing the self-discharge of the EDL electrodes.

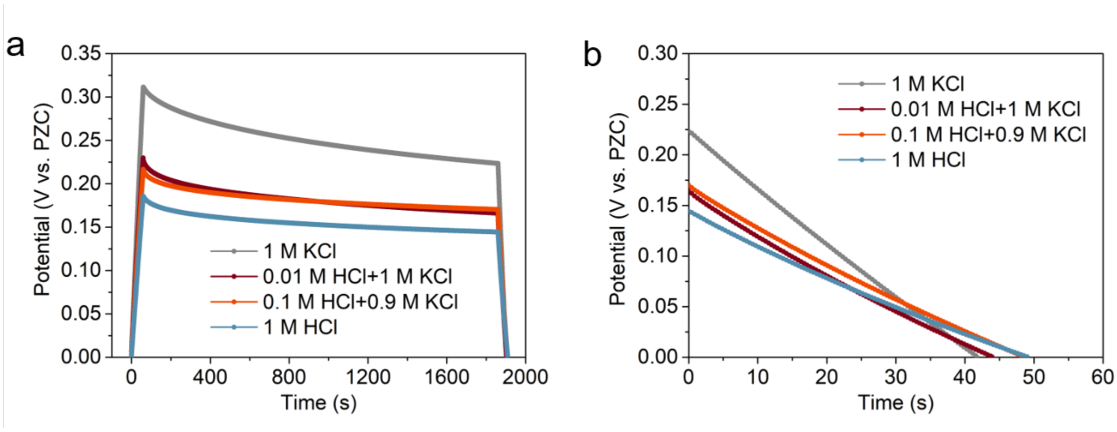

Figure 3.17. (a) Potential changes ('self-discharge profile') of the NPGE-0.7nm porous electrode under open-circuit conditions (after galvanostatic charging at 0.3 A/g for 60s); **(b)** galvanostatic discharge curves of the NPGE-0.7nm after self-discharge for 30 mins in 1 M HCl, 1M KCl, and mixture electrolytes.

3.5 Discussions of proton effects on EDL capacitance from simulations

To fully investigate the reason for better performance observed in HCl electrolyte than that in KCl electrolyte for positive polarization under thermodynamic charge condition, we further carried out simulations to investigate it. We consider that the H^+, K^+, and Cl^- ions have different ion radius even though their valence number is the same. The volume-exclusion effect could play a role in nearing the electrified surface with high concentration (~1M). Such an effect will influence the ion locations and ion electro-absorption density near the electrified surface. Here we applied three models to investigate the co-ion effects on capacitance performance: 1) the classic Poisson-Nernst-Plank (PNP) theory which induces a stern layer to identify ion density and ion distribution inside the EDL (called as PNP-S model)[46,102]; 2) the PNP theory which accounts for an asymmetric location of cations and anions near the electrified surface, and modifies the stern layer thickness of cations and anions, respectively (called as PNP-AS model); 3) the Poisson-Boltzmann (PB) theory which accounts for the ion volume-exclusion effect (called as PB-V model).[178]

The PNP theory used in PNP-S and PNP-AS models was presented as:

$$\epsilon_0 \epsilon \nabla^2 \emptyset = -\rho = -\sum_{i=1}^{N} z_i e N_A n_i \qquad (3\text{-}1)$$

$$\frac{\partial n_i}{\partial t} = D_i \nabla^2 n_i + e z_i \mu_i n_i \nabla \emptyset \qquad (3\text{-}2)$$

Where ϵ_0 and ϵ are the vacuum and relative permittivity of the solution; $\emptyset$ is the electric potential; ρ is the net charge density; N_A is the Avogadro constant; D_i, μ_i, z_i, and n_i are diffusivity, electro-mobility, valence number, and concentration for species i, respectively.

The PB theory with account volume-exclusion effect used in PB-V model was presented as:

$$\varepsilon \varepsilon_0 \nabla^2 \emptyset = -\sum_{i=1}^{N} z_i e\, c_i \qquad (3\text{-}3)$$

$$c_i = c_i^0 e^{\left(-\frac{z_i e \emptyset}{k_B T} + S_{trc}\right)} \qquad (3\text{-}4)$$

Where the $S_{trc} = \ln\left(\frac{1-\sum_{j=1}^{K} v_j c_j}{1-\sum_{j=1}^{K} v_j c_j^0}\right)$ is called the steric functional, which represents an excess potential-different for each ionic species-beyond that of an ideal dilute solution.[178]

3.5.1 Classic Poisson-Nernst-Plank (PNP) model with one stern layer.

This model is simulated on the COMSOL Multiphysics software (5.3a) and applies the Transport of diluted species and Electrostatic physical models. Based on our previous research, our graphene nanoporous electrode has three key structure parameters. They are graphene lateral size (L), aperture opening size (d), and channel height (h). According to our published works, we know that (L) is around 55 nm, (d) is about 2 nm, and in our case, we set the (h) as 10 nm.[102] Additionally, based on our previous molecule simulation (MD) results,[70] we know that the distance between ions and charged electrodes, and the dielectric of water in this space is much smaller compared to that of the bulk solution. Therefore we introduced a thin stern layer to our model with the stern layer thickness being around 0.33 nm.[70] The dielectric constant in the stern layer was around 2.5 based on our previous MD results.[70] The electrolytes that we used for the simulation study were 1 M KCl and 1 M HCl, respectively. The diffusion coefficient of Cl^-, K^+ and H^+ is 1.91 $*10^{-9}$ (m^2/s), 1.84 $*10^{-9}$ (m^2/s) and 9.3 $*10^{-9}$ (m^2/s) for the simulation model study.[172] The dielectric constant was 80, except for the stern layer. The dynamic charge storage behavior was analyzed based on the CV simulation curve. To obtain CV curve, the surface potential is imposed to vary periodically and linearly with time t.

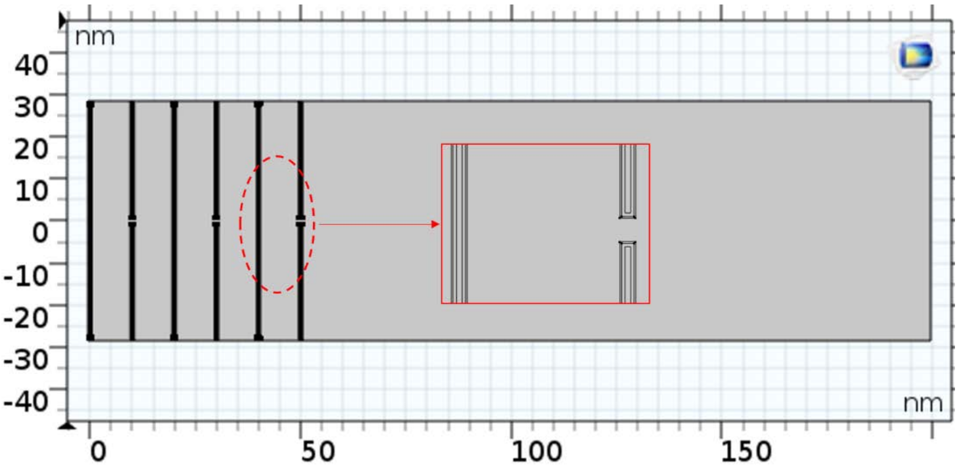

Figure 3.18. 2D continuum modeling system with 6 layers of graphene sheets with L = 55 nm, h = 10 nm, and d = 2 nm.

We did a series of CV simulations in both 1 M HCl and 1 M KCl electrolytes. **Fig. 3.19** shows the differential capacitance of the simulated graphene electrode in 1 M KCl and 1 M HCl under different scan rates. Considering the simulated electrode with only 6 layers of graphene with 10 nm pore size, which is much less than that of the 3-dimensional bulk graphene-based membrane electrode with around 8,000 layers of graphene, the 5 V/s scan rate simulated results should agree with the experimental results achieved at 2 mV/s. However, the simulated differential capacitances for these two electrolytes are almost the same, which is quite different from our experimental results. Then we further increased our scan rate to 500,000 V/s, which is around 100,000 times of the charge rate increase, while the difference of the calculated differential capacitance was still very weak. After increasing the scan rate to 5,000,000 V/s, the apparent capacitance difference appears. The above CV simulation results based on the PNP-S model confirm that the high diffusion coefficient of the proton would not contribute to the enhanced EDL capacitance in the HCl electrolyte for positive graphene electrode at the slow scan rate. This indicated the existence of other unexplored charge storage mechanisms for EDL capacitance increase.

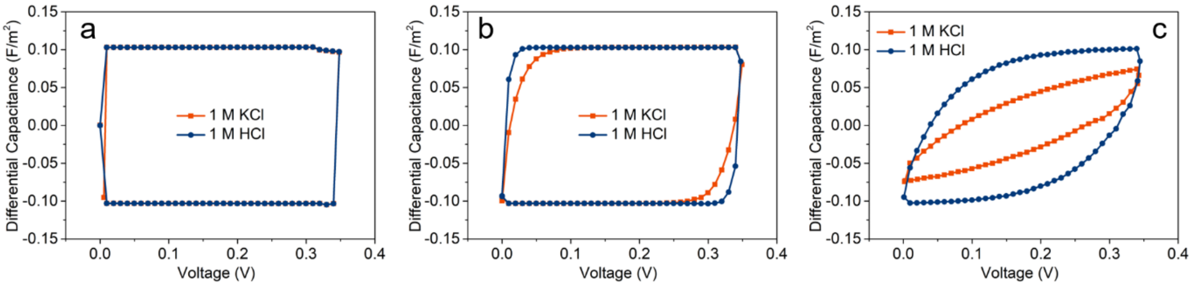

Figure 3.19. (a), (b) and **(c)** show the simulated CV curves of 10 nm pore size graphene layers in 1 M KCl and 1 M HCl electrolytes under the scan rates of 5 V/s, 500,000 V/s, and 5,000,000 V/s, respectively.

We also conducted a simulation to calculate the distribution of the ions in these two electrolytes after charging at different scan rates for investigating ions distribution and densities on the EDL capacitance. **Fig 3.20a** and **d** show that the density and distribution of the ions for the two electrolytes are the same, and there is no uneven ion concentration distribution along with the thickness direction for the large pore size graphene sheets at the slow charge rate (5 V/s). When increasing the scan rate to 5,000,000 V/s, we observed ion densities in the five channels are different for both the first and 10th cycle charge in the two electrolytes. Moreover, for the positively charged electrode under a fast charge rate, the surface counter ions concentration in HCl electrolyte is larger than that in KCl, and the surface concentration difference increase along the electrode thickness direction (The surface ion concentration difference for the innermost interface is much larger than that of the outer interface). At the same time, the surface co-ion concentration in HCl (H^+) is also larger than that in KCl (K^+) with fast positive charging. These calculated results are quite surprising because, based on previous understanding, the proton with a high diffusion coefficient should prefer expulsion from the interface, especially under a very fast charge rate.

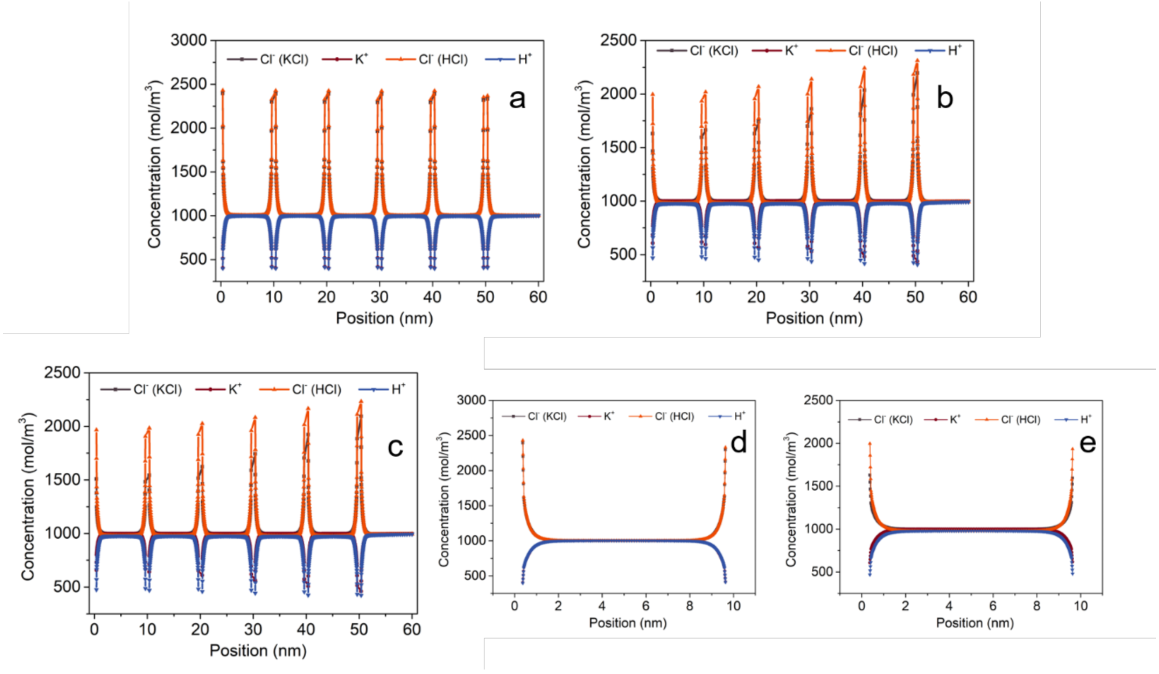

Figure 3.20. (a), (b) and **(c)** show the ion distribution curves of 10 nm pore size graphene layers in 1 M KCl, and 1 M HCl electrolytes charged to 0.35V with the scan rates of 5 V/s (10th cycle charge), 5,000,000 V/s (10th cycle charge), and 5,000,000 V/s (first cycle charge), respectively; **(d)** and **(e)** is the ion distribution curves of the innermost channel in 1 M KCl and 1 M HCl electrolytes charged to 0.35V with the scan rates of 5 V/s (10th cycle charge) and 5,000,000 V/s (10th cycles charge).

3.5.2 Classic PNP model accounting for the stern layer thickness of cations and anions.

We further explored the reason behind the capacitance difference observed on the large pore size (10 nm) electrode under the slow charging rate in HCl and KCl electrolytes. To do so we applied the modified PNP models accounting for an asymmetrical location of cations and anions near the electrified surface via modifying the stern layer thickness of cations and anions. We did this to evaluate the ion distribution and density profiles under a thermodynamic equilibrium state. The PNP-AS model was simulated on the COMSOL Multiphysics software (5.3a) with the application of the Transport of diluted species and Electrostatic physical models. The simulated electrode structure was the same as that in the PNP-S model with the difference of electrode thickness (in the PNP-AS model, only one nanoslit channel). Additionally, based on the previous molecule simulation (MD) results, we know that the first peak position of cations and ions to the electrode surface is different when charging the electrode with a positive surface charge.[70] Therefore, we introduced an asymmetric stern layer thickness to our model. The stern layer thickness is around 0.33 nm (Cl^-) and 0.8 nm (K^+) in KCl, and 0.33 nm in HCl.[70]

The dielectric constant for the stern layer of anions is around 2.5 based on our previous MD results.[70] The dielectric constant is 80 except for the anion stern layer. We studied the electrostatic stationary simulation test where the surface potential is imposed to 0.35 V to evaluate the ion concentration and distribution, as well as the stored surface charge under the thermodynamic equilibrium state.

Fig. 3.21a shows the densities of the ions, and the distribution of the two electrolytes are quite different after positive charge, the surface counter ions concentration in HCl electrolyte is larger than that in KCl. The highest EDL co-ions concentration in HCl (H^+) is smaller than that in KCl (K^+). **Fig. 3.21b** presents that the stored surface charge densities in two electrolytes are almost the same, which is quite different from the observed practical electrochemical results. This indicates the better performance observed in the HCl electrolyte compared to that in the KCl electrolyte for positive polarization under thermodynamic charge conditions do not come from the stern layer thickness difference between counter-ions and co-ions.

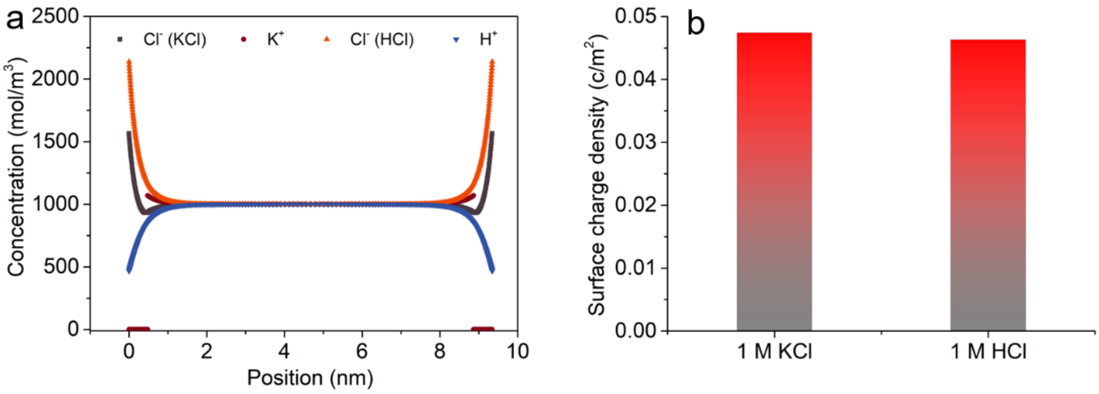

Figure 3.21. (a) shows the ion distribution curves of 10 nm pore size graphene layers in 1 M KCl and 1 M HCl electrolytes charged to 0.35V with thermodynamic charging condition; **(b)** The stored surface charge density of the electrode in 1 M KCl and 1 M HCl electrolytes.

3.5.3 Poisson-Boltzmann (PB) theory accounting for the ion volume-exclusion effect

Lastly, considering the different sizes of cation and anions, we further applied the modified PB models with consideration for the volume-exclusion effect of cations and anions to evaluate ion distribution and density profiles under the thermodynamic equilibrium state.[178] The PB-V model was simulated on the COMSOL Multiphysics software (5.3a) with Poisson's Equation physical model. The simulated electrode structure is the same as that in the PNP-S model without the introduction of the stern layer. Additionally, based on our previous molecule simulation (MD) results, the average dielectric constant inside the nano-slit channel of graphene is around 10. The hydration size of K^+, Cl^- and H^+ is 0.66 nm, 0.66 nm, and 0.56 nm.[171] The electrode surface potential was imposed to 0.35 V to evaluate the ion concentration and distribution as well as the stored surface charge under the thermodynamic equilibrium state.

From **Fig. 3.22a** and **b**, we can see the densities and distribution of the ions of the two electrolytes as well as the potential profile inside the nanoslit channel, and they are the same after the positive charge of the electrode surface. **Fig. 3.22c** presents that the stored surface charge density in two electrolytes is almost the same, which is quite different to the observed practical electrochemical results even with the considering of ions size. All these simulation results indicate that the better performance observed in the HCl electrolyte than in KCl electrolyte for positive polarization under thermodynamic charge conditions is not due to the ion size effect.

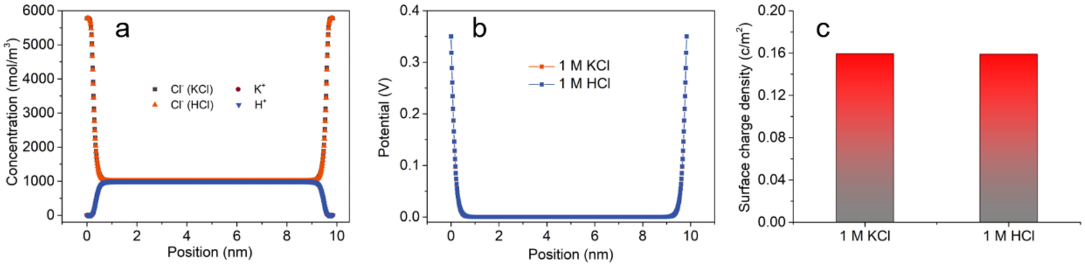

Figure 3.22. (a) shows the ion distribution curves of 10 nm pore size graphene layers in 1 M KCl and 1 M HCl electrolytes charged to 0.35V with thermodynamic charging condition; **(b)** Potential profiles of the EDL inside the slit channel; **(c)** The stored surface charge density of the electrode in 1 M KCl and 1 M HCl electrolytes.

3.6 Conclusion

Overall, this chapter systematically investigates the ion-specific effects on the EDL capacitance of nanoporous graphene-based electrodes in six different aqueous chloride-based electrolytes through the combination of electrochemical characterization and continuum simulations. The following conclusions can be drawn:

1. Based on our ion-specific effect studies on the graphene-based electrodes with three different average slit pore size (10 nm, 1 nm, and 0.7 nm), we conclude that the negative electrode EDL capacitance depends on the types of counter-ions (H^+, Li^+, Na^+, K^+, Cs^+, $Bmim^+$). At 2 mV/s, the EDL capacitance is quite similar (around 80 F/g), except in the 1 M HCl (about 140 F/g).

At high charging rates (20 – 200 mV/s), a similar trend is observed, i.e., 1 M HCl having significantly higher capacitances. These experimental results indicate the special EDL charge storage of proton in graphene-based electrodes, which also depends on the charging rate.

2. We also observed unusual co-ion effects (H^+, Li^+, Na^+, K^+, Cs^+, and $Bmim^+$) on EDL capacitance of the graphene-based positive electrodes. At 2 mV/s, the positive electrode capacitance of the NPGE-10nm in 1 M HCl is around 30% higher than those of other chloride-based electrolytes. Besides, with the increase of scan rate (from 2 to 1000 mV/s), there is an increase of capacitance ratio of the electrodes in 1 M HCl and KCl (NPGE-10nm: from 1.25 to 1.5; NPGE-1nm: from 1.3 to 1.8; NPGE-0.7nm: from 1.5 to 3.0), indicating the importance of electrode pore size and charging rates on the proton co-ion effect for EDL capacitance.

3. Increasing the proton concentration (from 0 to 1 M), there is an increase of the OCP (NPGE-10nm: from 0.2 to 0.42 V; NPGE-0.7nm: from 0.22 to 0.47 V) and PZC (NPGE-10nm: from 0.24 to 0.45 V; NPGE-0.7nm: from 0.22 to 0.47 V) of our graphene-based electrodes, suggesting the specific proton adsorption on the surface of graphene-based electrodes.

4. The potential change (after charging the same surface charge) and potential decrease (after resting the same time) of the NPGE-10nm in 1 M HCl are around 0.17 V and 37 mV, which is much lower than that of the NPGE-10nm in 1 M KCl (potential change: 0.27 V; potential decrease: 68 mV). These results indicate that when injecting positive charge to the graphene-based electrodes in 1 M HCl, the adsorbed proton is possibly repulsed from the electrode surface, leading to the increase of stored charge in the same potential range.

5. The discharge time (after resting for 1,800 s) of NPGE-10nm is the same as that of the NPGE-0.7nm (around 50 s in 1 M HCl and 42 s in 1M KCl), indicating that decreasing the pore size of graphene-based materials has a negligible contribution for suppressing the self-discharge. Instead, manipulating the ion-specific effect could be a promising way to suppress the self-discharge of the EDL electrodes due to the different self-discharge time in 1 M HCl (around 50 s) and KCl (around 42 s).

6. Our continuum model results show that the higher capacitance of the NPGE-10nm achieved in 1 M HCl electrolyte (compared to that of 1 M KCl electrolyte) for positive polarization under slow charging rate is not due to the high diffusion coefficient of proton, the asymmetric stern layer thickness of counter-ions and co-ions, and the ion steric effect. The underlying physical

mechanism still remains elusive. More works related to proton specific adsorption should be done in the future. Our systematic experimental works provide a solid ground.

The comprehensive ion-specific effect study in this chapter could also help to increase the understanding of ion properties in a nanoconfinement space. Particularly, the study results of the co-ion effect could contribute to new charging storage mechanism exploration and guiding the working electrolyte selection in the supercapacitor community. Additionally, the specific proton adsorption results and discussion presented in this chapter could provide inspiration and knowledge contribution for other research communities, such as metal corrosion, hydrogen evolution reaction (HER), and fuel cell design.

Chapter 4 Nanoconfinement effects on the electrochemical performance of the redox-active electrolytes

The charging storage mechanism of the EDLCs is based on physical ions adsorption to form EDL to store charge. Thus, the low energy density property is the intrinsic drawback feature of EDLCs. To further increase the energy density and keep the high-power delivery merit of the supercapacitors, the introduction of a surface redox-type charge storage mechanism to the EDLCs is a very promising concept to further increase the charge storage ability of the supercapacitors and keep the high-power delivery property.[116]

4.1 Introduction

With the development of smart electronic devices and the advantage of electric vehicles on building the low-carbon society, the designing of green energy storage devices for providing energy and power for these important electric devices is highly important.[62] While, currently, the developed energy storage devices (ESDs) are still not able to meet the high demand for energy storage devices, such as high energy and power density, long lifespan, low cost, and environmentally friendly. Surface-redox ESDs (also called pseudocapacitors) present relative high charge storage and fast charging storage ability due to the interface charge transfer mechanism, which is quite different from the batteries.[19] Besides, due to the advanced surface charge transfer mechanism, the surface-redox ESDs present a high potential to achieve high energy density and fast power delivery for the energy storage field.[4,116,179] Moreover, the nanoporous materials with the high specific surface area have been well demonstrated for the improvement of the charge storage performance compared to that of the micro or bulk materials. Thus, the fundamental understanding of the interface charge transfer mechanism in different nanoporous structure electrodes is the basis for advancing the design of next-generation ESDs.

Previously, the research concepts about improving the performance of surface-redox ESDs mainly focus on developing new electrochemical active materials, tailoring nano-morphology and composition, engineering electrolytes and electrode surfaces, and designing hybrid supercapacitors.[10,180-182] With the contribution of these research concepts on the energy storage community, the development of surface-redox ESDs has achieved considerable improvement. However, the fundamental understanding focusing on surface charge transfer at the electrode-electrolyte interface under different nanoconfinement level is much less. The in-depth theoretical knowledge and charge storage mechanism understanding at the nanoconfinement interface has the possibility to provide a relatively new charge storage theory or novel research concept for guiding the design of next-generation high-performance surface-redox ESDs.

With the importance and significant role of the electrochemical reaction behaviour at the nanoconfined interface for charging storage performance,[43] the comprehensive electrochemical study for different nanopore-size electrodes in redox-active electrolytes is necessary to reveal the relationship between interface reaction rate and pore size. Due to the limitation of the electrodes, which exhibit disorder and complex porous structure and untenable pore size, the fundamental research issues about confined redox-active ion effects on nanoporous graphene-based electrodes for energy storage have not been well studied and addressed from experimental results. Based on the previous pore size study on EDL structure and capacitance in Chapter 3, we propose the confined interface reaction rate possible depends on the nanopore size of the conductive electrodes due to the difference of the EDL structure. Engineering the nanopore structure could contribute to the design of ESDs with both high energy and high power densities. Taking advantage of our multilayered graphene membranes (MGMs) with a tunable slit pore size in the sub-10 nm range, we could carry out systematically experiment studies to gain deep insight understanding and knowledge about interface charge storage behaviour under different nanoconfinement level.

In this work, we systematically investigate the electrochemical performance of nanoporous graphene-based electrodes with different pore size in various aqueous electrolytes with redox-active ions (0.1 M ZnI_2, 1.0 M ZnI_2, and 1.0 M $ZnSO_4$). We find that the nanoporous electrode with a smaller pore size (1nm) presents a larger electrochemical reaction rate. Considering the studied graphene-based electrodes have the same surface chemistry and the same amounts of electrochemically active sites, the graphene-based electrodes should present a similar charge transfer behavior from the viewpoint of traditional electrochemical theory. Recently, some published research work about ‘the effects of confinement inside carbon nanotubes on catalysis’ demonstrate that the confined active materials (metals, metal oxides) could exhibit better catalytic activity compared to the same active materials located at the outer surface.[106] The continuum simulation studies show that there is a difference of EDL structure of graphene-based electrodes with different pore size during charging. The EDL structure of the small pore size graphene electrode is much compact than that of large pore size electrodes. The more compact EDL structure could induce a higher interface concentration of reactive ions. The research study presented in this chapter could stimulate the development and understanding of nanoconfined electrochemical theory and provide a new design concept for guiding the rational design of next-generation energy storage devices with both high energy and power densities. At the same time, the deep understanding and new charge storage behavior observation of charge transfer at the nanoconfined solid-liquid interface could also advance the design of high-efficient electrochemical catalysis.

4.2 Materials and Methods

4.2.1 Synthesis of nanoporous graphene-based electrodes.

Firstly, chemically converted graphene (CCG) dispersion was synthesized by following the method described in Reference.[166] Briefly, graphene oxide colloid (0.5 mg/ml, 200 ml) made from the modified Hummers' method was mixed with 0.35 ml hydrazine (64wt% in water) and 0.8 ml ammonia (28wt% in water) solution in a glass vial. After being vigorously shaken for a few minutes, the flask was put in a water bath (~100 ℃) for 3 hr.

Then nanoporous graphene-based electrodes (also called chemical converted graphene membrane electrodes) were fabricated by following the method we provided in chapter 3. Generally, taking 20 ml of the reduced CCG dispersion for the vacuum filtration until no CCG solution on the top of the membrane. After that, the achieved membranes were washed with distilled water several times to remove the extra hydrazine and ammonia. Then, the membranes were exchanged in the H_2SO_4 solution with different concentrations for two days, followed by a freezing dry process for two days. Afterword, the freezing dry membranes were washed with distilled water to remove the inside H_2SO_4. Through controlling the concentration of H_2SO_4 and filtration time, we could achieve the nanoporous graphene-based electrodes with different average slit pore sizes.

The thickness of the nanoporous graphene-based electrodes was measured using a digital micrometer at 1 um resolution. Based on the formula presented in chapter 3, we could calculate the average interlayer distance of our synthesized nanoporous graphene-based electrodes.

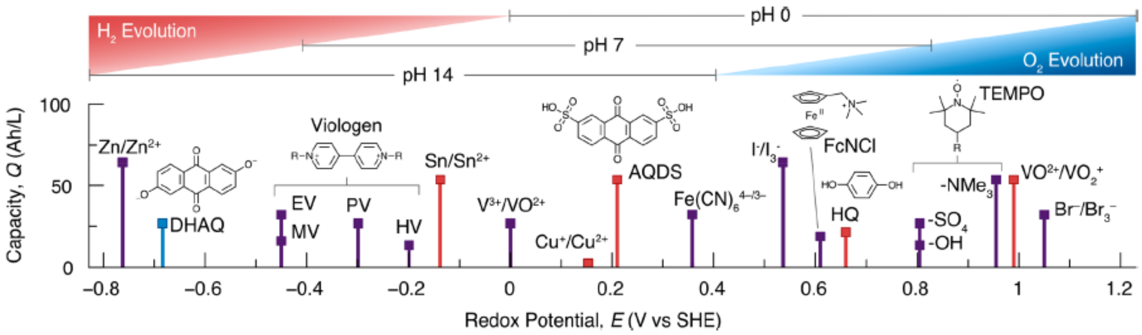

Figure 4.1. Reduction potential and demonstrated volumetric capacity for various aqueous redox couples.[116]

Considering the aqueous electrolytes have the advantages of low cost, high power delivery, more safety, and simple manufacture, we choose the aqueous electrolytes with redox-active ions as our research working electrolytes for the nanoconfinement charge transfer study. According to the advantage (easily achieved, suitable working voltage, and low cost) of iodide and zinc ions compared to other redox-active ions (**Fig. 4.1**),[116] we decided to choose ZnI_2 and $ZnSO_4$ aqueous electrolytes as the research electrolyte platform.

4.2.2 Electrochemical characterization of nanoporous graphene-based electrodes.

The electrochemical characterizations include open-circuit potential, electrochemical impedance spectroscopy (EIS), cyclic voltammetry (CV), galvanostatic cycling with potential limitation (GCPL). They were performed using Bio-logic VSP-300. Both three-electrode and two-electrode configuration setup are applied for the comprehensive electrochemical studies. In the two-electrode setup, the working electrode is our synthesized nanoporous graphene-based electrodes, the counter and reference electrodes are zinc foil. In the three-electrode test configuration, the working electrode is our synthesized nanoporous graphene-based electrodes, and the counter electrode is Zinc foil; the reference electrode is a saturated calomel electrode (SCE).

The electrodes used for the research study are the synthesized hydrogel nanoporous graphene-based electrode with an average pore size of 10 nm (NPGE-10nm), 0.1 M H_2SO_4 solution mediated nanoporous graphene-based electrode with an average pore size of 1.0 nm (NPGE-1nm), filtration dry nanoporous graphene-based electrode with the average pore size of 0.7 nm (NPGE-0.7nm). The area density of the electrodes is around 0.6 mg/cm^2.

4.2.3 The simulation model for EDL structure of nanoporous graphene-based electrodes

We apply a continuum model to identify ion density and ion distribution inside the EDL of the nanoporous graphene-based electrodes during charge/discharge based on the classic Poisson-Nernst-Plank (PNP) theory with inducing a stern layer (called as PNP-S model).

The PNP theory used in PNP-S was presented as:

$$\epsilon_0 \epsilon \nabla^2 \emptyset = -\rho = -\sum_{i=1}^{N} z_i e N_A n_i \qquad (4\text{-}1)$$

$$\frac{\partial n_i}{\partial t} = D_i \nabla^2 n_i + e z_i \mu_i n_i \nabla \emptyset \qquad (4\text{-}2)$$

Where ϵ_0 and ϵ are the vacuum and relative permittivity of the solution; $\emptyset$ is the electric potential; ρ is the net charge density; N_A is the Avogadro constant; D_i, μ_i, z_i, and n_i are diffusivity, electro-mobility, valence number, and concentration for species i, respectively.[46]

The model is simulated on the COMSOL Multiphysics software (5.3a) with the applying of the Transport of diluted species and Electrostatic physical models. Based on our previous research, our nanoporous electrode has three key structure parameters,[102] which is graphene lateral size (L), defect size (d) and nano-slit height (h), according to the published work, we know the (L) is around 55 nm, the (d) is around 2 nm, in our case, the average slit height is 10 nm and 1 nm. Additionally, based on our previous molecule simulation (MD) results, we know that there is the distance between ions and charged electrodes, and the dielectric of water in this space is much smaller (due to the high electric field intensity in this region) compared to that of the bulk solution. Therefore, we introduce a thin stern layer with a thickness of 0.33 nm to our model, the dielectric constant in this stern layer is around 2.5 based on our previous MD results.[70] The electrolytes that we used for the simulation study are 0.1 M and 1 MZnI_2, respectively. The diffusion coefficient of I^- and Zn^{2+} is 1.91 *10-9 (m^2/s), and 0.7 *10^{-9} (m^2/s) for the simulation model study.[172] The dielectric constant is 80, except for the stern layer.

4.3 Experimental Results and Discussion

4.3.1 Nanoconfined iodide ions on the charge storage performance of nanoporous graphene-based electrodes.

To explore the confined redox-active ion effects on the interface charge transfer of nanoporous electrodes, I studied the electrochemical characterization of nanoporous graphene-based electrodes with a different slit pore size (10 nm and 1 nm) in zinc iodide-redox active electrolytes (with the concentration of 1.0 M and 0.1 M) at different charge rates using a two-electrode configuration setup.

4.3.1.1 Zinc iodide redox-active electrolyte with a concentration of 0.1 M.

4.3.1.1.1 Electrochemical reaction rate

To explore the ion effects on the charge transfer rates of nanoporous electrodes, I first studied the cyclic voltammetry (CV) characterization of nanoporous graphene-based electrodes with different pore sizes (10 nm and 1 nm) at various dynamic charging rate in 0.1 M ZnI_2 aqueous electrolyte. **Fig. 4.2** presents the curves of current density-working potential at different scan rates. All these curves show pronounced redox peaks, which are corresponding to the electrochemical redox-reaction of I^-/I_3^-.[44] With the increase of the scan rate, there is an increase in the peak current density. Generally, during the charging process, when the overpotential for the I^-/I_3^- redox-reaction is small, the current density for the NPGE-1nm is smaller than that of the NPGE-10nm. Further increasing the overpotential, there is the appearance of peak currents for both NPGE-10nm and NPGE-1nm, and the peak current for the NPGE-10nm is smaller than that of the much confined nanoporous electrodes at low scan rates. For example, at the scan rate of 0.5 mV/s, the peak current for the NPGE-1nm is around 3 times that of the NPGE-10nm.

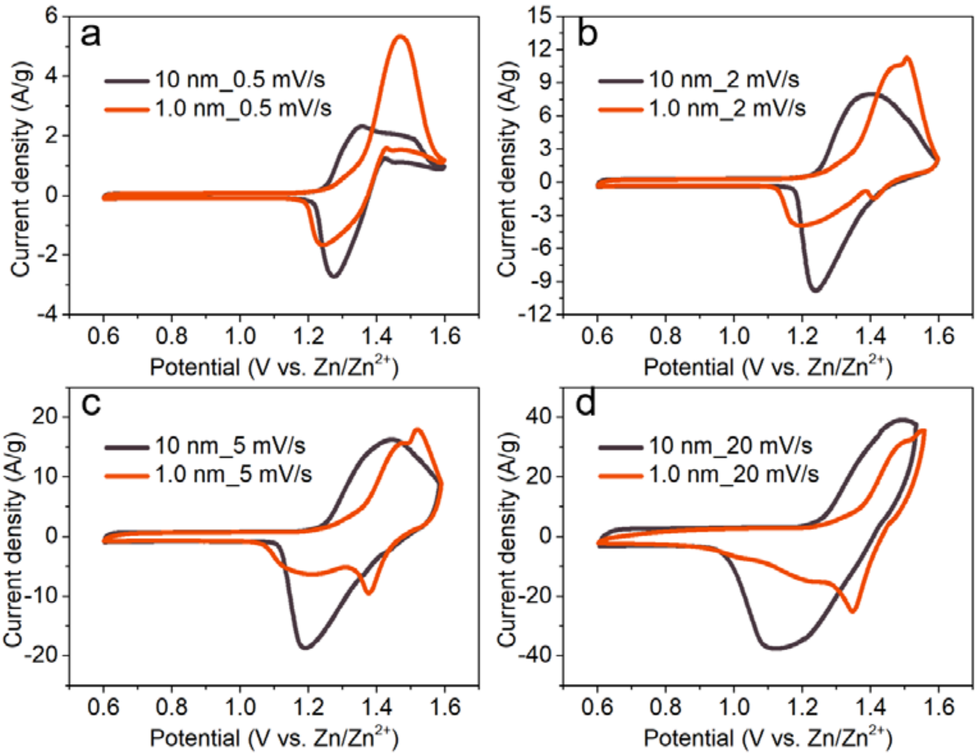

Figure 4.2. CV curves of NPGE-10nm and NPGE-1nm in 0.1 M ZnI_2 aqueous electrolyte under the scan rates of 0.5 mV/s **(a)**, 2 mV/s **(b)**, and 5 mV/s **(c)** and 20 mV/s **(d)**, respectively.

Later, I conducted the electrochemical impedance spectroscopy test for further investigating the confined interface charge transfer behaviors in the above redox-active electrolyte. **Fig. 4.3** shows the experimental Nyquist plots of the NPGE-10nm and NPGE-1nm in the 0.1 M ZnI_2 electrolyte at the frequency range from 1,000 kHz to 100 mHz at the working potential of 1.3 V vs. Zn/Zn^{2+}, 1.4 V vs. Zn/Zn^{2+}, 1.5 V vs. Zn/Zn^{2+}, and 1.6 V vs. Zn/Zn^{2+}. At 1.3 V and 1.4 V/Ref (**Fig. 4.3a** and **b**), in the middle frequency range, quite different plot shapes are observed for the NPGE-10nm and NPGE-1nm, which higher value of the real impedance for the NPGE-1nm is observed, which reveals there is a higher charge transfer resistance of the higher confined nanoporous electrode at these two working potentials. The charge transfer resistance results indicate that there is a smaller charge transfer current density of the NPGE-1nm compared to that of the NPGE-10nm in this potential range. Further increasing the working potential to 1.5 and 1.6 V/Ref (**Fig. 4.3c** and **d**), we can see the electrode with 1.0 nm pore size exhibits the lower value of the real impedance, which stands for better charge transfer behavior, especially at the working potential of 1.5 V/Ref. These observed EIS results quite agree with the CV results, further demonstrating the higher interface charge transfer rate of the higher confined nanoporous electrodes in the 0.1 M ZnI_2 redox-active electrolyte at the peak current working potential.

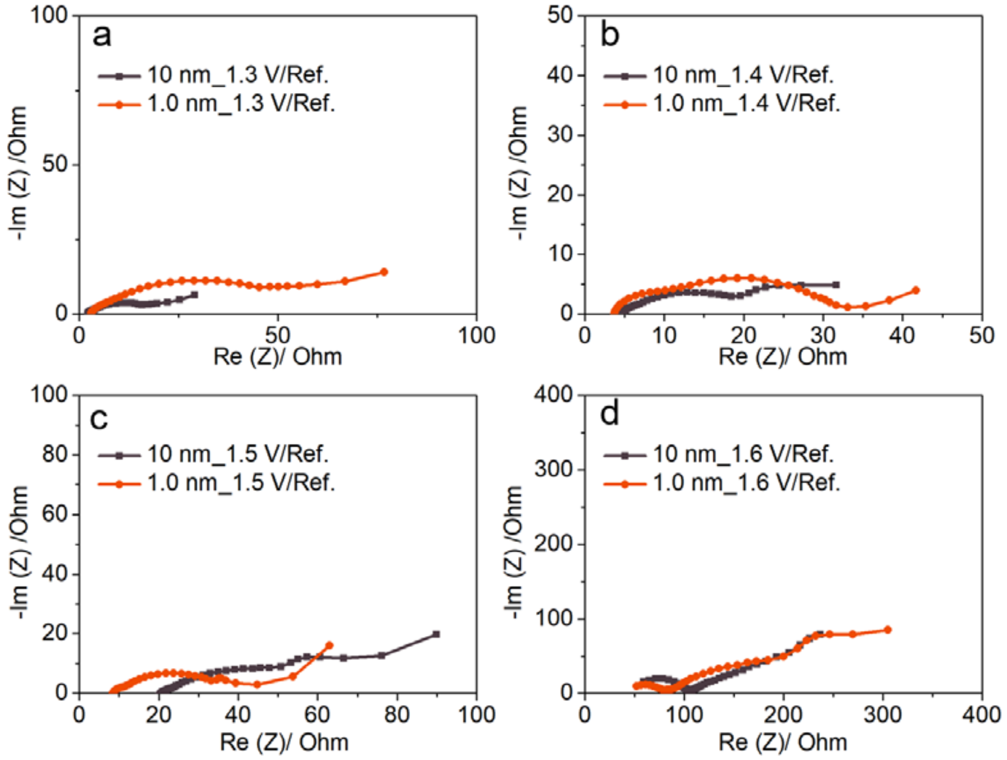

Figure 4.3. Nyquist plots of NPGE-10nm and NPGE-1nm in 0.1 M ZnI_2 electrolytes at the frequency of 1,000 kHz to 100 mHz at the working potential of 1.3 V vs. Zn/Zn^{2+} **(a)**, 1.4 V vs. Zn/Zn^{2+} **(b)**, 1.5 V vs. Zn/Zn^{2+} **(c)** and 1.6 V vs. Zn/Zn^{2+} **(d)**. Ref: Zn/Zn^{2+}.

According to the equation used to calculate the net rate of an electrode reaction[183]:

$$v = i/(nFA) \qquad (4\text{-}3)$$

Where v is the net reaction rate, i is the net reaction current, F is the Faraday constant, A is the electrode surface area or mass.

We could know that at the peak current potential, the 1.0 nm pore size electrode presents a higher interface reaction rate. Additionally, according to the well-established complete current-potential characteristic equation, we could achieve the following formula[183]:

$$i = FAK^0[C_{i^-}(0,t)e^{\alpha f\eta} - C_{i_3^-}(0,t)e^{-(1-\alpha)f\eta}] \qquad (4\text{-}4)$$

Where i is the net reaction current, F is the Faraday constant, A is the electrode surface area or mass, K^0 is the standard rate constant, $C_{i^-}(0,t)$ is the surface concentration of the reactant (I^-),

α is the anodic charge transfer coefficient, $f = \frac{F}{RT}$, R is the universal gas constant, T is absolute temperature, η is the applied over-potential, $C_{i_3^-}(0,t)$ is the surface concentration of the product (I_3^-).[183]

Therefore, from the equation (4-4), we know that the net current depends on the following parameters presented in that equation, which is effective active surface area, standard rate constant, anodic charge transfer coefficient, and reactant and product surface concentration at the interface. Thus, for revealing the behind mechanism, in the following text of this chapter, I will focus on the discussion about these parameters of the two electrodes to explain the possible reasons for the observed surprising increased interface reaction rate at the highly confined pore size electrode.

4.3.1.1.2 Effective active surface area

In the above CV characterization of nanoporous graphene-based electrodes with different pore sizes (10 nm and 1 nm) in 0.1 M ZnI_2 aqueous electrolyte, the mass and physical area of the two electrodes is the same (0.3 mg or 0.5 cm^2). In order to further compare the effective active surface area of the two electrodes, we conducted the CV test and compared the CV curves of the two samples at the EDL capacitance working potential range. From **Fig. 4.4a**, we can see the electrodes with 10 nm pore size and 1.0 nm pore size exhibit the same CV curves, and the capacitive current for the two samples is also almost the same, indicating the same effective active surface area of the two samples. With the increase of the applied scan rates, there is an increase in the current density difference between two electrodes (**Fig. 4.4b** and **c**), which is mainly due to the mass transport effect. Therefore, the EDL characterization results demonstrate that the two tested pore size samples possess the same effective active surface area, indicating the difference of interface charge transfer rate should come from other parameters.

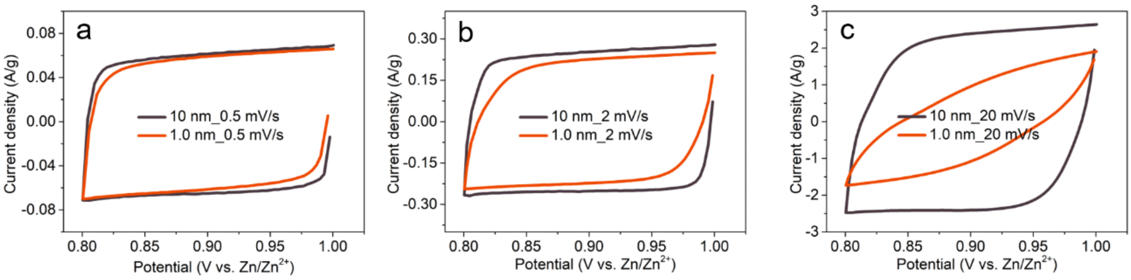

Figure 4.4. CV curves of NPGE-10nm and NPGE-1nm in 0.1 M ZnI_2 electrolytes at the scan rate of 0.5 mV/s **(a)**, 2 mV/s **(b)**, and 20 mV/s **(c)** with the capacitive working potential range.

4.3.1.1.3 The standard rate constant

According to equation (4-4), we know that the net interface reaction rate also depends on the standard rate constant of the redox-reaction. At the beginning of the CV test, the redox-active is I^-, and there is almost no I_3^- at the interface. Thus, the backward current contribution from the product could be negligible due to the very low concentration of the product when the overpotential is very low (less than 10 mV). Therefore, the equation (4-4) could derive to the following equation:

$$i = FAK^0 C_{i^-}(0,t) e^{\alpha f \eta} \qquad (4\text{-}5)$$

Considering the minimal value of over-potential η, the value of $\alpha f \eta$ will be small, the exponential $e^{\alpha f \eta}$ can be approximated as 1+ $\alpha f \eta$. In detail, the value of f is 38.95/V based on the definition ($f = \frac{F}{RT}$), α is in the range of [0, 1], so $\alpha f \eta$ is in the range of [0, 0.3895]. $e^{\alpha f \eta}$ is in the range of [1, 1.47], which is close to the range of [1, 1.39]. Therefore, when the over-potential is very small (≤10 mV), the above equation (4-5) could simplify to the following equation[183]:

$$i = FAK^0 C_{i^-}(0,t) * (1 + \alpha f \eta) \qquad (4\text{-}6)$$

$$i = FAK^0 C_{i^-}(0,t) + FAK^0 C_{i^-}(0,t) * \alpha f \eta \qquad (4\text{-}7)$$

We can see that equation (4-7) is a liner function. Then, we plotted the CV results at the low overpotential range and fitted the current-overpotential curve at the overpotential range of [0, 0.01 V] to achieve the onset potential of the I^-/I_3^- redox-reaction as well as the standard rate constant of the NPGE-10nm and NPGE-1nm (**Fig. 4.5a** and **b**). The results show that the two samples have a similar onset redox potential (**Fig. 4.5c**), and the slope of the liner function for NPGE-10nm is slightly higher than that of the NPGE-1nm (0.159 vs. 0.133) (**Fig. 4.5d**). Comparing the fitting results and the equation (4-7), we could achieve the following result:

$$0.159\ \text{mA/V} = FAK_{10nm}^0 C_{i^-}(0,t) * \alpha_{10nm} f;\ \ 0.133\ \text{mA/V} = FAK_{1nm}^0 C_{i^-}(0,t) * \alpha_{1nm} f \quad (4\text{-}8)$$

where F is the Faraday constant, A is the electrode surface area or mass, K_{10nm}^0 and K_{1nm}^0 are the standard rate constant of NPGE-10nm and NPGE-1nm, respectively, $C_{i^-}(0,t)$ is the surface concentration of the reactant (I^-) at this overpotential range, α_{10nm} and α_{1nm} are the anodic charge transfer coefficient of NPGE-10nm and NPGE-1nm. In our study, the NPGE-10nm and NPGE-1nm have the same effective active surface area, and the electrolyte concentration is 0.1 M. At the onset potential, the anodic charge transfer coefficient is close to

1 due to the absence of the I_3^- at the start of the electrochemical reaction. Therefore, in this study, the standard rate constant of the NPGE-10nm is around 1.19 times that of the NPGE-1nm. If we only consider the standard rate constant parameter on the interface charge transfer rate, theoretically, the net electrochemical reaction rate of a large pore size electrode should be slightly larger than that of the higher confined electrodes, which is quite a controversy with the experimental observation. Therefore, we could conclude that the standard rate constant is not the primary parameter for inducing the large net electrochemical reaction rate of the studied pore size electrodes.

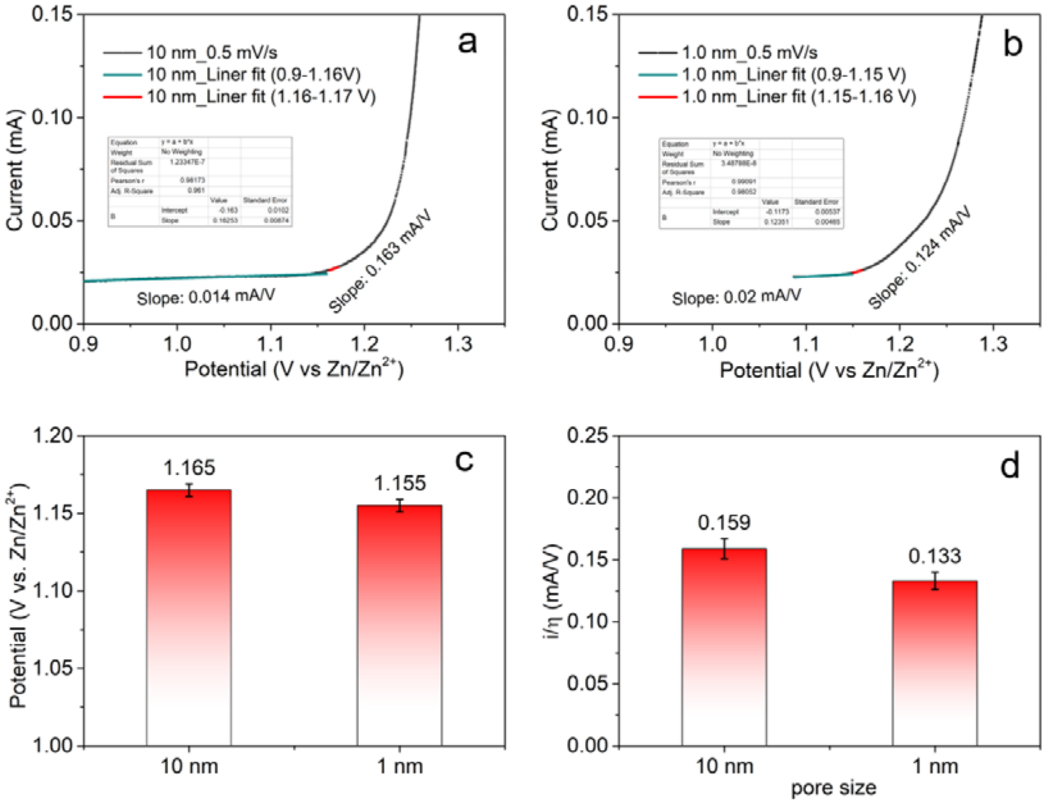

Figure 4.5. Fitting line of the CV curves of NPGE-10nm **(a)** and NPGE-1nm **(b)** at the scan rates of 0.5 mV/s with low overpotential range; **(c)** The onset potential of the I^-/I_3^- redox-reaction inside NPGE-10nm and NPGE-1nm. **(d)** The slope of the fitting line at the overpotential range of [0, 0.01V].

4.3.1.1.4 The anodic charge transfer coefficient

With the assumption of no mass (ion) transfer effects and the surface concentration of the redox-active ions do not differ appreciably from that of the bulk values during the charging process, then the complete current-potential characteristic could derive to the broadly know Butler-Volmer formulation[183,184]:

$$i = i_0[e^{\alpha f \eta} - e^{-(1-\alpha)f\eta}] \qquad (4\text{-}9)$$

Where i_0 is the exchange current. In our study case, $i_0 = FAK^0 C_{i^-}(0,0)$, where $C_{i^-}(0,0)$ is the surface concentration of the reactant (I^-) at the onset potential.

At large values of the overpotential (η), the current contribution from the $e^{-(1-\alpha)f\eta}$ part to the total net current could be very small, and in our case, we assume that when the current from the backward electrochemical reaction contributes less than 10% of the current, then the equation (8) could simplify to the following equation:

$$i = i_0 e^{\alpha f \eta} \qquad (4\text{-}10)$$

Or
$$\ln(i) = \ln(i_0) + \alpha f \eta \qquad (4\text{-}11)$$

Therefore, we selected the CV characterization results of NPGE-10nm and NPGE-1nm at the low scan rate (could largely avoid the mass transfer effect) and plotted the ln (i)-working potential curves. Considering the current from the backward electrochemical reaction contributes less than 10% of the current, then we could achieve the following relationship:

$$e^{-(1-\alpha)f\eta}/(e^{\alpha f \eta}) = e^{-f\eta} \leq 0.1 \qquad (4\text{-}12)$$

The calculation results imply the overpotential (η) is larger than 59 mV. Based on the previous research results (Fig.4.5c), we know the onset potentials of the NPGE-10nm and NPGE-1nm are 1.165 and 1.155 V, respectively. So when the working potentials on the NPGE-10nm and NPGE-1nm are larger than 1.165 V+0.059 V=1.224 V and 1.155 V+0.059 V=1.214 V, the equation (4-10) could be reliable based on the Butler-Volmer assumption. Fitting ln (i)-working potential curves with the potential range from 1.225 V to peak current potential, the αf results for NPGE-10nm and NPGE-1nm could be achieved (**Fig. 4.6a** and **b**). In detail, the αf value for NPGE-10nm at the working potential range from 1.225 V to 1.35 V (corresponding to peak current) is 23.5/V, which indicates the anodic charge transfer coefficient of the redox-reaction happened at the interface of 10 nm pore is around 0.6. The αf value for the NPGE-1nm at the working potential range from 1.225 V to 1.46 V (corresponding to peak current) is 16.2/V, which indicates the anodic charge transfer coefficient of the redox-reaction happened at the interface of the 1 nm pore is around 0.4. The smaller transfer coefficient value of the NPGE-1nm indicates at the same overpotential, the current of the NPGE-10nm should be larger than that of the NPGE-1nm (according to equation 4-11). However, from our experimental results, we can see the current of the nanoporous electrodes with 1.0 nm pore size, at 1.46 V (**Fig. 4.6c**), is much higher than that of the NPGE-10nm (around 2 times higher). Therefore, we could conclude the anodic charge transfer coefficient should not be the major parameter for inducing the high net electrochemical reaction rate of the studied pore size electrodes at the peak current potential.

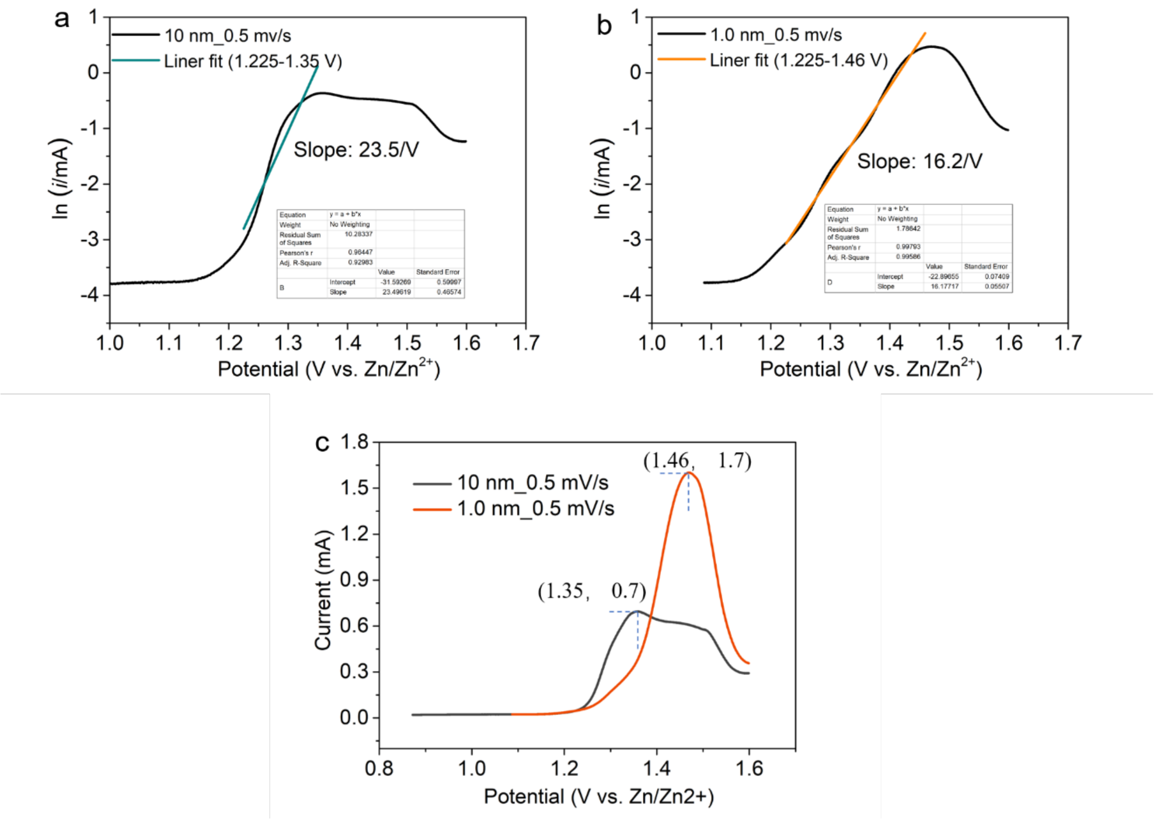

Figure 4.6. (a) ln (i)-potential curves of electrodes with 10 nm pore size and the corresponding linear fitting line at the potential range of [1.225V, 1.35 V]; **(b)** ln (i)-potential curves of the electrodes with 1.0 nm pore size and the corresponding linear fitting line at the potential range of [1.225V, 1.46 V]; **(c)** current-potential curves of the electrodes with 10 nm and 1nm pore sizes. Electrolyte: 0.1 M ZnI_2.

4.3.1.1.5 Interface iodide ion concentration

Based on the established knowledge of EDL, we know that increasing the potential of the electrode, there is the electrostatic attraction between the ions of the electrolyte and the charge confined at the electrode surface, which allows the formation of EDL at the electrode-electrolyte interface. In the case of our study, there is the formation of the EDL and charge transfer at the electrode/electrolyte interface during the potential scanning process. The EDL structure of the electrodes with 10 nm and 1 nm pore sizes could be different during the charging process and possibly leading to a different surface concentration of reactant ions. According to equation (4-4), we know the net redox-reaction rate depends on the surface iodide ion concentration. Therefore, we propose the different interface charge transfer rates could come from the different EDL structures of the two studied pore size electrodes.

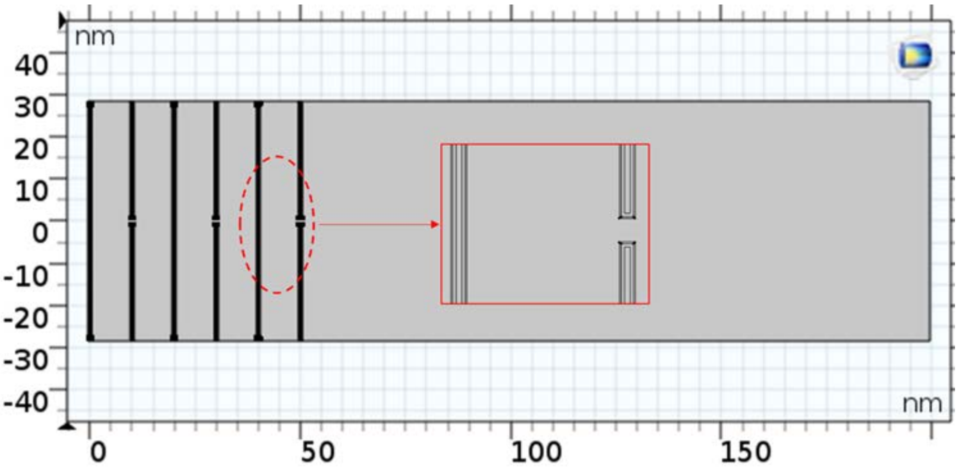

Figure 4.7. 2D continuum modeling system with 6 layers of graphene sheets with L=55 nm, h = 10 nm, and d = 2 nm.

Considering the difficulty of detecting EDL structure and surface ion concentration inside the nanopore from the experimental aspects, we carried out simulations to investigate the EDL structure and surface ion concentration during the dynamic charging process. The details about the simulation are presented in the materials and methods part (4.2.3). We studied the CV simulation test of the charge storage behavior of the 6 layers of graphene sheet electrodes (GSEs) using the simulation models, in which the surface potential is imposed to vary periodically and linearly with time t. **Fig.4.8** plots the surface charge density and ion concentration curves of the simulated graphene sheet electrodes with 10 nm (GSE-10nm) and 1 nm (GSE-1nm) slit pore size in 0.1 M ZnI_2 electrolyte at the scan rate of 5 V/s. Considering the simulated electrode with only 6 layers of the graphene sheets, which is much less than that of the 3-dimensional bulk graphene-based membrane electrode, which is around 8000 layers of graphene. Thus, the 5 V/s scan rate simulated results could be quite in agreement with the experimental results achieved at 0.5 mV/s. From **Fig.4.8a**, we can see the simulated surface charge density of the GSE-10nm and GSE-1nm are very similar, which quite agrees with the EDL test of these two pore size electrodes, demonstrating the negligible dynamic ion transport effect for the EDL at the low scan rate. We also calculate the I^- distribution inside the slit nanopore along with the electrode thickness for the two electrodes when charging the electrodes to 0.5 V (**Fig 4.8b** and **c**), the calculated results illustrate that the I^- concentration inside the 1 nm slit-nanopore is much higher than that of the 10 nm nanopore. Particularly, we observe the EDL overlap in the 1 nm slit pore, where the inside I^- concentration is much higher than that of the bulk I^- concentration (0.2 M). Importantly, the simulated results exhibited here (Fig 4.8d) show that the average I^- concentration at the interface of the GSE-1nm is around 5.2 M, which is about 2.4 times higher than that of the GSE-10nm. Interestingly, the surface concentration ratio ($\frac{C_{1nm}^{I^-}}{C_{10nm}^{I^-}} = 3.4$) of the two electrodes is quite close to the electrochemical current ratio ($I_{1\,nm}/I_{10\,nm} = 2.8$) of the two electrodes at the peak current potential. These simulation results indicate that the higher peak current achieved for the GSE-1nm possible due to the higher surface reactive ion concentration of the GSE-1nm compared to that of the GSE-10nm.

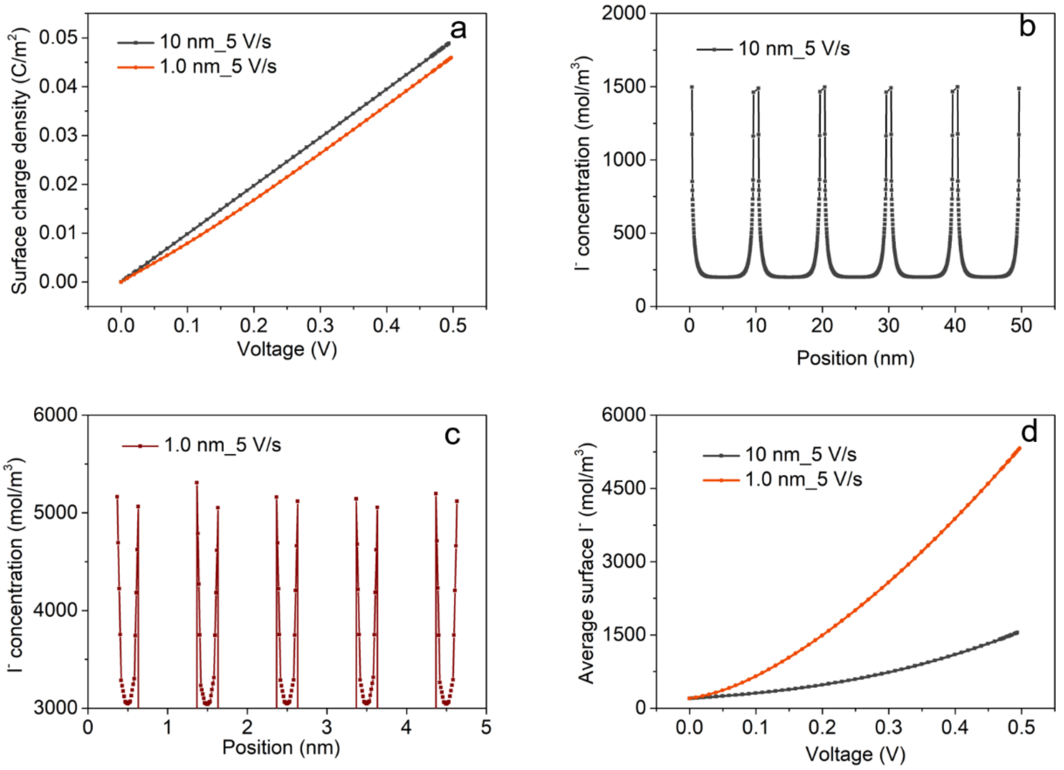

Figure 4.8. (a) shows the surface charge density of the GSE-10 nm and GSE-1nm at the scan rate of 5 V/s; **(b)** and **(c)** show the ion distribution curves of the GSE-10nm and GSE-1nm at the scan rate of 5 V/s; **(d)** shows the average surface concentration of I^- on the GSE-10nm and GSE-1nm at the scan rate of 5 V/s. Electrolyte: 0.1 M ZnI_2, working voltage: 0-0.5 V.

Then, we increased the scan rate to 5,000,000 V/s to further evaluate the surface charge density, ion distribution, and concentration at such a high dynamic charging rate, which is around 1,000,000 times the charge rate increases. We observed the surface charge densities of the two electrodes are quite different from the calculated results at 5 V/s (**Fig 4.9a**), in which the surface charge density of the larger slit pore graphene electrodes is much higher than that of the highly confined nanoslit graphene sheets, indicating the dynamic effect for the stored surface charge. Besides, with the charge/discharge cycling simulation, we found there was an increase of the surface charge density for these two nanoslit graphene electrodes, indicating there is the surface charge unbalance at the high charge/discharge rate. The ion distribution curves were simulated for achieving the ion profile inside the nanoslit channel after charging to 0.5 V with the first cycle charge (**Fig 4.9b** and **c**). The results show that the I^- concentration inside the five nanochannels is quite uneven, especially for the 1.0 nm nanoslit graphene electrode, in which there is a sharp I^- concentration decrease inside the nanochannels along with the graphene electrode thickness direction (from outer-surface to the 0 nm position). We further calculated the average surface concentration of I^- during the cycling dynamic charging process on the GSE-10 nm and GSE-1nm at the scan rate of 5,000,000 V/s (**Fig. 4.9d** and **e**). The results show that there is an increase in the average surface I^- concentration during the cycles for both nanoslit graphene electrodes. Especially during one charge/discharge cycle, the highest iodide ion concentration on the interface is not achieved at the highest voltage. Instead, the largest concentration is observed at the discharge process, which indicates there is the I^- concentration hysteresis during the charging process at a high charging rate, especially for GSE-1nm. Interestingly, even the GSE-1nm possesses a higher hysteretic response of the I^- concentration, while the average I^- concentration at the surface of GSE-1nm is still higher than that of the GSE-10nm (**Fig. 4.9f**), further revealing the special ion effects inside the high confined slit pore. Charging the electrodes to 0.5 V, the I^- concentration at the surface of GSE-1nm is around 2 times that of the GSE-10nm. Therefore, in theoretical, with the absence of the standard rate constant and the transfer coefficient effects on the current, the observed electrochemical redox current for GSE-1nm should also be around 2 times that of the GSE-10nm at fast charging rate, which is quite different from our observed experiment results (Fig. 4.2d). These controversial results possibly come from the un-negligible effect of the product (I_3^-) and the ion (mass) transfer at a high charge rate. At a very high charge rate, the I_3^- is not able to fully diffuse from the surface of the nanoconfinement space to the bulk electrolyte due to the time limitations, leading to the accumulation of the I_3^- at the interface. Considering the GSE-1nm has the slit pore size of 1nm which is much lower than that of the GSE-10nm, so with the accumulation of the same amount of I_3^-, the I_3^- concentration inside the 1 nm slit channel is 10 times that of the 10 nm slit channel, resulting to a much higher backward current contribute from the reduction of I_3^-. Therefore, the net current of GSE-1nm could be lower than that of GSE-10nm during the charging process at a high charge rate as observed from the experiment.

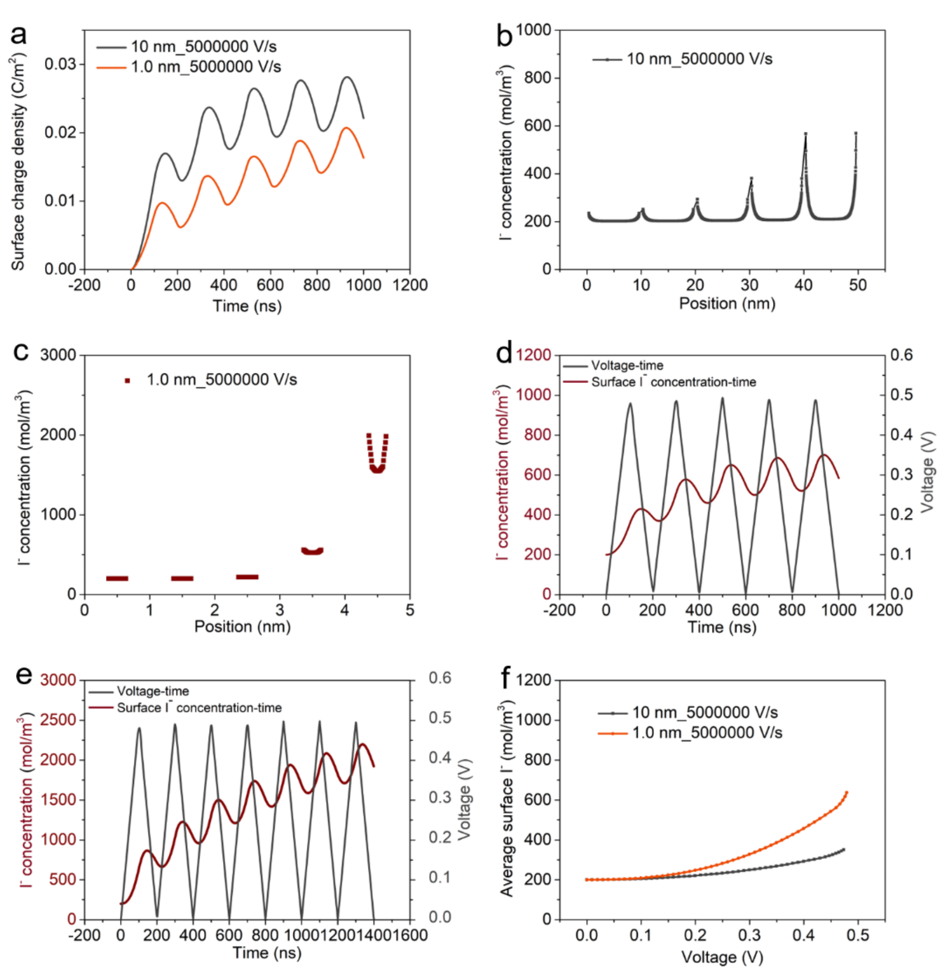

Figure 4.9. (a) shows the surface charge density of the GSE-10 nm and GSE-1nm with cycling charge/discharge at the scan rate of 5,000,000 V/s; **(b)** and **(c)** show the ion distribution curves of the GSE-10 nm and GSE-1nm after initial charging at the scan rate of 5,000,000 V/s; **(d)** and **(e)** present the average surface concentration of I^- during the cycling dynamic charging process on the GSE-10 nm and GSE-1nm at the scan rate of 5,000,000 V/s; **(f)** shows the average surface concentration of I^- on the GSE-10 nm and GSE-1nm for the initial charging process at the scan rate of 5,000,000 V/s. Electrolyte: 0.1 M ZnI_2, working voltage: 0-0.5 V. one cycle: 200 ns.

4.3.1.2 Zinc iodide redox-active electrolyte with a concentration of 1.0 M.

4.3.1.2.1 Electrochemical reaction rate

Considering the importance of electrolyte concentration on the EDL structure (debye length depends on ion concentration) as well as the energy storage performance (theoretically, the interface electrochemical reaction rate depends on I^- concentration), we further evaluated the redox-ion effects on the charge transfer rates of graphene-based nanoporous electrodes in 1.0 M ZnI_2 aqueous electrolyte. I first studied the cyclic voltammetry characterization of NPGE-10nm and NPGE-1nm at different dynamic charging rates in 1.0 M ZnI_2 aqueous electrolyte.

Fig. 4.10 presents the curves of current density-working potential at different scan rates. Generally, with the increase of the polarized potential from onset potential to peak current potential of NPGE-1nm, the observed current density for the NPGE-1nm is always higher than that of the NPGE-10nm except in the small overpotential range which is around 50 mV. Furthermore, the peak current observed at 1.0 M ZnI_2 electrolyte for both two porous electrodes at 0.5 mV/s are more than ten times of that in 0.1 M ZnI_2 electrolyte, which is about 20 times increase for the NPGE-1nm, 40 times increase for the NPGE-10nm compared in the 0.1 M ZnI_2. Note that, according to the classic Butler-Volmer formulation, in theoretical, the achieved current density for the identical electrode in 1.0 M ZnI_2 electrolyte should be ten times of that in 0.1 M ZnI_2. These interesting results indicate that nanoconfinement plays a significant role in determining the interface charge transfer rate, which profoundly demonstrates that the interface electrochemical reaction mechanism under nanoconfinement space is quite different from that of the well-studied bulk (or plane) interface.

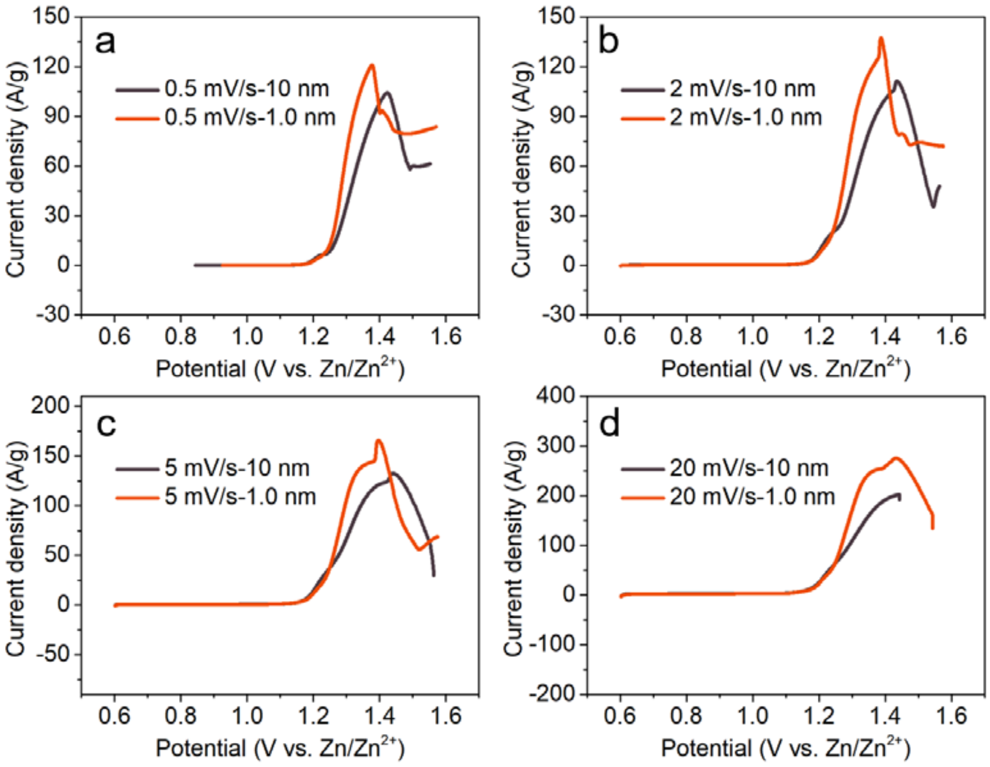

Figure 4.10. CV curves of NPGE-10nm and NPGE-1nm in 1.0 M ZnI_2 aqueous electrolyte under the scan rates of 0.5 mV/s **(a)**, 2 mV/s **(b)**, and 5 mV/s **(c)** and 20 mV/s **(d)**, respectively.

Later, we did the electrochemical impedance spectroscopy test for further investigating the confined interface charge transfer behaviors. **Fig. 4.11** shows the experimental Nyquist plots of the NPGE-10nm and NPGE-1nm in 1.0 M ZnI_2 electrolytes at the frequency range from 1,000 kHz to 100 mHz at the working potential of 1.2 V vs. Zn/Zn^{2+}, 1.3 V vs. Zn/Zn^{2+}, 1.4 V vs. Zn/Zn^{2+}, and 1.5 V vs. Zn/Zn^{2+}. At 1.2 V and 1.3 V/Ref (**Fig. 4.11a** and **b**), in the middle frequency range, quite different plot shapes are observed for the NPGE-10nm and NPGE-1nm, which higher value of the real impedance of the NPGE-1nm is observed, revealing the higher charge transfer resistance of the higher confined nanoporous electrode at these two working potentials. Increasing the working potential to 1.5 V/Ref (**Fig. 4.11d**), we can see NPGE-1nm exhibits the lower value of the real impedance, which stands for better charge transfer behavior. These observed EIS results quite agree with the CV results (the slight potential shift compare to the CV results possible due to inner resistance effect for the EIS study), further demonstrating the higher interface charge transfer rate of the higher confined 1.0 nm nanoporous electrodes in the redox-active electrolyte at the peak current working potential.

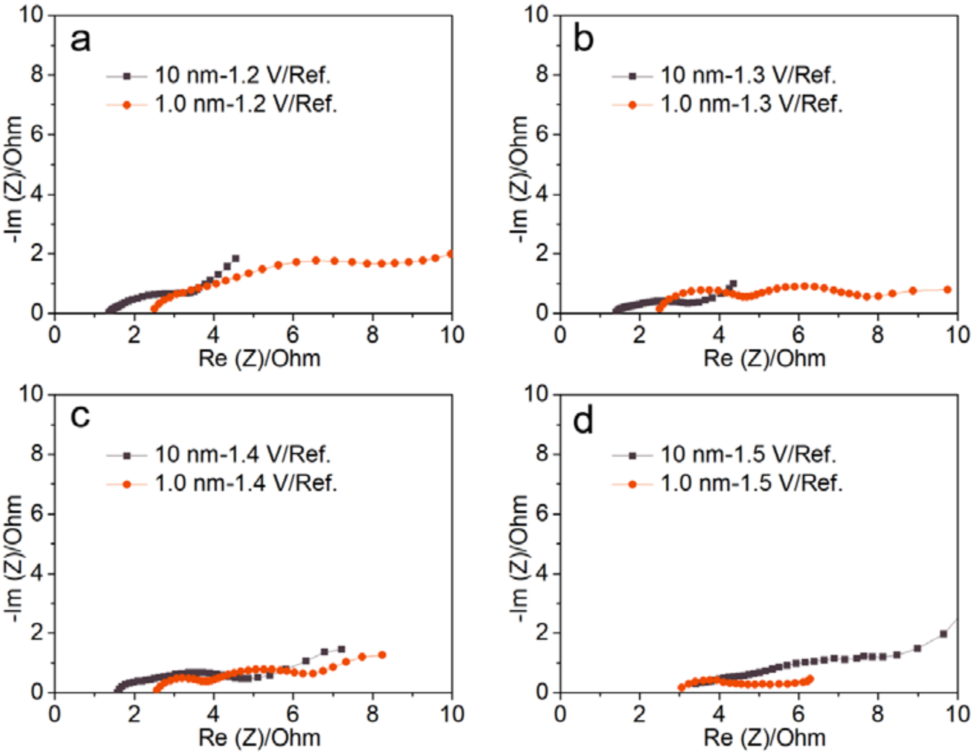

Figure 4.11. Nyquist plots of NPGE-10nm and NPGE-1nm in 1.0 M ZnI_2 electrolyte at the frequency of 1000 kHz to 100 mHz at the working potential of 1.2 V vs. Zn/Zn^{2+} **(a)**, 1.3 V vs. Zn/Zn^{2+} **(b)**, 1.4 V vs. Zn/Zn^{2+} **(c)** and 1.5 V vs. Zn/Zn^{2+} **(d)**. Ref: Zn/Zn^{2+}.

4.3.1.2.2 Effective surface area

Based on the discussion and equations presented in the electrochemical redox reaction study in 0.1 M ZnI_2, these studied parameters could direct transfer to the interface reaction rate study in 1 M ZnI_2 electrolyte. Therefore, firstly, I studied the cyclic voltammetry characterization of the nanoporous graphene-based electrodes in 1.0 M ZnI_2 aqueous electrolyte. The mass and physical area of the two electrodes is also the same (0.3 mg or 0.5 cm^2). To compare the effective surface area of the two electrodes, we did the CV test and compared the CV curves of the two samples at the EDL capacitance working potential range (**Fig. 4.12**). The results show that the NPGE-10nm and NPGE-1nm exhibit the very close current density at the scan rate of 0.5 and 2 mV/s (**Fig. 4.12a** and **b**), indicating a very similar effective surface area for the interface reaction of the two samples. Increase the scan rate to 20 mV/s, the difference of the current densities of the two samples become obvious (**Fig. 4.12c**), which is mainly due to the hindered ion transport in the higher confined nanoporous electrode. Generally, the EDL characterization results demonstrate that the two tested pore size samples have the closing effective surface area, and the difference of net reaction current should come from other parameters.

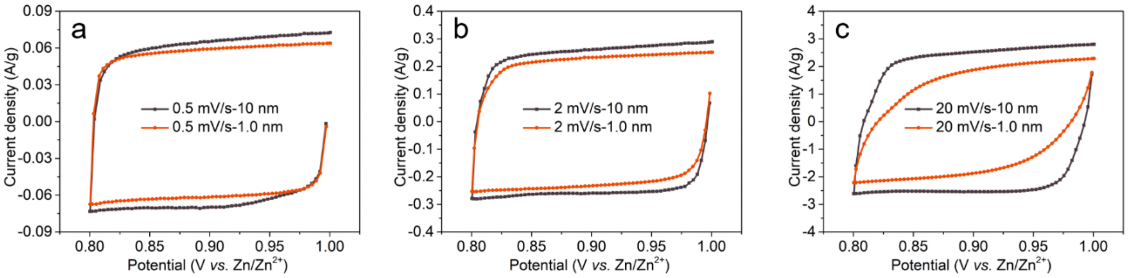

Figure 4.12. CV curves of NPGE-10nm and NPGE-1nm in 1.0 M ZnI_2 electrolyte with the scan rate of 0.5 mV/s **(a)**, 2 mV/s **(b)**, and 20 mV/s **(c)** at the capacitive working potential range.

4.3.1.2.3 The standard rate constant

Based on the discussion results about the standard rate constant above (3.1.1.3), the CV results of the NPGE-10nm and NPGE-1nm were fitted at the low overpotential range (0, 0.01 V) to calculate the onset potential of the I^-/I_3^- redox-reaction and the standard rate constants (**Fig. 4.13a** and **b**). From the results, we can see that the onset redox potential and the slope of the fitting line of the two electrodes is similar (**Fig. 4.13c** and **d**), indicating the same standard rate constant for the two pore-structure electrodes (referring 3.1.1.3). Therefore, in theoretical, the net electrochemical reaction rate of NPGE-1nm should be equal to that of the NPGE-1nm, which is quite different from the experimental observation results. Thus, the standard rate constant is not the major parameter which induces the difference of the net electrochemical reaction rates for the two pore-structure electrodes.

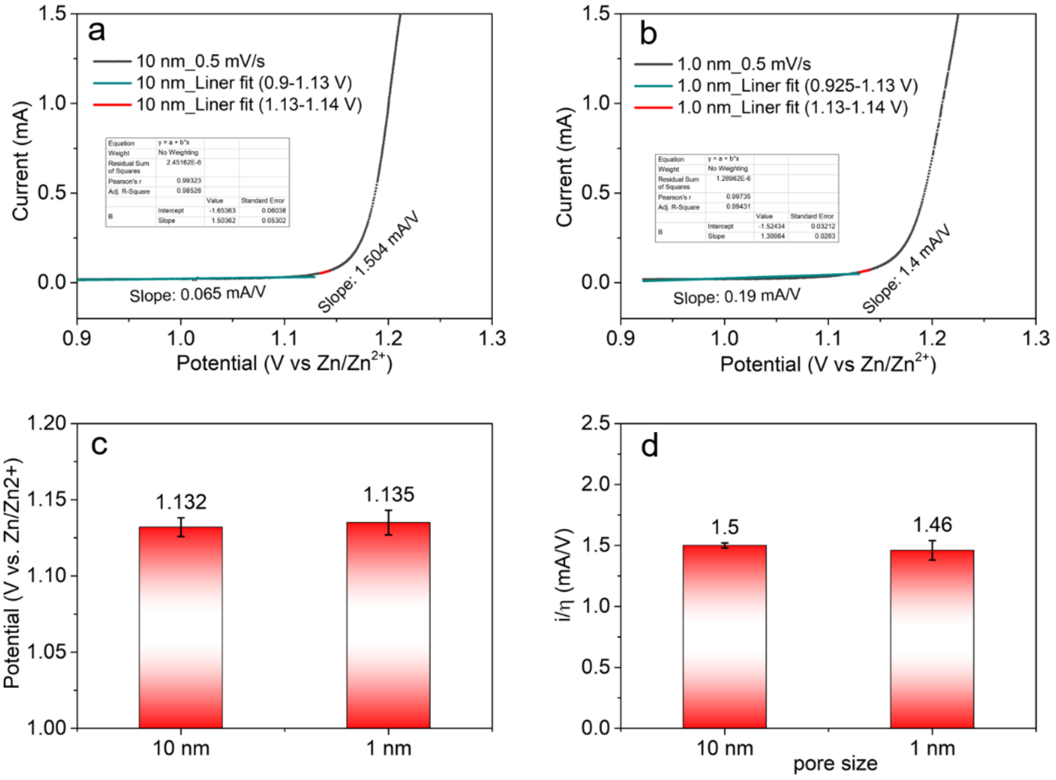

Figure 4.13. Fitting line of the CV curves of NPGE-10nm **(a)** and NPGE-1nm **(b)** with the scan rates of 0.5 mV/s at low overpotential range; **(c)** The onset potential of the I^-/I^{3-} redox-reaction inside the NPGE-10nm and NPGE-1nm; **(d)** The slope of the fitting line at the overpotential range of [0, 0.01V].

4.3.1.2.4 Charge transfer coefficient

Based on the discussion results about the anodic charge transfer coefficient of I^-/I_3^-, the ln (i)-potential curves of the NPGE-10nm and NPGE-1nm were fitted at the potential range from 1.25 V to 1.38 V to calculate the anodic charge transfer coefficient of the two electrodes (**Fig. 4.14a** and **b**). The fitted αf values for the NPGE-10nm and NPGE-1nm are 17.5/V and 15.9/V, respectively. Thus, the calculated anodic charge transfer coefficients of the NPGE-10nm and NPGE-1nm are around 0.45 and 0.41. The smaller anodic charge transfer coefficient value of the NPGE-1nm indicates that at the same overpotential, the current for the NPGE-10nm should be higher than that of the NPGE-1nm (according to equation 4-11). However, current-potential curves (**Fig. 4.14c** and **d**) show both the current and increasing rate of current for the NPGE-1nm is higher than that of the NPGE-10nm (around 1.35 times). Therefore, we could conclude the anodic charge transfer coefficient is not the major parameter for inducing the large net electrochemical reaction rate of the NPGE-1nm.

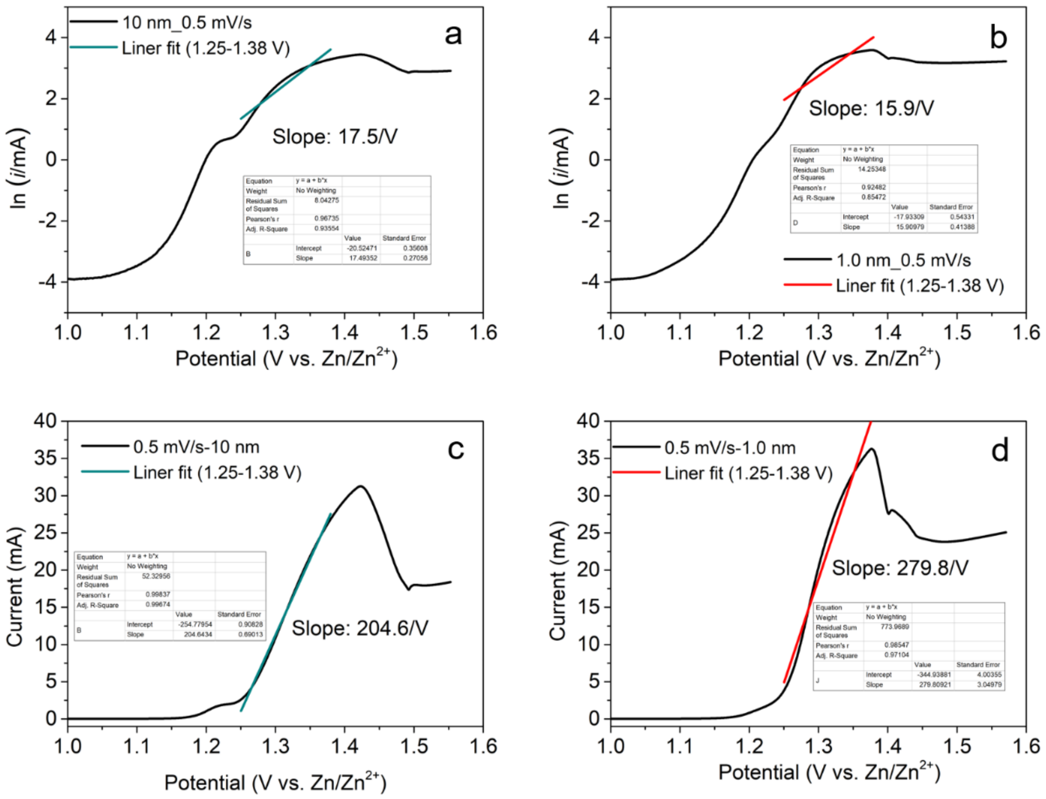

Figure 4.14. (a) ln (i)-potential curves of NPGE-10nm and the corresponding linear fitting line at the potential range of [1.25V, 1.38 V]; **(b)** ln (i)-potential curves of NPGE-1nm and the corresponding linear fitting line at the potential range of [1.25V, 1.38 V]; **(c)** Current-potential curves of NPGE-10nm and the corresponding linear fitting line at the potential range of [1.25V, 1.38 V]; **(d)** Current-potential curves of NPGE-1nm and the corresponding linear fitting line at the potential range of [1.25V, 1.38 V].

4.3.1.2.5 Interface iodide ion concentration

We carried out simulations to further investigate the EDL structure and surface ion concentration during the dynamic charging process in 1 M ZnI_2 electrolyte. The details about the simulation are presented in 4.2.3 and 4.3.1.1.5. The surface charge density of GSE-10 nm and GSE-1nm were plotted in **Fig. 4.15a**. We can see the simulated surface charge densities of the two electrodes in 1 M ZnI_2 electrolyte are the same at the low scan rate, which quite agrees with the experimental EDL test results, proving the negligible dynamic ion transport effect for the final electrochemical performance. The curves of I^- distribution inside the slit nanopore along with the electrode thickness for the two electrodes illustrate that the I^- concentration inside the 1 nm slit-nanopore is slightly higher than that of the 10 nm slit-nanopore (**Fig. 4.15b** and **c**). Particularly, we also observe the EDL overlap for the 1 nm slit pore in the 1 M ZnI_2

electrolyte, where the inside I$^-$ concentration is much higher than that of the bulk I$^-$ concentration (2.0 M).

Moreover, from **Fig. 4.15d**, we can see the simulated average interface I$^-$ concentration for the GSE-1nm is around 7.0 M, which is higher than that of the GSE-10nm (around 5.0 M). Interestingly, the surface concentration ratio ($\frac{C^{I^-}_{1nm}}{C^{I^-}_{10nm}} = 1.4$) of the two electrodes is quite similar to the electrochemical current ratio ($I_{1\,nm}/I_{10\,nm} = 1.35$) of the two electrodes at the peak current potential of NPGE-1nm, which further indicates the higher peak current achieved for the GSE-1nm, maybe comes from the higher surface reactive ion concentration of the GSE-1nm compared to that of the GSE-10nm.

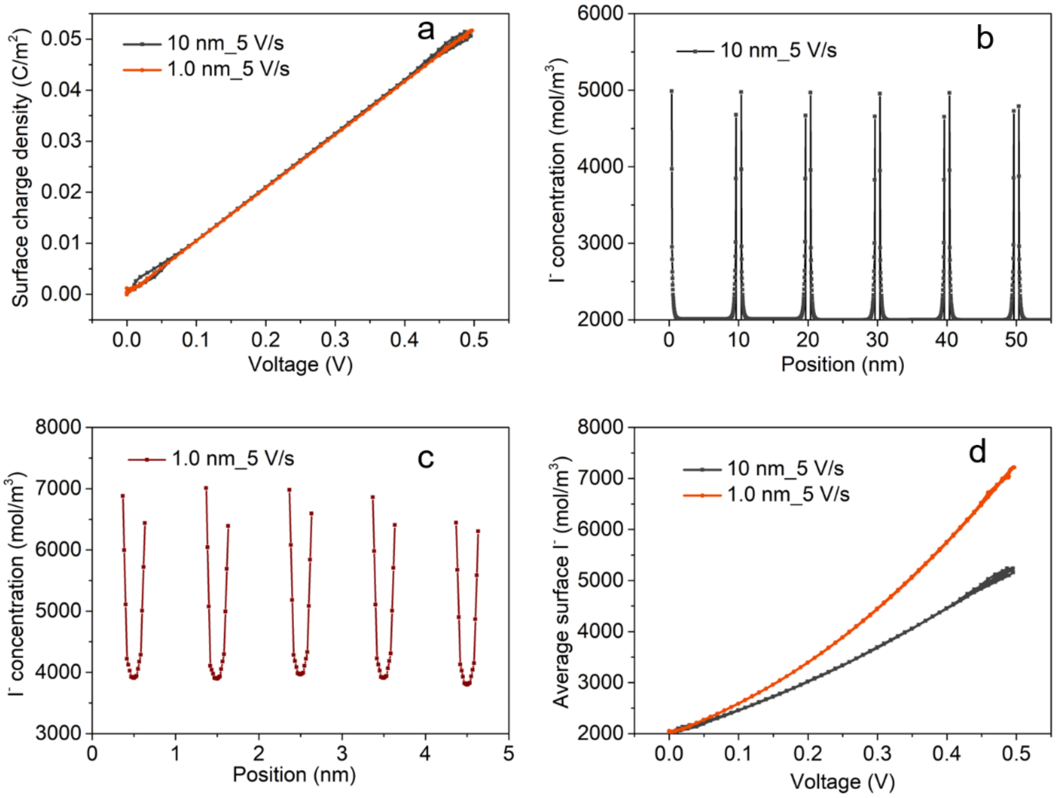

Figure 4.15. (a) shows the surface charge density of the GSE-10 nm and GSE-1nm at the scan rate of 5 V/s; **(b)** and **(c)** show the ion distribution curves of the GSE-10nm and GSE-1nm at the scan rate of 5 V/s; **(d)** shows the average surface concentration of I$^-$ on the GSE-10nm and GSE-1nm at the scan rate of 5 V/s. Electrolyte: 1.0 M ZnI_2, working voltage: 0-0.5 V.

Later, we further increased the scan rate to 5,000,000 V/s to study the surface charge density, ion distribution, and concentration at this high scan rate. The results presented here (**Fig. 4.16a**) show the surface charge densities of the two electrodes are quite different from that of 5 V/s, and the stored surface charge density here is also higher than that in 0.1 M ZnI_2. These simulated results indicate the dynamic ion transport and initial ion centration effects on the surface charge densities. Additionally, during the cycling simulation, the stored surface charge densities of the two electrodes are quite stable compared to the large variation of the stored charge with the cycling simulation in 0.1 M ZnI2 electrolyte. Moreover, the ion distribution profiles were also simulated for detecting the ion distribution inside the nano-slit channel after charging to 0.5 V at the initial cycling charge (**Fig. 4.16b** and **c**). The results show that the I^- concentration inside the nanochannels of the GSE-1nm is quite uneven, in which a sharp I^- concentration decrease is observed along with the electrode thickness direction (from outer-surface to the 0 nm position). We further calculated the average surface concentration of I^- during the cycling dynamic charging process of the GSE-10 nm and GSE-1nm at the scan rate of 5,000,000 V/s (**Fig. 4.9d** and **e**). The results show that the average surface I^- concentration during the cycles for both GSE-10 nm and GSE-1nm is much stable compared to the results in 0.1 M ZnI_2, especially for the large slit channel size electrode. Note that the hysteretic phenomenon of average surface I^- concentration during the charging/discharging process was still be observed in this electrolyte at the high scan rate simulation test. Interestingly, at the initial charging simulation, the average surface I^- concentration of GSE-1nm is much lower than that of the GSE-10nm, while with the cycling simulation, the average I^- concentration at the surface of GSE-1nm turns to higher than that of the GSE-10nm.

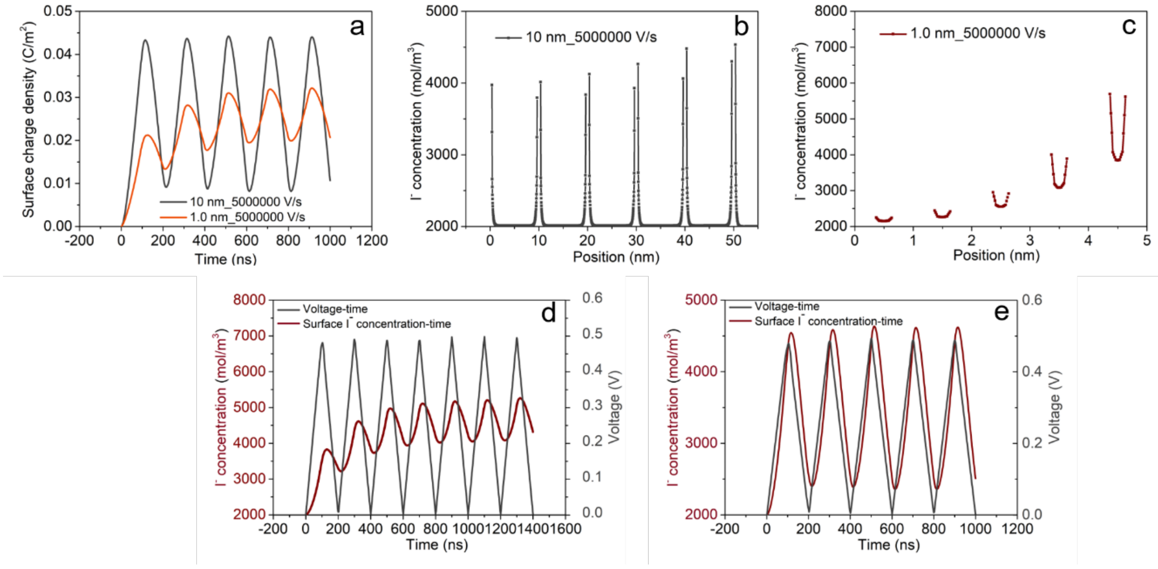

Figure 4.16. (a) shows the surface charge density of the GSE-10 nm and GSE-1nm with cycling charge/discharge at the scan rate of 5,000,000 V/s; **(b)** and **(c)** show the ion distribution curves of the GSE-10 nm and GSE-1nm after initial charging at the scan rate of 5,000,000 V/s; **(d)** and **(e)** present

the average surface concentration of I^- during the cycling dynamic charging process on the GSE-10 nm and GSE-1nm at the scan rate of 5,000,000 V/s. Electrolyte: 1.0 M ZnI_2, working voltage: 0-0.5 V. one cycle: 200 ns.

4.3.2 Nanoconfined zinc ions on the charge storage performance of nanoporous graphene-based electrodes.

Recently, the metal-ion batteries have been widely studied for engineering the energy storage devices with high charge storage performance.[185,186] Due to the tremendous advantage of directly applying metals as the negative electrodes for energy storage devices, the fundamental research studies on the electrochemical metal deposition play a crucial role in engineering the next-generation high-performance metal electrodes. In order to avoid the surface roughness effect on the electrochemical metal deposition, we control the filtration time instead of the mediated electrolyte concentration to tune the slit pore size of the electrodes.

To explore the electrochemical interface behaviour of the metal deposition, we studied the comprehensive electrochemical characterization of NPGE-10nm and NPGE-0.7nm in 1 M $ZnSO_4$ electrolyte. We first investigated the cyclic voltammetry characterization of the two electrodes at different dynamic scan rates. The EDL test (**Fig. 4.17a**) shows that the two electrodes have the same EDL current at a low scan rate (0.5 mV/s), indicating the two electrodes have the same effective surface area for ion adsorption. The NPGE-10nm exhibits a higher EDL current at the scan rate to 20 mV/s (**Fig. 4.17b**), which is mainly due to the hindered ion transport behaviour in the highly confined slit channel. The current-potential curves at the electrochemical reaction potential range show that the net current of NPGE-10nm and NPGE-0.7nm largely depends on the applied overpotential. In detail, at 0.5 mV/s, when the overpotential less than 50 mV, the NPGE-10nm presents a higher current, further increases the overpotential to 100 mV, the net current of the NPGE-0.7nm is higher than that of the NPGE-10nm (**Fig. 4.17c**). These results further indicate there are pore size effects on the electrochemical deposition rate. Increasing the scan rate to 20 mV/s, we can see the electrochemical zinc deposition rate of the NPGE-10nm is always higher than that of the NPGE-0.7nm (**Fig. 4.17d**), indicating that the dynamic ion transport effects paly dominate role on the zinc deposition rate at fast charging rate.

To better explore the nanoconfinement effects on the standard deposition rate of zinc, we further investigated the *i-v* curves of the two electrodes at the overpotential range of 5mV (**Fig. 4.17e** and **f**). The results show the onset potential of Zn^{2+}/Zn is almost the same in the two electrodes (**Fig. 4.17g**). The NPGE-10nm possesses a better electrochemical rate performance near the onset potential, which is quite an agreement with the CV results (**Fig. 4.17h**). The better electrochemical reaction rate observed near the onset potential may be due to the higher standard rate constant of the NPGE-10nm.

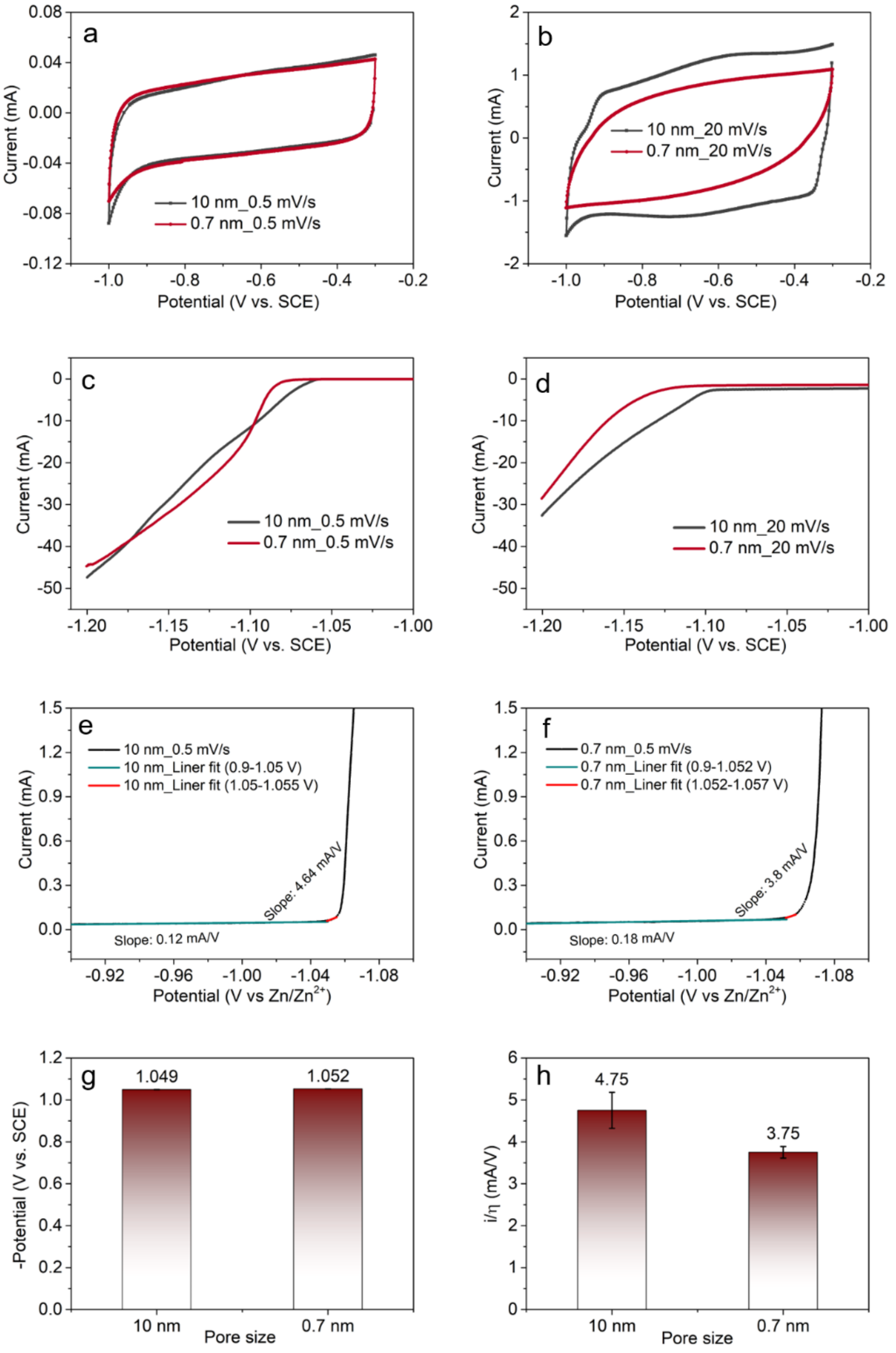

Figure 4.17. CV curves of NPGE-10nm and NPGE-0.7nm at the scan rate of 0.5 mV/s **(a)**, 20 mV/s **(b)**, at the capacitive working potential range. CV curves of NPGE-10nm and NPGE-0.7nm with the electrochemical working potential at the scan rate of 0.5 mV/s **(c)**, 20 mV/s **(d)**. Fitting line of the CV

curves of NPGE-10nm **(e)** and NPGE-0.7nm **(f)** with the scan rates of 0.5 mV/s at low overpotential range (5 mV); **(g)** The onset potential of the Zn^{2+}/Zn on the NPGE-10nm and NPGE-0.7nm; **(h)** The slope of the fitting line at the overpotential range of [0, 0.005V].

Next, we further did the constant charge and discharge characterization to analyze the charging platform, coulombic efficiency (CE), and cycling performance of the Zn^{2+}/Zn redox-reaction. The results presented here indicate that the energy barrier of the Zn^{2+}/Zn in NPGE-0.7nm is slightly higher than that in NPGE-10nm at the slow charge rate (**Fig. 4.18a**). Further increasing the charge rate to 25 mA/cm^2, there is an increase in the energy barrier, and the energy barrier of the zinc deposition in NPGE-0.7nm has a significant increase compared to that in NPGE-10nm (**Fig. 4.18b**). These observed charge rates-depend energy barrier of the zinc deposition possible comes from the dynamic ion transport effect. Furthermore, we evaluated the CE of the two electrodes during charge/discharge at different charge rates. The results show both electrodes present very high CE (above 98%) during the initial five cycles except at the low charge rate (0.5 mA/cm^2). The CE of the two electrodes is very similar, and only a slight difference of CE when charging/discharge at the low charge rate (**Fig. 4.18c**). The cycling performance of the two electrodes at a high charge rate (25 mA/cm^2) shows that the NPGE-0.7nm possesses a stable cycling performance with excellent CE retention during the 1000 cycles, which is much more stable than that of the NPGE-10nm (**Fig. 4.18d**). The electrochemical characterization results presented here indicate the nanoconfinement indeed could induce the difference of metal deposition, which could provide a new concept/strategy for further engineering the metal electrodes with comprehensive and excellent electrochemical performance. The results presented here also advance the knowledge development for the metal corrosion field.

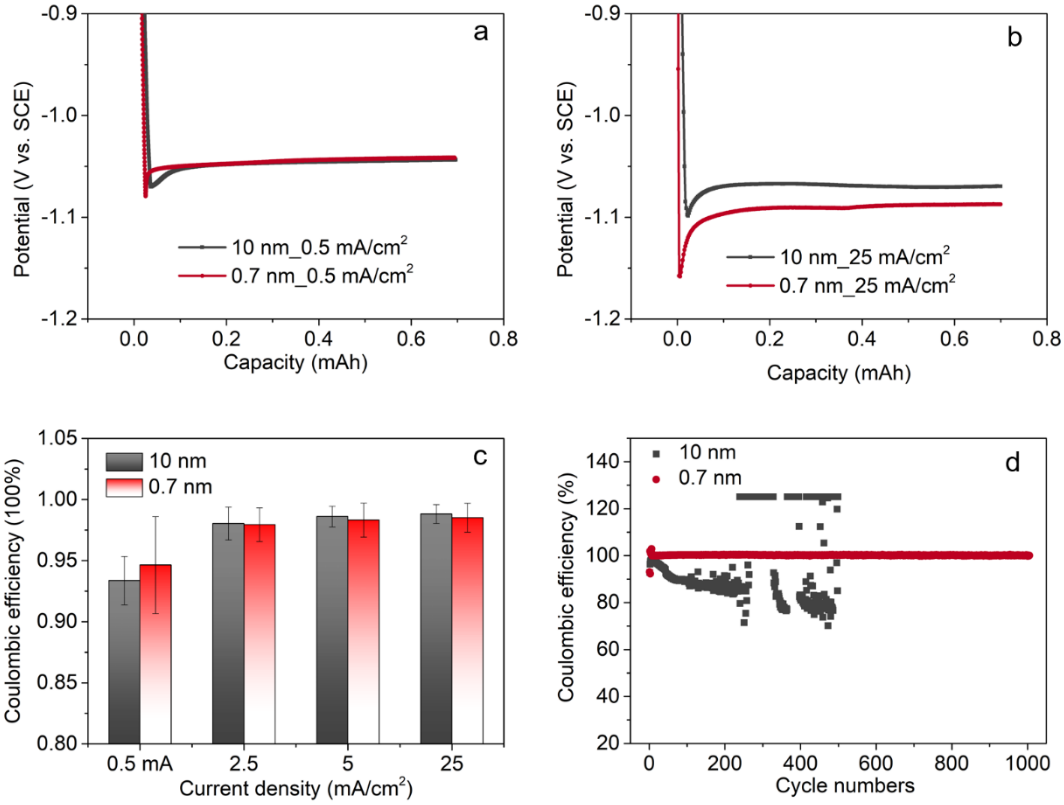

Figure 4.18. Initial charge curves of NPGE-10nm and NPGE-0.7nm at the charge rate of 0.5 mA/cm^2 **(a)**, 25 mA/cm^2 **(b)**; CE performance of NPGE-10nm and NPGE-0.7nm at different charge rates **(c)**; **(d)**. cycling performance of NPGE-10nm and NPGE-0.7nm at the charge rate of 25 mA/cm^2.

4.3.3 Nanoconfinement effects on the charge storage performance of nanoporous graphene-based devices

To further evaluate the nanoconfinement effect on the charge storage performance of the devices, we fabricated the two types of nanoporous graphene-based devices to do the electrochemical performance test. The positive electrode is nanoporous multilayered graphene electrodes with an average pore size of 1 nm and 10 nm, which has been fully exchanged with 1.0 M ZnI_2 electrolyte at 350 r/min for 3 days before the test. The negative electrode is the zinc foil (the mass of zinc is much higher than that of the multilayered graphene to avoid the insufficient charge/discharge of positive electrodes). The electrolyte is 5 M $ZnSO_4$ (the high concentration of electrolyte used here is to avoid the electrolyte effect on the performance). The devices are marked as NPGD-10nm and NPGD-1nm when the positive electrodes have an average pore size of 10 nm and 1nm, respectively.

Firstly, we studied the CV characterization to identify the redox peaks of the I^-/I_3^- for the devices, and the plotted curves show that both two devices exhibit pronounced redox peaks (**Fig. 4.19**). At the studied scan rates, the peak potential for the two devices is also very similar, and the peak potential only holds a very slight shift with the increase of the scan rate, which indicates good electrochemical kinetics of the I^-/I_3^- charge storage. The amounts of redox-active ions (I^-) confined in the NPGD-10nm positive electrodes is around 10 times that of NPGD-1nm. Theoretically, the total charge stored for the NPGD-10nm should be 10 times that of NPGD-1nm. While from the CV curves of the two devices, we observed the peak current of the NPGD-10nm was only around 4 times that of NPGD-1nm.

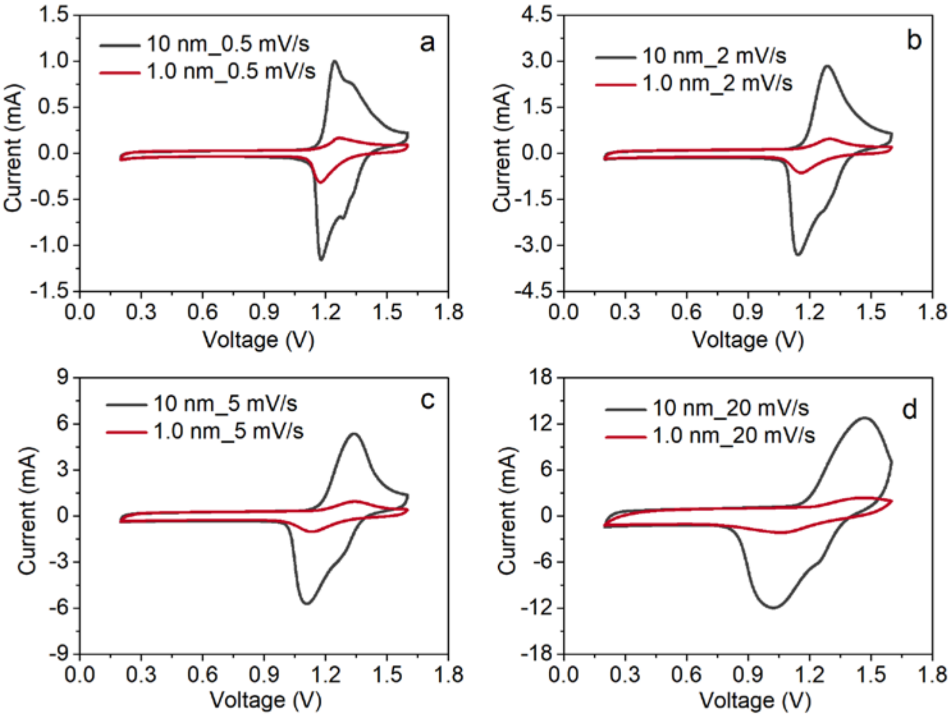

Figure 4.19. CV curves of NPG-10nm and NPG-1nm devices under the scan rates of 0.5 mV/s **(a)**, 2 mV/s **(b)**, and 5 mV/s **(c)** and 20 mV/s **(d)**, respectively.

Later, we further did the constant charge/discharge test of the two devices. The results show that the NPGD-1.0nm presents a higher volumetric capacity compared to that of the NPGD-10nm at the charge rate of 1 mA/cm^2 (**Fig. 4.20a**), which is around three times that of the NPGD-10nm. The cycling performance of the two fabricated devices was also conducted (**Fig. 4.20b**). The results show that both devices have high CE, which is close to 100% during cycling. Self-discharge is the main electrochemical performance feature of the redox-electrolyte type energy storage devices. To evaluate this feature, we rested the devices for a different time at the open-circuit voltage condition. The achieved results show that the NPGD-1.0nm holds much higher capacity retention compared to that of the NPGD-10nm after rest for 2 hours and 6 hours. The stored capacity retention of the NPGD-1.0nm could reach to 98% (**Fig. 4.20c** and **d**).

The charge storage performance presented here indicates the performance of the device depends on the confined level of the electrodes. The engineering of the nanoconfined electrode-electrolyte interface could provide the potential to achieve the EEDs with high comprehensive electrochemical performance.

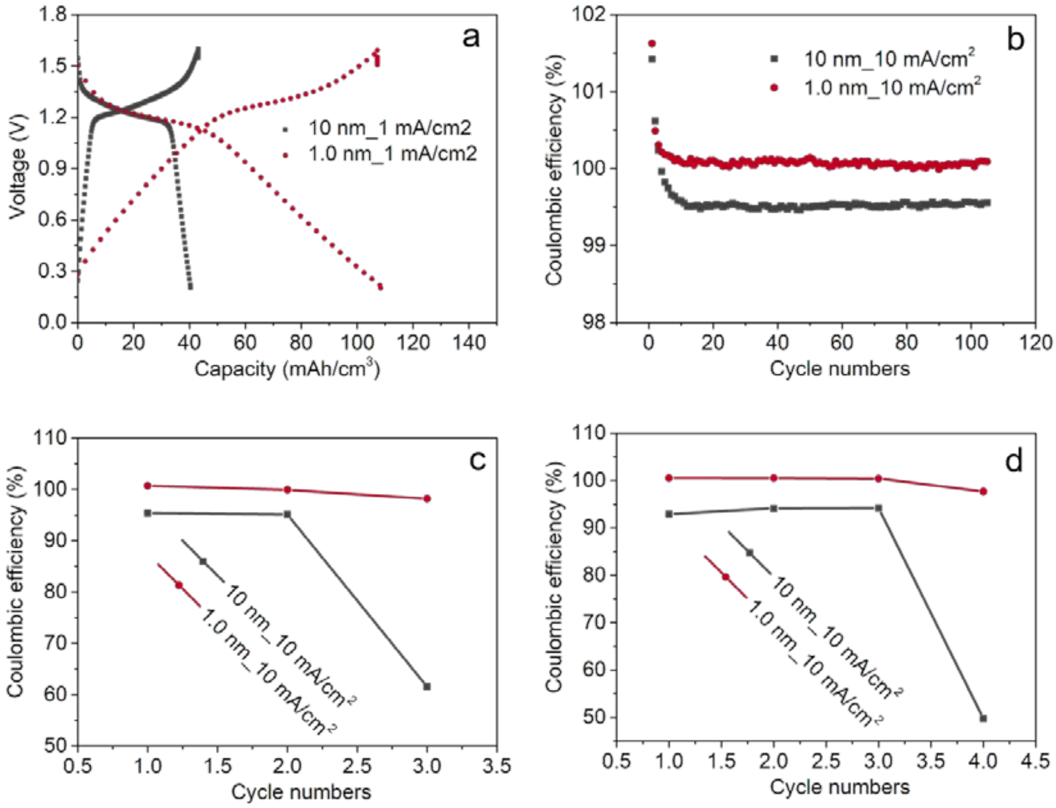

Figure 4.20. (a) Charge/discharge curves of NPGD-10nm and NPGD-1nm at the charge rate of 1 mA/cm^2; **(b)** Cycling performance of NPGD-10nm and NPGD-1nm at the charge rate of 10 mA/cm^2. The capacity retention of NPGD-10nm and NPGD-1nm after resting at OCV for 2 hours **(c)** and 6 hours **(d)**.

4.4 Conclusion

This chapter systematically investigates the nanoconfinement effects (graphene-based electrodes with average slit pore size of 10 nm, 1.0 nm, and 0.7 nm) on the electrochemical interface performance of redox-active ions (I^- and Zn^{2+}) through the combination of electrochemical characterization and continuum simulations. The following conclusions can be drawn:

1. At 0.5 mV/s, the peak current for the NPGE-1nm is around 2.8 times and 1.4 times of that of the NPGE-10nm in 0.1 M ZnI_2 and 1.0 M ZnI_2 electrolytes, respectively, indicating the interface reaction rate of I^- ions depend on the slit pore size of the graphene-based electrodes. This is a strong experimental evidence to demonstrate the nano-confinement effect on electrochemical reaction in graphene-based membranes.

2. Our studies demonstrate that the difference in the charge transfer rate of NPGE-1nm and NPGE-10nm is not due to the difference of active surface area, the standard rate constant, and the anodic charge transfer coefficient of these two electrodes. The continuum simulation results show that the concentration ratio $(C_{1nm}^{I^-}/C_{10nm}^{I^-})$ of surface I^- in the above electrodes are around 3.4 and 1.4 in 0.1 M and 1 M ZnI_2 electrolytes, which is close to the experiment peak current ratio (0.1 M ZnI_2: 2.8; 1 M ZnI_2: 1.35). These experimental and simulation results suggest that the higher charge transfer rate at peak current achieved for the NPGE-1nm possible due to the higher surface reactive ion concentration of the NPGE-1nm compared to that of the NPGE-10nm.

3. The NPGE-10nm and NPGE-1.0nm have very similar onset potential (vs. Zn^{2+}/Zn reference) in the studied redox-active electrolytes (0.1 M ZnI_2: 1.165 V vs. 1.155 V; 1.0 M ZnI_2: 1.132V vs. 1.135 V), indicating the negligible pore size (10 nm vs. 1nm) effect on the onset potential of I^- based redox-active electrolytes. There is a need to carry out more experimental works for nanoconfinement effect on the onset potential of other redox-active electrolytes.

4. At 25 mA/cm^2, the NPGE-0.7nm negative electrodes possess a stable cycling performance with excellent coulombic efficiency (around 100%) during the 1000 cycling test, which is much more stable than that of the NPGE-10nm (large variation of coulombic efficiency during cycling). This result indicates that engineering the pore size of the conductive electrode could be a very promising strategy to enhance the coulombic efficiency and cycling life of zinc deposition. Perhaps, this strategy is also available for the electrodeposition reaction of other metals, such as Li^+/Li, Na^+/Na, K^+/K, etc.

5. The NPGD-1nm has a volumetric capacity of 110 mAh/cm^3, which is higher than that of the NGGD-10nm (40 mAh/cm^3). Additionally, the NPGD-1.0nm holds much better capacity

retention compared to that of the NPGD-10nm after resting for 6 hours (98% vs. 50%). These results indicate that engineering the electrodes with micropore could be a promising strategy to increase the charge storage performance of the redox-active electrolyte based devices.

Overall, we believe our fundamental findings and comprehensive discussion about nanoconfined interface redox-reaction could contribute to the understanding of nanoconfinement effects on the interface electrochemical charge transfer. Our research results also indicate that the engineering of the EDL structure could be a very promising strategy for designing the next-generation electrode-electrolyte system with high energy and fast power delivery. Besides, the research results and discussion presented here also could provide inspiration and knowledge contribution for accelerating the design of better electrodes or devices in other research communities, such as the electrochemical catalysis.

Chapter 5 Machine learning-assisted device-level design of graphene-based supercapacitors

5.1 Introduction

Supercapacitors, also called electrochemical double-layer capacitors (EDLCs), store and deliver energy through ion adsorption/desorption at the electrical double layers.[19] They have attracted intense attention in the energy storage field in light of their fast charging capability, high power density, and long-life span.[23] However, their low volumetric energy density (amount of energy stored per unit volume) is a crucial drawback index for impeding the broad application of EDLCs. The strategies used to increase EDLC energy density include developing new capacitive materials, new electrode structures, applying high working voltage electrolytes, and designing asymmetric supercapacitors. Currently, quantitative, time and cost-effective optimization design of supercapacitor devices are crucial in accelerating supercapacitor development. However, due to the high dimensional design space consisting of variable main design parameters (pore size, thickness, working voltage, and operation charging rate), the optimal design of supercapacitor devices still remains a major challenge for the supercapacitor community.

Two-dimensional (2D) materials with a layered structure, high conductivity, favorable ion transport properties, and excellent volumetric capacitive performance, have been widely studied for engineering high-performance supercapacitor electrodes, such as graphene-based materials, Mexnes, and metal oxide.[10,47,156] As we know, the capacitance of electrodes largely depends on the electrode structure.[47] Therefore, a well-developed quantitative relationship between 2D active materials' structure and electrochemical performance could provide valuable information for the design of high-performance 2D active materials. The established relationship could boost the optimal design of high-performance supercapacitors. Additionally, the concepts used to design supercapacitors have been well developed. For example, the methods used, including asymmetric design, injecting free charge to the electrodes, and the introduction of mixture electrolyte, could all effectively increase the energy density of supercapacitors.[55,57,91,158]

Even though these design concepts could enhance the energy density of supercapacitors, we still need more information on the optimal design of the supercapacitors at the device-level.

Particularly, we need the device design that will cover the design parameters with an extensive value range instead of several random design combinations. Typically, there are two conventional methods used to study the electrochemical performance of electrodes and the design of supercapacitors: experimental measurement and computational simulation. In experiments, establishing a quantitative relationship between capacitance and electrode structure needs thousands of electrodes with various structures, which is an exceptionally complicated, time, and resource-consuming process.

Meanwhile, due to the complexity of the studied system, building and developing a reliable physical model to fully predict and capture the complicated relationship between the performance of electrodes and their related structure is extremely difficult. Notably, the physical model is also usually not on the same length scale as the experiment platform.[70] The optimal design based on the developed physical model is not able to directly transfer to the practical condition. Therefore, it is urgent to develop an intelligent and reliable model that could correctly predict the performance of electrode materials with time efficiently and cost-effectively. Machine learning (ML), as the study and construction of computer algorithms, could learn from data and has been successfully demonstrated as a powerful and useful tool in many disciplines.[95,101,187-189]

In this chapter, we present that utilizing an artificial neural network (ANN) could successfully predict the 2D materials electrode performance and thus efficiently guide and accelerate the supercapacitor device design. Briefly, we adopted the nanoporous multilayered graphene with a tunable slit pore size as the suitable materials platform with the standard KCl (1M) electrolyte. Using the capillary compression technique developed in our group, we tuned the pore size of nanoporous graphene-based electrodes (NPGEs) from 1.7 down to 0.8 nm. The thickness of the electrodes was varied from 11 to 276 um. We did 200 separate experiments to measure the capacitance of electrodes with different thicknesses and pore size under different charging rates. The obtained experimental database was used to train the ANN model. Then, we applied the well-trained ANN model to predict the capacitance of positive and negative electrodes with various electrode structures, leading to the establishment of a comprehensive and continuous quantitative relationship between NPGE structure and the capacitance of both electrodes. After that, the numerical method was applied to explore the high dimensional design space modeled by ANN for the optimized matching of positive and negative electrodes for achieving optimal design on the device-level. The calculation results indicate that there are more than 1 million matching combinations for positive and negative electrodes that meet the general design rules.

This result shows that it is an extremely complicated task for optimizing a supercapacitor design based on a conventional method. Additionally, a random forest regressor is employed to extract featured parameters of electrodes and devices, providing an insightful relationship between parameters and performance. Lastly, we carried out experiments to successfully confirm the validity of our optimized supercapacitor design. The optimal device design results indicate that the positive and negative electrode structures, including pore size and thickness, are hard to determine quantitatively from conventional trial-and-error experiments. Besides, the optimal design parameters depend on the charging rate. In conclusion, this work provides a general and effective solution to design graphene-based 2D materials supercapacitor devices on-demand. This project indicates that the introduction of machine learning to the energy storage filed is a promising research direction that is worthy of further exploration.

5.2 Overall picture of this project

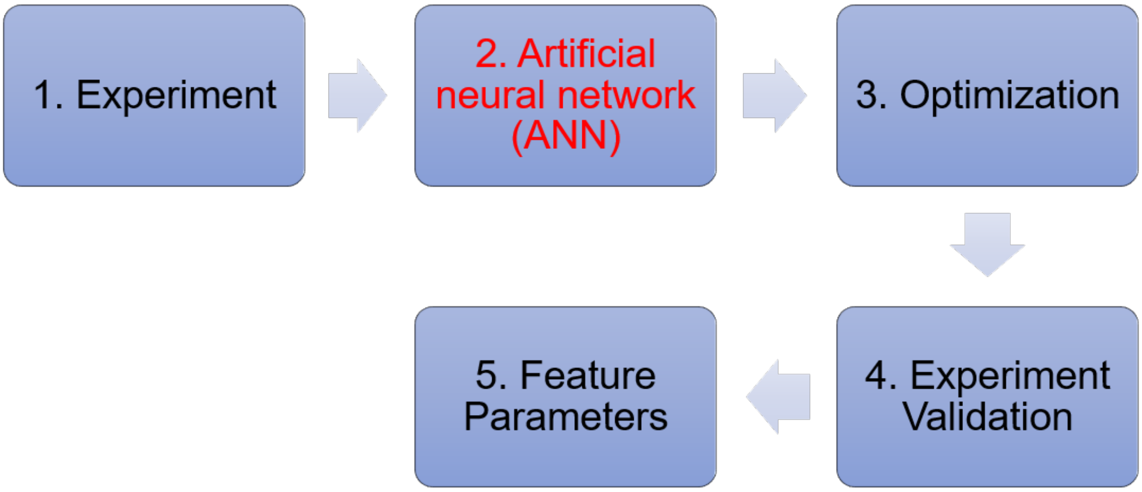

Figure 5.1. Flow chart of this project.

5.3 Methodology

5.3.1 Synthesis and characterization of NPGEs.

Chemically converted graphene (CCG) dispersion was synthesized by following the method described in Reference.[166] Briefly, graphene oxide colloid (0.5 mg/ml, 200 ml) made from the modified Hummers' method was mixed with 0.6 ml hydrazine (35wt% in water) and 0.8 ml ammonia (28wt% in water) solution in a glass vial. After being vigorously shaken for a few minutes, the flask was put in a water bath (~100 °C) for 3 hr.

Then NPGEs were fabricated by following the method we provided in chapter 3.

The average interlayer spacing can be estimated from the thickness of the membranes according to the formula[102]:

$$d = \frac{Areal\ density\ of\ graphene \times Thickness\ of\ CCGM}{Areal\ mass\ loading\ of\ CCGM}$$

where the areal mass density of graphene is reported to be 0.77 mg/m^2,[102] the thicknesses of the NPGEs were measured using a digital micrometer at 1 um resolution. The average slit pore (channel) size of our tunable NPGEs mediated with 0 M, 0.05 M, 0.1 M, 0.3 M, 0.5 M, and 3.0 M H_2SO_4 are 0.8 nm, 0.9 nm, 1.0nm, 1.2 nm, and 1.7 nm and 6.8 nm respectively.

Table 5.1 Pore size and thickness of NPGEs

Pore size (nm)	Thickness (um)	Thickness (um)	Thickness (um)	Thickness (um)	Thickness (um)
0.8	11	33	66	99	132
0.9	12	36	72	108	144
1.0	13	39	78	117	156
1.2	15.5	46.5	93	139.5	186
1.7	23	69	138	207	276

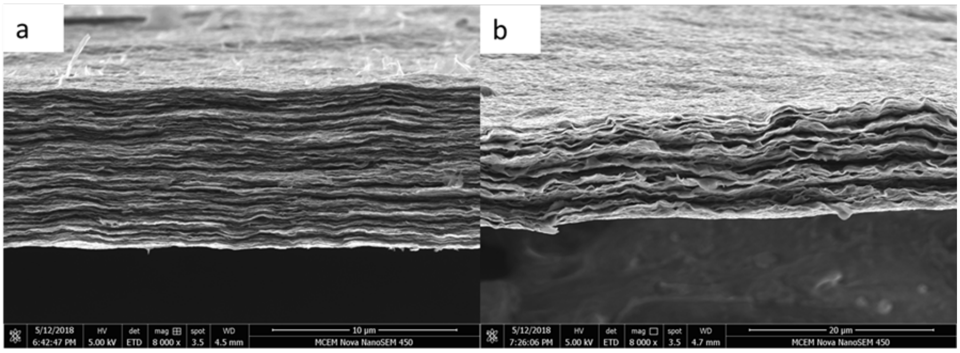

Figure 5.2. (a) and **(b)** are the SEM images of our synthesized freezing dry and H_2SO_4 mediated NPGEs respectively.

5.3.2 Electrochemical characterization of NPGEs

The electrochemical characterizations include open-circuit voltage and cyclic voltammetry (CV). They were performed using Bio-logic VMP300.

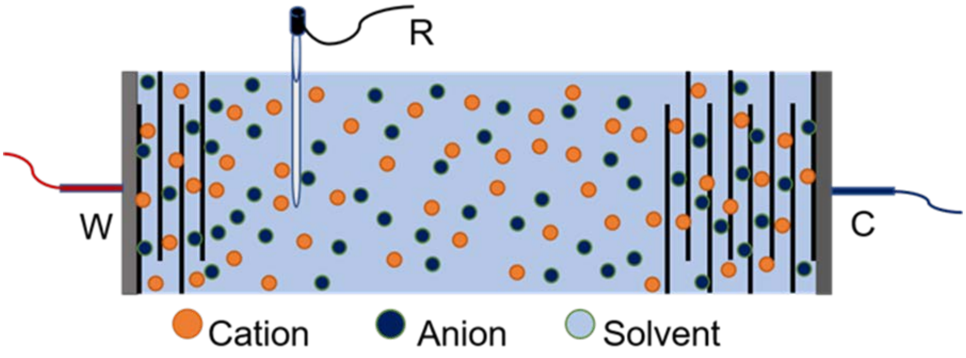

Figure 5.3. Three-electrode configuration setup, where the reference electrode is a saturated calomel electrode (SCE), the counter electrode is the hydrogel graphene membranes, which the mass is two times that of working electrodes.

The equation used for calculating the capacitance of various NPGEs (different pore size and thickness at different scan rates) are based on CV results: C=$\int_0^{v/s} jdt/v$, where C is gravimetric capacitance (F/g), j is absolute gravimetric current density (A/g), s is the scan rate (V/s), and v is the potential window (V). To calculate the volumetric capacitances, the gravimetric capacitance was multiplied by the volumetric (g/cm^3) density of the electrodes.

5.3.3 Artificial neural network model

Artificial neural network (ANN), a learning algorithm of machine learning, is inspired by biological neural networks. It can learn from data, which has been successfully applied for materials discovery, chemical synthesis planning, and energy management systems, etc. While due to the lack of suitable materials platform and reliable experiment database, applying the ANN to assist the system-level design of supercapacitors has not been successfully achieved. Inspired by the significant reported research works on ANN, we plan to develop reliable ANN models that have the ability to predict the capacitance of positive and negative electrodes for assisting the on-demand device-level design of graphene-based supercapacitors. An Artificial Neural Network (ANN) is a network that is connected by the input layer, hidden layers, and output layer. The basic unit for the ANNN is the neuron. The applied function between each layer is called the active function, and the connection between each layer is called weight (w). Normally, the Bias for each neuron is constant (usually set to 1).[190,191] In this work, we choose the backpropagation algorithm for training the ANN models. From the experimental results, we can conclude that the relationship between pore size, thickness, charging rate, and specific capacitance is nonlinear.

Additionally, based on the domain knowledge in the supercapacitor field, we know that the capacitance is convergent with minimum and maximum capacitance. Therefore, we chose sigmoid function as the activation function for training the network, and this function has the value range of (0,1). For better applying the sigmoid function, we normalized all input data (pore size, thickness, scan rates) and output data (specific volumetric capacitance) into the range between 0 and 1. Notably, the sigmoid function has the extremum of 0 and 1, which means with the significant change of the input over a specific range, there is almost no change of the sigmoid function value. This could lead to the over-saturated phenomenon in the ANN model during the training and validation process, which will primarily decrease the accuracy of the prediction results by the developed models. Therefore, for better solving this problem and minimizing the regularization value of the ANN model, we further normalized our output data in the range of (0.1, 0.9). The structure of the ANN is developed by python. In our case, for increasing the training speed, we choose three hidden layers for building the ANN architecture with 5, 6, and 2 neurons at each layer, respectively. The pore size, thickness, and scan rates are the input neurons at the input layer, and the specific volumetric capacitance is the output neuron at the output layer.

5.4 Results

5.4.1 Experimental results

Typically, apart from positive and negative electrodes and electrolytes, each supercapacitor device contains a separator (to prevent a short circuit between electrodes) and two current collectors. Additionally, for practical applications, particularly for portable electronics and vehicles, the volumetric energy density of supercapacitors is more critical than the gravimetric energy density. Therefore, the supercapacitor design in an ideal space is the system-level design issue, and the optimal matching of each component is the core challenge for achieving high-performance supercapacitors.

Additionally, according to the previous research and published papers, pore size, electrode thickness, charging rate, working voltage, and electrolytes play a significant role in determining the capacitance of electrodes. Therefore, to obtain the insightful quantitative relationship of these parameters and electrode performance, we firstly applied nanoporous graphene-based membranes with different pore size and thickness as the materials platform in 1 M KCl electrolyte. Then we studied the positive and negative charging/discharging under a dynamic process using the three-electrode configuration. Some preliminary experimental results and data were collected.

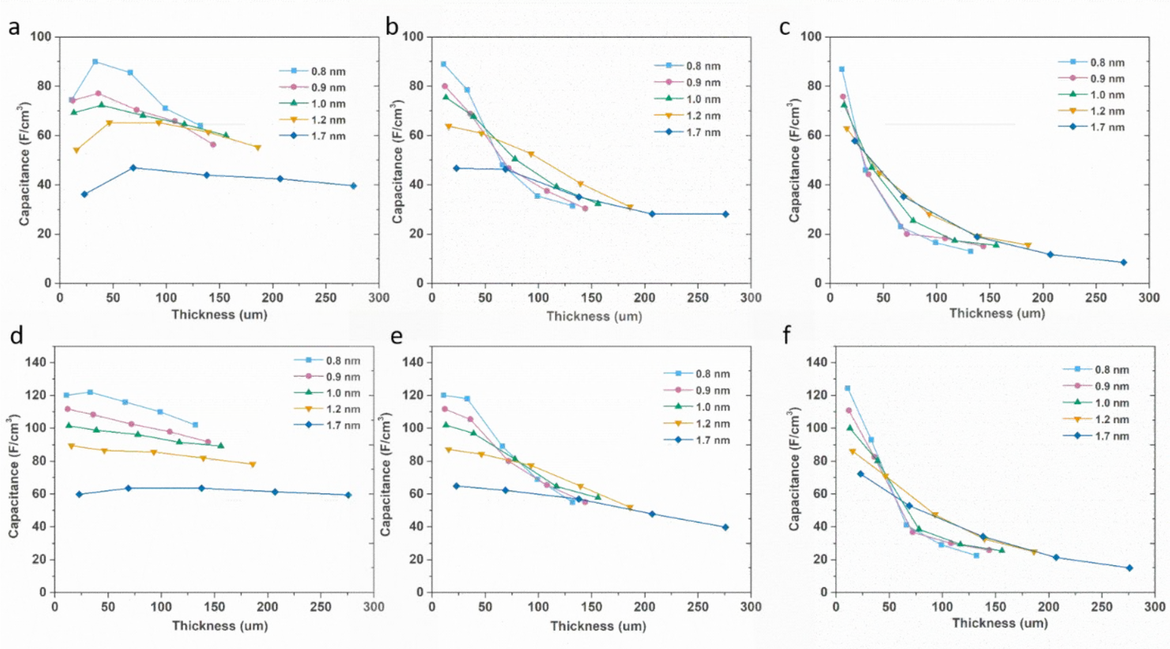

Figure 5.4. (a), **(b)**, and **(c)** show the capacitance of NPGEs with various pore size and thickness under the scan rates of 2 mV/s, 10 mV/s, and 50 mV/s for the positive electrodes; **(d)**, **(e)**, and **(f)** show the capacitance of graphene membrane electrodes with various pore size and thickness under the scan rates of 2 mV/s, 10 mV/s, and 50 mV/s for the negative electrodes, respectively.

The experimental results (**Fig. 5.4** and **Fig. 5.5**) further demonstrate that electrode structure, charging potential and frequency, largely determine the capacitance of both positive and negative electrodes in a typical choosing electrolyte. Therefore, we propose a hypothesis that there should exist a quantitative relationship among slit pore size (p), electrode thickness (t), charging rate (f), charging potential (v) and specific volumetric capacitance (Cs) of our developed NPGEs. We propose the numerical function as follows: Cs=$f\ (p.t.f.v)$. Especially, from the experimental results presented in **Fig. 5.4**, we observed that the specific capacitance of NPGE with a pore size of 1.7 nm is smaller than that of the NPGE with a pore size of 1.2 nm when their mass loading is the same. This result demonstrates that the optimized pore size is not larger than 1.7 nm. Moreover, as discussed before, the performance of the supercapacitor on device-level is determined by both positive and negative electrodes as well as electrolytes, separators and current collectors. All these results indicate that the design of supercapacitor on system level is a 10-dimensional design space, which is a complicated design task. Machine learning is an up-and-coming method for extracting the behind quantitative relationship from this complicated 10-dimensional space, while the large database is needed for training the machine learning model.

The separator in the supercapacitor is used to separate positive and negative electrodes to prevent short circuiting, and the current collector is applied for increasing charge transport in the electrical circuit. Theoretically, the separator and current collector do not store charge for the devices. Therefore, we controlled and determined their thickness in this work (the total thickness for one separator and two current collectors were 65 um). Then the system-level supercapacitor design is the matching of a positive electrode, a negative electrode, and electrolytes. In conclusion, for achieving the rational design of supercapacitors for practical application, it is much more reasonable and efficient to optimize the matching of positive and negative electrodes in the determined electrolyte.

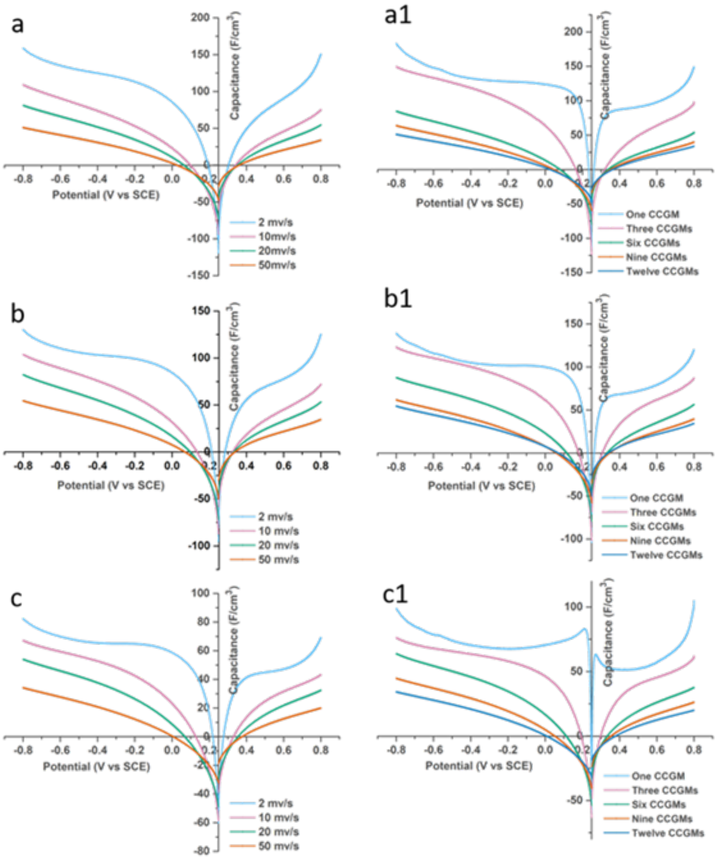

Figure 5.5. (a) (b) and **(c)** show the differential charging capacitance of graphene membrane positive (0.25-0.8 V) and negative (0.25- (-0.8) V) electrodes with 0.8 nm, 1.0 nm, and 1.7 nm pore size at the mass loading of 12 mg/cm2 under various scan rates in 1 M KCl; **(a1) (b1)** and **(c1)** show the differential charging capacitance of graphene membrane positive (0.25-0.8 V) and negative (0.25-(-0.8) V)

electrodes with 0.8 nm, 1.0 nm, and 1.7 nm pore size with different mass loading or thickness at the scan rate of 50 mV/s in 1 M KCl. *vs.* Saturated Calomel Electrode (SCE).

According to the energy density equation of supercapacitor: $E = \frac{1}{2} CV^2$, where C and V are the specific volumetric/gravimetric capacitance and a working voltage of the supercapacitor[175], respectively, we can conclude that for achieving the higher energy density, the terminate charging potential of positive and negative electrodes should be the onset potential of the electrolyte decomposition for the positive and negative charging process. Notably, according to the experimental results (**Fig. 5.5**), we observe that with the increase of the working voltage of positive and negative electrodes, there is an increase of the differential capacitance of the electrodes, resulting in higher specific capacitance in this charging potential range. Therefore, for achieving the highest specific capacitance and energy density of a supercapacitor in a determined volume, the optimized working potential range of the electrodes in 1 M KCl aqueous electrolyte is 0.25-0.8 V and 0.25- (-0.8 V) for positive and negative electrodes, respectively. 0.25 V (*vs.* SCE) is the open circuit potential of NPGEs in 1 M KCl aqueous electrolyte.

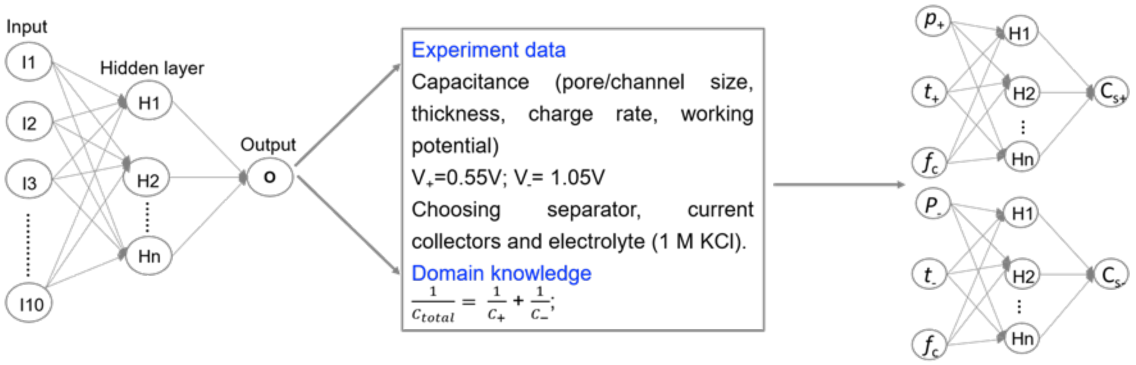

Figure 5.6. ANN model simplification based on experiment results and domain knowledge.

Fortunately, based on the domain knowledge in the supercapacitor field ($\frac{1}{c_{device}} = \frac{1}{C_+} + \frac{1}{C_-}$) and the determined positive and negative working potential[24,175], we could divide the sophisticated 10-dimensional design space into two 3-dimensional spaces. This could primarily simplify the machine learning model and decrease the essential database for the model training.

5.4.2 Results of the ANN model

Firstly, based on the achieved electrochemical performance data, we listed the capacitance distribution of positive and negative electrodes with the corresponding pore size, thickness, and charging rate (**Fig. 5.7a** and **b**). Due to the small quantity of experimental data used for training, partitioning to train and test sets was done with stratification to ensure that the distribution of data is maintained in both training and test sets. **Fig. 5.7 (c)** and **(d)** show the distribution of training and test sets with respect to the original dataset.

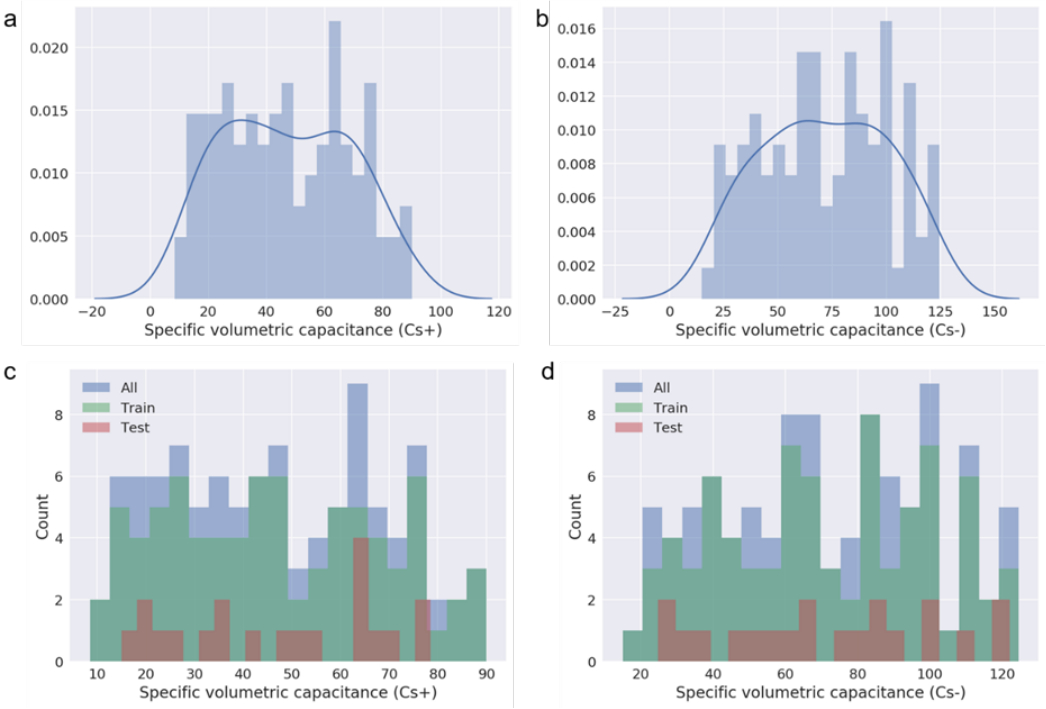

Figure 5.7. Distribution of specific volumetric capacitance for **(a)** positive and **(b)** negative electrode. Using stratification to split the experimental dataset: **(c)** positive and **(d)** negative.

Later, following from the previous discussion, we built two ANN models for positive and negative electrodes, respectively. We applied 80%, 10%, and 10% experimental data for training, validation, and test. According to the equation of gradient descent and loss function of ANN, the learning rate plays a core role in training the ANN model. A suitable learning rate could help us build a reliable model for performance prediction. Typically, the learning rate is in the range of (0,1), and it determines how quickly or how slowly to the update of weights. If the learning rate is minimal, the convergent speed is sluggish, and the loss function may not be able to reach the minimum value. If the learning rate is too large, the loss function will probably lose the global minimum value and induce an unreliable model. Therefore, for better training of the ANN model, we determined that the learning rate is a variable parameter with 56 different values in the range of (0, 1). After that, we trained our model with 56 learning rates and compared the loss function value of the validation process. For gradient descent: $\Delta w = -\eta\frac{\partial E}{\partial w}$ and loss function: $E = \frac{1}{N}\sum_{1}^{N}(Y_i - Y_i')^2$, where w is the weight, E is the loss function; N is the numbers of data used for training, validation or testing, Y_i is the output results from the model prediction, Y_i' is the experimental data.[190] From the validation results (**Fig. 5.8**), we can observe that the ANN model has the lowest mean squared error level when the learning rate is in the range of [0.48, 0.62] and [0.2, 0.42] for the positive and negative electrodes, respectively.

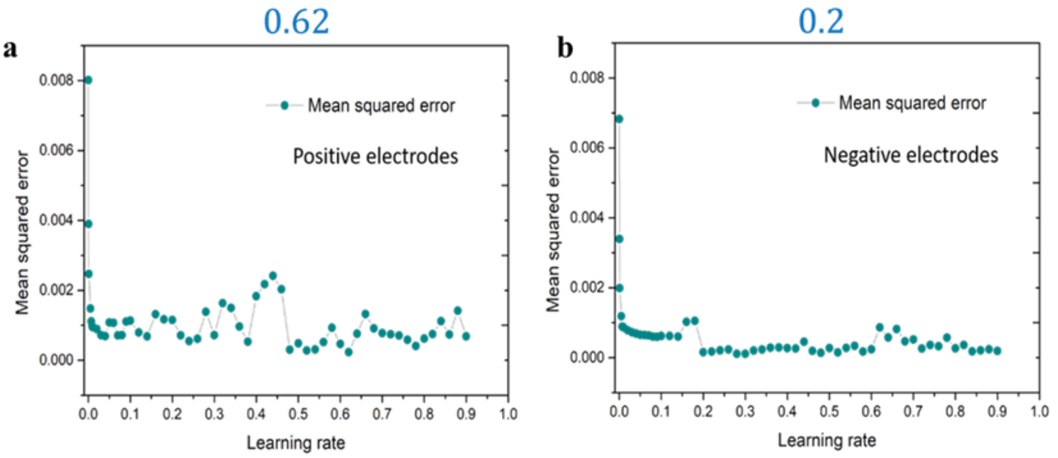

Figure 5.8. (a) and **(b)** are the loss function value of positive and negative models with 56 different learning rates, respectively.

Based on the ANN training and validation results, we determined that 0.62 and 0.2 were the suitable leaning rates to build reliable ANN models for positive and negative electrodes, respectively. We can see that all the model training results are well-matched with the experimental data (with the fitting slope of 0.982 and 0.997, respectively) when we apply the learning rates of 0.62 and 0.2 for the training process (**Fig. 5.9a** and **d**). The resulting mean squared error is 0.013% and 0.0096% for positive and negative ANN models, respectively.

To evaluate the well-trained ANN models, we compared the validation results and experimental data after the validation procedure (**Fig. 5.9b** and **e**). The achieved results show that the prediction results coming from the building ANN models agree with the experimental data of positive and negative electrodes (with the fitting slope of 0.976 and 1.003, respectively), and with loss function values of 0.023% and 0.016% respectively, based on the normalization data. These low mean squared errors indicate the accuracy and reliability of our developed ANN models.

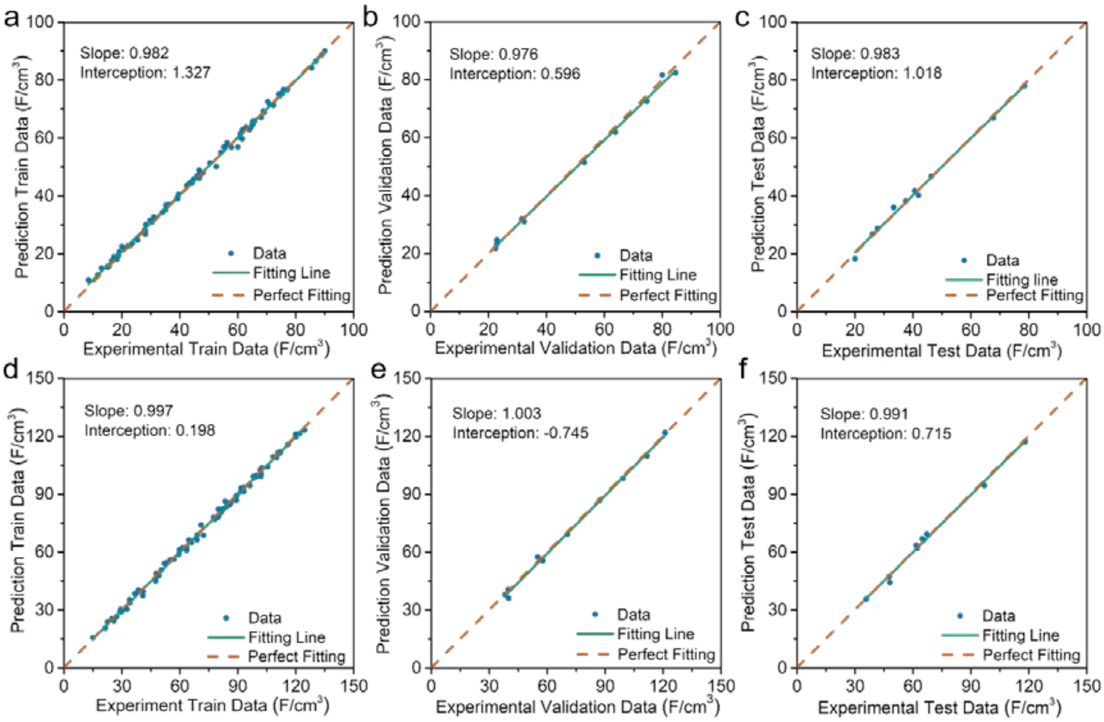

Figure 5.9. (a), **(b)** and **(c)** are the model training results *vs.* experimental data, model validation results *vs.* experimental data and model test results *vs.* experimental data for positive electrode ANN model when the learning rate is 0.62; **(d)**, **(e)** and **(f)** are the model training results *vs.* experimental data, model validation results *vs.* experimental data and model test results *vs.* experimental data for negative electrode ANN model when the learning rate is 0.2.

To further confirm the reliability of the predictive ANN model. We did the model test. The data that applied for the testing process is the rest ten sets of data that do not appear on the training and validation process. From the testing results, we can find that all the model prediction results infinitely approach the values of the experimental data, with the fitting slope of 0.983 and 0.991, respectively (**Fig. 5.9c** and **f**). According to normalization data, the corresponding mean squared error for positive and negative models is 0.017% and 0.017%. The test results demonstrate the correctness and reliability of our developed ANN models.

Lastly, to further confirm the reliability of the built ANN models, we also undertook the cross-validation (**Fig. 5.10**). With the increase of the training examples, there is an increase of the validation score for both positive and negative ANN models with narrow variance, thus further demonstrating the reliability of the built ANN models.

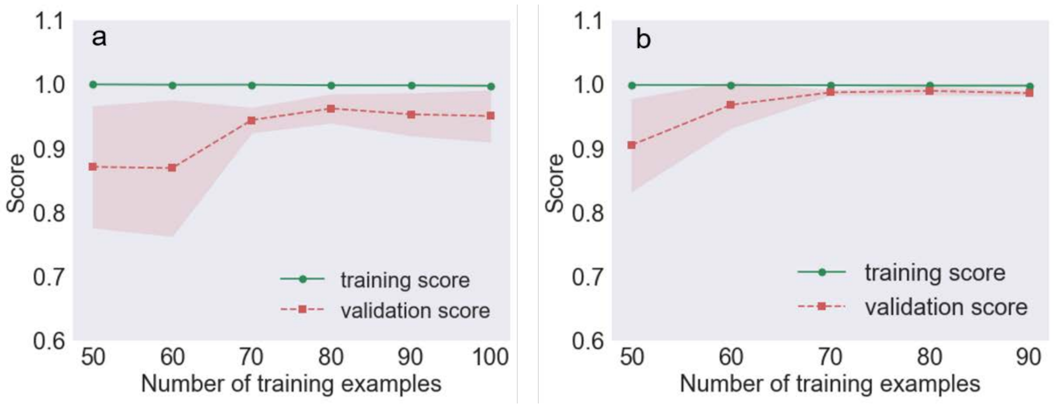

Figure 5.10. (a) and **(b)** are the cross-validation learning curves of the built positive and negative ANN models

5.4.3 Electrode performance prediction of positive and negative electrodes using developed ANN models.

After the building, updating, training, validating, testing, and cross-validation confirmation of the artificial neuron network models, the successfully developed network models could have the chance to predict the ANN response for any input. As a result, we propose to employ the developed ANN models to predict the specific volumetric capacitance of positive and negative electrodes with comprehensive pore size and thickness range under various charging/discharging frequencies.

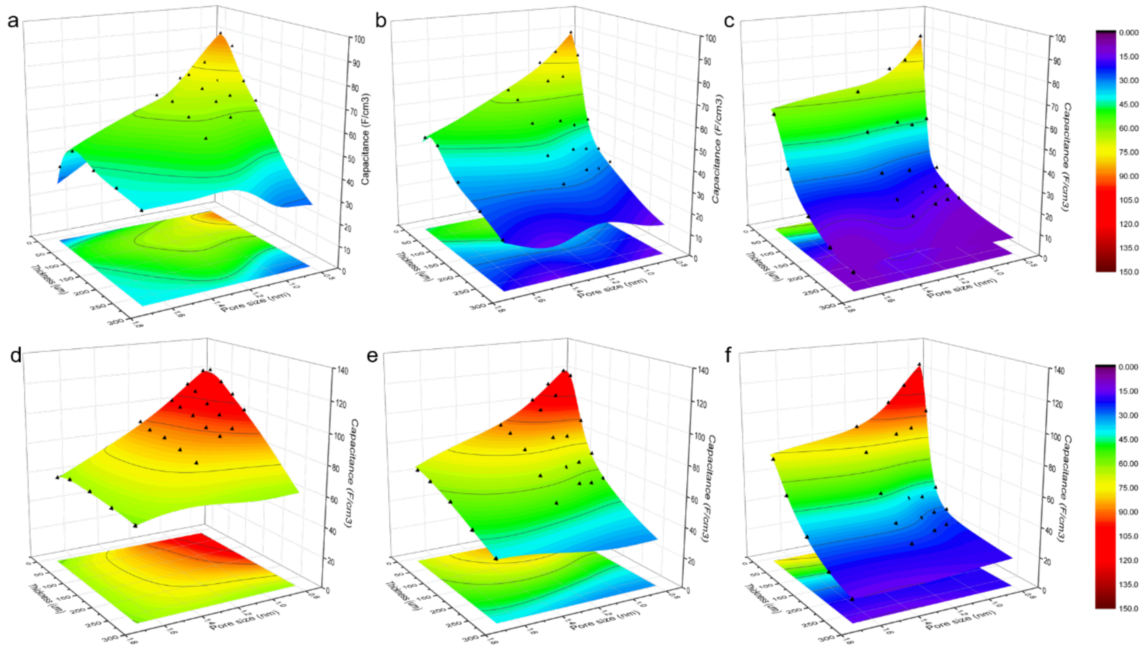

Figure 5.11. (a), **(b)**, and **(c)** are the 3D surface figures (specific volumetric capacitance *vs.* pore size and thickness) based on the designed ANN model under the scan rates of 2 mV/s, 10 mV/s, and 50 mV/s for the positive electrodes, respectively; **(d)**, **(e)** and **(f)** are the 3D surface figures (specific volumetric capacitance *vs.* pore size and thickness) based on the designed ANN model under the scan rates of 2 mV/s, 10 mV/s, and 50 mV/s for the negative electrodes, respectively. The Triangle with black color located at the surface of 3D figures are the corresponding experimental data.

The developed ANN models simulated outputs and predicted the specific capacitance of NPGEs on the comprehensive and continuous level with the pore size and thickness range of [0.8 nm, 1.7 nm] and [11 um, 276 um] under the scan rates of 2, 10, and 50 mv/s, respectively (**Fig. 5.11**). From the results, we can observe that all the experimental data are loaded on the predictive 3D graphs, and that they demonstrate the reliability of the ANN models as well as the prediction results. Thus, the electrode performance was well predicted by the predictive ANN model. The comprehensive and continuous quantitative relationship between performance and electrode structure has now been successfully achieved for the first time.

Moreover, we also predicted the quantitative relationship between the capacitance and main performance parameters with the consideration of separator and current collectors at different charge rates (**Fig. 5.12**). The results show that with an increase of the charge rates for positive and negative electrodes, there is a decrease in the optimal thickness of the active materials for achieving the highest specific capacitance, thus demonstrating that the supercapacitor design should be based on charging rates. Interesting, when we considered the thickness of separator and current collectors for evaluating the electrode performance, the highest specific capacitance of the electrodes (including the thickness of separator and current collectors) achieved was at a wide pore size range with almost the same thickness value for all the three different charging rates. These significant research results indicate the importance of the electrode thickness when designing a supercapacitor on the device-level.

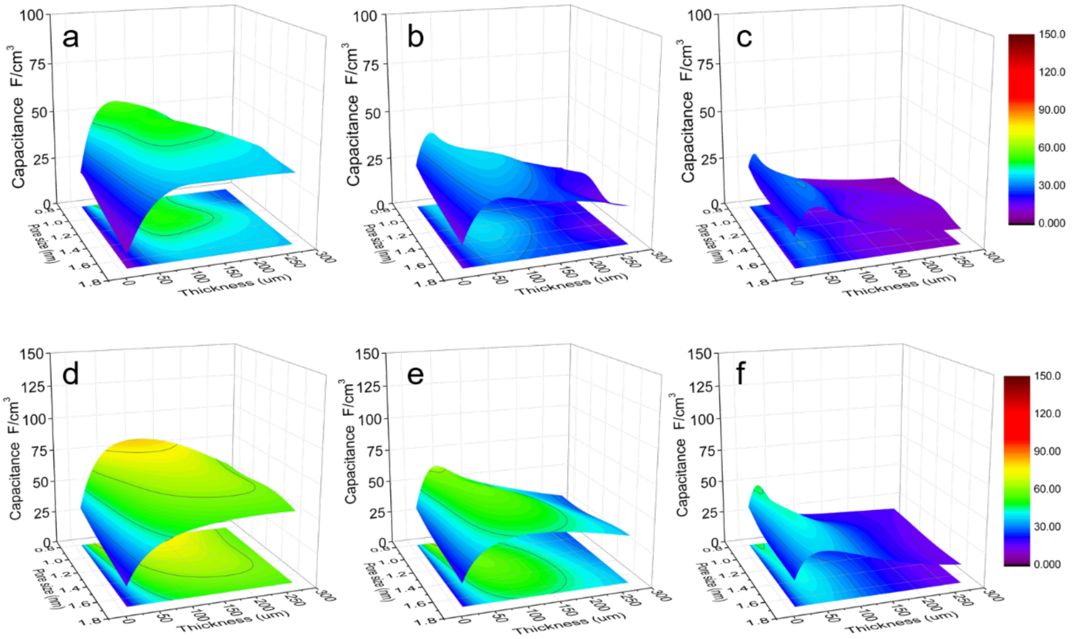

Figure 5.12. (a), **(b)**, and **(c)** are the 3D surface figures (specific volumetric capacitance *vs.* pore size and thickness) based on the designed ANN model under the scan rates of 2 mV/s, 10 mV/s, and 50 mV/s for the positive electrodes with the consideration of separator and current collectors, respectively. (d), (e) and (f) are the 3D surface figures (specific volumetric capacitance *vs.* pore size and thickness) based on the designed ANN model under the scan rates of 2 mV/s, 10 mV/s, and 50 mV/s for the negative electrodes with the consideration of separator and current collectors. The total thickness of separator and current collectors are 65 um.

5.4.4 On-demand optimizing design of supercapacitors on device-level

As we know, one supercapacitor module device is composited by two electrodes (positive and negative electrodes), electrolyte, one separator, and two current collectors. Importantly, the establishment of a quantitative relationship between basic parameters and capacitance of positive and negative electrodes lays the basis for guiding the optimal matching of positive and negative electrodes. It could profoundly accelerate the rational design of a high-performance supercapacitor on the device level. Based on the developed ANN models, there is the following relationship between specific volumetric capacitance of individual electrode and key parameters: $c_{s_+} = f\ (p_+, t_+, f, v_+)$, $c_{s_-} = f\ (p_-, t_-, f, v_-)$, where c_{s_+} and c_{s_-} are the specific volumetric capacitance of positive and negative electrodes, respectively, v_+, p_+, t_+ and v_-, p_-, *t*- are the charging potential window, pore size and thickness of positive and negative electrodes, respectively, and f is the charge rate.

Moreover, according to the charge balance of positive and negative electrodes, there is the following relationship between two electrodes: $Q_+ = Q_-$, $c_+ * v_+ = c_- * v_-$, where Q_+ , c_+, v_+ and Q_-, c_-, v_- are the stored charge, capacitance, and working voltage window for positive and negative electrodes in the supercapacitor device. Because of the developed reliable ANN models for electrodes and the domain knowledge that used to calculate the capacitance of the supercapacitor[175] ($\frac{1}{c_{device}} = \frac{1}{c_+} + \frac{1}{c_-}$, where c_{device}, c_+, and c_- are the capacitance of supercapacitor device, positive electrode, and negative electrode, respectively), the capacitance of the supercapacitor is available to be achieved. Lastly, we could apply the equation $C_v = C/(V_P + V_N + V_C)$, where C_v is the specific volumetric capacitance of supercapacitor, C is the total capacitance of supercapacitor; $V_P\ and\ V_N$ are the volume of positive and negative electrodes, respectively; V_C is the total volume of the current collectors and separator, which is a constant value in our case (65 um*0.85 cm^2)) to calculate the specific volumetric capacitance of the device.

Thanks to the developed ANN models, we simulated 50,000 specific volumetric capacitances of positive and negative electrodes each for the corresponding parameters (pore size and thickness) at each on-demand charging/discharging frequency. Based on these predictive results at each charging/discharging frequency, theoretically, there are 50,000×50,000 matching option for the supercapacitor design. As discussed before, for achieving higher energy density with the intrinsic electrodes and electrolyte, the working potential window of positive and negative electrodes are 0.55 and 1.05 V respectively. Therefore, there is the boundary condition: $c_+ * v_+ = c_- * v_-$, $v_+ = 0.55$ V, $v_- = 1.05$ V. The code for calculating the specific volumetric capacitance of the supercapacitor was written by Python. For avoiding the missing of the largest specific volumetric capacitance of supercapacitor, we output all specific volumetric capacitance with the corresponding design parameters when the stored charge ration between positive and negative electrodes is in the range of [0.99, 1.01].

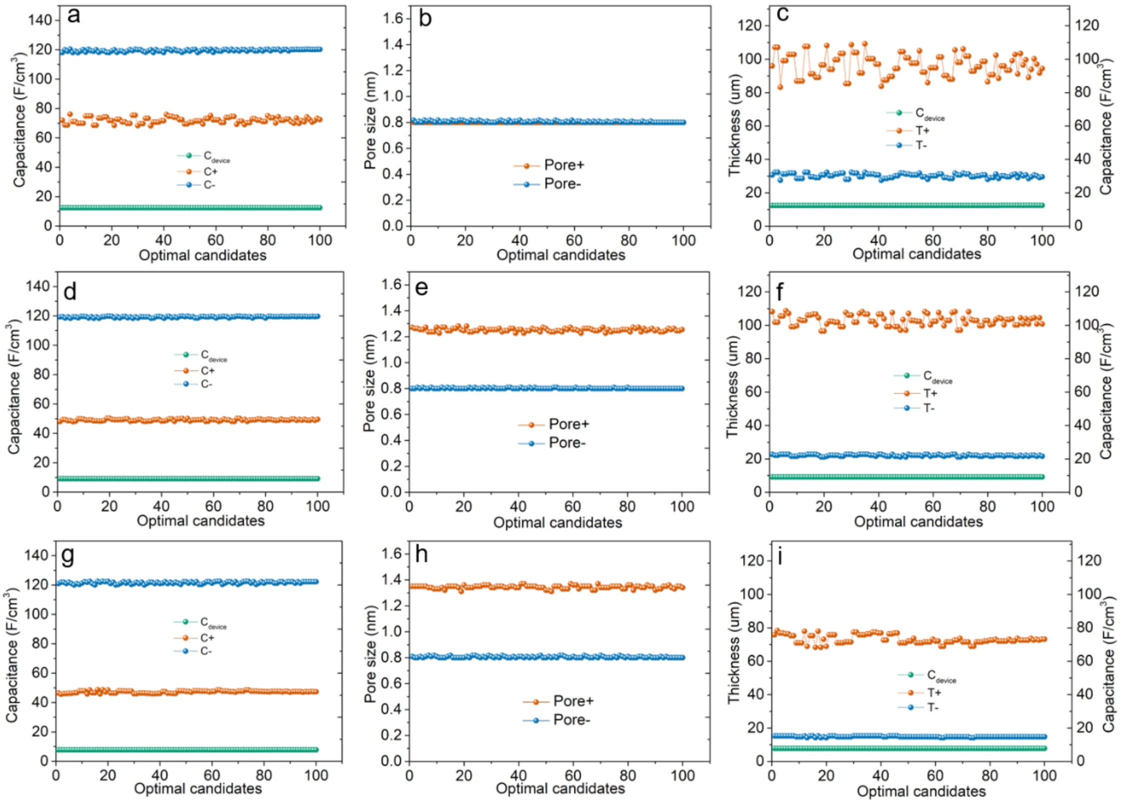

Figure 5.13. (a), **(d)** and **(g)** are the top 100 specific volumetric capacitances of supercapacitor and the corresponding specific volumetric capacitances of positive and negative electrodes at the scan rate of 6 mV/s, 30 mV/s and 75 mV/s, respectively. **(b)**, **(e)** and **(h)** are the corresponding pore size of positive and negative electrodes for the top 100 matching combinations. **(c)**, **(f)** and **(i)** are the corresponding thickness of positive and negative electrodes for the top 100 matching combinations.

The calculating results show that there are more than one million matching combinations of positive and negative electrodes that meet the general design rules. This result indicates that searching for optimal design is an extremely complicated and impossible task if we apply the traditional trial and error strategies. After obtaining all the required combinations, we selected the top 100 specific volumetric capacitances of the supercapacitors at each charging/discharge. Their corresponding specific volumetric capacitance, pore size, and thickness are presented in **Fig. 5.13**. From the results, we can observe that when the scan rate of the supercapacitor is 6 mV/s, the achieved highest specific volumetric capacitance of the device is 12.4 F/cm^3 (based on the total volume of positive electrode, negative electrode, current collectors and separator), the corresponding specific volumetric capacitance of positive and negative electrodes are around 70 and 120 F/cm^3 respectively (**Fig. 5.13a)**, the corresponding pore size of positive and negative electrodes are both around 0.8 nm (**Fig. 5.13b)**, the corresponding thickness of positive and negative electrodes are about 110 and 33 um (**Fig. 5.13c)**. When the scan rate of the supercapacitor increase to 30 mV/s, the calculated highest specific volumetric capacitance of supercapacitor is 9.1 F/cm^3 (based on the total volume of positive electrode, negative electrode, current collectors and separator), the corresponding specific volumetric capacitance of positive and negative electrodes are around 50 and 120 F/cm^3 respectively (**Fig. 5.13d)**. The corresponding pore size of positive and negative electrodes are approximately 1.25 and 0.8 nm (**Fig. 5.13e)**, the corresponding thickness of the positive and negative electrode are around 100 and 22 um (**Fig. 5.13f)**. When we further increase the scan rate of the supercapacitor to 75 mV/s, the highest specific volumetric capacitance of the device is 7.8 F/cm^3 (based on the total volume of positive electrode, negative electrode, current collectors and separator) with a corresponding specific volumetric capacitance for positive and negative electrodes of 47 and 120 F/cm^3 (**Fig. 5.13g)**. The corresponding pore size of positive and negative materials are about 1.35 and 0.8 nm (**Fig. 5.13h)**, the corresponding thickness of positive and negative electrodes are around 73 and 15 um (**Fig. 5.13i)**. The optimal prediction parameters show that the optimal prediction at high charge rate is quite different from that of the slow charge rate, highly indicating that these optimal design parameters achieved here are hardly predicted just from the experiments, especially for high charge rate situations.

5.5 Discussion

5.5.1 Experiment confirmation based on the predictive matching parameters

According to the developed ANN models, the quantitative structure-property relationship of supercapacitor electrodes is now successfully established. Meanwhile, the optimal design parameters of supercapacitors at the device-level at different charging rates are also predicted. For confirming the optimal supercapacitor design, we then fabricated the supercapacitor based on the predictive design parameters and did the experimental testing. The experiment results show that the specific capacitance of the supercapacitors matches very well with the predictive one (**Fig. 5.14**). In detail, at 6 mV/s, 30 mV/s, and 75 mV/s, the specific capacitance of the supercapacitor designed based on the predictive parameter values are 12.1 F/cm^3, 8.7 F/cm^{3,} and 7.4 F/cm^3, respectively. Moreover, from the experiment results, the charging/discharging potential window of positive and negative electrodes in these devices is around 0.55 and 1.05 V, respectively. These experiment results highly confirm the accuracy of the predictive optimal design parameters of the supercapacitor devices and further demonstrate the reliability of our developed ANN model.

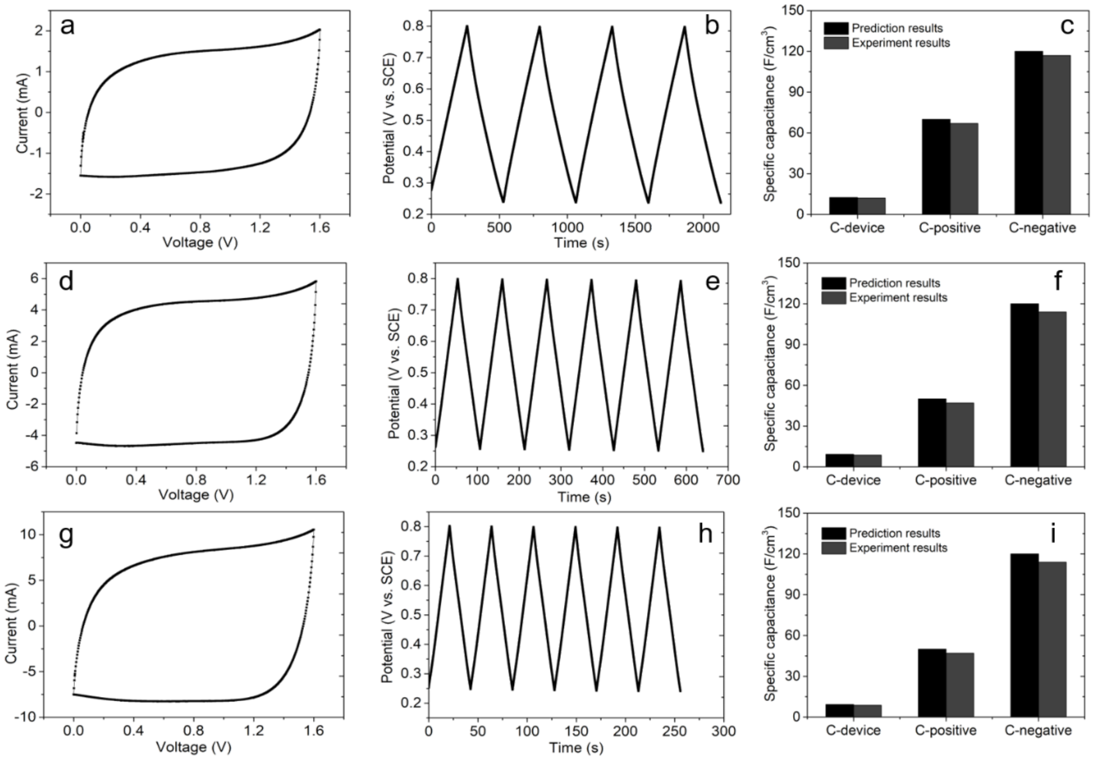

Figure 5.14. (a), **(d)** and **(g)** are the experiment CV curves of graphene-based supercapacitor devices based on predictive matching parameters at the scan rates of 6, 30 and 75 mV/s respectively; **(b)**, **(e)** and **(h)** are the experiment potential-time curves of the positive electrodes based on predictive matching parameters at the scan rates of 6, 30, and 75 mV/s respectively; **(c)**, **(f)** and **(i)** are the experiment and prediction capacitances based on predictive matching parameters at the scan rates of 6, 30, and 75 mV/s respectively.

5.5.2 Other design parameters and design results

Importantly, we also fabricated the supercapacitors with other design parameters to further validate the optimal prediction parameters at different charge rates. At 6 mV/s, we assembled two other asymmetric supercapacitors based on the optimal prediction parameters at 30 mV/s and 75 mV/s. When using the optimal parameters at 30 mV/s to design the supercapacitor for 6 mV/s case design, the design parameters for the positive electrode are the pore size of 1.25 nm, thickness of 100 um, the design parameters for the negative electrode are the pore size of 0.8 nm, thickness of 22 um. The achieved specific volumetric capacitance of the device is 9.3 F/cm^3, which is lower than that of 12.1 F/cm^3. The corresponding specific volumetric capacitance of positive and negative electrodes is around 53 and 119 F/cm^{3,} respectively. When selecting the optimal parameters at 75 mV/s to design the supercapacitor for 6 mV/s on-demand design, the design parameters for the positive electrode are the pore size of 1.35 nm, thickness of 73 um. The design parameters for the negative electrode are the pore size of 0.8 nm, thickness of 15 um. The achieved specific volumetric capacitance of the device is 8.3 F/cm^3, which is lower than that of 12.1 F/cm^3. the corresponding specific volumetric capacitance of positive and negative electrodes are around 51 and 126 F/cm^3 respectively (**Fig. 5.15**).

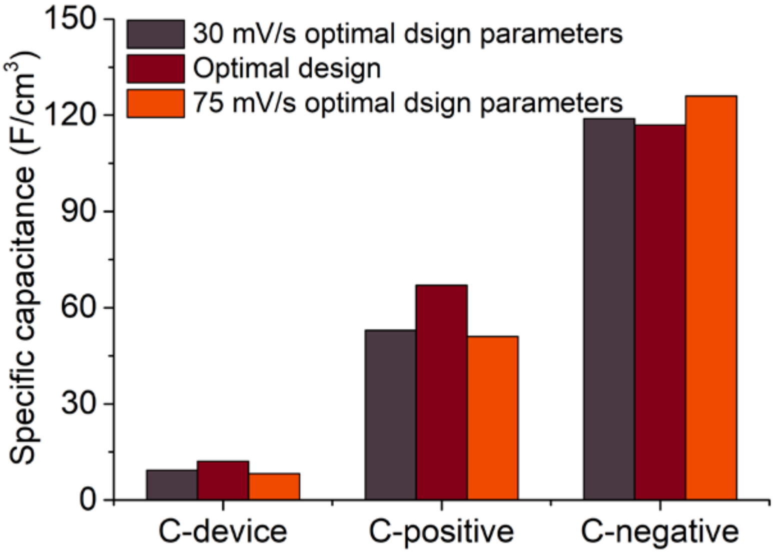

Figure 5.15. Capacitance results comparison for the 6 mV/s design study

At 30 mV/s, we fabricated other asymmetric supercapacitors based on the optimal prediction parameters at 75 mV/s. When selecting the optimal parameters at 75 mV/s to design the supercapacitor for 30 mV/s case design, the design parameters for the positive electrode are the pore size of 1.35 nm, thickness of 73 um, the design parameters for the negative electrode are the pore size of 0.8 nm, thickness of 13 um. The achieved specific volumetric capacitance of the device is 8.0 F/cm^3, which is lower than that of 8.7 F/cm^3. The corresponding specific volumetric capacitance of the positive and negative electrodes is around 49 and 125 F/cm^{3,} respectively (**Fig. 5.16**). Additionally, we also fabricated two symmetric supercapacitors based on the predictive design parameters at 30 mV/s. When the symmetric supercapacitor has the pore size of 0.8 nm, thickness of 22 um for both positive and negative electrodes, when charging the supercapacitor, when the potential of the positive electrode reach to 0.8 V which is the highest electrolyte potential (**Fig. 5.16a**), the working voltage of the supercapacitor is around 1.0 V (**Fig. 5.16b**), which is much lower than that of 1.6 V for the asymmetric design. The achieved specific capacitance of the device is around 8 F/cm^3, which is also smaller than that of the optimal design at 30 mV/s (**Fig. 5.16f**). When the symmetric supercapacitor has the pore size of 1.25 nm, thickness of 100 um for both positive and negative electrodes, when charging the supercapacitor, when the potential of the positive electrode reach to 0.8 V (**Fig. 5.16d**), the working voltage of the supercapacitor is around 1.2 V (**Fig. 5.16e**), which is much lower than the working voltage of the asymmetric design (1.6 V). The achieved specific capacitance of the device is around 8.6 F/cm^3, which is close to the optimal design capacitance at 30 mV/s (**Fig. 5.16 f**).

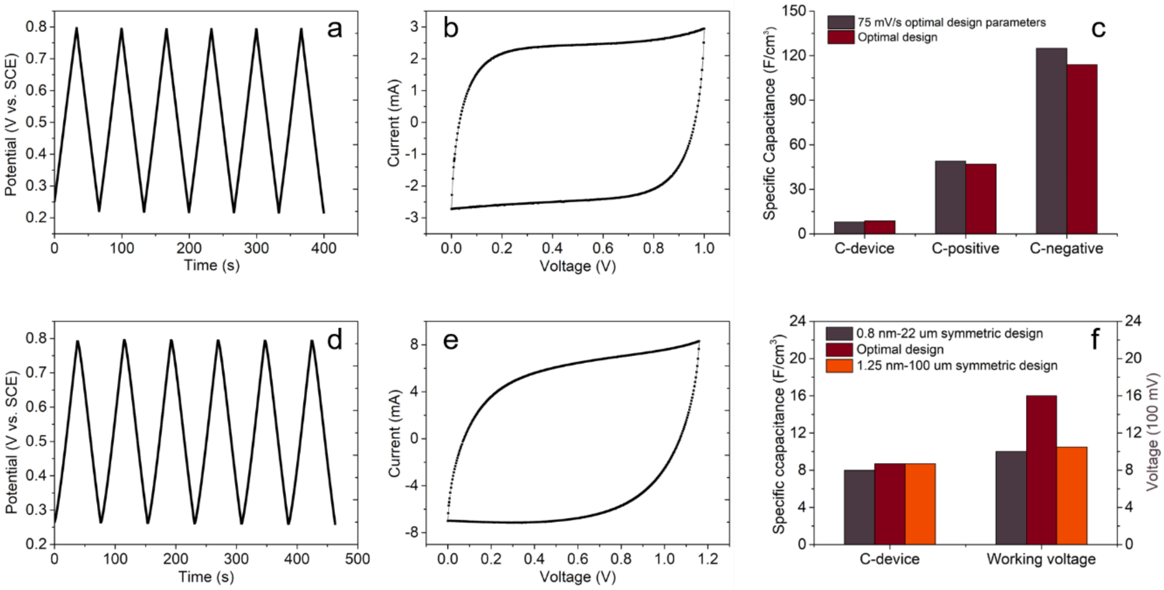

Figure 5.16. (a) and **(b)** are the experiment potential-time curve of the positive electrode and experiment CV curve of graphene-based supercapacitor device for the symmetric design with pore size of 0.8 nm, thickness of 22 um for both positive and negative electrodes at the scan rate of 30 mV/s; **(c)** the experiment capacitances based on predictive optimal and 75 mV/s optimal design parameters for the 30 mV/s design study; **(d)** and **(e)** are the experiment potential-time curves of the positive electrodes and experiment CV curves of graphene-based supercapacitor devices for the symmetric design with pore size of 1.25 nm, thickness of 100 um for both positive and negative electrodes at the scan rate of 30 mV/s; **(f)** the experiment capacitances based on predictive optimal and symmetric optimal design parameters for the 30 mV/s design study.

For 75 mV/s supercapacitor design, we fabricated other asymmetric supercapacitors based on the optimal prediction parameters at 6 and 30 mV/s. When selecting the optimal parameters at 6 mV/s to design the supercapacitor for 75 mV/s case design, the design parameters for the positive electrode are the pore size of 0.8 nm, thickness of 110 um. The design parameters for the negative electrode are the pore size of 0.8 nm, thickness of 33 um. The achieved specific volumetric capacitance of the device is 4.3 F/cm^3, which is lower than that of 7.4 F/cm^3. The corresponding specific volumetric capacitance of positive and negative electrodes is around 23.5 and 41 F/cm^3, respectively (**Fig. 5.17c**). When selecting the optimal parameters at 30 mV/s to design the supercapacitor for 75 mV/s case design, the design parameters for the positive electrode are the pore size of 1.25 nm, thickness of 100 um, the design parameters for the negative electrode are the pore size of 0.8 nm, thickness of 22 um. The achieved specific volumetric capacitance of the device is 7.0 F/cm^3, which is lower than that of 7.4 F/cm^3. The corresponding specific volumetric capacitance of positive and negative electrodes are around 36.5 and 96 F/cm^3 respectively.

Additionally, we also fabricated two symmetric supercapacitors based on the predictive design parameters at 75 mV/s. When the symmetric supercapacitor has the pore size of 0.8 nm, thickness of 15 um for both positive and negative electrodes, when charge the supercapacitor, when the potential of the positive electrode reach to 0.8 V (**Fig. 5.17a**), the working voltage of the supercapacitor is around 1.0 V (**Fig. 5.17b**), which is much lower than 1.6 V for the asymmetric design. The achieved specific capacitance of the device is approximately 6.3 F/cm^3, which is also lower than that of the optimal design at 75 mV/s (**Fig. 5.17f**). When the symmetric supercapacitor has the pore size of 1.35 nm, thickness of 73 um for both positive and negative electrodes, when charge the supercapacitor, when the potential of the positive electrode reach to 0.8 V (**Fig. 5.17d**), the working voltage of the supercapacitor is around 1.0 V (**Fig. 5.17e**), which is much lower than that of 1.6 V for the asymmetric design. The achieved specific capacitance of the device is around 7 F/cm^3, which is close to the optimal design capacitance at 75 mV/s (**Fig. 5.17f**).

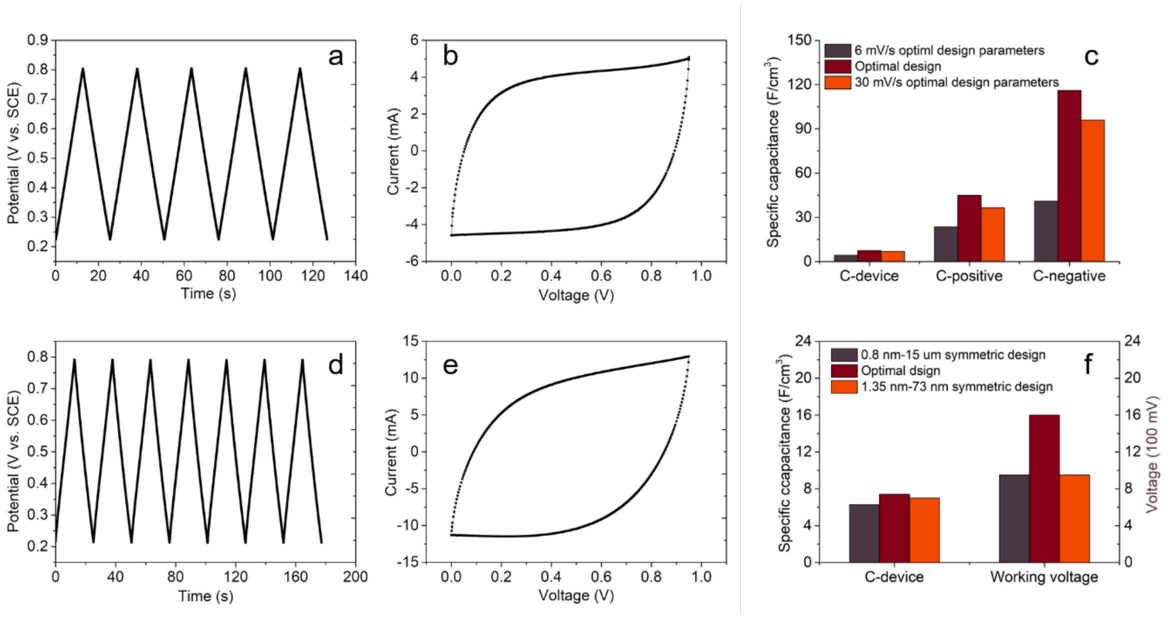

Figure 5.17. **(a)** and **(b)** are the experiment potential-time curve of the positive electrode and experiment CV curve of graphene-based supercapacitor device for the symmetric design with pore size

of 0.8 nm, thickness of 15 um for both positive and negative electrodes at the scan rate of 75 mV/s; **(c)** the experiment capacitances based on predictive optimal and 6 and 30 mV/s optimal design parameters for the 75 mV/s design study; **(d)** and **(e)** are the experiment potential-time curves of the positive electrodes and experiment CV curves of graphene-based supercapacitor devices for the symmetric design with pore size of 1.35 nm, thickness of 73 um for both positive and negative electrodes at the scan rate of 75 mV/s; **(f)** the experiment capacitances based on predictive optimal and symmetric optimal design parameters for the 75 mV/s design study.

The other design results further confirm the accuracy of the predictive optimal design parameters of the device. Moreover, these results also show that the optimal design parameters for one charge rate are not able to directly transfer to another charge rate, indicating the necessity of the optimal design based on charge rates and the limitations of the previous design strategies.

5.5.3 Important Design Parameters

Although ANNs can deliver high accuracies in modeling complex data, they are not interpretable. For this reason, we also did the work (supervised by Dr. Benyamin Motevalli from CSIRO, Australia), which is about applying a random forest regressor to define which design parameters are more influential in determining the capacitance. We have fitted a model for each positive and negative electrode as well as the combined supercapacitors. From **Fig. 5.18a** and **b**, we can see the importance of each design parameter in determining the specific volumetric capacitance value of electrodes. As seen in both electrodes, tuning the thickness has the highest effect for capacitance, which is followed by charge rate and pore size. Interestingly, in a positive electrode, the contribution of thickness looks more significant. The correlation matrix of the dataset corresponding to each electrode is also shown in **Fig. 5.18c** and **d**. This matrix shows the correlation intensity between any two dimensions in our dataset. As seen, sampling of charging rates is independent of the two main design parameters. A degree of correlation is observed on how the pore size and thickness were sampled. Meanwhile, the correlation intensity of each design parameter with corresponding capacitance is consistent with extracted feature importance from the random forest.

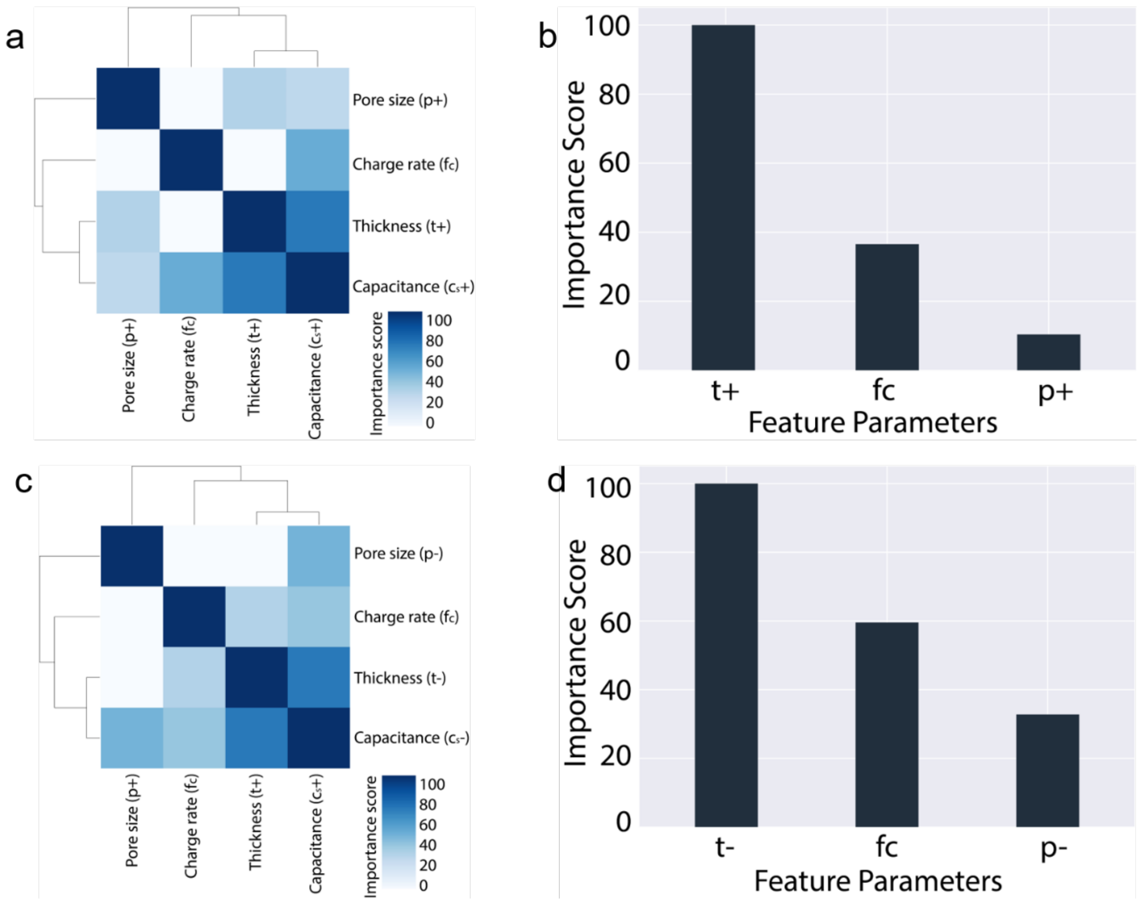

Figure 5.18. Correlation matrix for **(a)** positive and **(c)** negative electrodes; Feature importance for **(b)** positive and **(d)** negative electrodes.

Since the capacitance of a device is obtained from the prediction of our ANN model, we used the prediction dataset to analyze which design parameters are important in defining the device capacitance. In this regard, the random forest is employed to fit a model to the data generated by our ANN model. Then the feature importance is extracted. Due to the abundance of data, the random forest could perfectly fit our ANN predictions (with an R^2-score of ~ 1.0), which indicates that our random forest model could serve as an equivalent of the ANN model. Thus, the feature importance extracted from the random forest is relevant to the ANN model. The distribution of predicted capacitance values is given in **Fig. 5.19a, and d**. The correlation matrix between the device's performance and designing parameters is also revealed (**Fig. 5.19b and e)**. The correlation and feature parameter of the device at low and high charging rates show that the positive electrode plays a decisive role in determining the device capacitance. Interestingly, at a low charge rate for the device, the most important parameter is the pore size of the positive electrode, while when the charge rate increase to 75 mic-volt per second, the most influencing parameter becomes the thickness of the positive electrode (**Fig. 5.19c**, and **f**).

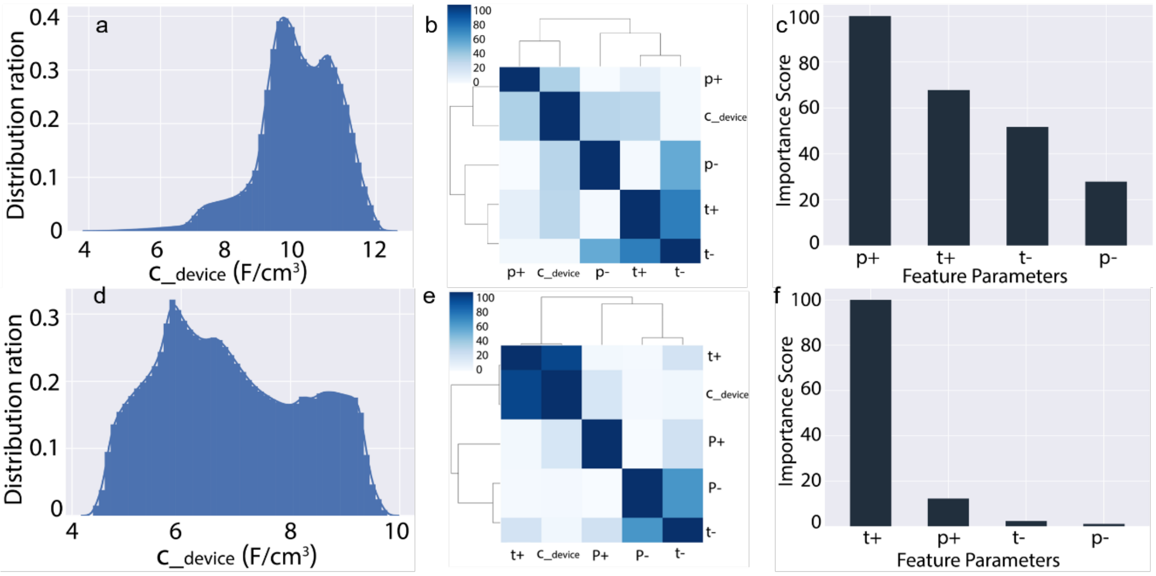

Figure 5.19. **(a)** and **(d)** are the distribution of specific volumetric capacitance of supercapacitor at 6 and 75 mV/s; **(b)** and **(e)** are the correlation matrix among specific volumetric capacitance of supercapacitor and various design parameters at 6 and 75 mV/s; **(c)** and **(f)** are the important level of different design parameters for the final supercapacitor capacitance at the scan rate of 6 and 75 mV/s.

5.6 Conclusions

This work highly indicates and demonstrates that data-driven modeling could be a promising, highly time, and cost-effective route for the electrode performance prediction and device design optimization. We build capacitance prediction models using the obtain 200 sets of experimental datasets to further achieve the optimization and feature parameter determination of graphene-based supercapacitors. For the ANN regression results, we obtain a test error of 0.017% and 0.017% for positive and negative models based on the normalization data. This level of accuracy, combined with our experimental results, demonstrates the reliability of our developed ANN models. The success of the achieved optimal design of the supercapacitor and feature parameters at the device-level further reveal the advantage of a machine learning tool in the design of a complex dynamic device system. Generally, machine learning-assisted on-demand optimal device-level design of supercapacitors is successfully demonstrated. The research presented here could also provide high promising design methodology and strategy for searching the optimal active materials and guiding the practical device design for other complex system fields, such as lithium-ion batteries, electrochemical catalysis, capacitive deionization.

Chapter 6 Conclusions and Perspective

6.1 Conclusions

This PhD thesis has studied the nanoconfinement effects on the electrochemical performance of nanoporous multilayered graphene-based electrodes in various aqueous electrolytes. It also explores the device-level design of the supercapacitor by using the machine learning method. Generally, the followings are the major contribution of this PhD thesis:

(1) The mechanism of ion-specific effect on capacitance depends on the operating condition and working electrodes, such as charging rate, working potential, and electrodes' nanostructure (pore size). The ion-specific adsorption effect could increase the EDL capacitance, especially for the proton adsorption.

(2) The co-ions in the electrolyte could affect the EDL capacitance of the electrodes during charging. The co-ion of proton shows much higher EDL capacitance during the positive polarization. The behind mechanism is the proton adsorption at the open circuit potential.

(3) There is a strong correlation between the interface reaction rate of ions and the slit pore size of the graphene-based electrodes (the electrodes have the same physical and chemical properties except for the slit pore size). For example, without mass-transfer effect, the redox-active ions inside the higher nanoconfined slit pore (1 nm) present a larger interface reaction rate compared to that of the large slit pore (10 nm), which is due to the higher surface ion concentration.

(4) The electrical double layer structure plays an important role in determining the interface reaction rate instead of the catalytic electrode itself. The high compact EDL structure could enhance the interface reaction rate, leading to improve the fast charging ability of electrodes and devices.

(5) The metal deposition performance depends on the slit pore size of the conducting electrodes. The graphene-based electrodes have high coulombic efficiency (more than 98% at 25 mA/cm^2). The electrodes with smaller pore sizes show higher cycling stability. Engineering the pore size of the conductive electrodes has the ability to regulate the nucleation, crystal growth, and charge/discharge reversibility of metal anodes for energy storage.

(6) Data-driven modeling is a promising, highly time, and cost-effective route for the electrode performance prediction and device-level design. The comprehensive quantitative relationship between capacitance and electrode structure is achieved. The optimal device-level design is successfully demonstrated through the combination of experiment and machine learning method.

(7) The optimal design parameters are hard to determine from experiments. The optimal design parameters depend on the charging rate.

In summary, the comprehensive nanoconfinement effect studies on interface electrochemical performance of nanoporous graphene-based materials contribute to the new knowledge and deep understanding of the interface EDL and redox-reaction, which provides solid clues for the establishment of new electrochemical theories under nanoconfinement and offers a new concept/view of designing the electrode-electrolyte system with high charge storage at fast charging rate. Furthermore, the success of the achieved optimal design of the supercapacitor and feature parameters at the device-level reveal the advantage of a machine learning tool in the design of a complex dynamic device system.

6.2 Perspective

The research findings and discussion presented in this PhD thesis indicate the following perspective research worthy to be further studied.

(1) The interface of the electrocatalytic hydrogen evolution reaction remains unclear. The results of proton adsorption on EDL capacitance under nanoconfinement presented in this thesis provide valuable information for the molecular dynamics simulation to reveal the proton/catalyst interface information, guiding the future design of a high efficient electrocatalytic system.

(2) Considering the difficulty and time-consuming of developing new materials with high catalytic performance, the fundamental study about the nanoconfinement effects on the electrochemical catalysis worthy of being studied for providing new theories for guiding the design of a high efficient electrocatalytic system.

(3) The ion effects on the EDL capacitance indicates there is the different ion behaviour under nanoconfinement. In the future, regulating the EDL structure of the ions under

nanoconfinement could be a promising strategy to achieve ion selectivity in the mixture electrolytes.

(4) The cathode electrodes limit the energy density of the lithium-ion battery, which is due to the insufficient ion intercalation. In the future, the study of the nanoconfinement effects on the ion intercalation worthy of being studied for achieving the cathode electrodes with multilayered ion intercalation.

(5) The performance of batteries depends on many parameters (such as pore size, thickness, working potential, charging rates electrolytes, temperature, etc.). In the future, the machine learning method could be applied to identify the importance of each parameter and design the batteries on the device-level.

References

1 Goodenough, J. B. & Park, K. S. The Li-ion rechargeable battery: a perspective. *J Am Chem Soc* **135**, 1167-1176, doi:10.1021/ja3091438 (2013).

2 Dubal, D. P., Ayyad, O., Ruiz, V. & Gomez-Romero, P. Hybrid energy storage: the merging of battery and supercapacitor chemistries. *Chem Soc Rev* **44**, 1777-1790, doi:10.1039/c4cs00266k (2015).

3 Larcher, D. & Tarascon, J. M. Towards greener and more sustainable batteries for electrical energy storage. *Nat Chem* **7**, 19-29, doi:10.1038/nchem.2085 (2015).

4 Lukatskaya, M. R. *et al.* Ultra-high-rate pseudocapacitive energy storage in two-dimensional transition metal carbides. *Nature Energy* **2**, doi:10.1038/nenergy.2017.105 (2017).

5 Cano, Z. P. *et al.* Batteries and fuel cells for emerging electric vehicle markets. *Nature Energy* **3**, 279-289, doi:10.1038/s41560-018-0108-1 (2018).

6 Elouarzaki, K., Cheng, D., Fisher, A. C. & Lee, J.-M. Coupling orientation and mediation strategies for efficient electron transfer in hybrid biofuel cells. *Nature Energy* **3**, 574-581, doi:10.1038/s41560-018-0166-4 (2018).

7 Hollas, A. *et al.* A biomimetic high-capacity phenazine-based anolyte for aqueous organic redox flow batteries. *Nature Energy* **3**, 508-514, doi:10.1038/s41560-018-0167-3 (2018).

8 Stamenkovic, V. R., Strmcnik, D., Lopes, P. P. & Markovic, N. M. Energy and fuels from electrochemical interfaces. *Nat Mater* **16**, 57-69, doi:10.1038/nmat4738 (2016).

9 Lukatskaya, M. R., Dunn, B. & Gogotsi, Y. Multidimensional materials and device architectures for future hybrid energy storage. *Nature Communications* **7**, doi:10.1038/ncomms12647 (2016).

10 Anasori, B., Lukatskaya, M. R. & Gogotsi, Y. 2D metal carbides and nitrides (MXenes) for energy storage. *Nature Reviews Materials* **2**, doi:10.1038/natrevmats.2016.98 (2017).

11 Luo, B., Ye, D. & Wang, L. Recent Progress on Integrated Energy Conversion and Storage Systems. *Adv Sci (Weinh)* **4**, 1700104, doi:10.1002/advs.201700104 (2017).

12 Choi, J. W. & Aurbach, D. Promise and reality of post-lithium-ion batteries with high energy densities. *Nature Reviews Materials* **1**, doi:10.1038/natrevmats.2016.13 (2016).

13 El-Kady, M. F., Shao, Y. & Kaner, R. B. Graphene for batteries, supercapacitors and beyond. *Nature Reviews Materials* **1**, doi:10.1038/natrevmats.2016.33 (2016).

14 Li, W., Liu, J. & Zhao, D. Mesoporous materials for energy conversion and storage devices. *Nature Reviews Materials* **1**, doi:10.1038/natrevmats.2016.23 (2016).

15 Sheberla, D. *et al.* Conductive MOF electrodes for stable supercapacitors with high areal capacitance. *Nat Mater* **16**, 220-224, doi:10.1038/nmat4766 (2017).

16 Bruce, P. G., Freunberger, S. A., Hardwick, L. J. & Tarascon, J. M. Li-O2 and Li-S batteries with high energy storage. *Nat Mater* **11**, 19-29, doi:10.1038/nmat3191 (2011).

17 Simon, P. & Gogotsi, Y. in *Nanoscience and technology: a collection of reviews from Nature journals* 320-329 (World Scientific, 2010).

18 Choi, N. S. *et al.* Challenges facing lithium batteries and electrical double-layer capacitors. *Angew Chem Int Ed Engl* **51**, 9994-10024, doi:10.1002/anie.201201429 (2012).

19 Salanne, M. *et al.* Efficient storage mechanisms for building better supercapacitors. *Nature Energy* **1**, doi:10.1038/nenergy.2016.70 (2016).

20 Wang, F. *et al.* Latest advances in supercapacitors: from new electrode materials to novel device designs. *Chem Soc Rev* **46**, 6816-6854, doi:10.1039/c7cs00205j (2017).

21 Lin, Z. *et al.* Materials for supercapacitors: When Li-ion battery power is not enough. *Materials Today* **21**, 419-436, doi:10.1016/j.mattod.2018.01.035 (2018).

22 Liu, C. *et al.* Toward Superior Capacitive Energy Storage: Recent Advances in Pore Engineering for Dense Electrodes. *Adv Mater* **30**, e1705713, doi:10.1002/adma.201705713 (2018).

23 Shao, Y. *et al.* Design and Mechanisms of Asymmetric Supercapacitors. *Chem Rev* **118**, 9233-9280, doi:10.1021/acs.chemrev.8b00252 (2018).

24 Noori, A., El-Kady, M. F., Rahmanifar, M. S., Kaner, R. B. & Mousavi, M. F. Towards establishing standard performance metrics for batteries, supercapacitors and beyond. *Chem Soc Rev* **48**, 1272-1341, doi:10.1039/c8cs00581h (2019).

25 Ghidiu, M., Lukatskaya, M. R., Zhao, M. Q., Gogotsi, Y. & Barsoum, M. W. Conductive two-dimensional titanium carbide 'clay' with high volumetric capacitance. *Nature* **516**, 78-81, doi:10.1038/nature13970 (2014).

26 Wang, K. *et al.* Lithium-antimony-lead liquid metal battery for grid-level energy storage. *Nature* **514**, 348-350, doi:10.1038/nature13700 (2014).

27 Huskinson, B. *et al.* A metal-free organic-inorganic aqueous flow battery. *Nature* **505**, 195-198, doi:10.1038/nature12909 (2014).

28 Kang, B. & Ceder, G. Battery materials for ultrafast charging and discharging. *Nature* **458**, 190-193, doi:10.1038/nature07853 (2009).

29 Gogotsi, Y. & Simon, P. True performance metrics in electrochemical energy storage. *Science* **334**, 917-918 (2011).

30 Xu, F. *et al.* Facile synthesis of ultrahigh-surface-area hollow carbon nanospheres for enhanced adsorption and energy storage. *Nat Commun* **6**, 7221, doi:10.1038/ncomms8221 (2015).

31 Molinari, A. *et al.* Hybrid supercapacitors for reversible control of magnetism. *Nat Commun* **8**, 15339, doi:10.1038/ncomms15339 (2017).

32 Peng, L. *et al.* Holey two-dimensional transition metal oxide nanosheets for efficient energy storage. *Nat Commun* **8**, 15139, doi:10.1038/ncomms15139 (2017).

33 Son, I. H. *et al.* Graphene balls for lithium rechargeable batteries with fast charging and high volumetric energy densities. *Nat Commun* **8**, 1561, doi:10.1038/s41467-017-01823-7 (2017).

34 Cong, G., Wang, W., Lai, N. C., Liang, Z. & Lu, Y. C. A high-rate and long-life organic-oxygen battery. *Nat Mater* **18**, 390-396, doi:10.1038/s41563-019-0286-7 (2019).

35 Ponrouch, A., Frontera, C., Barde, F. & Palacin, M. R. Towards a calcium-based rechargeable battery. *Nat Mater* **15**, 169-172, doi:10.1038/nmat4462 (2016).

36 Sun, Y., Liu, N. & Cui, Y. Promises and challenges of nanomaterials for lithium-based rechargeable batteries. *Nature Energy* **1**, doi:10.1038/nenergy.2016.71 (2016).

37 Pomerantseva, E. & Gogotsi, Y. Two-dimensional heterostructures for energy storage. *Nature Energy* **2**, doi:10.1038/nenergy.2017.89 (2017).

38 Bae, J. H., Han, J. H. & Chung, T. D. Electrochemistry at nanoporous interfaces: new opportunity for electrocatalysis. *Phys Chem Chem Phys* **14**, 448-463, doi:10.1039/c1cp22927c (2012).

39 Bae, J. H., Han, J. H., Han, D. & Chung, T. D. Effects of adsorption and confinement on nanoporous electrochemistry. *Faraday Discuss* **164**, 361-376, doi:10.1039/c3fd00014a (2013).

40 Li, Z. *et al.* Confinement Effects on an Electron Transfer Reaction in Nanoporous Carbon Electrodes. *J Phys Chem Lett* **8**, 1925-1931, doi:10.1021/acs.jpclett.7b00458 (2017).

41 Seo, M. & Chung, T. D. Nanoconfinement effects in electrochemical reactions. *Current Opinion in Electrochemistry* **13**, 47-54, doi:10.1016/j.coelec.2018.10.011 (2019).

42 Fichtner, M. Nanoconfinement effects in energy storage materials. *Phys Chem Chem Phys* **13**, 21186-21195, doi:10.1039/c1cp22547b (2011).

43 Augustyn, V. & Gogotsi, Y. 2D Materials with Nanoconfined Fluids for Electrochemical Energy Storage. *Joule* **1**, 443-452, doi:10.1016/j.joule.2017.09.008 (2017).

44 Lee, J. *et al.* Nanoconfinement of redox reactions enables rapid zinc iodide energy storage with high efficiency. *Journal of Materials Chemistry A* **5**, 12520-12527, doi:10.1039/c7ta03589f (2017).

45 Sun, Y. *et al.* Proton Redox and Transport in MXene-Confined Water. *ACS Appl Mater Interfaces* **12**, 763-770, doi:10.1021/acsami.9b18139 (2020).

46 Cheng, C., Jiang, G., Simon, G. P., Liu, J. Z. & Li, D. Low-voltage electrostatic modulation of ion diffusion through layered graphene-based nanoporous membranes. *Nat Nanotechnol* **13**, 685-690, doi:10.1038/s41565-018-0181-4 (2018).

47 Yang, X., Cheng, C., Wang, Y., Qiu, L. & Li, D. Liquid-mediated dense integration of graphene materials for compact capacitive energy storage. *science* **341**, 534-537 (2013).

48 Merlet, C. *et al.* Highly confined ions store charge more efficiently in supercapacitors. *Nat Commun* **4**, 2701, doi:10.1038/ncomms3701 (2013).

49 Borchardt, L., Oschatz, M. & Kaskel, S. Tailoring porosity in carbon materials for supercapacitor applications. *Mater. Horiz.* **1**, 157-168, doi:10.1039/c3mh00112a (2014).

50 Gogotsi, Y. *et al.* Carbon electrodes for energy storage: general discussion. *Faraday Discuss* **172**, 239-260, doi:10.1039/C4FD90026J (2014).

51 Kondrat, S., Wu, P., Qiao, R. & Kornyshev, A. A. Accelerating charging dynamics in subnanometre pores. *Nat Mater* **13**, 387-393, doi:10.1038/nmat3916 (2014).

52 Pean, C. *et al.* Confinement, Desolvation, And Electrosorption Effects on the Diffusion of Ions in Nanoporous Carbon Electrodes. *J Am Chem Soc* **137**, 12627-12632, doi:10.1021/jacs.5b07416 (2015).

53 Futamura, R. *et al.* Partial breaking of the Coulombic ordering of ionic liquids confined in carbon nanopores. *Nat Mater* **16**, 1225-1232, doi:10.1038/nmat4974 (2017).

54 Zhan, C. *et al.* Specific ion effects at graphitic interfaces. *Nat Commun* **10**, 4858, doi:10.1038/s41467-019-12854-7 (2019).

55 Choudhary, N. *et al.* Asymmetric Supercapacitor Electrodes and Devices. *Adv Mater* **29**, doi:10.1002/adma.201605336 (2017).

56 Wang, L., Morishita, T., Toyoda, M. & Inagaki, M. Asymmetric electric double layer capacitors using carbon electrodes with different pore size distributions. *Electrochimica Acta* **53**, 882-886, doi:10.1016/j.electacta.2007.07.069 (2007).

57 Wen, Y., Cheng, J., Cao, G. & Yang, Y. Matching ratio between positive and negative electrodes for double-layer capacitors. *Journal of Applied Electrochemistry* **37**, 543-548, doi:10.1007/s10800-006-9244-6 (2007).

58 Li, J. & Gao, F. Analysis of electrodes matching for asymmetric electrochemical capacitor. *Journal of Power Sources* **194**, 1184-1193, doi:10.1016/j.jpowsour.2009.06.017 (2009).

59 Peng, C., Zhang, S., Zhou, X. & Chen, G. Z. Unequalisation of electrode capacitances for enhanced energy capacity in asymmetrical supercapacitors. *Energy & Environmental Science* **3**, 1499, doi:10.1039/c0ee00228c (2010).

60 Sun, G. *et al.* Capacitive matching of pore size and ion size in the negative and positive electrodes for supercapacitors. *Electrochimica Acta* **56**, 9248-9256, doi:10.1016/j.electacta.2011.07.139 (2011).

61 Bocquet, L. & Tabeling, P. Physics and technological aspects of nanofluidics. *Lab Chip* **14**, 3143-3158, doi:10.1039/c4lc00325j (2014).

62 Raccichini, R., Varzi, A., Passerini, S. & Scrosati, B. The role of graphene for electrochemical energy storage. *Nat Mater* **14**, 271-279, doi:10.1038/nmat4170 (2015).

63 Bocquet, L. & Charlaix, E. Nanofluidics, from bulk to interfaces. *Chem Soc Rev* **39**, 1073-1095, doi:10.1039/b909366b (2010).

64 Duan, C. & Majumdar, A. Anomalous ion transport in 2-nm hydrophilic nanochannels. *Nat Nanotechnol* **5**, 848-852, doi:10.1038/nnano.2010.233 (2010).

65 Sparreboom, W., van den Berg, A. & Eijkel, J. C. T. Transport in nanofluidic systems: a review of theory and applications. *New Journal of Physics* **12**, 015004, doi:10.1088/1367-2630/12/1/015004 (2010).

66 Beu, T. A. Molecular dynamics simulations of ion transport through carbon nanotubes. III. Influence of the nanotube radius, solute concentration, and applied electric fields on the transport properties. *J Chem Phys* **135**, 044516, doi:10.1063/1.3615728 (2011).

67 Siwy, Z. S. & Howorka, S. Engineered voltage-responsive nanopores. *Chem Soc Rev* **39**, 1115-1132, doi:10.1039/b909105j (2010).

68 Zangle, T. A., Mani, A. & Santiago, J. G. Theory and experiments of concentration polarization and ion focusing at microchannel and nanochannel interfaces. *Chem Soc Rev* **39**, 1014-1035, doi:10.1039/b902074h (2010).

69 Daiguji, H. Ion transport in nanofluidic channels. *Chemical Society Reviews* **39**, 901-911 (2010).

70 Jiang, G., Cheng, C., Li, D. & Liu, J. Z. Molecular dynamics simulations of the electric double layer capacitance of graphene electrodes in mono-valent aqueous electrolytes. *Nano Research* **9**, 174-186, doi:10.1007/s12274-015-0978-5 (2016).

71 Maier, J. Nanoionics: size effects and storage in small systems. *Journal of Electroceramics* **34**, 69-73, doi:10.1007/s10832-013-9886-9 (2013).

72 Yeh, L. H., Zhang, M. & Qian, S. Ion transport in a pH-regulated nanopore. *Anal Chem* **85**, 7527-7534, doi:10.1021/ac401536g (2013).

73 Barry, E., McBride, S. P., Jaeger, H. M. & Lin, X. M. Ion transport controlled by nanoparticle-functionalized membranes. *Nat Commun* **5**, 5847, doi:10.1038/ncomms6847 (2014).

74 Lee, J., Laoui, T. & Karnik, R. Nanofluidic transport governed by the liquid/vapour interface. *Nat Nanotechnol* **9**, 317-323, doi:10.1038/nnano.2014.28 (2014).

75 Choi, W., Chun, K.-Y., Kim, J. & Han, C.-S. Ion transport through thermally reduced and mechanically stretched graphene oxide membrane. *Carbon* **114**, 377-382, doi:10.1016/j.carbon.2016.12.041 (2017).

76 Gao, J., Feng, Y., Guo, W. & Jiang, L. Nanofluidics in two-dimensional layered materials: inspirations from nature. *Chem Soc Rev* **46**, 5400-5424, doi:10.1039/c7cs00369b (2017).

77 Chmiola, J., Largeot, C., Taberna, P. L., Simon, P. & Gogotsi, Y. Desolvation of ions in subnanometer pores and its effect on capacitance and double-layer theory. *Angew Chem Int Ed Engl* **47**, 3392-3395, doi:10.1002/anie.200704894 (2008).

78 Zhang, H., Cao, G., Yang, Y. & Gu, Z. Capacitive performance of an ultralong aligned carbon nanotube electrode in an ionic liquid at 60°C. *Carbon* **46**, 30-34, doi:10.1016/j.carbon.2007.10.023 (2008).

79 Daffos, B., Taberna, P. L., Gogotsi, Y. & Simon, P. Recent Advances in Understanding the Capacitive Storage in Microporous Carbons. *Fuel Cells* **10**, 819-824, doi:10.1002/fuce.200900192 (2010).

80 Eliad, L., Salitra, G., Soffer, A. & Aurbach, D. Ion sieving effects in the electrical double layer of porous carbon electrodes: estimating effective ion size in electrolytic solutions. *The Journal of Physical Chemistry B* **105**, 6880-6887 (2001).

81 Levi, M. D., Sigalov, S., Salitra, G., Aurbach, D. & Maier, J. The effect of specific adsorption of cations and their size on the charge-compensation mechanism in carbon micropores: the role of anion desorption. *Chemphyschem* **12**, 854-862, doi:10.1002/cphc.201000653 (2011).

82 Brown, M. A., Goel, A. & Abbas, Z. Effect of Electrolyte Concentration on the Stern Layer Thickness at a Charged Interface. *Angew Chem Int Ed Engl* **55**, 3790-3794, doi:10.1002/anie.201512025 (2016).

83 Forse, A. C., Merlet, C., Griffin, J. M. & Grey, C. P. New Perspectives on the Charging Mechanisms of Supercapacitors. *J Am Chem Soc* **138**, 5731-5744, doi:10.1021/jacs.6b02115 (2016).

84 Lian, C. *et al.* Enhancing the Capacitive Performance of Electric Double-Layer Capacitors with Ionic Liquid Mixtures. *ACS Energy Letters* **1**, 21-26, doi:10.1021/acsenergylett.6b00010 (2016).

85 Neal, J. N., Wesolowski, D. J., Henderson, D. & Wu, J. Electric double layer capacitance for ionic liquids in nanoporous electrodes: Effects of pore size and ion composition. *Journal of Molecular Liquids* **270**, 145-150, doi:10.1016/j.molliq.2017.10.128 (2018).

86 Feng, G. *et al.* The importance of ion size and electrode curvature on electrical double layers in ionic liquids. *Phys Chem Chem Phys* **13**, 1152-1161, doi:10.1039/c0cp02077j (2011).

87 Vatamanu, J., Borodin, O. & Smith, G. D. Molecular simulations of the electric double layer structure, differential capacitance, and charging kinetics for N-methyl-N-propylpyrrolidinium bis(fluorosulfonyl)imide at graphite electrodes. *J Phys Chem B* **115**, 3073-3084, doi:10.1021/jp2001207 (2011).

88 Deschamps, M. *et al.* Exploring electrolyte organization in supercapacitor electrodes with solid-state NMR. *Nat Mater* **12**, 351-358, doi:10.1038/nmat3567 (2013).

89 Presser, V., McDonough, J., Yeon, S.-H. & Gogotsi, Y. Effect of pore size on carbon dioxide sorption by carbide derived carbon. *Energy & Environmental Science* **4**, 3059, doi:10.1039/c1ee01176f (2011).

90 Segalini, J., Daffos, B., Taberna, P. L., Gogotsi, Y. & Simon, P. Qualitative Electrochemical Impedance Spectroscopy study of ion transport into sub-nanometer carbon pores in Electrochemical Double Layer Capacitor electrodes. *Electrochimica Acta* **55**, 7489-7494, doi:10.1016/j.electacta.2010.01.003 (2010).

91 Van Aken, K. L., Beidaghi, M. & Gogotsi, Y. Formulation of ionic-liquid electrolyte to expand the voltage window of supercapacitors. *Angew Chem Int Ed Engl* **54**, 4806-4809, doi:10.1002/anie.201412257 (2015).

92 Yuyama, K., Masuda, G., Yoshida, H. & Sato, T. Ionic liquids containing the tetrafluoroborate anion have the best performance and stability for electric double layer capacitor applications. *Journal of Power Sources* **162**, 1401-1408, doi:10.1016/j.jpowsour.2006.09.002 (2006).

93 Kalluri, R. K. *et al.* Unraveling the potential and pore-size dependent capacitance of slit-shaped graphitic carbon pores in aqueous electrolytes. *Phys Chem Chem Phys* **15**, 2309-2320, doi:10.1039/c2cp43361c (2013).

94 Beguin, F., Presser, V., Balducci, A. & Frackowiak, E. Carbons and electrolytes for advanced supercapacitors. *Adv Mater* **26**, 2219-2251, 2283, doi:10.1002/adma.201304137 (2014).

95 Liu, Y., Zhao, T., Ju, W. & Shi, S. Materials discovery and design using machine learning. *Journal of Materiomics* **3**, 159-177, doi:10.1016/j.jmat.2017.08.002 (2017).

96 Menon, A. *et al.* Elucidating multi-physics interactions in suspensions for the design of polymeric dispersants: a hierarchical machine learning approach. *Molecular Systems Design & Engineering* **2**, 263-273, doi:10.1039/c7me00027h (2017).

97 Wu, B., Han, S., Shin, K. G. & Lu, W. Application of artificial neural networks in design of lithium-ion batteries. *Journal of Power Sources* **395**, 128-136, doi:10.1016/j.jpowsour.2018.05.040 (2018).

98 Zhu, S. *et al.* Artificial neural network enabled capacitance prediction for carbon-based supercapacitors. *Materials Letters* **233**, 294-297, doi:10.1016/j.matlet.2018.09.028 (2018).

99 Gu, G. H., Noh, J., Kim, I. & Jung, Y. Machine learning for renewable energy materials. *Journal of Materials Chemistry A* **7**, 17096-17117, doi:10.1039/c9ta02356a (2019).

100 Kauwe, S., Rhone, T. & Sparks, T. Data-Driven Studies of Li-Ion-Battery Materials. *Crystals* **9**, 54, doi:10.3390/cryst9010054 (2019).

101 Severson, K. A. *et al.* Data-driven prediction of battery cycle life before capacity degradation. *Nature Energy* **4**, 383-391, doi:10.1038/s41560-019-0356-8 (2019).

102 Cheng, C. *et al.* Ion transport in complex layered graphene-based membranes with tuneable interlayer spacing. *Science advances* **2**, e1501272 (2016).

103 Zhan, H. *et al.* Solvation‐Involved Nanoionics: New Opportunities from 2D Nanomaterial Laminar Membranes. *Advanced Materials*, 1904562 (2019).

104 Pan, X. & Bao, X. Reactions over catalysts confined in carbon nanotubes. *Chem Commun (Camb)*, 6271-6281, doi:10.1039/b810994j (2008).

105 Pan, X. *et al.* Enhanced ethanol production inside carbon-nanotube reactors containing catalytic particles. *Nat Mater* **6**, 507-511, doi:10.1038/nmat1916 (2007).

106 Pan, X. & Bao, X. The effects of confinement inside carbon nanotubes on catalysis. *Accounts of chemical research* **44**, 553-562 (2011).

107 Li, H., Xiao, J., Fu, Q. & Bao, X. Confined catalysis under two-dimensional materials. *Proceedings of the National Academy of Sciences* **114**, 5930-5934 (2017).

108 Noked, M., Soffer, A. & Aurbach, D. The electrochemistry of activated carbonaceous materials: past, present, and future. *Journal of Solid State Electrochemistry* **15**, 1563-1578, doi:10.1007/s10008-011-1411-y (2011).

109 Sigalov, S. *et al.* Selective adsorption of multivalent ions into TiC-derived nanoporous carbon. *Carbon* **50**, 3957-3960, doi:10.1016/j.carbon.2012.04.002 (2012).

110 Levi, M. D., Sigalov, S., Aurbach, D. & Daikhin, L. In Situ Electrochemical Quartz Crystal Admittance Methodology for Tracking Compositional and Mechanical Changes in Porous Carbon Electrodes. *The Journal of Physical Chemistry C* **117**, 14876-14889, doi:10.1021/jp403065y (2013).

111 Dash, R. *et al.* Titanium carbide derived nanoporous carbon for energy-related applications. *Carbon* **44**, 2489-2497, doi:10.1016/j.carbon.2006.04.035 (2006).

112 Raymundo-Piñero, E., Kierzek, K., Machnikowski, J. & Béguin, F. Relationship between the nanoporous texture of activated carbons and their capacitance properties in different electrolytes. *Carbon* **44**, 2498-2507, doi:10.1016/j.carbon.2006.05.022 (2006).

113 Pech, D. *et al.* Ultrahigh-power micrometre-sized supercapacitors based on onion-like carbon. *Nat Nanotechnol* **5**, 651-654, doi:10.1038/nnano.2010.162 (2010).

114 Luo, G. *et al.* Hole defects and nitrogen doping in graphene: implication for supercapacitor applications. *ACS Appl Mater Interfaces* **5**, 11184-11193, doi:10.1021/am403427h (2013).

115 Augustyn, V., Simon, P. & Dunn, B. Pseudocapacitive oxide materials for high-rate electrochemical energy storage. *Energy & Environmental Science* **7**, 1597, doi:10.1039/c3ee44164d (2014).

116 Evanko, B., Boettcher, S. W., Yoo, S. J. & Stucky, G. D. Redox-Enhanced Electrochemical Capacitors: Status, Opportunity, and Best Practices for Performance Evaluation. *ACS Energy Letters* **2**, 2581-2590, doi:10.1021/acsenergylett.7b00828 (2017).

117 Dyatkin, B. & Gogotsi, Y. Effects of structural disorder and surface chemistry on electric conductivity and capacitance of porous carbon electrodes. *Faraday Discuss* **172**, 139-162, doi:10.1039/c4fd00048j (2014).

118 Hao, G.-P. *et al.* Design of Hierarchically Porous Carbons with Interlinked Hydrophilic and Hydrophobic Surface and Their Capacitive Behavior. *Chemistry of Materials* **28**, 8715-8725, doi:10.1021/acs.chemmater.6b03964 (2016).

119 Chmiola, J. *et al.* Anomalous increase in carbon capacitance at pore sizes less than 1 nanometer. *science* **313**, 1760-1763 (2006).

120 Kim, Y. J. *et al.* Correlation between the pore and solvated ion size on capacitance uptake of PVDC-based carbons. *Carbon* **42**, 1491-1500, doi:10.1016/j.carbon.2004.01.049 (2004).

121 Eliad, L. *et al.* Assessing optimal pore-to-ion size relations in the design of porous poly(vinylidene chloride) carbons for EDL capacitors. *Applied Physics A* **82**, 607-613, doi:10.1007/s00339-005-3440-9 (2005).

122 Heon, M. *et al.* Continuous carbide-derived carbon films with high volumetric capacitance. *Energy Environ. Sci.* **4**, 135-138, doi:10.1039/c0ee00404a (2011).

123 Sillars, F. B., Fletcher, S. I., Mirzaeian, M. & Hall, P. J. Effect of activated carbon xerogel pore size on the capacitance performance of ionic liquid electrolytes. *Energy Environ. Sci.* **4**, 695-706, doi:10.1039/c0ee00337a (2011).

124 Jäckel, N., Simon, P., Gogotsi, Y. & Presser, V. Increase in Capacitance by Subnanometer Pores in Carbon. *ACS Energy Letters* **1**, 1262-1265, doi:10.1021/acsenergylett.6b00516 (2016).

125 Kondrat, S. & Kornyshev, A. A. Pressing a spring: what does it take to maximize the energy storage in nanoporous supercapacitors? *Nanoscale Horizons* **1**, 45-52, doi:10.1039/c5nh00004a (2016).

126 Cheng, C., Uhe, J., Yang, X., Wu, Y. & Li, D. Multilayered graphene membrane as an experimental platform to probe nano-confined electrosorption. *Progress in Natural Science: Materials International* **22**, 668-672, doi:10.1016/j.pnsc.2012.11.002 (2012).

127 Segalini, J., Iwama, E., Taberna, P.-L., Gogotsi, Y. & Simon, P. Steric effects in adsorption of ions from mixed electrolytes into microporous carbon. *Electrochemistry Communications* **15**, 63-65, doi:10.1016/j.elecom.2011.11.023 (2012).

128 Dou, Q., Liu, L., Yang, B., Lang, J. & Yan, X. Silica-grafted ionic liquids for revealing the respective charging behaviors of cations and anions in supercapacitors. *Nat Commun* **8**, 2188, doi:10.1038/s41467-017-02152-5 (2017).

129 Banda, H. *et al.* Ion Sieving Effects in Chemically Tuned Pillared Graphene Materials for Electrochemical Capacitors. *Chemistry of Materials* **30**, 3040-3047, doi:10.1021/acs.chemmater.8b00759 (2018).

130 Pal, B., Yang, S., Ramesh, S., Thangadurai, V. & Jose, R. Electrolyte selection for supercapacitive devices: a critical review. *Nanoscale Advances* **1**, 3807-3835, doi:10.1039/c9na00374f (2019).

131 Wang, H. *et al.* Real-time NMR studies of electrochemical double-layer capacitors. *J Am Chem Soc* **133**, 19270-19273, doi:10.1021/ja2072115 (2011).

132 Richey, F. W., Dyatkin, B., Gogotsi, Y. & Elabd, Y. A. Ion dynamics in porous carbon electrodes in supercapacitors using in situ infrared spectroelectrochemistry. *J Am Chem Soc* **135**, 12818-12826, doi:10.1021/ja406120e (2013).

133 Wang, H. *et al.* In situ NMR spectroscopy of supercapacitors: insight into the charge storage mechanism. *J Am Chem Soc* **135**, 18968-18980, doi:10.1021/ja410287s (2013).

134 Zhong, Y. X. *et al.* Resolving fine structures of the electric double layer of electrochemical interfaces in ionic liquids with an AFM tip modification strategy. *J Am Chem Soc* **136**, 14682-14685, doi:10.1021/ja508222m (2014).

135 Griffin, J. M. *et al.* In situ NMR and electrochemical quartz crystal microbalance techniques reveal the structure of the electrical double layer in supercapacitors. *Nat Mater* **14**, 812-819, doi:10.1038/nmat4318 (2015).

136 Prehal, C. *et al.* Tracking the structural arrangement of ions in carbon supercapacitor nanopores using in situ small-angle X-ray scattering. *Energy & Environmental Science* **8**, 1725-1735, doi:10.1039/c5ee00488h (2015).

137 Chu, M., Miller, M. & Dutta, P. Crowding and Anomalous Capacitance at an Electrode-Ionic Liquid Interface Observed Using Operando X-ray Scattering. *ACS Cent Sci* **2**, 175-180, doi:10.1021/acscentsci.6b00014 (2016).

138 Shpigel, N. *et al.* In situ hydrodynamic spectroscopy for structure characterization of porous energy storage electrodes. *Nat Mater* **15**, 570-575, doi:10.1038/nmat4577 (2016).

139 Forse, Alexander C. *et al.* Direct observation of ion dynamics in supercapacitor electrodes using in situ diffusion NMR spectroscopy. *Nature Energy* **2**, doi:10.1038/nenergy.2016.216 (2017).

140 Prehal, C. *et al.* Quantification of ion confinement and desolvation in nanoporous carbon supercapacitors with modelling and in situ X-ray scattering. *Nature Energy* **2**, doi:10.1038/nenergy.2016.215 (2017).

141 Burt, R. *et al.* Capacitance of Nanoporous Carbon-Based Supercapacitors Is a Trade-Off between the Concentration and the Separability of the Ions. *J Phys Chem Lett* **7**, 4015-4021, doi:10.1021/acs.jpclett.6b01787 (2016).

142 Merlet, C., Rotenberg, B., Madden, P. A. & Salanne, M. Computer simulations of ionic liquids at electrochemical interfaces. *Phys Chem Chem Phys* **15**, 15781-15792, doi:10.1039/c3cp52088a (2013).

143 Merlet, C., Salanne, M., Rotenberg, B. & Madden, P. A. Influence of solvation on the structural and capacitive properties of electrical double layer capacitors. *Electrochimica Acta* **101**, 262-271, doi:10.1016/j.electacta.2012.12.107 (2013).

144 Li, Z., Jeanmairet, G., Méndez-Morales, T., Rotenberg, B. & Salanne, M. Capacitive Performance of Water-in-Salt Electrolytes in Supercapacitors: A Simulation Study. *The Journal of Physical Chemistry C* **122**, 23917-23924, doi:10.1021/acs.jpcc.8b07557 (2018).

145 Li, Z., Mendez-Morales, T. & Salanne, M. Computer simulation studies of nanoporous carbon-based electrochemical capacitors. *Current Opinion in Electrochemistry* **9**, 81-86, doi:10.1016/j.coelec.2018.04.007 (2018).

146 Mendez-Morales, T., Burbano, M., Haefele, M., Rotenberg, B. & Salanne, M. Ion-ion correlations across and between electrified graphene layers. *J Chem Phys* **148**, 193812, doi:10.1063/1.5012761 (2018).

147 Zhu, Y., Gao, T., Fan, X., Han, F. & Wang, C. Electrochemical Techniques for Intercalation Electrode Materials in Rechargeable Batteries. *Acc Chem Res* **50**, 1022-1031, doi:10.1021/acs.accounts.7b00031 (2017).

148 Nitta, N., Wu, F., Lee, J. T. & Yushin, G. Li-ion battery materials: present and future. *Materials Today* **18**, 252-264, doi:10.1016/j.mattod.2014.10.040 (2015).

149 Wang, Y. *et al.* Emerging non-lithium ion batteries. *Energy Storage Materials* **4**, 103-129, doi:10.1016/j.ensm.2016.04.001 (2016).

150 Brezesinski, T., Wang, J., Tolbert, S. H. & Dunn, B. Ordered mesoporous alpha-MoO3 with iso-oriented nanocrystalline walls for thin-film pseudocapacitors. *Nat Mater* **9**, 146-151, doi:10.1038/nmat2612 (2010).

151 Feng, J. *et al.* Metallic few-layered VS2 ultrathin nanosheets: high two-dimensional conductivity for in-plane supercapacitors. *J Am Chem Soc* **133**, 17832-17838, doi:10.1021/ja207176c (2011).

152 Augustyn, V. *et al.* High-rate electrochemical energy storage through Li+ intercalation pseudocapacitance. *Nat Mater* **12**, 518-522, doi:10.1038/nmat3601 (2013).

153 Li, X. *et al.* High energy flexible supercapacitors formed via bottom-up infilling of gel electrolytes into thick porous electrodes. *Nat Commun* **9**, 2578, doi:10.1038/s41467-018-04937-8 (2018).

154 Feng, N. *et al.* A polymer-direct-intercalation strategy for MoS2/carbon-derived heteroaerogels with ultrahigh pseudocapacitance. *Nat Commun* **10**, 1372, doi:10.1038/s41467-019-09384-7 (2019).

155 Lukatskaya, M. R. *et al.* Cation intercalation and high volumetric capacitance of two-dimensional titanium carbide. *Science* **341**, 1502-1505 (2013).

156 Acerce, M., Voiry, D. & Chhowalla, M. Metallic 1T phase MoS2 nanosheets as supercapacitor electrode materials. *Nat Nanotechnol* **10**, 313-318, doi:10.1038/nnano.2015.40 (2015).

157 Mourad, E. *et al.* Biredox ionic liquids with solid-like redox density in the liquid state for high-energy supercapacitors. *Nat Mater* **16**, 446-453, doi:10.1038/nmat4808 (2017).

158 Weng, Z., Li, F., Wang, D. W., Wen, L. & Cheng, H. M. Controlled electrochemical charge injection to maximize the energy density of supercapacitors. *Angew Chem Int Ed Engl* **52**, 3722-3725, doi:10.1002/anie.201209259 (2013).

159 Wu, T.-H., Hsu, C.-T., Hu, C.-C. & Hardwick, L. J. Important parameters affecting the cell voltage of aqueous electrical double-layer capacitors. *Journal of Power Sources* **242**, 289-298, doi:10.1016/j.jpowsour.2013.05.080 (2013).

160 Wang, L., Toyoda, M. & Inagaki, M. Performance of asymmetric electric double layer capacitors—predominant contribution of the negative electrode. *Adsorption Science & Technology* **26**, 491-500 (2008).

161 Zhan, C. *et al.* Computational Insights into Materials and Interfaces for Capacitive Energy Storage. *Adv Sci (Weinh)* **4**, 1700059, doi:10.1002/advs.201700059 (2017).

162 Quesada-Perez, M., Martin-Molina, A. & Hidalgo-Alvarez, R. Simulation of electric double layers with multivalent counterions: ion size effect. *J Chem Phys* **121**, 8618-8626, doi:10.1063/1.1798932 (2004).

163 Lauw, Y., Horne, M. D., Rodopoulos, T., Nelson, A. & Leermakers, F. A. Electrical double-layer capacitance in room temperature ionic liquids: ion-size and specific adsorption effects. *J Phys Chem B* **114**, 11149-11154, doi:10.1021/jp105317e (2010).

164 Si, X., Li, S., Wang, Y., Ye, S. & Yan, T. Effects of specific adsorption on the differential capacitance of imidazolium-based ionic liquid electrolytes. *Chemphyschem* **13**, 1671-1676, doi:10.1002/cphc.201200013 (2012).

165 Luo, Z. X., Xing, Y. Z., Ling, Y. C., Kleinhammes, A. & Wu, Y. Electroneutrality breakdown and specific ion effects in nanoconfined aqueous electrolytes observed by NMR. *Nat Commun* **6**, 6358, doi:10.1038/ncomms7358 (2015).

166 Kovtyukhova, N. I. *et al.* Layer-by-layer assembly of ultrathin composite films from micron-sized graphite oxide sheets and polycations. *Chemistry of materials* **11**, 771-778 (1999).

167 Pelekani, C. & Snoeyink, V. L. Competitive adsorption between atrazine and methylene blue on activated carbon: the importance of pore size distribution. *Carbon* **38**, 1423-1436 (2000).

168 Cheng, C. *et al.* Dynamic electrosorption analysis: a viable liquid-phase characterization method for porous carbon? *Journal of Materials Chemistry A* **1**, 9332, doi:10.1039/c3ta10801e (2013).

169 Zhu, J. *et al.* Dynamic electrosorption analysis as an effective means to characterise the structure of bulk graphene assemblies. *Chemistry* **19**, 3082-3089, doi:10.1002/chem.201203219 (2013).

170 Zhang, H. *et al.* Ultrafast selective transport of alkali metal ions in metal organic frameworks with subnanometer pores. *Science advances* **4**, eaaq0066 (2018).

171 Volkov, A., Paula, S. & Deamer, D. Two mechanisms of permeation of small neutral molecules and hydrated ions across phospholipid bilayers. *Bioelectrochemistry and Bioenergetics* **42**, 153-160 (1997).

172 Yuan-Hui, L. & Gregory, S. Diffusion of ions in sea water and in deep-sea sediments. *Geochimica et cosmochimica acta* **38**, 703-714 (1974).

173 Gil, P. S., Jorgenson, S. J., Riet, A. R. & Lacks, D. J. Relationships between Molecular Structure, Interfacial Structure, and Dynamics of Ionic Liquids near Neutral and Charged Surfaces. *The Journal of Physical Chemistry C* **122**, 27462-27468, doi:10.1021/acs.jpcc.8b08644 (2018).

174 Fumagalli, L. *et al.* Anomalously low dielectric constant of confined water. *Science* **360**, 1339-1342 (2018).

175 Conway, B. E. *Electrochemical supercapacitors: scientific fundamentals and technological applications*. (Springer Science & Business Media, 2013).

176 Andreas, H. A. & Conway, B. E. Examination of the double-layer capacitance of an high specific-area C-cloth electrode as titrated from acidic to alkaline pHs. *Electrochimica Acta* **51**, 6510-6520, doi:10.1016/j.electacta.2006.04.045 (2006).

177 Oh, Y. J. *et al.* Oxygen functional groups and electrochemical capacitive behavior of incompletely reduced graphene oxides as a thin-film electrode of supercapacitor. *Electrochimica Acta* **116**, 118-128, doi:10.1016/j.electacta.2013.11.040 (2014).

178 Liu, J.-L. & Eisenberg, B. Correlated ions in a calcium channel model: a Poisson–Fermi theory. *The Journal of Physical Chemistry B* **117**, 12051-12058 (2013).

179 Xia, Y. *et al.* Thickness-independent capacitance of vertically aligned liquid-crystalline MXenes. *Nature* **557**, 409-412, doi:10.1038/s41586-018-0109-z (2018).

180 Chun, S. E. *et al.* Design of aqueous redox-enhanced electrochemical capacitors with high specific energies and slow self-discharge. *Nat Commun* **6**, 7818, doi:10.1038/ncomms8818 (2015).

181 Sankar, K. V. & Kalai Selvan, R. Improved electrochemical performances of reduced graphene oxide based supercapacitor using redox additive electrolyte. *Carbon* **90**, 260-273, doi:10.1016/j.carbon.2015.04.023 (2015).

182 Benoit, C., Demeter, D., Belanger, D. & Cougnon, C. A Redox-Active Binder for Electrochemical Capacitor Electrodes. *Angew Chem Int Ed Engl* **55**, 5318-5321, doi:10.1002/anie.201601395 (2016).

183 Bard, A. J. & Faulkner, L. R. Fundamentals and applications. *Electrochemical Methods* **2**, 580-632 (2001).

184 Newman, J. & Thomas-Alyea, K. E. *Electrochemical systems*. (John Wiley & Sons, 2012).

185 Wang, F. *et al.* Highly reversible zinc metal anode for aqueous batteries. *Nature materials* **17**, 543-549 (2018).

186 Zheng, J. *et al.* Reversible epitaxial electrodeposition of metals in battery anodes. *Science* **366**, 645-648 (2019).

187 Liu, R. *et al.* A predictive machine learning approach for microstructure optimization and materials design. *Sci Rep* **5**, 11551, doi:10.1038/srep11551 (2015).

188 Raccuglia, P. *et al.* Machine-learning-assisted materials discovery using failed experiments. *Nature* **533**, 73-76, doi:10.1038/nature17439 (2016).

189 Segler, M. H. S., Preuss, M. & Waller, M. P. Planning chemical syntheses with deep neural networks and symbolic AI. *Nature* **555**, 604-610, doi:10.1038/nature25978 (2018).

190 Dănilă, E., Livint, G. & Lucache, D. D. in *2014 International Conference and Exposition on Electrical and Power Engineering (EPE).* 642-645 (IEEE).

191 Weigert, T., Tian, Q. & Lian, K. State-of-charge prediction of batteries and battery–supercapacitor hybrids using artificial neural networks. *Journal of Power Sources* **196**, 4061-4066, doi:10.1016/j.jpowsour.2010.10.075 (2011).